Universidad de Concepción
Dirección de Postgrado
Facultad de Ciencias Físicas y Matemáticas
Programa de Doctorado en Ciencias Aplicadas
con Mención en Ingeniería Matemática

MODELOS DE SEDIMENTACIÓN REACTIVA PARA EL TRATAMIENTO DE AGUAS SERVIDAS

MODELS OF REACTIVE SETTLING FOR WASTEWATER TREATMENT

Tesis para optar al grado de Doctor en Ciencias Aplicadas
con mención en Ingeniería Matemática

Romel Tarquino Pineda Frias

concepción-chile
2023

Profesor Guía: Dr. Raimund Bürger
CI^{2}MA y Departamento de Ingeniería Matemática
Universidad de Concepción, Chile

Cotutor: Dr. Stefan Diehl
Centre for Mathematical Sciences
Lund University, Sweden

Cotutor: Dr. Julio Careaga
Department of Mathematics
Radboud University, The Netherlands

Models of reactive settling for wastewater treatment

Romel Tarquino Pineda Frias

Directores de Tesis: Raimund Bürger, Universidad de Concepción, Chile.
Stefan Diehl, Lund University, Sweden.
Julio Careaga, Radboud University, The Netherlands.

Director de Programa: Raimund Bürger, Universidad de Concepción, Chile.

Comisión evaluadora

Prof.

Prof.

Prof.

Prof.

Comisión examinadora

Firma: _____
Prof.

Firma: _____
Prof.

Firma: _____
Prof.

Firma: _____
Prof.

Calificación: _____

Concepción, 09 de junio de 2023

Abstract

In this thesis, special emphasis is placed on the activated sludge process in reactive settling, in *secondary settling tanks* (SSTs) and *sequencing batch reactors* (SBRs). Among the topics covered are the development of a modern one-dimensional mathematical model and the implementation of numerical schemes to simulate reactive settling in the SBRs. The governing model consists of a coupled system of strongly degenerate parabolic convection-diffusion-reaction conservation law equations, with unknowns being the concentrations of solid (bacteria; activated sludge) and liquid (substrates) components as functions of height and time. It is also of interest to develop the fitting of experimental data obtained from a pilot SST with variable cross-sectional area to the model of reactive settling. The thesis has the following objectives:

First, to formulate a physical-mathematical model based on mass conservation equations to model the reactive settling process of the SBRs where the upper surface is a moving boundary.

Second, to develop a reliable numerical scheme (consistent and stable) for the governing equations derived from the first objective, considering a space discretization with a fixed number of cells across which the surface moves, and to demonstrate that the numerical scheme is monotone and satisfies an invariant region property (in particular, it preserves positivity) when executed in a simple splitting formulation.

Third, to fit a reactive settling model to experimental data from a pilot plant which has a variable cross-sectional area, where the model equations are extended, including additional terms for hydrodynamic dispersion and heuristic mixing.

Fourth, to perform an appropriate spatial transformation of the governing equations from the first objective to a fixed domain and discretize them using a monotone explicit scheme and a semi-implicit variant, formulations which among other advantages are easier to implement compared to the approach of the second objective.

Resumen

En esta tesis, se pone especial énfasis en el proceso de lodo activado en la sedimentación reactiva, en *tanques de sedimentación secundarios* (SSTs, por sus siglas en inglés) y *reactores por lotes secuenciales* (SBRs, por sus siglas en inglés). Entre los temas tratados se encuentran el desarrollo de un modelo matemático unidimensional moderno y la implementación de esquemas numéricos para simular la sedimentación reactiva en los SBRs. El modelo gobernante consiste en un sistema acoplado de ecuaciones de leyes de conservación parabólicas de convección-difusión-reacción fuertemente degeneradas, siendo las incógnitas las concentraciones de los componentes sólidas (bacterias; lodos activados) y líquidos (substratos) en función de la altura y el tiempo. También es de interés desarrollar el ajuste de datos experimentales obtenidos de un SST piloto con área de sección transversal variable al modelo de sedimentación reactiva. La tesis tiene los siguientes objetivos:

Primero, formular un modelo físico-matemático basado en ecuaciones de conservación de masa para modelar el proceso de sedimentación reactiva de los SBRs donde la superficie superior es una frontera móvil.

Segundo, desarrollar un esquema numérico confiable (consistente y estable) para las ecuaciones gobernantes derivadas del primer objetivo, considerando una discretización espacial con un número fijo de celdas a través de las cuales se mueve la superficie, y demostrar que el esquema numérico es monótono y satisface una propiedad de región invariante (en particular, preserva la positividad) cuando se ejecuta en una formulación de división simple.

Tercero, ajustar un modelo de sedimentación reactiva a datos experimentales de una planta piloto que tiene un área de sección transversal variable, donde las ecuaciones del modelo se extienden, incluyendo términos adicionales para la dispersión hidrodinámica y la mezcla heurística.

Cuarto, realizar una transformación espacial adecuada de las ecuaciones gobernantes del primer objetivo a un dominio fijo y discretizarlas utilizando un esquema explícito monótono y una variante semi-implícita, formulaciones que, entre otras ventajas, son más fáciles de implementar en comparación con el enfoque del segundo objetivo.

Agradecimientos

Proyectos de investigación y apoyo institucional

Esta tesis ha sido preparada en el marco y con el apoyo financiero de las siguientes instituciones y proyectos de investigación:

- Universidad de Concepción con la Beca de Estipendio durante el primer año de doctorado
- Agencia Nacional de Investigación y Desarrollo (ANID) a través de su programa de becas ANID-PCHA/Doctorado Nacional/2020-21200939
- Proyecto Anillo ANID/PIA/ACT210030
- Centro de Modelamiento Matemático con los proyectos BASAL ACE210010 y FB210005
- Proyecto Fondecyt 1210610
- Centro de Recursos Hídrico para la Agricultura y Minería (CRHIAM) con el proyecto ANID/FONDAP/15130015
- Consejo Sueco de Investigación (Vetenskapsrådet, 2019-04601)

Estoy profundamente agradecido por el apoyo recibido de cada una de las instituciones, así como también de los proyectos de investigación. Que han contribuido a la realización de esta tesis.

Romel Tarquino Pineda Frias

En primer lugar, agradezco a Dios por su bendición y permitirme llegar a este momento tan importante. Quiero agradecer a mi familia por todo el apoyo y aliento que me han brindado. A mis queridos padres, Teresa Frias y Hugo Pineda, por el apoyo incondicional a lo largo de este viaje; por ser los pilares más importantes de mi vida.

Quisiera expresar mi más sincero agradecimiento a mi director de tesis, el profesor Raimund Bürger, quien, además de ser el director del programa, me ha brindado valiosas enseñanzas como docente y ha sido un guía paciente durante el desarrollo de mi tesis.

A mi co-tutor, Stefan Diehl, le agradezco por darme la oportunidad de trabajar con él y por su incondicional apoyo en este trabajo. Su amabilidad y disposición para resolver todas mis dudas han sido fundamentales en el desarrollo de esta tesis.

A mi co-tutor, Julio Careaga, le agradezco su enorme paciencia y constante apoyo. Por estar pendiente de mis avances y brindarme sus valiosos consejos que han sido de gran ayuda.

Agradezco a mis profesores: Raimund Bürger, Leonardo Figueroa, Mauricio Sepúlveda, Gabriel Gatica, por sus enseñanzas y la cordialidad que me mostraron. Gracias al Centro de Investigación en Ingeniería Matemática ($\mathrm{CI}^2\mathrm{MA}$) de la Universidad de Concepción (UdeC) y a sus respectivos directores por proporcionarme un entorno académico estimulante y enriquecedor, así como acceso a las instalaciones y recursos necesarios durante mis estudios. De igual forma, gracias por toda su ayuda, al personal administrativo del $\mathrm{CI}^2\mathrm{MA}$ y del Departamento de Ingeniería Matemática de la UdeC, Cecilia, Jorge, Iván y Sra. Lorena Carrasco, Sra. Paola Castro, por su buena disposición de ayudarme siempre, así como su amabilidad.

A mi hermana Fernanda y su esposo Rogelio, gracias por su apoyo incondicional y constante aliento. De manera muy especial dedico esta tesis a mis padres y a mi sobrina Samira, que son mi fuente de inspiración y motivación constante. Agradezco también a mis amigos de Ecuador que se hicieron presentes: Tatiana, Isabel, Yesseña, Fabián, Patricio, Karla. Muchas gracias por haber estado ahí pendientes de mí y dándome aliento. Fui afortunado de conocer gente amable y solidaria durante mis estudios en Chile. Un agradecimiento especial a la Sra. Silvia Cortez por acogerme en su casa y estar pendiente de mí durante estos tres últimos años.

También mi agradecimiento para todas las personas que me brindaron su amistad en estos años, por hacer de mi estancia en Chile una gran experiencia. Gracias a todos los compañeros del doctorado, todos aquellos con los que compartí clases y/o agradables momentos de convivencia en el $\mathrm{CI}^2\mathrm{MA}$; en especial quiero agradecer a mis compañeros de generación: Jorge y Juan Paulo, con quienes pude compartir cursos y oficina. A Juan Paulo, gracias por brindarme tu amistad y todas esas charlas que teníamos, apoyarme durante todos estos años y sobre todo convertirte en un buen amigo para mí, así como innumerables buenos momentos compartidos. Ha sido muy grato compartir este camino con ustedes.

Romel Tarquino Pineda Frias

Contents

List of Tables

List of Figures

Introduction

Motivation

Water scarcity is a problem that affects more than 40 percent of the world's population. As a result, the situation is likely to worsen as the world's population continues to grow. For this reason, the United Nations General Assembly in 2015 adopted the so-called 2030 Agenda for Sustainable Development, which set out *17 Sustainable Development Goals* covering the economic, social and environmental spheres [91]. This research aims to contribute to the environmental theme. Specifically, Sustainable Development Goal No. 6 [92] refers to *"Ensure availability and sustainable management of water and sanitation for all"*, and one of its targets is to improve water quality by halving pollution from untreated wastewater, which implies a significant decrease of pollution in water bodies. The implementation of mathematical strategies and engineering techniques in wastewater treatment can be essential to achieve this goal, thus contributing to the overall well-being and sustainable development of communities. In this sense, the contribution of this PhD thesis is to provide reliable computational simulators for wastewater treatment.

In a biological wastewater treatment plant, the activated sludge process (ASP) is the most widely used technology for biological removal of nutrients and reduction of organic material. A key component in this process is reactive settling, which consists of a solid and liquid phase, each composed of several components. The solid phase contains solid particulate components (bacteria; activated sludge), which can be organic and inorganic compounds. The liquid phase is composed of water, which contains substrates (nutrients) diluted in the water.

Reactive settling combines the sedimentation of small solid particles that are immersed in a fluid (composed of substrates and water) and the simultaneous occurrence of biological reactions between the components of both phases. A significant part of the biological reactions in the activated sludge process for wastewater treatment takes place in the *secondary settling tanks* (SSTs) that follow the biological reactors in a treatment plant. These reactions also occur in *sequencing batch reactors* (SBRs) during the sedimentation stage. Therefore, it is of interest to develop so-called reactive settling models that describe the biological reactions that take place in the sludge blanket of the settler.

An SBR is a tank (with a possibly variable cross-sectional area) used for wastewater treatment

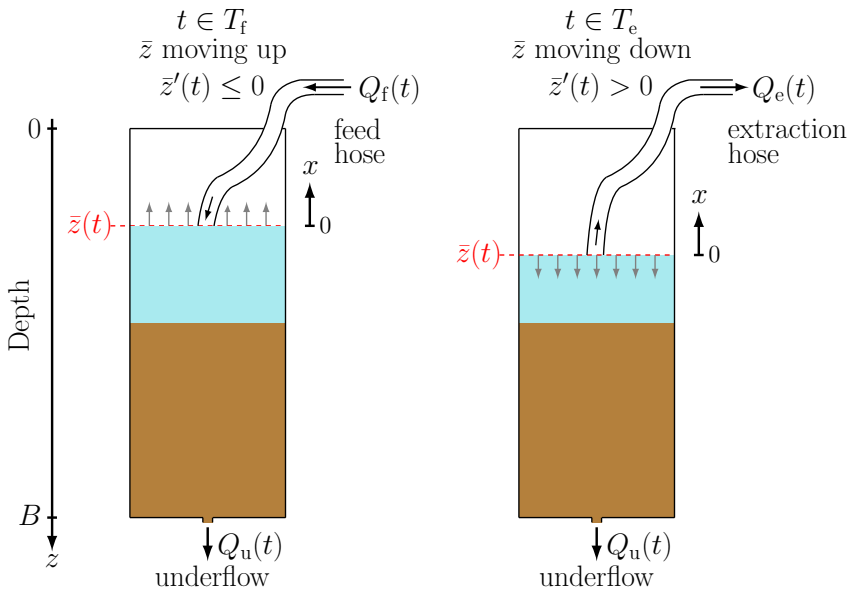

Figure 1: Illustration of an SBR in the two stages that involve flow through the hose: (left) feed and (right) extraction. The boundary $\bar{z}$ moves upward at time t when $\bar{z}'(t) < 0$ and downward when $\bar{z}'(t) > 0$, and T_f and T_e are the feed and extraction time intervals, respectively.

(e.g., [30, 46, 89]). This system has a controlled outlet at the bottom and a floating device at the surface of the mixture that allows for controlled filling or removal of the mixture (see Figure 1). The operation of an SBR is batchwise in a sequence of filling, reaction, settling, extraction and idle cycles (see Figure 2). The mixture consists of flocculated biomass particles with various components that react with the substrates dissolved in the liquid. One of the objectives of SBR is to quantify and remove the substrates from the liquid phase.

The process of an SBR works as follows: Initially, the tank is filled with wastewater with a volumetric flow rate $Q_\mathrm{f}(t) > 0$ and feed concentrations $\boldsymbol{C}_\mathrm{f}(t)$, $\boldsymbol{S}_\mathrm{f}(t)$ of solid particles and substrates, respectively, which causes the surface of the mixture to rise. After filling, reactions take place; during this stage, biological reactions occur under complete mixing by means of an impeller or by aeration to homogenize the mixture. A time interval is allowed for the biochemical reactions to take place. This is followed by the sedimentation stage, in which the settle and form a sludge layer. Then the clarified liquid is extracted and, at the same time, the surface of the mixture is lowered. Finally, the system is left idle and part of the sludge is removed via the controlled outlet at the bottom of the tank. In this way, the tank is prepared to receive another operational cycle.

In this research, a mathematical model and numerical schemes for multicomponent reactive settling of flocculated particles in SBRs are developed, as detailed in Chapter 1, 2 and 4. The governing model consists of the following assumptions and variables. We let $A(z)$ denote the cross-sectional area of the tank that may depend on depth z, where the top of the

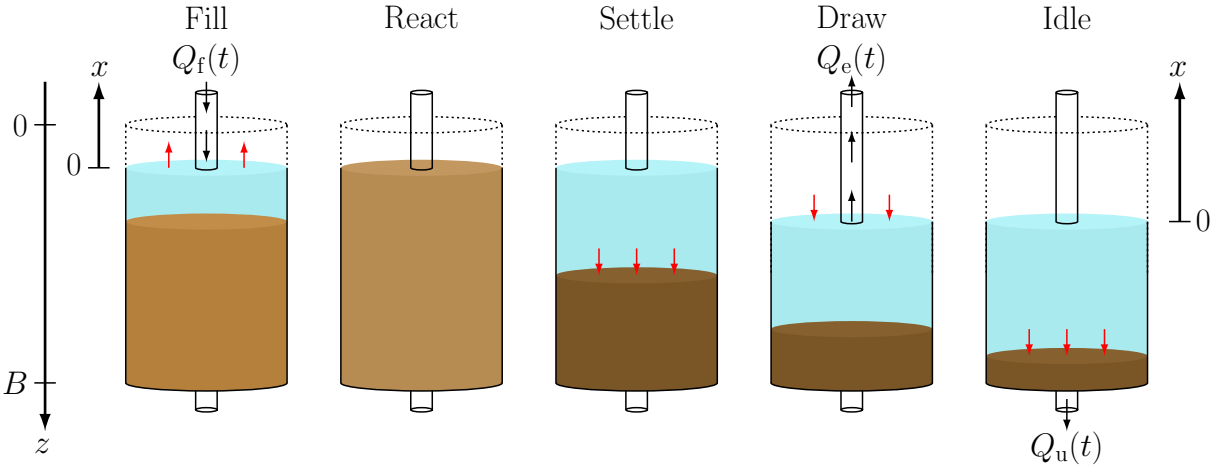

Figure 2: Schematic of the five stages of an SBR. The red arrows show the movement of the boundary or the sediment level during each stage. The black arrows show the direction of the bulk flows Q_{f} (feed), Q_{e} (extraction) and Q_{u} (underflow).

tank is at $z = 0$ and the bottom is at $z = B$. The characteristic function γ equals one inside the mixture and zero otherwise, i.e., $\gamma(z,t) = \chi_{\{\bar{z}(t)<z<B\}}$, where χ_I is the indicator function which equals one if and only if I is true, $z = \bar{z}(t)$ is the position of the surface of the mixture and t is time. The unknowns are the vectors $\boldsymbol{C} = \boldsymbol{C}(z,t) = (C^{(1)}, \ldots, C^{(k_{\boldsymbol{C}})})^{\mathrm{T}}$ of solids concentrations and $\boldsymbol{S} = \boldsymbol{S}(z,t) = (S^{(1)}, \ldots, S^{(k_{\boldsymbol{S}})})^{\mathrm{T}}$ concentration of soluble components. These vectors make up the components of the solid and liquid phase, respectively. With $X = X(z,t) = c(C^{(1)}(z,t) + \cdots + C^{(k_{\boldsymbol{C}})}(z,t))$, where c is a conversion factor. The reactive settling process can be modeled by the following system of convection-diffusion-reaction equations, where $t > 0$ and by $z \in \mathbb{R}$:

$$\begin{aligned} A(z)\frac{\partial \boldsymbol{C}}{\partial t} + \frac{\partial}{\partial z}\big(A(z)\mathcal{V}_{\boldsymbol{C}}(X, \partial_z X, z, t)\boldsymbol{C}\big) &= \delta\big(z - \bar{z}(t)\big)Q_{\mathrm{f}}(t)\boldsymbol{C}_{\mathrm{f}}(t) + \gamma(z,t)A(z)\boldsymbol{R}_{\boldsymbol{C}}(\boldsymbol{C}, \boldsymbol{S}), \\ A(z)\frac{\partial \boldsymbol{S}}{\partial t} + \frac{\partial}{\partial z}\big(A(z)\mathcal{V}_{\boldsymbol{S}}(X, \partial_z X, z, t)\boldsymbol{S}\big) &= \delta\big(z - \bar{z}(t)\big)Q_{\mathrm{f}}(t)\boldsymbol{S}_{\mathrm{f}}(t) + \gamma(z,t)A(z)\boldsymbol{R}_{\boldsymbol{S}}(\boldsymbol{C}, \boldsymbol{S}). \end{aligned} \tag{1}$$

This system is coupled to a model of the effluent pipe consisting of convective transport equations on a half-line $x \geq 0$, where $x = 0$ is attached to the moving boundary $z = \bar{z}(t)$ (cf. Figure 1). The coupling conditions between the systems are mass-preserving algebraic equations with fluxes on the z- and x-axes. The scalar functions $\mathcal{V}_{\boldsymbol{C}}$ and $\mathcal{V}_{\boldsymbol{S}}$ in (1) are nonlinear velocity functions that depend on X and represent the solid and liquid phase velocity, respectively. The terms with the delta function $\delta(z - \bar{z}(t))$ model the operation of the floating device on the surface during the feed of mixture. The last term of each partial differential equation (PDE) in (1) contains the reaction rates (local increase of mass per unit time and volume) $\boldsymbol{R}_{\boldsymbol{C}}$ and $\boldsymbol{R}_{\boldsymbol{S}}$ for the solid and soluble components, respectively. All ingredients are specified in detail in Chapter 1. The model equations in (1) are supplied with suitable initial conditions and no boundary conditions are required because the nonlinear convective and diffusive fluxes are considered to be zero at the pipes.

Related Work

SBR technology has been used for several decades and has been a subject of intense research [101]. Its use for wastewater treatment is outlined in many handbooks (e.g., [30, 46, 89]). Furthermore, it is also employed for recovery of selenium [102], radioactively labeled pharmaceuticals [98], nitrogen removal processes [94], pharmaceutically active compounds [106], synthetic chemical components [66], swine manure slurry [87], applications in the petrochemical industry [27], and saline wastewater treatment [5] among others.

Most of the literature on mathematical models related to SBRs focus on ordinary differential equations (ODEs) that model the reactions using established models of activated sludge [53, 63, 74, 88]. Other studies are dedicated to solving optimization and control problems [54, 76, 96, 97, 103], and to the developing of statistical methods [81, 82]. Less attention has been paid to sedimentation in an SBR during which reactions occur. Models of reactive settling in continuously operating SSTs based on PDEs are presented in [12, 13, 23] (see also references cited in these papers). The Bürger-Diehl model for non-reactive settling in cylindrical vessels is introduced in [20, 24], and the extension to vessels with variable cross-section area can be found in [11]. It is important to mention that the SBR model differs from an SST model. In an SBR, $Q_{\mathrm{u}}(t)$, $Q_{\mathrm{f}}(t)$ and $Q_{\mathrm{e}}(t)$ are independently given control functions that give rise to a moving surface, whereas in an SST, only two of them are known and the third, often $Q_{\mathrm{e}}(t)$, is defined by the other two and possibly by volume-changing reactions in the tank [24].

Models for SBRs with reactions during all stages, including the settle, have rarely been proposed in the literature. ODEs are used for reactions outside the settle stage, which is either not included in the analysis (e.g., [10, 32]), or is assumed to occur during a fixed time interval without any reaction (e.g., [100, 103]), or is modeled without the well-known nonlinear behavior of sedimentation; e.g., [67]. Chauvon et al. [29] use the sedimentation-compression PDEs model by Bürger et al. [26] with constitutive functions by DeClercq [36] for the settling stage. They simulate the reaction-sedimentation process during the sedimentation stage avoiding modeling the moving boundary. Models of reactive settling in continuously operating SSTs based on PDEs and their respective numerical approximations are presented in [12, 13, 23]. However, none of these models include a moving boundary, which is the main problem addressed in Chapters 1, 2 and 4.

The location of the moving boundary is not an unknown, so the problem is different from, for example, Stefan-type problems. The present type of problem, where the moving boundary is known, and a Cartesian space grid is used for the numerical scheme, is common in two or three dimensions and several types of "built-in" boundary methods have been developed. See in [8], where the authors provide a review with references to different types of approaches, some of which are non-conservative, while conservative methods include 'cell cutting', 'flow redistribution' and 'cell merging' techniques. The main idea of conservative techniques is to use standard numerical fluxes for the cartesian mesh of the problem at hand, and to adjust these

fluxes carefully near the boundary using detailed information on the geometry of the cutting cell and its velocity. This is precisely what we do in Chapter 2 for the SBR problem, where the "standard" fluxes are those of the presented numerical scheme [12] when there is no moving boundary. An additional challenge in the model formulation of SBRs and in the derivation of an appropriate numerical scheme involves addressing the source/sink that is placed on the moving boundary. Although in normal operation only liquid is extracted through the pipe in the extraction phase, the model and numerical scheme proposed here are able to handle any concentration at the surface of the mixture.

The moving-boundary problem (1) has a connected semi-axis with mass-preserving non-linear transport equations and coupling conditions that do not define the coupling concentrations uniquely. This non-uniqueness problem already arises for a scalar conservation law with discontinuous flux (fixed boundary), which has been extensively investigated [1, 7, 42, 56, 71, 72]; in particular, in the context of continuous sedimentation [11, 26, 28, 43, 44] where a monotone numerical scheme properly approximates the physically relevant solutions [26]. Specifically, for the nonlinear PDEs systems presented here, the existence and uniqueness of entropy solutions has not yet been established; the existence of solutions is obtained by proving the convergence of numerical solutions obtained by a monotone scheme.

One-dimensional simulation models based on numerical schemes for PDEs governing non-reactive continuous sedimentation in wastewater treatment and water reclamation facilities (WRRFs) have been studied extensively, see, for example, [6, 26, 28, 37, 39, 43]. Non-reactive models that address the vessel geometry as a function of varying cross-sectional area include those of [11, 28, 44]. The relevance of studying the reactions occurring in SSTs has been raised by numerous authors [3, 50, 53, 55, 57, 59, 63, 74, 77, 83, 88, 95].

Motivated by the results of [77, 78] and their experimental data, which are also gratefully used in this thesis. Kirim [77] expands the so-called Bürger-Diehl model [20, 24] to include the activated sludge model no. 1 (ASM1) biokinetic [63] and an SST with a variable cross-sectional area. In Chapter 3, the model of [12] is described, which can be stated as a system of convection-diffusion-reaction PDEs where the unknowns are the particulate and dissolved components of the ASM1. The simultaneous identification of the hindered settling velocity and compression functions from experimental data of non-reactive settling, and the elimination of the induction period have been studied by [36, 45, 105]. More elaborate methods for measuring the concentration of solid particles in the whole tank are presented by [38, 52, 84].

The model presented in this thesis (1) considers the movement of the boundary due to the volumetric flows in the SBR stages. A conservative and positivity-preserving numerical scheme developed on a fixed mesh grid was introduced in [16]. The scheme of [16] employs careful mass distributions in cells near the moving boundary to ensure the conservation of mass. The trajectory of $\bar{z}(t)$ is given, and not part of the solution of the problem, so the governing PDE model (1) is a moving boundary problem, but not a free boundary problem. Nevertheless, extensions of the SBR model to a free boundary problem are conceivable. Finally, we mention

that the formulation and partial analysis of the semi-implicit scheme presented in Chapter 4 is based on analyses of schemes of that type for degenerate parabolic PDE in [19, 48].

Organization of this thesis

The present research work is organized as follows:

In Chapter 1, the governing equations for a reactive settling model in sequencing batch reactors used in wastewater treatment plants are introduced. Modeling an SBR involves a system of strongly degenerate one-dimensional convection-diffusion-reaction parabolic equations. This system is coupled by mass conservation conditions to transport equations on a half-line, whose origin is located on a moving boundary and which model the effluent conduit. Numerical simulations illustrate the simplified denitrification process in the absence of oxygen and are obtained using the numerical method developed in Chapter 2.

The contents of Chapter 1 correspond to the article [15]:

- R. Bürger, J. Careaga, S. Diehl, and R. Pineda, *A moving-boundary model of reactive settling in wastewater treatment. part 1: Governing equations*, Appl. Math. Model., 106 (2022), pp. 390–401.

In Chapter 2, a numerical scheme is developed for the governing equations modeling the SBR process, presented in Chapter 1. A monotone explicit numerical scheme is formulated to approximate the solutions, and it is proven that this scheme satisfies an invariant region property, implying that the concentrations of solids and substrates maintain non-negative values. This approach ensures the stability and accuracy of the numerical solutions. Simulations using the ASM1 are presented. Additionally, simulations of effluent concentrations for different computational cell numbers are shown.

The contents of Chapter 2 correspond to the article [16]:

- R. Bürger, J. Careaga, S. Diehl, and R. Pineda, *A moving-boundary model of reactive settling in wastewater treatment. part 2: Numerical scheme*, Appl. Math. Model., 111 (2022), pp. 247–269.

In Chapter 3, a reactive settling model for SSTs is fitted to experimental data obtained from a pilot plant with a variable cross-sectional area. The model proposed in reference [12] is used, including hydrodynamic dispersion terms for flocculated particles in suspension and dissolved substrates in the fluid, as well as a term modeling the mixing of the suspension near the feed inlet. For the reactions, the ASM1 model with standard coefficients adjusted to the pilot plant temperature is used. Finally, simulations for one of the steady-state scenarios are presented.

The contents of Chapter 3 correspond to the article [17]:

- R. Bürger, J. Careaga, S. Diehl, and R. Pineda, *A model of reactive settling of activated sludge: Comparison with experimental data*, Chem. Eng. Sci., 267 (2023), p. 118244.

In Chapter 4, the model presented in Chapter 1 is reformulated using a spatial transformation into a fixed domain problem. In addition, two alternative numerical schemes to the one described in Chapter 2 are introduced. The model is discretized using a monotone explicit scheme together with an alternative semi-implicit variant. It is shown that the semi-implicit scheme is well-posed and that both variants generate approximations that satisfy an invariant region principle, which is achieved under a Courant-Friedrichs-Lewy (CFL) condition that is less restrictive for the semi-implicit scheme than for the explicit one. Finally, numerical examples with realistic parameters are presented to illustrate that, as one of the outcomes, the semi-implicit variant is more efficient than the explicit scheme.

The contents of Chapter 4 correspond to the following submitted manuscript [14]:

- R. Bürger, J. Careaga, S. Diehl, and R. Pineda, *Numerical schemes for a moving-boundary convection-diffusion-reaction model of sequencing batch reactors*. Preprint 2023–11, Centro de Investigación en Ingeniería Matemática (CI^{2}MA), Universidad de Concepción, Chile.

In Table 1, the models used in this thesis are summarized, including those related to SBR and SST, as well as the biokinetic processes employed and their respective numerical methods. The "SBR2" method refers to the one described in [16].

Table 1: Summary of the structure and contents of the doctoral thesis

Chapter	Process design	Biokinetic model	Numerical method
1 [15]	SBR	Denitrification	"SBR2" (fixed mesh size)
2 [16]	SBR	ASM1 (without alkalinity)	"SBR2" (fixed mesh size)
3 [17]	SST	ASM1 (complete)	MOL formulation [12]
4 [14]	SBR	ASM1 (modified)	Explicit & semi-implicit methods, variable mesh size

Introducción

Motivación

La escasez de agua es un problema que afecta a más del 40 por ciento de la población mundial. Como resultado, es probable que la situación empeore a medida que la población mundial continué aumentando. Por esta razón, la Asamblea General de la Organización de las Naciones Unidas adoptó en 2015 la llamada Agenda 2030 para el Desarrollo Sostenible, que establece *17 Objetivos de Desarrollo Sostenible* que abarcan los ámbitos económicos, social y ambiental [91]. Esta investigación tiene como objetivo contribuir al tema ambiental. Específicamente, el Objetivo de Desarrollo Sostenibles Nro. 6 [92] se refiere a *"Garantizar la disponibilidad y gestión sostenible del agua y el saneamiento para todos"*, y una de sus metas es mejorar la calidad del agua reduciendo a la mitad la contaminación de las aguas residuales no tratadas, lo que implica una disminución significativa de la contaminación en los cuerpos hídricos. La implementación de estrategias matemáticas y técnicas de ingeniería en el tratamiento de aguas residuales puede ser esencial para alcanzar este objetivo, contribuyendo así al bienestar general y al desarrollo sostenible de las comunidades. En este sentido, la contribución de esta tesis doctoral es proporcionar simuladores computacionales confiables para el tratamiento de aguas residuales.

En una planta de tratamientos biológicos de aguas residuales, el proceso de lodos activados (ASP, por sus siglas en inglés) es la tecnología más utilizada para la eliminación biológica de nutrientes y la reducción de la materia orgánica. Un componente clave en este proceso es la sedimentación reactiva, que consta de una fase sólida y líquida, cada una compuesta por varios componentes. La fase sólida contiene componentes sólidos particulados (bacterias; lodos activados), que pueden ser compuestos orgánicos e inorgánicos. La fase líquida está compuesta de agua, que contiene sustratos (nutrientes) diluidos en el agua.

La sedimentación reactiva combina la sedimentación de pequeñas partículas sólidas que están inmersas en un fluido (compuestos por sustratos y agua) y la ocurrencia simultánea de reacciones biológicas entre los componentes de ambas fases. Una parte significativa de las reacciones biológicas en el proceso de lodos activados para el tratamiento de aguas residuales tiene lugar en los *tanques de sedimentación secundarios* (SSTs, por sus siglas en inglés) que siguen a los reactores biológicos en una planta de tratamiento. Estas reacciones también ocurren en *reactores*

por lotes secuenciales (SBRs, por sus siglas en inglés) durante la etapa de sedimentación. Por lo tanto, es de interés desarrollar los llamados modelos de sedimentación reactiva que describen las reacciones biológicas que tienen lugar en el manto de lodo del sedimentador.

Un SBR es un tanque (con un área de sección transversal posiblemente variable) utilizado para el tratamiento de aguas residuales (por ejemplo, [30, 46, 89]). Este sistema tiene una salida controlada en el fondo y un dispositivo flotante en la superficie de la mezcla que permite el llenado o la extracción controlada de la mezcla (véase la Figura 3). La operación de un SBR es por lotes en una secuencia de ciclos de llenado, reacción, sedimentación, extracción e inactividad (véase la Figura 4). La mezcla consiste en partículas de biomasa floculada con varios componentes que reaccionan con los sustratos disueltos en el líquido. Uno de los objetivos del SBR es cuantificar y eliminar los sustratos de la fase líquida.

El proceso de un SBR funciona de la siguiente manera: Inicialmente, se llena el tanque con aguas residuales con una tasa de flujo volumétrico $Q_{\mathrm{f}}(t) > 0$ y concentraciones de alimentación $\boldsymbol{C}_{\mathrm{f}}(t)$, $\boldsymbol{S}_{\mathrm{f}}(t)$ de partículas sólidas y sustratos, respectivamente, lo que provoca que la superficie de la mezcla aumente. Después del llenado, tiene lugar las reacciones; durante esta etapa, las reacciones biológicas ocurren bajo una mezcla completa mediante un impulsor o por aireación para homogeneizar la mezcla. Se espera un intervalo de tiempo para que las reacciones bioquímicas puedan ocurrir. A continuación, sucede la etapa de sedimentación, en la que los sedimentos se asientan y forman una capa de lodo. Luego se extrae el líquido clarificado y, al mismo tiempo, se baja la superficie de la mezcla. Finalmente, el sistema se deja inactivo y se elimina parte del lodo a través de la salida controlada en la parte inferior del tanque. De este manera, el tanque queda preparado para recibir otro ciclo operacional.

En esta investigación, se desarrolla un modelo matemático y esquemas numéricos para la sedimentación reactiva multicomponente de partículas floculadas en SBRs, como se detalla en Capítulos 1, 2 y 4. El modelo gobernante consta de las siguientes suposiciones y variables. Sea $A(z)$ el área de la sección transversal del tanque que puede depender de la profundidad z, donde la parte superior del tanque está en $z = 0$ y el fondo está en $z = B$. La función característica γ es igual a uno en el interior de la mezcla y cero en caso contrario, es decir, $\gamma(z,t) = \chi_{\{\bar{z}(t)<z<B\}}$, donde χ_I es la función indicatriz que es igual a uno si y solo si I es verdadero, $z = \bar{z}(t)$ es la posición de la superficie de la mezcla y t es el tiempo. Las incógnitas son los vectores $\boldsymbol{C} = \boldsymbol{C}(z,t) = (C^{(1)}, \ldots, C^{(k_{\boldsymbol{C}})})^{\mathrm{T}}$ de concentraciones de sólidas y $\boldsymbol{S} = \boldsymbol{S}(z,t) = (S^{(1)}, \ldots, S^{(k_{\boldsymbol{S}})})^{\mathrm{T}}$ concentraciones de componentes solubles. Estos vectores constituyen los componentes de la fase sólida y líquida, respectivamente. Con $X = X(z,t) = c(C^{(1)}(z,t) + \cdots + C^{(k_{\boldsymbol{C}})}(z,t))$, donde c es un factor de conversión. El proceso de sedimentación reactiva puede ser modelado por el siguiente sistema de ecuaciones de convección-difusión-reacción, donde $t > 0$ y por $z \in \mathbb{R}$:

$$\begin{aligned} A(z)\frac{\partial \boldsymbol{C}}{\partial t} + \frac{\partial}{\partial z}\big(A(z)\mathcal{V}_{\boldsymbol{C}}(X, \partial_z X, z, t)\boldsymbol{C}\big) &= \delta\big(z - \bar{z}(t)\big)Q_{\mathrm{f}}(t)\boldsymbol{C}_{\mathrm{f}}(t) + \gamma(z,t)A(z)\boldsymbol{R}_{\boldsymbol{C}}(\boldsymbol{C}, \boldsymbol{S}), \\ A(z)\frac{\partial \boldsymbol{S}}{\partial t} + \frac{\partial}{\partial z}\big(A(z)\mathcal{V}_{\boldsymbol{S}}(X, \partial_z X, z, t)\boldsymbol{S}\big) &= \delta\big(z - \bar{z}(t)\big)Q_{\mathrm{f}}(t)\boldsymbol{S}_{\mathrm{f}}(t) + \gamma(z,t)A(z)\boldsymbol{R}_{\boldsymbol{S}}(\boldsymbol{C}, \boldsymbol{S}). \end{aligned} \tag{2}$$

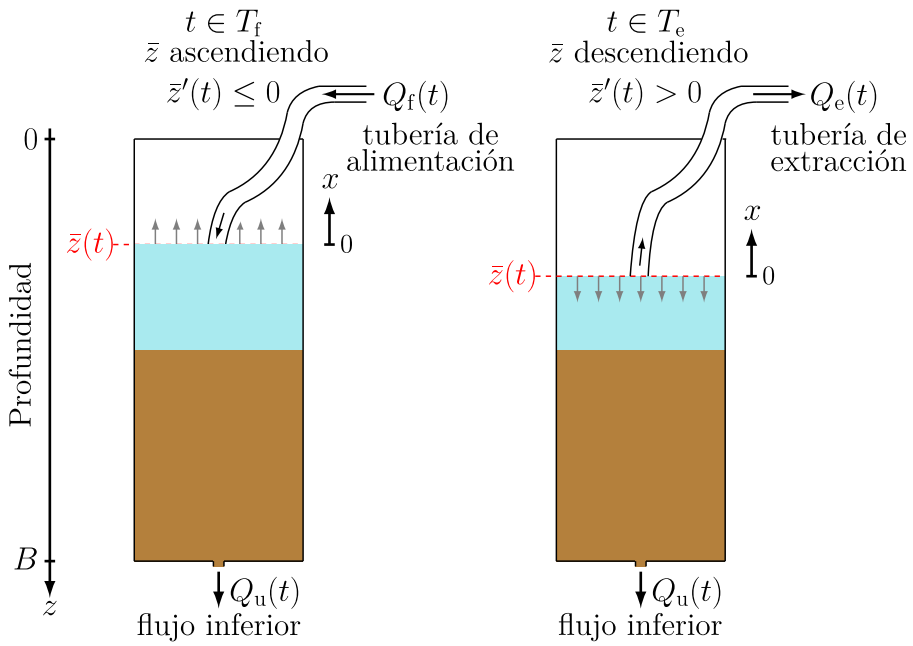

Figure 3: Ilustración de un SBR en las dos etapas que implican el flujo a través de la tubería: (izquierda) alimentación y (derecha) extracción. El límite $\bar{z}$ se mueve hacia arriba en el tiempo t cuando $\bar{z}'(t) < 0$ y hacia abajo cuando $\bar{z}'(t) > 0$, y T_f y T_e son los intervalos de tiempo de alimentación y extracción, respectivamente.

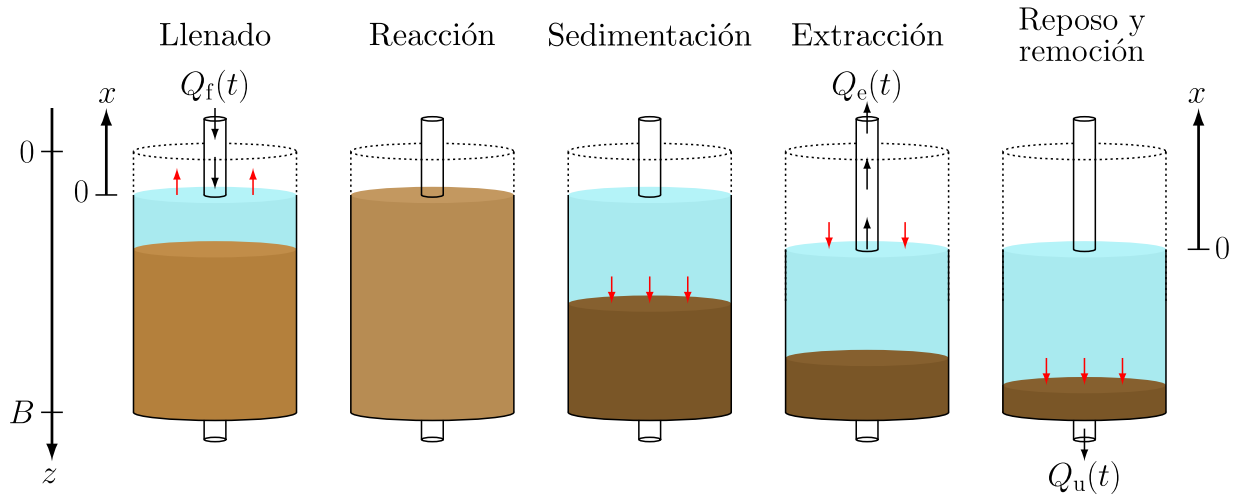

Figure 4: Esquema de las cinco etapas de un SBR. Las flechas rojas muestran el movimiento de la frontera o del nivel de sedimentos durante cada etapa. Las flechas negras muestran la dirección de los flujos Q_f (alimentación), Q_e (extracción) y Q_u (flujo inferior).

Este sistema está acoplado a un modelo de tubería de efluente que consiste en ecuaciones de transporte convectivo en una semirrecta $x \ge 0$, donde $x = 0$ está conectado a la frontera móvil $z = \bar{z}(t)$ (véase la Figura 3). Las condiciones de acoplamiento entre los sistemas son ecuaciones algebraicas conservadoras de masa con flujos en los ejes z y x. Las funciones escalares

$\mathcal{V}_{\boldsymbol{C}}$ y $\mathcal{V}_{\boldsymbol{S}}$ en (2) son funciones de velocidad no lineales que dependen de X y representan la velocidad de la fase sólida y líquida, respectivamente. Los términos con la función delta $\delta(z - \bar{z}(t))$ modelan el funcionamiento del dispositivo flotante en la superficie durante la alimentación de la mezcla. El último término de cada ecuación diferencial parcial (EDP) en (2) contiene las tasas de reacción (aumento local de masa por unidad de tiempo y volumen) $\boldsymbol{R}_{\boldsymbol{C}}$ y $\boldsymbol{R}_{\boldsymbol{S}}$ para los componentes sólidos y solubles, respectivamente. Todos los ingredientes se especifican en detalle en el Capítulo 1. Las ecuaciones del modelo en (2) se proporcionan con condiciones iniciales adecuadas y no se requieren condiciones de frontera porque los flujos convectivos y difusivos no lineales se consideran cero en las tuberías.

Trabajo relacionado

La tecnología SBR se utiliza desde hace varias décadas y ha sido tema de intensa investigación [101]. Su uso para el tratamiento de aguas residuales se describe en muchos manuales (por ejemplo, [30, 46, 89]). Además, también se emplea para la recuperación de selenio [102], productos farmacéuticos marcados radiactivamente [98], procesos de eliminación de nitrógeno [94], compuestos farmacéuticamente activos [106], componentes químicos sintéticos [66], purines de cerdo [87], aplicaciones en la industria petroquímica [27], y tratamiento de aguas residuales salinas [5] entre otros.

La mayor parte de la literatura sobre modelos matemáticos relacionados con los SBRs se centran en ecuaciones diferenciales ordinarias (EDOs) que modelan las reacciones utilizando modelos establecidos de lodos activados [53, 63, 74, 88]. Otros estudios se dedican a resolver problemas de optimización y control [54, 76, 96, 97, 103], y al desarrollo de métodos estadísticos [81, 82]. Se ha prestado menos atención a la sedimentación en un SBR durante la cual se producen reacciones. Los modelos de sedimentación reactiva en SST de funcionamiento continuo basados en EDPs se presentan en [12, 13, 23] (ver también las referencias citadas en estos trabajos). El modelo de Bürger-Diehl para la sedimentación no reactiva en recipientes cilíndricos se introduce en [20, 24], y la extensión a recipientes con área de sección transversal variable puede encontrarse en [11]. Es importante mencionar que el modelo SBR difiere de un modelo SST. En un SBR, $Q_{\mathrm{u}}(t)$, $Q_{\mathrm{f}}(t)$ y $Q_{\mathrm{e}}(t)$ son funciones de control dadas independientemente que dan lugar a una superficie móvil, mientras que en un SST, solo se conocen dos de ellas y la tercera, a menudo $Q_{\mathrm{e}}(t)$, viene definida por las otras dos y posiblemente por reacciones que cambian de volumen en el tanque [24].

Los modelos para SBRs con reacciones durante todas las etapas, incluida la sedimentación, rara vez se han propuesto en la literatura. Se utilizan EDOs para las reacciones fuera de la etapa de sedimentación, que no se incluye en el análisis (por ejemplo, [10, 32]), o se supone que ocurre durante un intervalo de tiempo fijo sin ninguna reacción (por ejemplo, [100, 103]), o se modela sin el comportamiento no lineal de sedimentación; por ejemplo, [67]. Chauvon et al. [29] emplean el modelo de sedimentación-compresión por EDPs de de Bürger et al. [26] con

funciones constitutivas de DeClercq [36] para la etapa de sedimentación. Simulan el proceso de reacción-sedimentación durante la etapa de sedimentación evitando modelar la frontera móvil. Los modelos de sedimentación reactiva en SSTs de funcionamiento continuo basados en EDPs y sus respectivas aproximaciones numéricas se presentan en [12, 13, 23]. Sin embargo, ninguno de estos modelos incluye una frontera móvil, que es el principal problema abordado en los Capítulos 1, 2 y 4.

La ubicación de la frontera móvil no es desconocida, por lo que el problema es diferente de, por ejemplo, los problemas de tipo Stefan. El presente tipo de problema, en el que se conoce la frontera móvil y se utiliza una malla espacial cartesiana para el esquema numérico, es común en dos o tres dimensiones y se han desarrollado varios tipos de métodos de frontera "incorporada". Véase en [8], donde los autores proporcionan una revisión con referencias a diferentes tipos de enfoques, algunos de los cuales no son conservadores, mientras que los métodos conservadores incluyen técnicas de 'corte de celdas', 'redistribución de flujos' y 'fusión de celdas'. La idea principal de las técnicas conservadoras es usar flujos numéricos estándar para la malla cartesiana del problema en cuestión, y ajustar estos flujos cuidadosamente cerca de la frontera utilizando información detallada sobre la geometría de la celda de corte y su velocidad. Esto es precisamente lo que hacemos en el Capítulo 2 para el problema del SBR, donde los flujos "estándar" son los del esquema numérico presentado [12] cuando no hay frontera móvil. Un reto adicional en la formulación del modelo de SBRs y en la derivación de un esquema numérico apropiado implica abordar la fuente/sumidero que se sitúa en la frontera móvil. Aunque en funcionamiento normal solo se extrae líquido a través de la tubería en la fase de extracción, el modelo y el esquema numérico propuesto aquí son capaces de manejar cualquier concentración en la superficie de la mezcla.

El problema de frontera móvil (2) tiene un semieje conectado con ecuaciones de transporte no lineales que preservan la masa y condiciones de acoplamiento que no definen unívocamente las concentraciones de acoplamiento. Este problema de no unicidad ya se plantea para una ley de conservación escalar con flujo discontinuo (frontera fija), que ha sido ampliamente investigado [1, 7, 42, 56, 71, 72]; en particular, en el contexto de la sedimentación continua [11, 26, 28, 43, 44] donde un esquema numérico monótono aproxima adecuadamente las soluciones físicamente relevantes [26]. Específicamente, para los sistemas de EDPs no lineales aquí presentados, aún no se ha establecido la existencia y unicidad de soluciones de entropía; la existencia de soluciones se obtiene probando la convergencia de las soluciones numéricas obtenidas por un esquema monótono.

Los modelos de simulación unidimensionales basados en esquemas numéricos para las EDPs que gobiernan la sedimentación continua no reactiva en instalaciones de tratamiento de aguas residuales y recuperación de recursos hídricos (WRRF, por sus siglas en inglés) se han estudiado ampliamente, véase, por ejemplo, [6, 26, 28, 37, 39, 43]. Los modelos no reactivos que abordan la geometría del recipiente en función de la variación del área de la sección transversal incluyen los de [11, 28, 44]. La relevancia de estudiar las reacciones que ocurren en los SST ha sido planteada por numerosos autores [3, 50, 53, 55, 57, 59, 63, 74, 77, 83, 88, 95].

Motivados por los resultados de [77, 78] y en sus datos experimentales, que también se utilizan con gratitud en esta tesis. Kirim [77] amplía el llamado modelo de Bürger-Diehl [20, 24] para incluir el modelo de lodos activados no. 1 (ASM1) biocinético [63] y un SST con área de sección transversal variable. En el Capítulo 3, se describe el modelo de [12], que puede enunciarse como un sistema de EDPs de convección-difusión-reacción donde las incógnitas son los componentes particulados y disueltos del ASM1. La identificación simultánea de las funciones de velocidad de sedimentación-obstaculizada y de compresión a partir de datos experimentales de sedimentación no reactiva, y la eliminación del período de inducción han sido estudiadas por [36, 45, 105]. Métodos más elaborados para medir la concentración de partículas sólidas en todo el tanque son presentados por [38, 52, 84].

El modelo presentado en esta tesis (2) considera el movimiento de la frontera debido a los flujos volumétricos en las etapas del SBR. En [16] se introdujo un esquema numérico conservativo y que preserva la positividad desarrollado sobre una malla fija. El esquema de [16] emplea cuidadosas distribuciones de masa en las celdas cercanas a la frontera móvil para garantizar la conservación de la masa. La trayectoria de $\bar{z}(t)$ está dada y no forma parte de la solución del problema, por lo que el modelo EDP gobernante (2) es un problema de frontera móvil, pero no un problema de frontera libre. Sin embargo, las extensiones del modelo SBR a un problema de frontera libre son concebibles. Finalmente, mencionamos que la formulación y análisis parcial del esquema semi-implícito presentado en el Capítulo 4 se basa en los análisis de tales esquemas de ese tipo para EDP parabólicas degeneradas en [19, 48].

Organización de esta tesis

El presente trabajo de investigación está organizado de la siguiente manera:

En el Capítulo 1, se introducen las ecuaciones gobernantes para un modelo de sedimentación reactiva en reactores por lotes secuenciales utilizados en plantas de tratamiento de aguas residuales. El modelado de un SBR implica un sistema de ecuaciones parabólicas unidimensionales fuertemente degeneradas de convección-difusión-reacción. Este sistema está acoplado mediante condiciones de conservación de masa a ecuaciones de transporte en una semirrecta, cuyo origen se encuentra en una frontera móvil y que modelan el conducto del efluente. Las simulaciones numéricas ilustran el proceso simplificado de desnitrificación en ausencia de oxígeno y se obtienen utilizando el método numérico desarrollado en el Capítulo 2.

Los contenidos del Capítulo 1 corresponden al artículo [15]:

- R. Bürger, J. Careaga, S. Diehl, and R. Pineda, *A moving-boundary model of reactive settling in wastewater treatment. part 1: Governing equations*, Appl. Math. Model., 106 (2022), pp. 390–401.

En el Capítulo 2, se desarrolla un esquema numérico para las ecuaciones gobernantes que

modelan el proceso del SBR, presentadas en el Capítulo 1. Se formula un esquema numérico explícito monótono para aproximar las soluciones, y se demuestra que este esquema satisface una propiedad de región invariante, lo que implica que las concentraciones de sólidos y sustratos mantienen valores no negativos. Este enfoque garantiza la estabilidad y precisión de las soluciones numéricas. Se presentan simulaciones usando el ASM1. Además, se muestran simulaciones de las concentraciones de efluentes para diferentes números de celdas computacionales.

Los contenidos del Capítulo 2 corresponden al artículo [16]:

- R. Bürger, J. Careaga, S. Diehl, and R. Pineda, *A moving-boundary model of reactive settling in wastewater treatment. part 2: Numerical scheme*, Appl. Math. Model., 111 (2022), pp. 247–269.

En el Capítulo 3, se ajusta un modelo de sedimentación reactiva para SST a datos experimentales obtenidos en una planta piloto con un área de sección transversal variable. Se utiliza el modelo propuesto en la referencia [12], incluyendo términos de dispersión hidrodinámica para partículas floculadas en suspensión y sustratos disueltos en el fluido, así como un término que modela la mezcla de la suspensión cerca de la entrada de alimentación. Para las reacciones, se usa el modelo ASM1 con coeficientes estándar ajustados a la temperatura de la planta piloto. Finalmente, se presentan las simulaciones para uno de los escenarios en estado estacionario.

Los contenidos del Capítulo 3 corresponden al artículo [17]:

- R. Bürger, J. Careaga, S. Diehl, and R. Pineda, *A model of reactive settling of activated sludge: Comparison with experimental data*, Chem. Eng. Sci., 267 (2023), p. 118244.

En el Capítulo 4, el modelo presentado en el Capítulo 1 se reformula utilizando una transformación espacial en un problema de dominio fijo. Además, se introducen dos esquemas numéricos alternativos al descrito en el Capítulo 2. El modelo se discretiza utilizando un esquema explícito monótono junto con una variante semi-implícita alternativa. Se demuestra que el esquema semi-implícito está bien planteado y que ambas variantes generan aproximaciones que satisfacen un principio de región invariante, lo que se consigue bajo una condición de Courant-Friedrichs-Lewy (CFL) que es menos restrictiva para el esquema semi-implícito que para el explícito. Finalmente, se presentan ejemplos numéricos con parámetros realistas para ilustrar que, como uno de los resultados, la variante semi-implícita es más eficiente que el esquema explícito.

Los contenidos del Capítulo 4 corresponden al siguiente manuscrito sometido [14]:

- R. Bürger, J. Careaga, S. Diehl, and R. Pineda, *Numerical schemes for a moving-boundary convection-diffusion-reaction model of sequencing batch reactors*. Preprint 2023–11, Centro de Investigación en Ingeniería Matemática (CI^2MA), Universidad de Concepción, Chile.

En la Tabla 2 se resumen los modelos utilizados en esta tesis, tanto los relacionados con SBR como con SST, además de los procesos biocinéticos empleados y sus respectivos métodos numéricos. El método "SBR2" hace referencia al descrito en [16].

Table 2: Resumen de la estructura y los contenidos de la tesis doctoral

Capítulo	Diseño de proceso	Modelo biocinético	Método numérico
1 [15]	SBR	Desnitrificación	"SBR2" (malla de tamaño fijo)
2 [16]	SBR	ASM1 (sin alcalinidad)	"SBR2" (malla de tamaño fijo)
3 [17]	SST	ASM1 (completo)	Formulación MOL [12]
4 [14]	SBR	ASM1 (modificado)	Métodos explícito & semi-implícito, malla de tamaño variable

CHAPTER 1

A moving-boundary model of reactive settling in wastewater treatment. Part 1: Governing equations

1.1 Introduction

1.1.1 Scope

The purpose of Chapter 1 is to derive the governing equations for a reactive settling model of the SBR commonly used for wastewater treatment, where batch operations of reactions and sedimentation are applied in sequence in time, with fill and draw (extraction) operations between or during these stages. We present simulations when the reaction terms model a simplified denitrification process in wastewater treatment that occurs in the absence of oxygen. The main difficulties for the analysis of the entire PDE model arise partly from the presence of a moving boundary where both a source is located and a half-line model attached, and partly from strong type degeneracy; the function D is zero for X-values on an interval of positive length. The simulations are made with a new positivity-preserving numerical scheme that handles these difficulties and is presented in Chapter 2. The full PDE model is specified in Section 1.2. During the react stage of an SBR, full mixing occurs and the system of PDEs (1.29) reduces to a system of ODEs.

We present a one-dimensional model of reactive settling in a tank (with a possibly varying cross-sectional area). At the bottom, the tank has a controlled outlet. At the surface of the mixture, a floating device allows for controlled fill or extraction of mixture.

1.1.2 Outline of the chapter

The remainder of this chapter is organized as follows. In Section 1.2, the mathematical model is presented, beginning with general assumptions in Section 1.2.1 and continuing with a description of the local balance law for all components, as well as the description of the moving

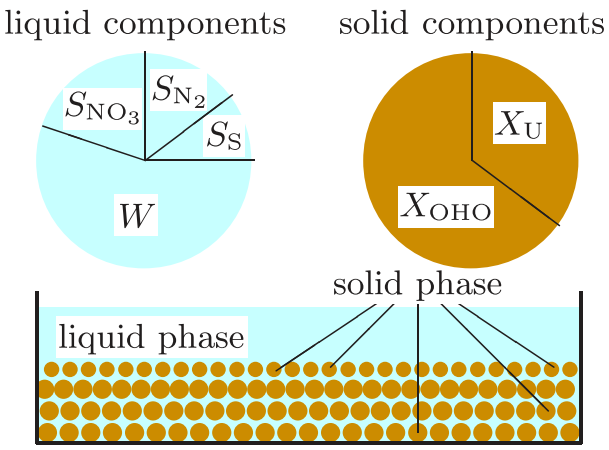

Figure 1.1: Components of the liquid and solid phases in the denitrification examples in Section 1.4

boundary and the modeling of the extraction pipe in Section 1.2.2. Then in Section 1.2.3 the relative velocity of solids and fluids is described, given by constitutive assumptions for hindered and compressive settling, taking into account the local concentration X and its spatial derivative $\partial_z X$. In Section 1.2.4, we outline the derivation of the governing equations (1.29) from the conservation of mass equations of the solid and the fluid. Section 1.3 presents the derivation of the full mixing ODE model. In Section 1.4, two examples of simulations with tanks of constant and variable cross-sectional area presented in Sections 1.4.1 to 1.4.2 respectively. In particular, the extreme cases of filling and extraction are demonstrated in Example 1.2 of Section 1.4.2, demonstrating the model's ability to handle such situations.

1.2 Derivation of the model of reactive settling

1.2.1 Preliminaries

The solid phase consists of flocculated particles of $k_{\boldsymbol{C}}$ types with concentrations $C^{(1)}, \ldots, C^{(k_{\boldsymbol{C}})}$. The components of the liquid phase are water of concentration W and $k_{\boldsymbol{S}}$ dissolved substrates of concentrations $S^{(1)}, \ldots, S^{(k_{\boldsymbol{S}})}$ (cf. Figure 1.1). The total concentrations of solids X and liquid L are

$$X := C^{(1)} + \cdots + C^{(k_{\boldsymbol{C}})}, \quad L := W + S^{(1)} + \cdots + S^{(k_{\boldsymbol{S}})}. \tag{1.1}$$

All these concentrations depend on z and t, and our notation is the same as in [12].

For computational purposes, we define a maximal concentration $\hat{X}$ of solids and assume that the density of all solids is the same, namely $\rho_X > \hat{X}$. Similarly, we assume that the liquid phase has density $\rho_L < \rho_X$, typically the density of water. The reaction terms for all components are

collected in the vectors of the form

$$\boldsymbol{R_C}(\boldsymbol{C},\boldsymbol{S}) = \boldsymbol{\sigma_C}\boldsymbol{r}(\boldsymbol{C},\boldsymbol{S}), \qquad \boldsymbol{R_S}(\boldsymbol{C},\boldsymbol{S}) = \boldsymbol{\sigma_S}\boldsymbol{r}(\boldsymbol{C},\boldsymbol{S}), \tag{1.2}$$

which model the increase of solid and soluble components, respectively, where $\boldsymbol{\sigma_C}$ and $\boldsymbol{\sigma_S}$ are constant stoichiometric matrices and $\boldsymbol{r}(\boldsymbol{C},\boldsymbol{S}) \geq \boldsymbol{0}$ is a vector of non-negative reaction rates, which are assumed to be bounded and Lipschitz continuous functions. We set

$$\tilde{R}_{\boldsymbol{C}}(\boldsymbol{C},\boldsymbol{S}) := R_{\boldsymbol{C}}^{(1)}(\boldsymbol{C},\boldsymbol{S}) + \cdots + R_{\boldsymbol{C}}^{(k_{\boldsymbol{C}})}(\boldsymbol{C},\boldsymbol{S})$$

(analogously for $\tilde{R}_{\boldsymbol{S}}(\boldsymbol{C},\boldsymbol{S})$). The water concentration W is not active in any reaction.

The matrices $\boldsymbol{\sigma_C}$ and $\boldsymbol{\sigma_S}$ and the vector $\boldsymbol{r}$ are given by expressions that represent a slightly modified version of the activated sludge model no. 1, usually abbreviated 'ASM1' in wastewater engineering. The model was the first comprehensive activated sludge model developed by a task group of the International Water Association (IWA) (see [62]). The model describes the principal biochemical reactions that occur within the activated sludge process, which is the most widespread technology for the secondary treatment of municipal wastewater and, as commented in [86], constitutes 'the heart' of many wastewater treatment plants. Later versions, known as ASM2, ASM2d and ASM3, account for additional reactions such as fermentation and chemical or biological phosphorus removal (not considered in the present research). Commercial software packages that include these models are used commonly by wastewater process design engineers for the process design of various activated sludge system configurations [89]. In Section 2.3 of Chapter 2, we describe the modified ASM1 model implemented in this research, along with its variations discussed in Chapters 3 and 4, and for to [30, 86, 89] for further information on activated sludge models.

In Chapters 2 and 4, we establish an invariant-region property for the numerical solution and make some technical assumptions. To ensure that the numerical solution for the solids does not exceed the maximal concentration $\hat{X}$, we assume that

$$\text{there exists an } \varepsilon > 0 \text{ such that } \boldsymbol{R_C}(\boldsymbol{C},\boldsymbol{S}) = \boldsymbol{0} \text{ for all } X \geq \hat{X} - \varepsilon \tag{1.3}$$

This condition means that when the concentration is near the maximal one, biomass cannot grow any more.

To obtain positivity of component k of the concentration vector $\boldsymbol{C}$ (analogously for $\boldsymbol{S}$), we let

$$I_{\boldsymbol{C},k}^{-} := \big\{l \in \mathbb{N} : \sigma_{\boldsymbol{C}}^{(k,l)} < 0\big\}, \qquad I_{\boldsymbol{C},k}^{+} := \big\{l \in \mathbb{N} : \sigma_{\boldsymbol{C}}^{(k,l)} > 0\big\},$$

denote the sets of indices l that have negative and positive stoichiometric coefficients, respectively, and assume that

$$\text{if } l \in I_{\boldsymbol{C},k}^{-}, \text{ then } r^{(l)}(\boldsymbol{C},\boldsymbol{S}) = \bar{r}^{(l)}(\boldsymbol{C},\boldsymbol{S})C^{(k)} \text{ with } \bar{r}^{(l)} \text{ bounded} \tag{1.4}$$

Assumption (1.4) implies that

$$R_{\boldsymbol{C}}^{(k)}(\boldsymbol{C},\boldsymbol{S})\big|_{C^{(k)}=0} \geq 0 \quad \text{for } k = 1,\ldots,k_{\boldsymbol{C}}$$

(analogously for $\boldsymbol{S}$), which means that the system of ODEs

$$\frac{\mathrm{d}}{\mathrm{d}t}\begin{pmatrix}\boldsymbol{C}\\ \boldsymbol{S}\end{pmatrix} = \begin{pmatrix}\boldsymbol{R}_{\boldsymbol{C}}(\boldsymbol{C},\boldsymbol{S})\\ \boldsymbol{R}_{\boldsymbol{S}}(\boldsymbol{C},\boldsymbol{S})\end{pmatrix} \tag{1.5}$$

has a non-negative solution if the initial data are non-negative [51]. (The system (1.5) is autonomous with Lipschitz continuous right-hand side. Due to uniqueness, solution orbits cannot cross each other; hence, any positive solution cannot cross the zero solution because of (1.4).) This positivity property is carried over to the numerical splitting scheme presented in Chapter 2.

We let v_X and v_L denote the velocities of the solid and liquid phases, respectively. It is assumed that the relative velocity $v_X - v_L =: v_{\mathrm{rel}} = v_{\mathrm{rel}}(X, \partial_z X, z)$ is given by a constitutive function of X and its spatial derivative $\partial_z X$, modeling hindered and compressive settling; see Section 1.2.3. The reason for the dependence on the total concentration X (and its spatial derivative) is that the particles are flocculated consisting of all solid components. All components within a particle settle with the same velocity.

It is assumed that in the inlet and outlet pipes no reactions take place and all the components have the same velocity. At the bottom, $z = B$, one can withdraw mixture at a given volume rate $Q_{\mathrm{u}}(t) \geq 0$. The underflow region $z > B$ is for simplicity modeled by setting $A(z) := A(B)$, where $A(z)$ represents the cross-sectional area of the tank that may depend on depth z. We are only interested in the underflow concentration $\boldsymbol{C}_{\mathrm{u}}(t)$, which is an outcome of the model (analogously for $\boldsymbol{S}_{\mathrm{u}}(t)$).

At the surface of the mixture, $z = \bar{z}(t)$, we model a floating device connected to a pipe through which one can feed the tank with given volume rate $Q_{\mathrm{f}}(t)$ and feed concentrations $\boldsymbol{C}_{\mathrm{f}}(t)$ and $\boldsymbol{S}_{\mathrm{f}}(t)$; see Figure 1. This gives rise to a source term in the model equation with the fluxes $Q_{\mathrm{f}}(t)\boldsymbol{C}_{\mathrm{f}}(t)$ and $Q_{\mathrm{f}}(t)\boldsymbol{S}_{\mathrm{f}}(t)$. Alternatively, this floating device allows one to extract mixture at a given volume rate $Q_{\mathrm{e}}(t) > 0$ through the same pipe; hence, one cannot fill and extract simultaneously.

If $[0, T]$ denotes the total time interval of modeling (and simulation in Section 1.4, Section 2.4, and Section 4.6), we assume that $T := T_{\mathrm{e}} \cup T_{\mathrm{f}}$, where

$$T_{\mathrm{e}} := \big\{t \in \mathbb{R}_+ : Q_{\mathrm{e}}(t) > 0, Q_{\mathrm{f}}(t) = 0\big\}, \qquad T_{\mathrm{f}} := \big\{t \in \mathbb{R}_+ : Q_{\mathrm{e}}(t) = 0, Q_{\mathrm{f}}(t) \geq 0\big\}.$$

Periods when there is neither extraction nor filling are for convenience included in T_{f}. When $t \in T_{\mathrm{e}}$, we model the extraction flow in the effluent pipe by a moving coordinate system; a half line $x \geq 0$, where $x = 0$ is attached to $z = \bar{z}(t)$. Along this half line, we denote the solids concentration by $\tilde{\boldsymbol{C}} = \tilde{\boldsymbol{C}}(x, t)$. The effluent concentration $\boldsymbol{C}_{\mathrm{e}}(t) := \tilde{\boldsymbol{C}}(0^+, t)\chi_{\{t\in T_{\mathrm{e}}\}}$ is also a model outcome (analogously for $\boldsymbol{S}_{\mathrm{e}}(t)$).

It is convenient to define the volume fractions

$$\phi := X/\rho_X, \qquad \phi_L := L/\rho_L, \qquad \phi_{\mathrm{M}} := \phi + \phi_L, \tag{1.6}$$

where the volume fraction of the mixture satisfies $\phi_{\mathrm{M}} = \chi_{\{z>\bar{z}(t)\}}$. Below the surface, $\phi+\phi_L = 1$, or equivalently, $L = \rho_L(1 - X/\rho_X)$. The same holds for the feed concentrations. For known $\boldsymbol{C}$ and $\boldsymbol{S}$, (1.1) implies the water concentration

$$W = \rho_L(1 - X/\rho_X) - \big(S^{(1)} + \cdots + S^{(k_{\boldsymbol{S}})}\big). \tag{1.7}$$

This concentration is not part of any reaction and can be computed afterwards.

The volume of the mixture is defined by

$$\bar{V}(t) := V\big(\bar{z}(t)\big), \quad \text{where} \quad V(z) := \int_z^B A(\xi)\,\mathrm{d}\xi \quad \text{for } 0 \le z \le B. \tag{1.8}$$

The function V is invertible since $V'(z) = -A(z) < 0$; in particular,

$$\bar{V}'(t) = V'\big(\bar{z}(t)\big)\bar{z}'(t) = -A\big(\bar{z}(t)\big)\bar{z}'(t). \tag{1.9}$$

1.2.2 Balance laws

The balance laws for all components in local form imply

$$\frac{\partial}{\partial t}\big(A(z)\boldsymbol{C}\big) + \frac{\partial}{\partial z}\big(A(z)v_X\boldsymbol{C}\big) = \delta\big(z - \bar{z}(t)\big)Q_{\mathrm{f}}\boldsymbol{C}_{\mathrm{f}} + \gamma(z,t)A(z)\boldsymbol{R}_{\boldsymbol{C}}, \quad z \in \mathbb{R}, \tag{1.10a}$$

$$\frac{\partial}{\partial t}\big(A(z)\boldsymbol{S}\big) + \frac{\partial}{\partial z}\big(A(z)v_L\boldsymbol{S}\big) = \delta\big(z - \bar{z}(t)\big)Q_{\mathrm{f}}\boldsymbol{S}_{\mathrm{f}} + \gamma(z,t)A(z)\boldsymbol{R}_{\boldsymbol{S}}, \quad z \in \mathbb{R}. \tag{1.10b}$$

This system along with $v_{\mathrm{rel}} = v_X - v_L$ and (1.6) are $k_{\boldsymbol{C}} + k_{\boldsymbol{S}} + 2$ equations for the same number of scalar unknowns, i.e., the components of $\boldsymbol{C}$ and $\boldsymbol{S}$, plus v_X and v_L. It is coupled to the following model of the effluent pipe with cross - area A_{e}:

$$A_{\mathrm{e}}\frac{\partial \tilde{\boldsymbol{C}}}{\partial t} + Q_{\mathrm{e}}\frac{\partial \tilde{\boldsymbol{C}}}{\partial x} = \boldsymbol{0}, \qquad x > 0, \tag{1.11a}$$

$$A_{\mathrm{e}}\frac{\partial \tilde{\boldsymbol{S}}}{\partial t} + Q_{\mathrm{e}}\frac{\partial \tilde{\boldsymbol{S}}}{\partial x} = \boldsymbol{0}, \qquad x > 0, \tag{1.11b}$$

$$-Q_{\mathrm{e}}(t)\tilde{\boldsymbol{C}}(0^+,t) = A\big(\bar{z}(t)^+\big)\big(v_X|_{z=\bar{z}(t)^+} - \bar{z}'(t)\big)\boldsymbol{C}\big(\bar{z}(t)^+,t\big), \tag{1.11c}$$

$$-Q_{\mathrm{e}}(t)\tilde{\boldsymbol{S}}(0^+,t) = A\big(\bar{z}(t)^+\big)\big(v_L|_{z=\bar{z}(t)^+} - \bar{z}'(t)\big)\boldsymbol{S}\big(\bar{z}(t)^+,t\big). \tag{1.11d}$$

The coupling equations (1.11c) and (1.11d) preserve mass at the surface during extraction periods. The purpose of (1.11) is to define the concentrations during periods of extraction when $Q_{\mathrm{e}}(t) > 0$. For $t > 0$ the outlet concentrations are given by

$$\boldsymbol{C}_{\mathrm{u}}(t) := \boldsymbol{C}(B^+,t), \qquad \boldsymbol{S}_{\mathrm{u}}(t) := \boldsymbol{S}(B^+,t), \tag{1.12}$$

$$\boldsymbol{C}_{\mathrm{e}}(t) := \tilde{\boldsymbol{C}}(0^+,t)\chi_{\{t\in T_{\mathrm{e}}\}}, \qquad \boldsymbol{S}_{\mathrm{e}}(t) := \tilde{\boldsymbol{S}}(0^+,t)\chi_{\{t\in T_{\mathrm{e}}\}}. \tag{1.13}$$

The transport PDEs (1.11a) and (1.11b) are easily solved once the boundary data (1.13) are known, which in turn have to satisfy (1.11c) and (1.11d). The right-hand sides of the latter

equations are however nonlinear functions of $\boldsymbol{C}(\bar{z}(t)^+,t)$ (via v_X and v_L) and to obtain unique boundary concentrations on either side of a spatial discontinuity, an additional entropy condition is needed. Our experience is, however, that correct concentrations can be obtained by a conservative and monotone numerical method [26].

The volume-average bulk velocity is defined by $q(z,t) := (\phi v_X + \phi_L v_L)\chi_{\{z>\bar{z}(t)\}}$. Since $\phi_{\mathrm{M}} = 0$ for $z < \bar{z}(t)$, we have $\phi = \phi_L = 0$ there. Summing all the equations of (1.10a) and (1.10b), respectively, and using (1.1) and (1.6), we get the scalar PDEs

$$\begin{aligned}
\frac{\partial}{\partial t}\big(A(z)\rho_X\phi\big) + \frac{\partial}{\partial z}\big(A(z)\rho_X\phi v_X\big) &= \delta\big(z-\bar{z}(t)\big)\rho_X\phi_{\mathrm{f}}Q_{\mathrm{f}} + \gamma(z,t)A(z)\tilde{R}_{\boldsymbol{C}},\\
\frac{\partial}{\partial t}\big(A(z)\rho_L\phi_L\big) + \frac{\partial}{\partial z}\big(A(z)\rho_L\phi_L v_L\big) &= \delta\big(z-\bar{z}(t)\big)\rho_L\phi_{L,\mathrm{f}}Q_{\mathrm{f}} + \gamma(z,t)A(z)\tilde{R}_{\boldsymbol{S}}.
\end{aligned}$$

Dividing away the constant densities and adding the results, we get

$$\frac{\partial}{\partial t}\big(A(z)\phi_{\mathrm{M}}\big) + \frac{\partial}{\partial z}\big(A(z)q\big) = \delta\big(z-\bar{z}(t)\big)\phi_{\mathrm{M,f}}Q_{\mathrm{f}} + \gamma(z,t)A(z)\mathcal{R}, \tag{1.14}$$

where $\mathcal{R} := \tilde{R}_{\boldsymbol{C}}/\rho_X + \tilde{R}_{\boldsymbol{S}}/\rho_L$, and $\phi_{\mathrm{M,f}} = 1$ by definition. The first term of (1.14) is

$$\frac{\partial}{\partial t}\big(A(z)\phi_{\mathrm{M}}\big) = A(z)\frac{\partial}{\partial t}\chi_{\{z>\bar{z}(t)\}} = -A(z)\delta\big(z-\bar{z}(t)\big)\bar{z}'(t).$$

The same procedure for the algebraic equations (1.11c) and (1.11d) ($t \in I_{\mathrm{e}}$) yields

$$-Q_{\mathrm{e}}(t) = A\big(\bar{z}(t)^+\big)\big(q(\bar{z}(t)^+,t) - \bar{z}'(t)\big). \tag{1.15}$$

Integrating (1.14) (with or without the source term) from $z \in (\bar{z}(t)^+, B)$ to B, we get

$$A(B)q(B,t) - A(z)q(z,t) = \int_z^B A(\xi)\mathcal{R}\big(\boldsymbol{C}(\xi,t),\boldsymbol{S}(\xi,t)\big)\,\mathrm{d}\xi =: Q_{\mathrm{reac}}(z,t;\boldsymbol{C},\boldsymbol{S}),$$

where $A(B)q(B,t) = Q_{\mathrm{u}}(t)$. Hence, inside the mixture, i.e., in the interval $(\bar{z}(t),B)$, the volume-average velocity q is given by $A(z)q(z,t) = Q_{\mathrm{u}}(t) - Q_{\mathrm{reac}}(z,t;\boldsymbol{C},\boldsymbol{S})$. In view of this equation and $q = (\phi v_X + \phi_L v_L)\chi_{\{z>\bar{z}(t)\}}$, we integrate (1.14) from $z = \bar{z}(t) - h$ to $\bar{z}(t) + h$ and let $0 < h \to 0$ to get

$$-A\big(\bar{z}(t)\big)\bar{z}'(t) + Q_{\mathrm{u}}(t) - Q_{\mathrm{reac}}(z,t;\boldsymbol{C},\boldsymbol{S})\big|_{z=\bar{z}(t)} = Q_{\mathrm{f}}(t), \tag{1.16}$$

where the first term can be written $\bar{V}'(t)$; see (1.9). For $t \in T_{\mathrm{e}}$, (1.15) implies

$$-Q_{\mathrm{e}}(t) = Q_{\mathrm{u}}(t) - Q_{\mathrm{reac}}(z,t;\boldsymbol{C},\boldsymbol{S})\big|_{z=\bar{z}(t)} + V'(t). \tag{1.17}$$

The term Q_{reac} seems to be negligible in the application to wastewater treatment [23] and we set $Q_{\mathrm{reac}} := 0$ from now on. Consequently, we define

$$q(z,t) := \big(Q_{\mathrm{u}}(t)/A(z)\big)\chi_{\{z>\bar{z}(t)\}}. \tag{1.18}$$

Then (1.16) and (1.17) can be written (with $Q_{\text{reac}} = 0$) as

$$\bar{V}'(t) = \bar{Q}(t) - Q_{\text{u}}(t), \quad \text{where} \quad \bar{Q}(t) = \begin{cases} -Q_{\text{e}}(t) < 0 & \text{if } t \in T_{\text{e}}, \\ Q_{\text{f}}(t) \geq 0 & \text{if } t \in T_{\text{f}}. \end{cases} \tag{1.19}$$

Solving this ODE and utilizing (1.8), we obtain

$$\bar{z}(t) = V^{-1}\left(\bar{V}(0) + \int_0^t \left(\bar{Q}(s) - Q_{\text{u}}(s)\right) \mathrm{d}s\right). \tag{1.20}$$

Alternatively, $\bar{z}(t)$ can be obtained from (see (1.9))

$$\bar{z}'(t) = \frac{Q_{\text{u}}(t) - \bar{Q}(t)}{A(\bar{z}(t))}. \tag{1.21}$$

1.2.3 Constitutive functions for hindered and compressive settling

The surface location $z = \bar{z}(t)$ is now specified, so we may focus on the mixture in $z > \bar{z}(t)$. For the given functions q and the relative velocity v_{rel}, we set $v := (1-\phi)v_{\text{rel}}$, where $\phi = X/\rho_X$, and obtain from $v_{\text{rel}} = v_X - v_L$ and $q = (\phi v_X + \phi_L v_L)\chi_{\{z>\bar{z}(t)\}}$ the phase velocities

$$v_X = q + (1-\phi)v_{\text{rel}} = q + v \quad \text{and} \quad v_L = q - \phi v_{\text{rel}} = q - \frac{\phi}{1-\phi}v \tag{1.22}$$

of the solid and fluid, respectively. We assume that the relative velocity $v_{\text{rel}} = v/(1-\phi)$ is given through the following commonly used expression [24, 26] for v:

$$v(X, \partial_z X, z, t) := \gamma(z,t) v_{\text{hs}}(X)\left(1 - \frac{\rho_X \sigma_{\text{e}}'(X)}{X g \Delta\rho}\partial_z X\right) = \gamma(z,t)\left(v_{\text{hs}}(X) - \partial_z D(X)\right), \tag{1.23}$$

where

$$D(X) := \int_{X_c}^{X} d(s)\,\mathrm{d}s, \qquad d(X) := v_{\text{hs}}(X)\frac{\rho_X \sigma_{\text{e}}'(X)}{g X \Delta\rho}. \tag{1.24}$$

Here $\Delta\rho := \rho_X - \rho_L$ is the density difference of the flocculated particles and the liquid, g is the acceleration of gravity, $v_{\text{hs}} = v_{\text{hs}}(X)$ is the hindered-settling velocity function, which is assumed to satisfy

$$v_{\text{hs}}(X) \begin{cases} > 0 & \text{for } X \in [0, \hat{X}), \\ = 0 & \text{for } X \geq \hat{X}, \end{cases} \tag{1.25}$$

The second constitutive function is the effective solids stress $\sigma_{\text{e}}(X)$, which satisfies

$$\sigma_{\text{e}}'(X) \begin{cases} = 0 & \text{for } X \leq X_{\text{c}}, \\ > 0 & \text{for } X > X_{\text{c}}, \end{cases}$$

where X_{c} is a critical concentration above which the particles touch each other and form a network that can bear a certain stress. Note that $d(X) = 0$ for $X \leq X_{\text{c}}$, which causes the strongly degenerate type behavior.

The determination of these constitutive assumptions including the critical concentration X_{c} is a topic in itself; see e.g. [45, 104] and references therein.

1.2.4 Model equations in final form

In [15], the mass-balance law for each component was utilized to derive a system of PDEs, This system was then reformulated into s form more suitable for developing of a numerical scheme, which is presented in Chapter 2. With q defined by (1.18), we define and use (1.22) and (1.23) to write the velocities

$$\begin{aligned}\mathcal{V}_{\boldsymbol{C}} &:= \mathcal{V}_{\boldsymbol{C}}(X, \partial_z X, z, t) := q(z,t) + \gamma(z,t)\big(v_{\mathrm{hs}}(X) - \partial_z D(X)\big),\\ \mathcal{V}_{\boldsymbol{S}} &:= \mathcal{V}_{\boldsymbol{S}}(X, \partial_z X, z, t) := q(z,t) - \gamma(z,t)\frac{(v_{\mathrm{hs}}(X) - \partial_z D(X))X}{\rho_X - X},\end{aligned} \tag{1.26}$$

and then express the total mass fluxes of the balance laws (1.10) in light of (1.22):

$$\begin{aligned}\boldsymbol{\Phi}_{\boldsymbol{C}} &:= \boldsymbol{\Phi}_{\boldsymbol{C}}(\boldsymbol{C}, X, \partial_z X, z, t) := A(z)\mathcal{V}_{\boldsymbol{C}}\boldsymbol{C},\\ \boldsymbol{\Phi}_{\boldsymbol{S}} &:= \boldsymbol{\Phi}_{\boldsymbol{S}}(\boldsymbol{S}, X, \partial_z X, z, t) := A(z)\mathcal{V}_{\boldsymbol{S}}\boldsymbol{S}.\end{aligned}$$

Then we define and rewrite the right-hand side of (1.11c) with (1.21), (1.22) and (1.23):

$$\begin{aligned}\boldsymbol{\Phi}_{\boldsymbol{C},\mathrm{e}}(z,t) &:= A(\bar z(t))\big(v_X(\bar z(t)^+, t) - \bar z'(t)\big)\boldsymbol{C}(\bar z(t)^+, t)\\ &= \Big(A(z)\big(q + v_{\mathrm{hs}}(X) - \partial_z D(X)\big) - Q_{\mathrm{u}} - Q_{\mathrm{e}}\Big)\boldsymbol{C}\Big|_{z=\bar z(t)^+}\\ &= \Big(A(z)\big(v_{\mathrm{hs}}(X) - \partial_z D(X)\big) - Q_{\mathrm{e}}\Big)\boldsymbol{C}\Big|_{z=\bar z(t)^+}.\end{aligned} \tag{1.27}$$

Analogously, we define $\boldsymbol{\Phi}_{\boldsymbol{S},\mathrm{e}}$ corresponding to (1.11d):

$$\begin{aligned}\boldsymbol{\Phi}_{\boldsymbol{S},\mathrm{e}}(z,t) &:= A(\bar z(t))\big(v_L(\bar z(t)^+, t) - \bar z'(t)\big)\boldsymbol{S}(\bar z(t)^+, t)\\ &= \left(A(z)\left(q - \frac{X(v_{\mathrm{hs}}(X) - \partial_z D(X))}{\rho_X - X}\right) - (Q_{\mathrm{u}} + Q_{\mathrm{e}})\right)\boldsymbol{S}\Big|_{z=\bar z(t)^+}\\ &= -\left(A(z)\frac{X(v_{\mathrm{hs}}(X) - \partial_z D(X))}{\rho_X - X} + Q_{\mathrm{e}}\right)\boldsymbol{S}\Big|_{z=\bar z(t)^+}.\end{aligned} \tag{1.28}$$

The final model can now be described as follows. Given the in- and outgoing volumetric flows, one computes the surface level by (1.20) or (1.21). The concentrations $\boldsymbol{C}$ and $\boldsymbol{S}$ are given by the system (1.10), while the effluent and underflow concentrations are given by (1.12) and (1.13), respectively. This can be written as

$$A(z)\frac{\partial \boldsymbol{C}}{\partial t} + \frac{\partial \boldsymbol{\Phi}_{\boldsymbol{C}}}{\partial z} = \delta\big(z - \bar z(t)\big)Q_{\mathrm{f}}\boldsymbol{C}_{\mathrm{f}} + \gamma(z,t)A(z)\boldsymbol{R}_{\boldsymbol{C}}, \qquad z \in \mathbb{R}, \tag{1.29a}$$

$$A(z)\frac{\partial \boldsymbol{S}}{\partial t} + \frac{\partial \boldsymbol{\Phi}_{\boldsymbol{S}}}{\partial z} = \delta\big(z - \bar z(t)\big)Q_{\mathrm{f}}\boldsymbol{S}_{\mathrm{f}} + \gamma(z,t)A(z)\boldsymbol{R}_{\boldsymbol{S}}, \qquad z \in \mathbb{R}, \tag{1.29b}$$

$$\boldsymbol{C}_{\mathrm{e}}(t) = -\boldsymbol{\Phi}_{\boldsymbol{C},\mathrm{e}}(t)/Q_{\mathrm{e}}(t), \qquad t \in T_{\mathrm{e}}, \tag{1.29c}$$

$$\boldsymbol{S}_{\mathrm{e}}(t) = -\boldsymbol{\Phi}_{\boldsymbol{S},\mathrm{e}}(t)/Q_{\mathrm{e}}(t), \qquad t \in T_{\mathrm{e}}, \tag{1.29d}$$

$$\boldsymbol{C}_{\mathrm{u}}(t) := \boldsymbol{C}(B^+, t), \qquad t > 0, \tag{1.29e}$$

$$\boldsymbol{S}_{\mathrm{u}}(t) := \boldsymbol{S}(B^+, t), \qquad t > 0, \tag{1.29f}$$

The water concentration W can always be calculated from (1.7). No initial data are needed for the outlet concentrations, but for the following:

$$\boldsymbol{C}^0 = \big(C^{(1),0}, C^{(2),0}, \dots, C^{(k_{\boldsymbol{C}}),0}\big)^{\mathrm{T}}, \qquad \boldsymbol{S}^0 = \big(S^{(1),0}, S^{(2),0}, \dots, S^{(k_{\boldsymbol{S}}),0}\big)^{\mathrm{T}}.$$

1.3 Application to sequencing batch reactors

An SBR cycle consists of five stages; see Figure 2. During some of these periods, mixing may occur due to aeration or the movement of an impeller. For the sake of simplicity, we ignore partial mixing and exemplify the cases of either no mixing or full mixing. The PDE model (1.29) excludes mixing and we next derive the special case of full mixing.

1.3.1 Model during a full mixing react stage

Full mixing means that the relative velocity v_{rel} is negligible. We set $v_{\mathrm{rel}} \equiv 0$ and assume that concentrations only depend on t (below the surface). Then $v_X = v_L = q$, hence,

$$\boldsymbol{\Phi}_{\boldsymbol{C}} = A(z)q(z,t)\boldsymbol{C} = Q_{\mathrm{u}}(t)\chi_{\{z>\bar{z}(t)\}}\boldsymbol{C}, \qquad \boldsymbol{\Phi}_{\boldsymbol{S}} = Q_{\mathrm{u}}(t)\chi_{\{z>\bar{z}(t)\}}\boldsymbol{S}. \tag{1.30}$$

Integrating the PDEs (1.29a) and (1.29b) from $\bar{z}(t)^-$ to B, one gets the governing ODEs. The integral of the time-derivative term of (1.29a) can, by means of (1.21), be written as

$$\begin{aligned}\int_{\bar{z}(t)}^{B} \frac{\mathrm{d}\boldsymbol{C}}{\mathrm{d}t} A(\xi)\,\mathrm{d}\xi &= \frac{\mathrm{d}}{\mathrm{d}t}\int_{\bar{z}(t)}^{B} \boldsymbol{C}(t)A(\xi)\,\mathrm{d}\xi - \big(-\boldsymbol{C}(t)A(\bar{z}(t))\bar{z}'(t)\big)\\ &= \frac{\mathrm{d}\boldsymbol{C}(t)}{\mathrm{d}t}\bar{V}(t) - \boldsymbol{C}(t)\big(Q_{\mathrm{u}}(t) - \bar{Q}(t)\big).\end{aligned}$$

The spatial-derivative term of (1.29a) becomes, with (1.30),

$$\int_{\bar{z}(t)}^{B} \frac{\mathrm{d}\boldsymbol{\Phi}_{\boldsymbol{C}}}{\mathrm{d}z}\,\mathrm{d}\xi = Q_{\mathrm{u}}(t)\boldsymbol{C}(t) - \boldsymbol{0}.$$

The same can be done for the substrate equations and we obtain the following system of ODEs for the homogeneous concentrations in $\bar{z}(t) < z < B$:

$$\bar{V}(t)\frac{\mathrm{d}\boldsymbol{C}}{\mathrm{d}t} = \big(Q_{\mathrm{u}}(t) - \bar{Q}(t)\big)\boldsymbol{C} + Q_{\mathrm{f}}(t)\boldsymbol{C}_{\mathrm{f}}(t) + \bar{V}(t)\boldsymbol{R}_{\boldsymbol{C}}, \tag{1.31a}$$

$$\bar{V}(t)\frac{\mathrm{d}\boldsymbol{S}}{\mathrm{d}t} = \big(Q_{\mathrm{u}}(t) - \bar{Q}(t)\big)\boldsymbol{S} + Q_{\mathrm{f}}(t)\boldsymbol{S}_{\mathrm{f}}(t) + \bar{V}(t)\boldsymbol{R}_{\boldsymbol{S}}, \tag{1.31b}$$

where all the concentrations depend only on time, since they are averages (below the surface). As before, W can be obtained afterwards from (1.7). In the region $0 < z < \bar{z}(t)$ all concentrations are zero. Because of (1.11c) and (1.27), we have $\boldsymbol{C}_{\mathrm{u}}(t) = \boldsymbol{C}(t)$ and $\boldsymbol{C}_{\mathrm{e}}(t) = \boldsymbol{C}(t)\chi_{\{t\in T_{\mathrm{e}}\}}$ (analogously for $\boldsymbol{S}$). The system (1.31) thus models a completely stirred tank with reactions, possibly a moving upper boundary because of in- and outflow streams.

1.4 Numerical simulations

We employed the numerical method outline in Chapter 2 to illustrate the entire SBR process, we adopt the denitrification model from [13], which consists of two solid components: ordinary heterotrophic organisms X_{OHO} and undegradable organics X_{U}; and three soluble components: nitrate $S_{\mathrm{NO_3}}$, readily biodegradable substrate S_{S} and nitrogen $S_{\mathrm{N_2}}$ (where we identify the denomination of a component and the corresponding concentration variable). Thus, we utilize $\boldsymbol{C} = (X_{\mathrm{OHO}}, X_{\mathrm{U}})^{\mathrm{T}}$ and $\boldsymbol{S} = (S_{\mathrm{NO_3}}, S_{\mathrm{S}}, S_{\mathrm{N_2}})^{\mathrm{T}}$, corresponding to $k_{\boldsymbol{C}} = 2$ and $k_{\boldsymbol{S}} = 3$, respectively. Shortly described, the denitrification process converts nitrate (NO_3) to nitrogen gas (N_2) by a series of reactions involving the particulate biomass. Since denitrification occurs without the presence of oxygen, the mixing during the react stage of the SBR process is achieved by an impeller. The reaction vectors $\boldsymbol{R_C} = \boldsymbol{\sigma_C} \boldsymbol{r}$ and $\boldsymbol{R_S} = \boldsymbol{\sigma_S} \boldsymbol{r}$ have the stoichiometric matrices and reaction-rate vector

$$\boldsymbol{\sigma_C} = \begin{bmatrix} 1 & -1 \\ 0 & f_{\mathrm{P}} \end{bmatrix}, \qquad \boldsymbol{\sigma_S} = \begin{bmatrix} -\bar{Y} & 0 \\ -1/Y & 1 - f_{\mathrm{P}} \\ \bar{Y} & 0 \end{bmatrix}, \qquad \boldsymbol{r} = X_{\mathrm{OHO}} \begin{pmatrix} \mu(\boldsymbol{S}) \\ b \end{pmatrix}.$$

Here $\bar{Y} = (1 - Y)/(2.86Y)$ where $Y = 0.67$ is a yield factor, $b = 6.94 \times 10^{-6}\,\mathrm{s}^{-1}$ is the decay rate of heterotrophic organisms, and $f_{\mathrm{P}} = 0.2$ is the portion of these that decays to undegradable organics. The growth rate function

$$\mu(\boldsymbol{S}) = \mu_{\max} \frac{S_{\mathrm{NO_3}}}{K_{\mathrm{NO_3}} + S_{\mathrm{NO_3}}} \frac{S_{\mathrm{S}}}{K_{\mathrm{S}} + S_{\mathrm{S}}}$$

has the parameters $\mu_{\max} = 5.56 \times 10^{-5}\,\mathrm{s}^{-1}$, $K_{\mathrm{NO_3}} = 5 \times 10^{-4}\,\mathrm{kg/m^3}$ and $K_{\mathrm{S}} = 0.02\,\mathrm{kg/m^3}$. The first component of $\boldsymbol{R_C}$ models partly the growth of heterotrophic organisms (X_{OHO}) due to consumption of substrates with a rate proportional to its concentration with proportionality coefficient $\mu(\boldsymbol{S})$ and partly the decay the with coefficient b. The consumption of substrates ($S_{\mathrm{NO_2}}, S_{\mathrm{S}}$) is modeled by negative terms proportional to $\mu(\boldsymbol{S})$.

The maximal total solids concentration is set to $\hat{X} = 30\,\mathrm{kg/m^3}$, a value our simulated solutions never reach. The constitutive functions used in all simulations are

$$v_{\mathrm{hs}}(X) \coloneqq \frac{v_0}{1 + (X/\breve{X})^{\eta}}, \quad \sigma_{\mathrm{e}}(X) \coloneqq \begin{cases} 0 & \text{if } X < X_{\mathrm{c}}, \\ \sigma_0 (X - X_{\mathrm{c}}) & \text{if } X \geq X_{\mathrm{c}} \end{cases} \tag{1.32}$$

with $v_0 = 1.76 \times 10^{-3}\,\mathrm{m/s}$, $\breve{X} = 3.87\,\mathrm{kg/m^3}$, $\eta = 3.58$, $X_{\mathrm{c}} = 5\,\mathrm{kg/m^3}$ and $\sigma_0 = 0.2\,\mathrm{m^2/s^2}$. Other parameters are $\rho_X = 1050\,\mathrm{kg/m^3}$, $\rho_L = 998\,\mathrm{kg/m^3}$, $g = 9.81\,\mathrm{m/s^2}$, and $B = 3\,\mathrm{m}$. The soluble feed concentrations in both examples are

$$\boldsymbol{S}_{\mathrm{f}}(t) \equiv (6.00 \times 10^{-3}, 9.00 \times 10^{-4}, 0)^{\mathrm{T}}\,\mathrm{kg/m^3}. \tag{1.33}$$

For visualization purposes, we do not plot zero numerical concentrations above the surface, but fill this region with grey colour.

1.4.1 Example 1.1: An SBR cycle

A cylindrical tank with cross-sectional area $A = 400\,\mathrm{m}^2$ is simulated during 6 h. The lengths of the five stages are chosen primarily for illustration; see Table 1.1. The initial concentrations are $\boldsymbol{C}^0(z) = X^0(z)(5/7, 2/7)^{\mathrm{T}}$, where

$$\begin{aligned} X^0(z) &= 0\,\mathrm{kg/m^3}, \quad \boldsymbol{S}^0(z) = \boldsymbol{0}\,\mathrm{kg/m^3} && \text{if } z < 2.0\,\mathrm{m}, \\ X^0(z) &= 10\,\mathrm{kg/m^3} \quad \boldsymbol{S}^0(z) = (6\times10^{-3}, 9\times10^{-4}, 0)^{\mathrm{T}}\,\mathrm{kg/m^3} && \text{if } z \geq 2.0\,\mathrm{m}. \end{aligned}$$

Table 1.1: Example 1.1: Time functions for an SBR cycle. 'Model' refers to either PDE (1.29) or ODE (1.31).

Stage	Time period [h]	$Q_{\mathrm{f}}(t)[\mathrm{m}^3/\mathrm{h}]$	$Q_{\mathrm{u}}(t)[\mathrm{m}^3/\mathrm{h}]$	$Q_{\mathrm{e}}(t)[\mathrm{m}^3/\mathrm{h}]$	Model
Fill	$0 \leq t < 1$	790	0	0	PDE
React	$1 \leq t < 3$	0	0	0	ODE
Settle	$3 \leq t < 5$	0	0	0	PDE
Draw	$5 \leq t < 5.5$	0	0	1570	PDE
Idle	$5.5 \leq t < 6$	0	10	0	PDE

No biomass is fed to the tank; $\boldsymbol{C}_{\mathrm{f}}(t) \equiv \boldsymbol{0}$. Figure 1.2 shows the simulation results. The reactions converting NO_3 to N_2 start immediately and are fast. (The downwards-pointing peaks in the S_{NO_3} plot arise since we do not plot zero concentrations above the surface.) A short time after the react stage has started at $t = 1$ h, all NO_3 has been consumed. During this short time period, S_{S} decreases slightly when there is still sufficient NO_3, but then increases during the react stage because of the decay of heterotrophic organisms.

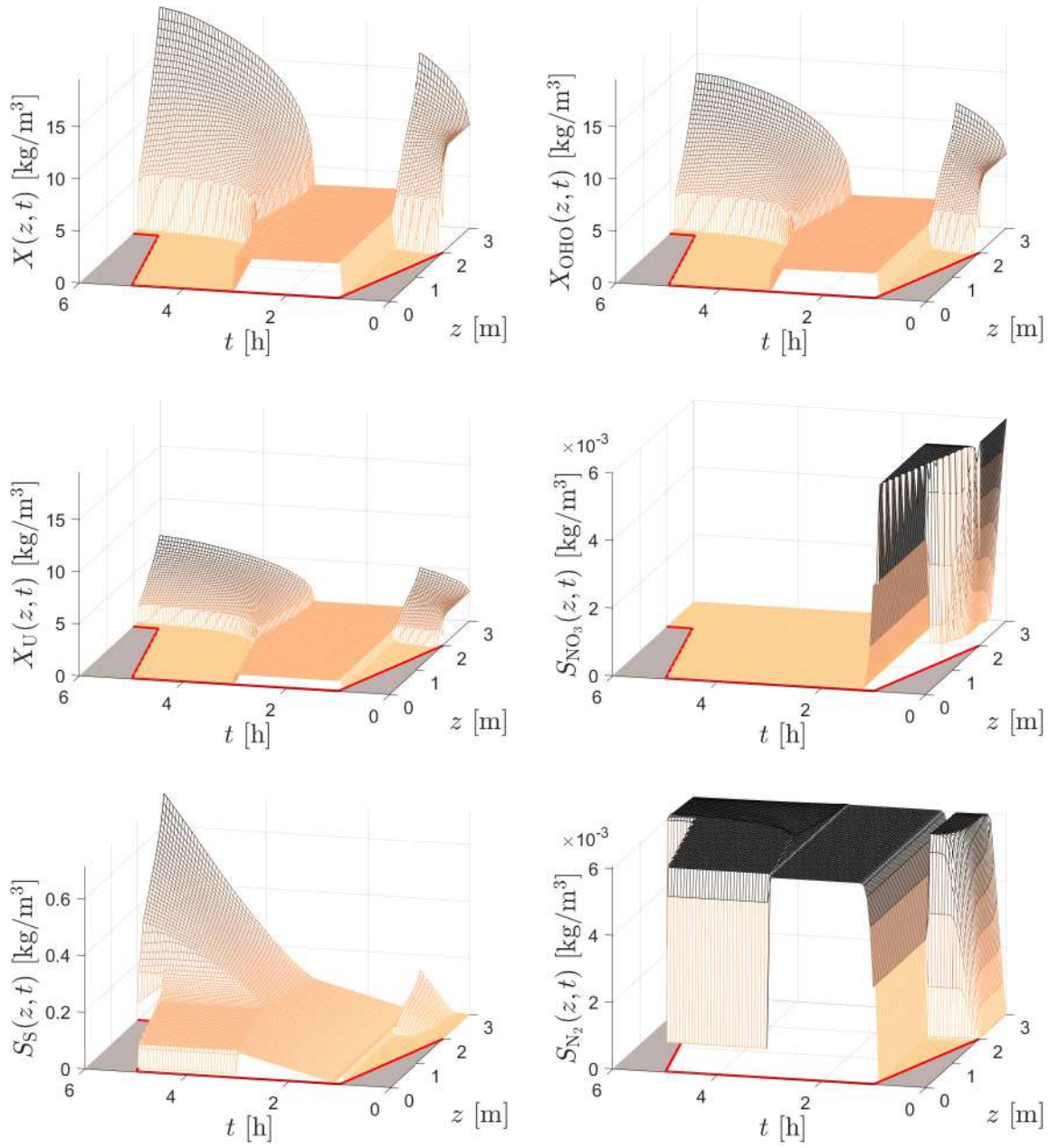

Figure 1.2: Example 1.1: Simulation results during $T = 6$ hours. The red lines show the location of the surface and the region above the surface is filled with grey colour.

1.4.2 Example 1.2

We now choose a truncated cone (cf. Figure 1.3) of the same volume 1200 m^3 as the cylinder of Example 1 and demonstrate what the numerical scheme can handle during extreme cases of fill and draw when solids concentrations are positive at the surface. We use the same initial data as in Example 1 but with $\bar{z}(0) \approx 1.8429$ m to obtain the same initial volume of mixture as

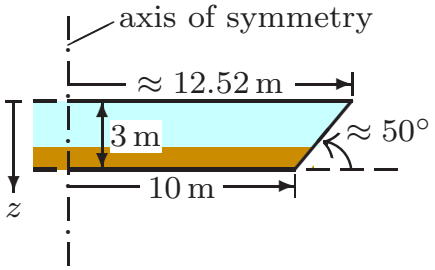

Figure 1.3: Example 1.2: Schematic of the truncated cone.

in Example 1. The fill and draw periods are specified in Table 1.2. The feed concentrations of the substrates are given by (1.33) and those of the biomass by $\boldsymbol{C}_{\mathrm{f}}(t) = X_{\mathrm{f}}(t)(5/7, 2/7)^{\mathrm{T}}$, where the piecewise constant function $X_{\mathrm{f}}(t)$ follows from Table 1.2.

Table 1.2: Example 1.2. Schematic of the truncated cone and time functions for the simulation. 'Model' refers to either PDE (1.29) or ODE (1.31).

Time period [h]	$X_{\mathrm{f}}(t)[\mathrm{kg/m^3}]$	$Q_{\mathrm{f}}(t)[\mathrm{m^3/h}]$	$Q_{\mathrm{u}}(t)[\mathrm{m^3/h}]$	$Q_{\mathrm{e}}(t)[\mathrm{m^3/h}]$	Model
$0 \le t < 1$	5	790	0	0	PDE
$1 \le t < 2$	0	0	100	0	ODE
$2 \le t < 3$	0	0	0	100	ODE
$3 \le t < 5$	5	100	0	0	PDE
$5 \le t < 6$	0	0	0	790	PDE

Figure 1.4 shows the simulated concentrations. During the first hour, there is a discontinuity in the solids concentration X rising with a lower speed than the surface. Then full mixing occurs during two hours and the surface is lowered because of the outlet flows at the bottom and top. At $t = 3\,\mathrm{h}$, the mixing stops and the solids settle again. During $3\,\mathrm{h} < t < 5\,\mathrm{h}$, the tank is filled up again with solids and substrates. The solids feed concentration $X_{\mathrm{f}} = 5\,\mathrm{kg/m^3}$ is the same as during the first hour, but now the feed flow Q_{f} is much lower, and hence the mass flow much lower. The result is a very low concentration X below the surface during $3\,\mathrm{h} < t < 5\,\mathrm{h}$. Since also X_{OHO} is low, there are hardly any reactions and most of the fed NO_3 remains in the mixture above the sludge blanket of the solids. At the surface level around $t = 3\,\mathrm{h}$, there is also biomass present and a high production of N_2 occurs. However, the sludge blanket drops and the high concentration of N_2 remains at this height until it is extracted through the effluent during the last hour. The latter is shown in Figure 1.5, which also shows that solids are extracted.

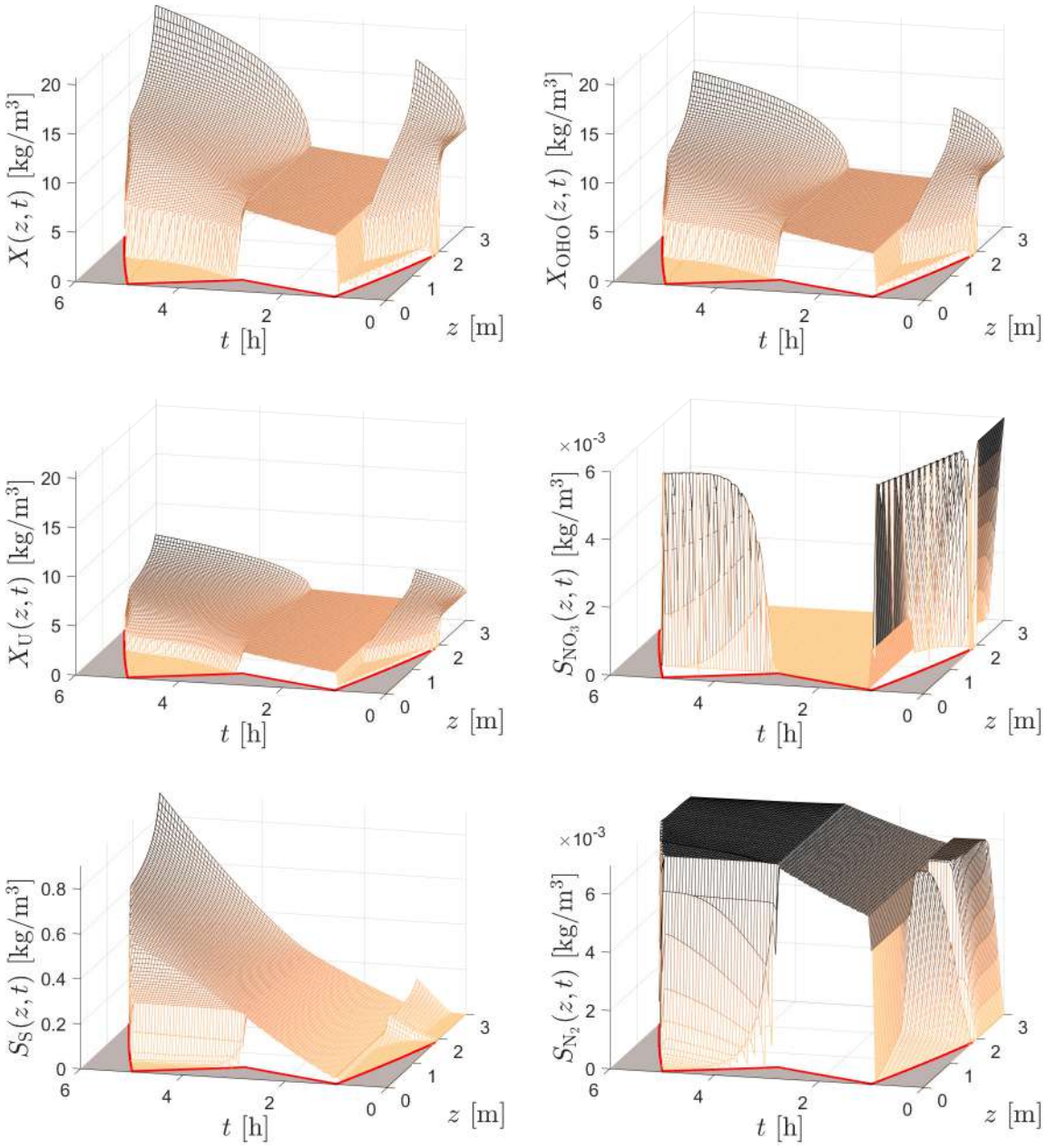

Figure 1.4: Example 1.2: Simulated results during $T = 6$ hours.

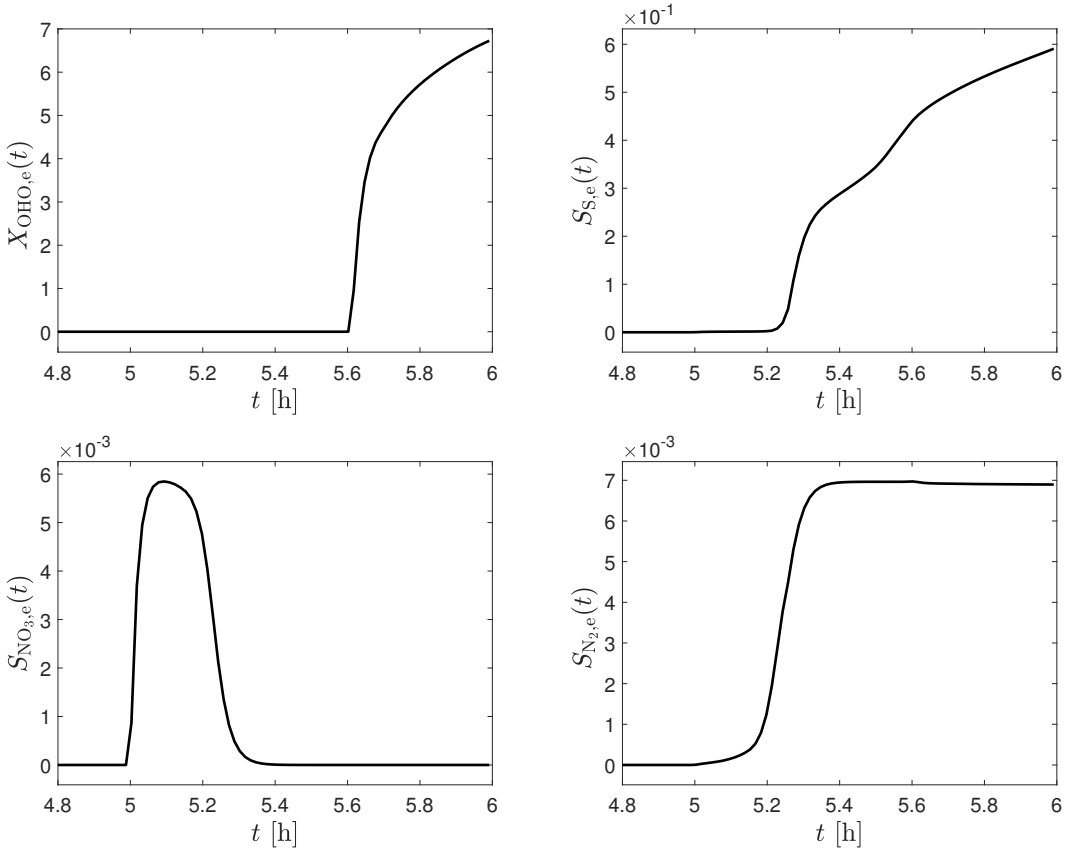

Figure 1.5: Example 1.2: Simulated effluent concentrations, all in kg/m^3, during $t \in [4.8\,\mathrm{h}, 6\,\mathrm{h}]$ obtained by the discretization where the number of computational cells within the tank is 100.

CHAPTER 2

A moving-boundary model of reactive settling in wastewater treatment. Part 2: Numerical scheme

2.1 Introduction

2.1.1 Scope

The purpose of this Chapter 2 is to present a numerical scheme that can handle the moving boundary where both a source is located and a half-line model attached. The scheme utilizes several of the favorable ingredients from the proven successful schemes for analogous types of scalar equations. The numerical scheme is therefore consistent with the PDE system. Mass conservation and non-negativity of solutions are two fundamental requirements on reliable simulators of real processes where the outputs are physical concentrations [51, 85, 90, 108]. It is of key importance that the scheme is derived from the mass balance law of each material component, which in particular means that the conservation of mass is ensured across the moving boundary during the fill and draw stages. The derivation of the numerical update formulas is carried out in several cases depending on the direction of movement of the boundary and whether it stays within a numerical cell or passes the boundary to an adjacent cell. These boundary update formulas are the novel elements of this scheme. The scheme is monotone when the reaction terms are zero. We prove that if the scheme is used in the simple Lie-Trotter-Kato splitting way (e.g. [64]), namely, one explicit time step is taken without reactions and another step with reactions only, then the numerical solutions have an invariant-region property under a convenient Courant-Friedrichs-Lewy (CFL) condition. In particular, concentrations are nonnegative.

Many of the properties defined in Chapter 1 will be used in this chapter.

2.1.2 Outline of the chapter

Section 2.2 contains the numerical scheme based on the one proposed in [12] but modified to handle the moving boundary. The fully discrete and explicit scheme is presented in Section 2.2.4 and its splitting version with the CFL condition and invariant-region property is presented in Section 2.2.5. The numerical scheme during the full mixing stage can be found in Section 2.2.6. A pseudocode for the numerical division scheme is provided in Section 2.2.7. The modified ASM1 for the biochemical reactions is presented in Section 2.3. In Section 2.4, we show a numerical example of SBR operation with a constant cross-sectional area (cylindrical vessel) and a commonly used activated sludge model for the biokinetic reactions; however, slightly adjusted to deliver non-negative concentrations only.

2.2 Numerical scheme

In Chapter 1, Section 1.2.4, we derived the governing model from balance laws applied to each material component, $\boldsymbol{C}$ and $\boldsymbol{S}$, leading to a system of PDEs as shown in equation (1.29). Building on this foundation, we now present the spatial, temporal discretization and numerical fluxes for the numerical scheme in this section.

2.2.1 Spatial discretization and numerical fluxes

The tank is divided into N computational cells each having depth $h = B/N$. Assume that the midpoint of cell j has the coordinate z_j, hence, the cell is the interval $[z_{j-1/2}, z_{j+1/2}]$. The top cell 1 is thus $[z_{1/2}, z_{3/2}] = [0, h]$, and the bottom location is $z = z_{N+1/2} = B$. To obtain the underflow concentrations, we add one cell below $z = B$. To obtain the extraction concentrations, we add one cell $[0, \Delta x]$ of the x-coordinate system. To approximate the cell volumes, we define the average cross-sectional areas

$$A_{j-1/2} := \frac{1}{h}\int_{z_{j-1}}^{z_j} A(\xi)\,\mathrm{d}\xi \quad \text{and} \quad A_j := \frac{1}{h}\int_{z_{j-1/2}}^{z_{j+1/2}} A(\xi)\,\mathrm{d}\xi.$$

The unknowns are approximated by functions that are piecewise constant in each cell j, i.e.

$$C^{(k)}(z,t) \approx C_j^{(k)}(t), \quad z \in [z_{j-1/2}, z_{j+1/2}],$$

which are collected in the vector $\boldsymbol{C}_j(t)$. We define $\bar{j}(t) := \lceil \bar{z}(t)/h \rceil$, which is the smallest integer larger than or equal to $\bar{z}(t)/h$. Then the surface $z = \bar{z}(t)$ is located in the surface cell $\bar{j}(t)$.

We let $\gamma_{j+1/2}(t) := \gamma(z_{j+1/2}, t)$ and define the approximate volume-average velocity $q_{j+1/2}(t) := q(z_{j+1/2}, t)$ in accordance with (1.18) via

$$A_{j+1/2} q_{j+1/2}(t) := Q_{\mathrm{u}}(t) \chi_{\{j+1/2 > \bar{j}(t)\}}.$$

Using the notation $a^- := \min\{a, 0\}$ and $a^+ := \max\{a, 0\}$, we define

$$\begin{aligned}
J^{\boldsymbol{C}}_{j+1/2} &= J^{\boldsymbol{C}}_{j+1/2}(X_j, X_{j+1}) := \big(D(X_{j+1}) - D(X_j)\big)/h,\\
v^X_{j+1/2} &= v^X_{j+1/2}(X_j, X_{j+1}, t) := q_{j+1/2} + \gamma_{j+1/2}\big(v_{\mathrm{hs}}(X_{j+1}) - J^{\boldsymbol{C}}_{j+1/2}\big),\\
F^X_{j+1/2} &= F^X_{j+1/2}(X_j, X_{j+1}, t) := (v_X X)_{j+1/2} := v^{X,-}_{j+1/2} X_{j+1} + v^{X,+}_{j+1/2} X_j,\\
\boldsymbol{\Phi}^{\boldsymbol{C}}_{j+1/2} &:= A_{j+1/2}\big(v^{X,-}_{j+1/2}\boldsymbol{C}_{j+1} + v^{X,+}_{j+1/2}\boldsymbol{C}_j\big),\\
\boldsymbol{\Phi}^{\boldsymbol{S}}_{j+1/2} &:= A_{j+1/2}\left(\frac{(\rho_X q_{j+1/2} - F^X_{j+1/2})^-}{\rho_X - X_{j+1}}\boldsymbol{S}_{j+1} + \frac{(\rho_X q_{j+1/2} - F^X_{j+1/2})^+}{\rho_X - X_j}\boldsymbol{S}_j\right).
\end{aligned} \tag{2.1}$$

For more details on these expressions, we refer to [12]. In particular, $\boldsymbol{\Phi}^{\boldsymbol{C}}_{j+1/2} = \boldsymbol{\Phi}^{\boldsymbol{S}}_{j+1/2} = \boldsymbol{0}$ for $j < \bar{j}(t)$. We denote by $[\Delta\boldsymbol{\Phi}]_j := \boldsymbol{\Phi}_{j+1/2} - \boldsymbol{\Phi}_{j-1/2}$ the flux difference associated with cell j. For the single cell on the x-axis, the advective fluxes at $x = \Delta x$ are $Q_{\mathrm{e}}(t)\boldsymbol{C}_{\mathrm{e}}(t)$ and $Q_{\mathrm{e}}(t)\boldsymbol{S}_{\mathrm{e}}(t)$.

2.2.2 Time discretization and surface fluxes

We let T denote the time length of the simulated process, t_n, $n = 0, 1, \ldots, N_T$, the discrete time points and $\tau := T/N_T$ the time step that should satisfy a certain CFL condition; see below. The value of a variable at time t_n is denoted by an upper index, e.g., $\boldsymbol{C}^n_j$ and it is thus assumed to be constant in time during $t_n \le t < t_{n+1}$. The discrete surface index is defined by $\bar{j}^n := \bar{j}(t_n)$ and we let $\bar{z}^n := \bar{z}(t_n)$. For the volumetric flows, we define the averages

$$Q^n_{\mathrm{f}} := \frac{1}{\tau}\int_{t_n}^{t_{n+1}} Q_{\mathrm{f}}(t)\,\mathrm{d}t$$

and assume for simplicity that any of the volumetric flows changes sign at most at the discrete time points t_n. This implies that $\bar{z}(t)$ is monotone on every interval $[t_n, t_{n+1}]$. To ensure that the surface does not travel more than one cell width h during τ, the CFL condition has to imply (cf. (1.21))

$$\tau \max_{0\le t\le T}|\bar{z}'(t)| \le \tau \max_{\substack{0\le t\le T,\\ 0\le z\le B}}\left\{\frac{|Q_{\mathrm{u}}(t) - Q_{\mathrm{f}}(t)|}{A(z)}, \frac{|Q_{\mathrm{u}}(t) + Q_{\mathrm{e}}(t)|}{A(z)}\right\} \le h. \tag{2.2}$$

To show that the cell concentrations $\boldsymbol{C}^n_{\bar{j}^n}$ do not exceed the maximal one $\hat{X}$, we also introduce the concentration $\bar{\boldsymbol{C}}^n_{\bar{j}^n}$ obtained when all the mass in the surface cell $\bar{j}^n$ is located below the surface within the cell; cf. Figure 2.1 (a). The mass in the cell is

$$\bar{\boldsymbol{C}}^n_{\bar{j}^n} A_{\bar{j}^n}\alpha^n h = \boldsymbol{C}^n_{\bar{j}^n} A_{\bar{j}^n} h, \quad \text{where} \quad \alpha^n h := z_{\bar{j}^n+1/2} - \bar{z}^n. \tag{2.3}$$

We set $\bar{X}^n_j := \bar{C}^{(1),n}_j + \ldots + \bar{C}^{(k_{\boldsymbol{C}}),n}_j$. Integrating (1.19) from t_n to t_{n+1}, one obtains

$$V\big(\bar{z}^{n+1}\big) - V\big(\bar{z}^n\big) = \big(\bar{Q}^n - Q^n_{\mathrm{u}}\big)\tau. \tag{2.4}$$

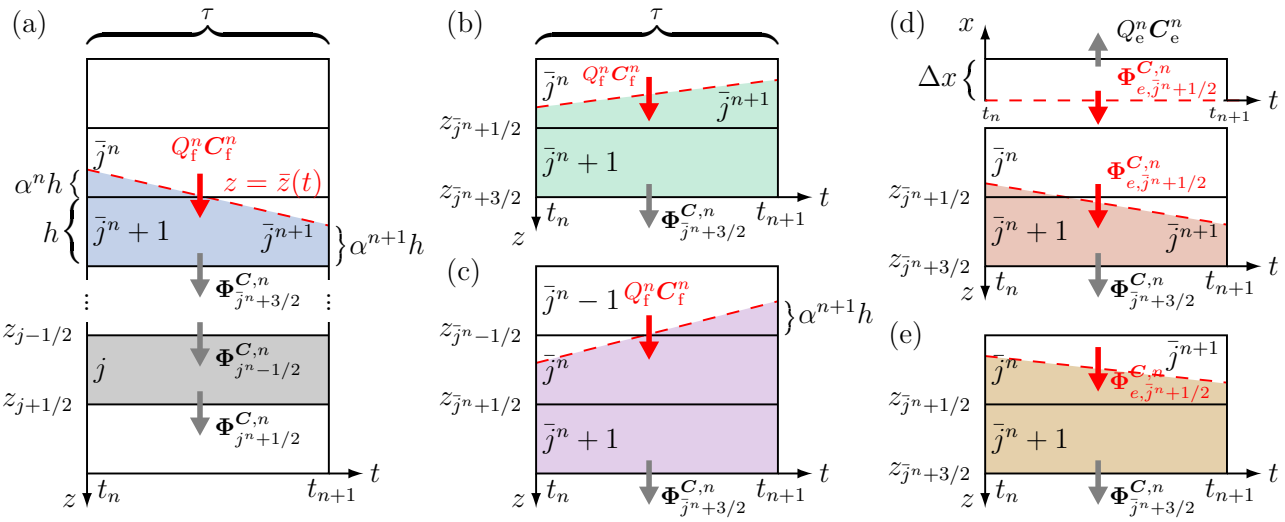

Figure 2.1: Fluxes over cell boundaries shown by grey arrows and the flux at the surface with red arrows. The surface level $z = \bar{z}(t)$ is drawn with a red dashed line. Plot (d) shows the extraction pipe cell where the origin of the x-axis located on the red dashed surface $z = \bar{z}(t)$ in plots (d) and (e).

If the surface stays within one cell between t_n and t_{n+1}; then (2.4) is equivalent to

$$A_j(\alpha^{n+1} - \alpha^n)h = \left(\bar{Q}^n - Q_\mathrm{u}^n\right)\tau \tag{2.5}$$

(cf. Figure 2.1 (b) and (e)). During extraction, the surface cannot rise and is thus located somewhere in cells $\bar{j}^n$ and $\bar{j}^n + 1$ (cf. Figure 2.1 (d) and (e)). In light of (1.27) and (1.28), we approximate the fluxes, which have to be non-positive, just below the surface in the following way:

$$\boldsymbol{\Phi}^{\boldsymbol{C},n}_{\mathrm{e},\bar{j}^n+1/2} := \left(A_{\bar{j}^n+1/2}\left(v_\mathrm{hs}(X^n_{\bar{j}^n+1}) - \frac{D(X^n_{\bar{j}^n+1})}{h}\right) - Q_\mathrm{e}^n\right)^- \boldsymbol{C}^n_{\bar{j}^n+1}, \tag{2.6}$$

$$\boldsymbol{\Phi}^{\boldsymbol{S},n}_{\mathrm{e},\bar{j}^n+1/2} := \left(-\frac{A_{\bar{j}^n+1/2}X^n_{\bar{j}^n+1}}{\rho_X - X^n_{\bar{j}^n+1}}\left(v_\mathrm{hs}(X^n_{\bar{j}^n+1}) - \frac{D(X^n_{\bar{j}^n+1})}{h}\right) - Q_\mathrm{e}^n\right)^- \boldsymbol{S}^n_{\bar{j}^n+1}. \tag{2.7}$$

2.2.3 Derivation of update formulas

We here derive the update formulas for $\boldsymbol{C}_j^n$. Analogous formulas hold for $\boldsymbol{S}_j^n$ when replacing $\boldsymbol{C}$ by $\boldsymbol{S}$; however, with different definitions of velocities and fluxes. We first consider the cells that lie below the surface $z = \bar{z}(t)$ at t_n and t_{n+1}. Special treatment is needed for the cells near the surface. All cells strictly above the surface have zero concentrations. Let $\kappa := \tau/h$.

Cells away from the surface

Using the integrated form of the balance law on a rectangle $[z_{j-1/2}, z_{j+1/2}] \times [t_n, t_{n+1}]$ strictly below the surface; see the gray rectangle in Figure 2.1 (a), we get the update formula (mass per h)

$$A_j \boldsymbol{C}_j^{n+1} = A_j \boldsymbol{C}_j^n + \kappa\big(-[\Delta \boldsymbol{\Phi}^{\boldsymbol{C}}]_j^n + h A_j \boldsymbol{R}_{\boldsymbol{C},j}^n\big),$$

and the analogous one for $\boldsymbol{S}_j^n$. For cell $N+1$, we get in the similar way the update formula for the underflow concentration; see Section 2.2.4.

Cells near the surface during fill ($t \in T_{\mathrm{f}}$)

To obtain a monotone scheme with an invariant-region property, we determine how the mass in the surface cell and the one below evolves; see the trapezoids in Figure 2.1. The mass per h at t_n is (we use (2.3))

$$\boldsymbol{m}_{\bar{j}^n}^{\boldsymbol{C},n} = A_{\bar{j}^n} \alpha^n \bar{\boldsymbol{C}}_{\bar{j}^n}^n + A_{\bar{j}^n+1} \boldsymbol{C}_{\bar{j}^n+1}^n = A_{\bar{j}^n} \boldsymbol{C}_{\bar{j}^n}^n + A_{\bar{j}^n+1} \boldsymbol{C}_{\bar{j}^n+1}^n. \tag{2.8}$$

During τ, the feed source along the moving surface is $Q_{\mathrm{f}}^n \boldsymbol{C}_{\mathrm{f}}^n$, whereas the outflux is $\boldsymbol{\Phi}_{\bar{j}^n+3/2}^{\boldsymbol{C},n}$. Thus, by the balance law on any trapezoid the mass (per h) at t_{n+1} is

$$\boldsymbol{m}_{\bar{j}^n}^{\boldsymbol{C},n+1} = \boldsymbol{m}_{\bar{j}^n}^{\boldsymbol{C},n} + \kappa \boldsymbol{\Psi}_{\mathrm{f},\bar{j}^n}^{\boldsymbol{C},n} \tag{2.9}$$

where the in- and outflux and source terms are

$$\boldsymbol{\Psi}_{\mathrm{f},\bar{j}^n}^{\boldsymbol{C},n} := Q_{\mathrm{f}}^n \boldsymbol{C}_{\mathrm{f}}^n - \boldsymbol{\Phi}_{\bar{j}^n+3/2}^{\boldsymbol{C},n} + h\left(\alpha^n A_{\bar{j}^n} \boldsymbol{R}_{\boldsymbol{C}}\left(\frac{\boldsymbol{C}_{\bar{j}^n}^n}{\alpha^n}, \frac{\boldsymbol{S}_{\bar{j}^n}^n}{\alpha^n}\right) + A_{\bar{j}^n+1} \boldsymbol{R}_{\boldsymbol{C},\bar{j}^n+1}^n\right)$$

(the concentration in cell $\bar{j}^n$ below the surface is $\bar{\boldsymbol{C}}_{\bar{j}^n}^n$).

Case (a): Fill case $\bar{j}^n = \bar{j}^{n+1} - 1$, Figure 2.1 (a): The surface moves downwards and crosses a cell boundary. All the mass ends up in one cell: $A_{\bar{j}^n+1} \boldsymbol{C}_{\bar{j}^n+1}^{n+1} = \boldsymbol{m}_{\bar{j}^n}^{\boldsymbol{C},n+1}$.

Case (b): Fill case $\bar{j}^n = \bar{j}^{n+1}$, Figure 2.1 (b): When the surface does not cross any cell boundary during τ, the mass (2.9) is distributed among the two cells with respect to their volumes (below the surface):

$$\begin{aligned} A_{\bar{j}^n} \boldsymbol{C}_{\bar{j}^n}^{n+1} &= \frac{\alpha^{n+1} A_{\bar{j}^n}}{\alpha^{n+1} A_{\bar{j}^n} + A_{\bar{j}^n+1}} \boldsymbol{m}_{\bar{j}^n}^{\boldsymbol{C},n+1}, \\ A_{\bar{j}^n+1} \boldsymbol{C}_{\bar{j}^n+1}^{n+1} &= \frac{A_{\bar{j}^n+1}}{\alpha^{n+1} A_{\bar{j}^n} + A_{\bar{j}^n+1}} \boldsymbol{m}_{\bar{j}^n}^{\boldsymbol{C},n+1}. \end{aligned} \tag{2.10}$$

Case (c): Fill case $\bar{j}^n = \bar{j}^{n+1} + 1$, Figure 2.1 (c): After the balance law is used on the purple trapezoid, the final mass (per h) is distributed among three cells:

$$A_{\bar{j}^n-1} \boldsymbol{C}_{\bar{j}^n-1}^{n+1} = \frac{\alpha^{n+1} A_{\bar{j}^n-1}}{\alpha^{n+1} A_{\bar{j}^n-1} + A_{\bar{j}^n} + A_{\bar{j}^n+1}} \boldsymbol{m}_{\bar{j}^n}^{\boldsymbol{C},n+1},$$

$$A_{\bar{j}^n}\boldsymbol{C}_{\bar{j}^n}^{n+1} = \frac{A_{\bar{j}^n}}{\alpha^{n+1}A_{\bar{j}^n-1} + A_{\bar{j}^n} + A_{\bar{j}^n+1}}\boldsymbol{m}_{\bar{j}^n}^{\boldsymbol{C},n+1},$$
$$A_{\bar{j}^n+1}\boldsymbol{C}_{\bar{j}^n+1}^{n+1} = \frac{A_{\bar{j}^n+1}}{\alpha^{n+1}A_{\bar{j}^n-1} + A_{\bar{j}^n} + A_{\bar{j}^n+1}}\boldsymbol{m}_{\bar{j}^n}^{\boldsymbol{C},n+1}.$$

Cells near the surface during extraction ($t \in T_\mathrm{e}$)

During extraction, the surface necessarily moves downwards. The initial mass is (2.8) and the balance law on a red trapezoid (Figures 2.1 (d) and (e)) gives $\boldsymbol{m}_{\bar{j}^n}^{\boldsymbol{C},n+1} = \boldsymbol{m}_{\bar{j}^n}^{\boldsymbol{C},n} + \kappa\boldsymbol{\Psi}_{\mathrm{e},\bar{j}^n}^{\boldsymbol{C},n}$, where

$$\boldsymbol{\Psi}_{\mathrm{e},\bar{j}^n}^{\boldsymbol{C},n} := \boldsymbol{\Phi}_{\mathrm{e},\bar{j}^n+1/2}^{\boldsymbol{C},n} - \boldsymbol{\Phi}_{\bar{j}^n+3/2}^{\boldsymbol{C},n} + h\left(\alpha^n A_{\bar{j}^n}\boldsymbol{R}_{\boldsymbol{C}}\left(\frac{\boldsymbol{C}_{\bar{j}^n}^n}{\alpha^n}, \frac{\boldsymbol{S}_{\bar{j}^n}^n}{\alpha^n}\right) + A_{\bar{j}^n+1}\boldsymbol{R}_{\boldsymbol{C},\bar{j}^n+1}^n\right).$$

Extraction case $\bar{j}^n = \bar{j}^{n+1} - 1$, *Figure 2.1 (d)*: All the mass ends up in one cell:

$$A_{\bar{j}^n+1}\boldsymbol{C}_{\bar{j}^n+1}^{n+1} = \boldsymbol{m}_{\bar{j}^n}^{\boldsymbol{C},n+1}$$

Extraction case $\bar{j}^n = \bar{j}^{n+1}$, *Figure 2.1 (e)*: The surface stays in one cell and we distribute the mass $\boldsymbol{m}_{\bar{j}^n}^{\boldsymbol{C},n+1}$ into two cells with (2.10).

The cell in the extraction pipe

The conservation law for the cell on the x-axis gives the mass equality (Figure 2.1 (d))

$$A_\mathrm{e}\Delta x\boldsymbol{C}_\mathrm{e}^{n+1} = A_\mathrm{e}\Delta x\boldsymbol{C}_\mathrm{e}^n + \tau\big(-Q_\mathrm{e}^n\boldsymbol{C}_\mathrm{e}^n - \boldsymbol{\Phi}_{\mathrm{e},\bar{j}^n+1/2}^{\boldsymbol{C},n}\big),$$

where the cross-sectional area A_e of the effluent pipe is of less importance, since we are only interested in $\boldsymbol{C}_\mathrm{e}^n$ and therefore may choose any Δx; we set $A_\mathrm{e}\Delta x := A_1 h$.

2.2.4 Explicit fully discrete scheme

Given data at t_n and the values $\bar{z}^{n+1}$ and $\bar{j}^{n+1}$, the update formulas for the particulate concentrations are given here and we distinguish between fill and extraction. We define $\lambda_j := \kappa/A_j = \tau/(A_j h)$ and

$$T_\mathrm{e}^\mathrm{num} := \big\{t_n : Q_\mathrm{e}^n > 0, Q_\mathrm{f}^n = 0\big\}, \qquad \eta^{n+1} := \frac{A_{\bar{j}^n}}{\alpha^{n+1}A_{\bar{j}^n} + A_{\bar{j}^n+1}},$$
$$T_\mathrm{f}^\mathrm{num} := \big\{t_n : Q_\mathrm{e}^n = 0, Q_\mathrm{f}^n \geq 0\big\}, \qquad \theta^{n+1} := \frac{A_{\bar{j}^n}}{\alpha^{n+1}A_{\bar{j}^n-1} + A_{\bar{j}^n} + A_{\bar{j}^n+1}}.$$

The update formulas for the top cells below the surface are different depending on whether fill or extraction occurs.

Update formulas for top cells during fill

If $t_n \in T_{\mathrm{f}}^{\mathrm{num}}$, then $\boldsymbol{C}_{\mathrm{e}}^{n+1} = \boldsymbol{0}$. The numerical flux is given by (2.6) and the marching formulas depending on each layer are computed as follows for the top cells $j \in \{\bar{j}^n - 1, \bar{j}^n, \bar{j}^n + 1\}$:

$$\begin{aligned}\boldsymbol{C}_j^{n+1} &= \omega_j^{\mathrm{f},n}\Bigg(\boldsymbol{C}_{\bar{j}^n}^n + \frac{A_{\bar{j}^n+1}}{A_{\bar{j}^n}}\boldsymbol{C}_{\bar{j}^n+1}^n + \lambda_{\bar{j}^n}\big(Q_{\mathrm{f}}^n\boldsymbol{C}_{\mathrm{f}}^n - \boldsymbol{\Phi}_{\bar{j}^n+3/2}^{\boldsymbol{C},n}\big) \\ &\qquad + \tau\Bigg(\alpha^n\boldsymbol{R}_{\boldsymbol{C}}\bigg(\frac{\boldsymbol{C}_{\bar{j}^n}^n}{\alpha^n}, \frac{\boldsymbol{S}_{\bar{j}^n}^n}{\alpha^n}\bigg) + \frac{A_{\bar{j}^n+1}}{A_{\bar{j}^n}}\boldsymbol{R}_{\boldsymbol{C},\bar{j}^n+1}^n\Bigg)\Bigg) \\ &= \omega_j^{\mathrm{f},n}\Bigg(\boldsymbol{C}_{\bar{j}^n}^n + \frac{A_{\bar{j}^n+1}}{A_{\bar{j}^n}}\boldsymbol{C}_{\bar{j}^n+1}^n + \lambda_{\bar{j}^n}\boldsymbol{\Psi}_{\mathrm{f},\bar{j}^n}^{\boldsymbol{C},n}\Bigg)\end{aligned}$$

(analogously for $\boldsymbol{S}$), where the coefficients $\omega_j^{\mathrm{f},n}$ are defined in the cases described in Figure 2.1 by

$$\begin{aligned}&\text{Case (a): } \bar{j}^n = \bar{j}^{n+1} - 1: && \omega_{\bar{j}^n-1}^{\mathrm{f},n} := 0, && \omega_{\bar{j}^n}^{\mathrm{f},n} := 0, && \omega_{\bar{j}^n+1}^{\mathrm{f},n} := A_{\bar{j}^n}/A_{\bar{j}^n+1},\\ &\text{Case (b): } \bar{j}^n = \bar{j}^{n+1}: && \omega_{\bar{j}^n-1}^{\mathrm{f},n} := 0, && \omega_{\bar{j}^n}^{\mathrm{f},n} := \alpha^{n+1}\eta^{n+1}, && \omega_{\bar{j}^n+1}^{\mathrm{f},n} := \eta^{n+1},\\ &\text{Case (c): } \bar{j}^n = \bar{j}^{n+1} + 1: && \omega_{\bar{j}^n-1}^{\mathrm{f},n} := \alpha^{n+1}\theta^{n+1}, && \omega_{\bar{j}^n}^{\mathrm{f},n} := \theta^{n+1}, && \omega_{\bar{j}^n+1}^{\mathrm{f},n} := \theta^{n+1}.\end{aligned}$$

Update formulas for top cells during extraction

If $t_n \in T_{\mathrm{e}}^{\mathrm{num}}$, then we compute the numerical fluxes with (2.7) and for the top layers $j \in \{\bar{j}^n, \bar{j}^n + 1\}$. The formula is

$$\begin{aligned}\boldsymbol{C}_j^{n+1} &= \omega_j^{\mathrm{e},n}\Bigg(\boldsymbol{C}_{\bar{j}^n}^n + \frac{A_{\bar{j}^n+1}}{A_{\bar{j}^n}}\boldsymbol{C}_{\bar{j}^n+1}^n + \lambda_{\bar{j}^n}\big(\boldsymbol{\Phi}_{\mathrm{e},\bar{j}^n+1/2}^{\boldsymbol{C},n} - \boldsymbol{\Phi}_{\bar{j}^n+3/2}^{\boldsymbol{C},n}\big) \\ &\qquad + \tau\Bigg(\alpha^n\boldsymbol{R}_{\boldsymbol{C}}\bigg(\frac{\boldsymbol{C}_{\bar{j}^n}^n}{\alpha^n}, \frac{\boldsymbol{S}_{\bar{j}^n}^n}{\alpha^n}\bigg) + \frac{A_{\bar{j}^n+1}}{A_{\bar{j}^n}}\boldsymbol{R}_{\boldsymbol{C},\bar{j}^n+1}^n\Bigg)\Bigg) \\ &= \omega_j^{\mathrm{e},n}\Bigg(\boldsymbol{C}_{\bar{j}^n}^n + \frac{A_{\bar{j}^n+1}}{A_{\bar{j}^n}}\boldsymbol{C}_{\bar{j}^n+1}^n + \lambda_{\bar{j}^n}\boldsymbol{\Psi}_{\mathrm{e},\bar{j}^n}^{\boldsymbol{C},n}\Bigg)\end{aligned}$$

(analogously for $\boldsymbol{S}$), where the coefficients $\omega_j^{\mathrm{e},n}$ are defined in the cases described in Figure 2.1 by

$$\begin{aligned}&\text{Case (d): } \bar{j}^n = \bar{j}^{n+1}: && \omega_{\bar{j}^n}^{\mathrm{e},n} := \alpha^{n+1}\eta^{n+1}, && \omega_{\bar{j}^n+1}^{\mathrm{e},n} := \eta^{n+1},\\ &\text{Case (e): } \bar{j}^n = \bar{j}^{n+1} - 1: && \omega_{\bar{j}^n}^{\mathrm{e},n} := 0, && \omega_{\bar{j}^n+1}^{\mathrm{e},n} := A_{\bar{j}^n}/A_{\bar{j}^n+1}.\end{aligned}$$

The effluent concentration is given by

$$\boldsymbol{C}_{\mathrm{e}}^{n+1} = \boldsymbol{C}_{\mathrm{e}}^n - \lambda_1\big(Q_{\mathrm{e}}^n\boldsymbol{C}_{\mathrm{e}}^n + \boldsymbol{\Phi}_{\mathrm{e},\bar{j}^n+1/2}^{\boldsymbol{C},n}\big).$$

Other concentrations

For the cells $j = \bar{j}^n+2, \dots, N$, the update formula is (analogously for $\boldsymbol{S}$), at every time point t_n,

$$\boldsymbol{C}_j^{n+1} = \boldsymbol{C}_j^n - \lambda_j[\Delta\boldsymbol{\Phi}^{\boldsymbol{C}}]_j^n + \tau \boldsymbol{R}_{\boldsymbol{C},j}^n, \tag{2.11}$$

$$\boldsymbol{C}_{\mathrm{u}}^{n+1} = \boldsymbol{C}_{\mathrm{u}}^n + \lambda_{N+1}\big(\boldsymbol{\Phi}_{N+1/2}^{\boldsymbol{C},n} - Q_{\mathrm{u}}^n \boldsymbol{C}_{\mathrm{u}}^n\big). \tag{2.12}$$

where the numerical flux is computed by (2.1). For the cells above the surface, $\boldsymbol{C}_j^{n+1} = \boldsymbol{0}$ for $j < \bar{j}^n - 1$. Finally, one computes

$$X_j^n = C_j^{(1),n} + \cdots + C_j^{(k_{\boldsymbol{C}}),n}, \qquad W_j^n = \rho_L(1 - X_j^n/\rho_X) - \big(S_j^{(1),n} + \cdots + S_j^{(k_{\boldsymbol{S}}),n}\big).$$

2.2.5 A splitting scheme and invariant-region property

It is desirable that the solution vectors $\boldsymbol{\mathcal{U}} := (\boldsymbol{C}, \boldsymbol{S})$ and $\boldsymbol{\mathcal{U}}_{\mathrm{e}} := (\boldsymbol{C}_{\mathrm{e}}, \boldsymbol{S}_{\mathrm{e}})$ of (1.29) stay in the set

$$\Omega := \big\{\boldsymbol{\mathcal{U}} \in \mathbb{R}^{k_{\boldsymbol{C}}+k_{\boldsymbol{S}}} : \boldsymbol{C} \geq \boldsymbol{0},\ \boldsymbol{S} \geq \boldsymbol{0},\ C^{(1)} + \cdots + C^{(k_{\boldsymbol{C}})} \leq \hat{X}\big\}.$$

To ensure that Ω is an invariant set for the numerical solutions, we split the scheme in Section 2.2.4 by taking one time step without the reaction terms and then one time step with only the reaction terms. For a cell strictly below the surface and the solid concentrations, the update formula (2.11) can be written

$$\boldsymbol{C}_j^{n+1} = \big\{\boldsymbol{C}_j^n - \lambda_j[\Delta\boldsymbol{\Phi}^{\boldsymbol{C}}]_j^n\big\} + \tau \boldsymbol{R}_{\boldsymbol{C}}\big(\boldsymbol{C}_j^n, \boldsymbol{S}_j^n\big)$$

and similarly for $\boldsymbol{S}_j^n$. The splitting principle is to compute the expression in the curled brackets first and then use the result for the second step as follows:

$$\check{\boldsymbol{C}}_j^{n+1} = \boldsymbol{C}_j^n - \lambda_j[\Delta\boldsymbol{\Phi}^{\boldsymbol{C}}]_j^n, \qquad \check{\boldsymbol{S}}_j^{n+1} = \boldsymbol{S}_j^n - \lambda_j[\Delta\boldsymbol{\Phi}^{\boldsymbol{S}}]_j^n, \tag{2.13}$$

$$\boldsymbol{C}_j^{n+1} = \check{\boldsymbol{C}}_j^{n+1} + \tau \boldsymbol{R}_{\boldsymbol{C}}\big(\check{\boldsymbol{C}}_j^{n+1}, \check{\boldsymbol{S}}_j^{n+1}\big), \qquad \boldsymbol{S}_j^{n+1} = \check{\boldsymbol{S}}_j^{n+1} + \tau \boldsymbol{R}_{\boldsymbol{S}}\big(\check{\boldsymbol{C}}_j^{n+1}, \check{\boldsymbol{S}}_j^{n+1}\big). \tag{2.14}$$

For the cells involving the surface, the first-step-update formulas, $j \in \{\bar{j}^n - 1, \bar{j}^n, \bar{j}^n + 1\}$ are

$$\check{\boldsymbol{C}}_j^{n+1} = \omega_j^{\mathrm{f},n}\Big(\boldsymbol{C}_{\bar{j}^n}^n + (A_{\bar{j}^n+1}/A_{\bar{j}^n})\boldsymbol{C}_{\bar{j}^n+1}^n + \lambda_{\bar{j}^n}\big(Q_{\mathrm{f}}^n \boldsymbol{C}_{\mathrm{f}}^n - \boldsymbol{\Phi}_{\bar{j}^n+3/2}^{\boldsymbol{C},n}\big)\Big) \qquad \text{if } t_n \in T_{\mathrm{f}}^{\mathrm{num}}, \tag{2.15}$$

$$\check{\boldsymbol{S}}_j^{n+1} = \omega_j^{\mathrm{f},n}\Big(\boldsymbol{S}_{\bar{j}^n}^n + (A_{\bar{j}^n+1}/A_{\bar{j}^n})\boldsymbol{S}_{\bar{j}^n+1}^n + \lambda_{\bar{j}^n}\big(Q_{\mathrm{f}}^n \boldsymbol{S}_{\mathrm{f}}^n - \boldsymbol{\Phi}_{\bar{j}^n+3/2}^{\boldsymbol{S},n}\big)\Big) \qquad \text{if } t_n \in T_{\mathrm{f}}^{\mathrm{num}}, \tag{2.16}$$

$$\check{\boldsymbol{C}}_j^{n+1} = \omega_j^{\mathrm{e},n}\Big(\boldsymbol{C}_{\bar{j}^n}^n + (A_{\bar{j}^n+1}/A_{\bar{j}^n})\boldsymbol{C}_{\bar{j}^n+1}^n + \lambda_{\bar{j}^n}\big(\boldsymbol{\Phi}_{\mathrm{e},\bar{j}^n+1/2}^{\boldsymbol{C},n} - \boldsymbol{\Phi}_{\bar{j}^n+3/2}^{\boldsymbol{C},n}\big)\Big) \qquad \text{if } t_n \in T_{\mathrm{e}}^{\mathrm{num}}, \tag{2.17}$$

$$\check{\boldsymbol{S}}_j^{n+1} = \omega_j^{\mathrm{e},n}\Big(\boldsymbol{S}_{\bar{j}^n}^n + (A_{\bar{j}^n+1}/A_{\bar{j}^n})\boldsymbol{S}_{\bar{j}^n+1}^n + \lambda_{\bar{j}^n}\big(\boldsymbol{\Phi}_{\mathrm{e},\bar{j}^n+1/2}^{\boldsymbol{S},n} - \boldsymbol{\Phi}_{\bar{j}^n+3/2}^{\boldsymbol{S},n}\big)\Big) \qquad \text{if } t_n \in T_{\mathrm{e}}^{\mathrm{num}}. \tag{2.18}$$

The second step consists in the formulas

$$\boldsymbol{C}_j^{n+1} = \check{\boldsymbol{C}}_j^{n+1} + \omega_j^{\mathrm{f},n}\tau\left(\alpha^n \boldsymbol{R}_{\boldsymbol{C}}\left(\frac{\check{\boldsymbol{C}}_{\bar{j}^n}^{n+1}}{\alpha^n}, \frac{\check{\boldsymbol{S}}_{\bar{j}^n}^{n+1}}{\alpha^n}\right) + \frac{A_{\bar{j}^n+1}}{A_{\bar{j}^n}} \boldsymbol{R}_{\boldsymbol{C}}\big(\check{\boldsymbol{C}}_{\bar{j}^n+1}^{n+1}, \check{\boldsymbol{S}}_{\bar{j}^n+1}^{n+1}\big)\right) \qquad \text{if } t_n \in T_{\mathrm{f}}^{\mathrm{num}}, \tag{2.19}$$

$$\boldsymbol{S}_j^{n+1} = \check{\boldsymbol{S}}_j^{n+1} + \omega_j^{\mathrm{f},n}\tau\left(\alpha^n \boldsymbol{R}_{\boldsymbol{S}}\left(\frac{\check{\boldsymbol{C}}_{\bar{\jmath}^n}^{n+1}}{\alpha^n}, \frac{\check{\boldsymbol{S}}_{\bar{\jmath}^n}^{n+1}}{\alpha^n}\right) + \frac{A_{\bar{\jmath}^n+1}}{A_{\bar{\jmath}^n}} \boldsymbol{R}_{\boldsymbol{S}}\big(\check{\boldsymbol{C}}_{\bar{\jmath}^n+1}^{n+1}, \check{\boldsymbol{S}}_{\bar{\jmath}^n+1}^{n+1}\big)\right) \quad \text{if } t_n \in T_{\mathrm{f}}^{\mathrm{num}}, \tag{2.20}$$

$$\boldsymbol{C}_j^{n+1} = \check{\boldsymbol{C}}_j^{n+1} + \omega_j^{\mathrm{e},n}\tau\left(\alpha^n \boldsymbol{R}_{\boldsymbol{C}}\left(\frac{\check{\boldsymbol{C}}_{\bar{\jmath}^n}^{n+1}}{\alpha^n}, \frac{\check{\boldsymbol{S}}_{\bar{\jmath}^n}^{n+1}}{\alpha^n}\right) + \frac{A_{\bar{\jmath}^n+1}}{A_{\bar{\jmath}^n}} \boldsymbol{R}_{\boldsymbol{C}}\big(\check{\boldsymbol{C}}_{\bar{\jmath}^n+1}^{n+1}, \check{\boldsymbol{S}}_{\bar{\jmath}^n+1}^{n+1}\big)\right) \quad \text{if } t_n \in T_{\mathrm{e}}^{\mathrm{num}}, \tag{2.21}$$

$$\boldsymbol{S}_j^{n+1} = \check{\boldsymbol{S}}_j^{n+1} + \omega_j^{\mathrm{e},n}\tau\left(\alpha^n \boldsymbol{R}_{\boldsymbol{S}}\left(\frac{\check{\boldsymbol{C}}_{\bar{\jmath}^n}^{n+1}}{\alpha^n}, \frac{\check{\boldsymbol{S}}_{\bar{\jmath}^n}^{n+1}}{\alpha^n}\right) + \frac{A_{\bar{\jmath}^n+1}}{A_{\bar{\jmath}^n}} \boldsymbol{R}_{\boldsymbol{S}}\big(\check{\boldsymbol{C}}_{\bar{\jmath}^n+1}^{n+1}, \check{\boldsymbol{S}}_{\bar{\jmath}^n+1}^{n+1}\big)\right) \quad \text{if } t_n \in T_{\mathrm{e}}^{\mathrm{num}}. \tag{2.22}$$

The time step τ has to be bounded by the CFL condition

$$\tau \max\left\{\beta_1, \beta_2, M_{\boldsymbol{C}}(1+M_2), M_{\boldsymbol{S}}(1+M_2), \tilde{M}/\varepsilon\right\} \le 1, \tag{CFL}$$

where β_1 and β_2 depend on h, h^2, the volumetric flows, and the constitutive functions by

$$\beta_1 := \frac{\|Q\|_T}{A_{\min}h} + \frac{M_1}{h}\left(\hat{X}\left(\|v_{\mathrm{hs}}'\| + \frac{\|d\|}{h}\right) + 2v_{\mathrm{hs}}(0) + 2\frac{D(\hat{X})}{h}\right),$$
$$\beta_2 := \frac{M_1}{h(\rho_X - \hat{X})}\left((\rho_X + \hat{X})\frac{\|Q\|_T}{A_{\min}} + 2\hat{X}v_{\mathrm{hs}}(0) + \frac{\hat{X}D(\hat{X})}{h}\right),$$

and where the constants are given by (here, ξ represents $v_{\mathrm{hs}}, v_{\mathrm{hs}}'$ or d) (cf. (1.4))

$$M_{\boldsymbol{\xi}} := \sup_{\substack{\boldsymbol{\mathcal{U}}\in\Omega,\\ 1\le k\le k_{\boldsymbol{\xi}}}} \sum_{l\in I_{\boldsymbol{\xi},k}^-} |\sigma_{\boldsymbol{\xi}}^{(k,l)}|\bar{r}_{\boldsymbol{\xi}}^{(l)}(\boldsymbol{C},\boldsymbol{S}), \quad \boldsymbol{\xi}\in\{\boldsymbol{C},\boldsymbol{S}\}, \qquad \tilde{M} := \sup_{\boldsymbol{\mathcal{U}}\in\Omega} \tilde{R}_{\boldsymbol{C}}(\boldsymbol{C},\boldsymbol{S}),$$
$$\|\xi\| := \max_{0\le X\le\hat{X}} |\xi(X)|, \qquad \|Q\|_T := \max_{0\le t\le T}\big\{|Q_{\mathrm{u}}(t) - Q_{\mathrm{f}}(t)|, Q_{\mathrm{u}}(t) + Q_{\mathrm{e}}(t)\big\},$$
$$M_1 := \max_{j=1,\dots,N}\left\{\frac{A_{j+1/2}}{A_j}, \frac{A_{j-1/2}}{A_j}\right\}, \qquad M_2 := \max_{j=1,\dots,N-1}\left\{\frac{A_j}{A_{j+1}}\right\}, \qquad A_{\min} := \min_{j=1,\dots,N} A_j.$$

Theorem 2.1. *Consider the numerical splitting method (2.13)–(2.21). If $\boldsymbol{\mathcal{U}}_j^n := (\boldsymbol{C}_j^n, \boldsymbol{S}_j^n) \in \Omega$ for all $j \ne \bar{\jmath}^n$, $\bar{\boldsymbol{\mathcal{U}}}_{\bar{\jmath}^n}^n := (\bar{\boldsymbol{C}}_{\bar{\jmath}^n}^n, \bar{\boldsymbol{S}}_{\bar{\jmath}^n}^n) \in \Omega$, $\boldsymbol{\mathcal{U}}_{\mathrm{e}}^n := (\boldsymbol{C}_{\mathrm{e}}^n, \boldsymbol{S}_{\mathrm{e}}^n) \in \Omega$ and (CFL) holds, then*

$$\boldsymbol{\mathcal{U}}_j^{n+1}, \bar{\boldsymbol{\mathcal{U}}}_{\bar{\jmath}^n}^{n+1}, \boldsymbol{\mathcal{U}}_{\mathrm{e}}^{n+1} \in \Omega.$$

Theorem 2.1 is proved by the following lemmas and by the fact that (CFL) implies (2.2), which we have used in the derivation of the scheme. Summing for fixed j all components of the update formula (2.11) for $\boldsymbol{C}_j^{n+1}$, one gets

$$X_j^{n+1} = X_j^n + \lambda_j[\Delta\tilde{\Phi}^{\boldsymbol{C}}]_j^n + \tau\tilde{R}_{\boldsymbol{C},j}^n, \tag{2.23}$$

where $\tilde{\Phi}^{\boldsymbol{C}}$ and $\tilde{R}_{\boldsymbol{C},j}^n$ denote the sum of all components, respectively. Analogous considerations lead to formulas for $\bar{X}_j^n$ and X_{e}^{n+1}.

For the proofs write the update formulas as

$$C_j^{(k),n+1} = \mathcal{H}_{\boldsymbol{C},j}^{(k),n}\big(\boldsymbol{C}_{j-1}^n, \dots, \boldsymbol{C}_{j+3}^n, \boldsymbol{S}_j^n\big)$$

for one component $k \in \{1, \dots, k_{\boldsymbol{C}}\}$ (see Section 2.2.4). That formula includes the underflow concentrations (2.12) for $j = N+1$.

Lemma 2.1. *Assume that* $\boldsymbol{\mathcal{U}}_j^n := (\boldsymbol{C}_j^n, \boldsymbol{S}_j^n) \in \Omega$ *for all* $j \neq \bar{j}^n$, $\bar{\boldsymbol{\mathcal{U}}}_{\bar{j}^n}^n := (\bar{\boldsymbol{C}}_{\bar{j}^n}^n, \bar{\boldsymbol{S}}_{\bar{j}^n}^n) \in \Omega$, $\boldsymbol{\mathcal{U}}_{\mathrm{e}}^n := (\boldsymbol{C}_{\mathrm{e}}^n, \boldsymbol{S}_{\mathrm{e}}^n) \in \Omega$ *and* (CFL) *holds. If* $\boldsymbol{R}_{\boldsymbol{C}} \equiv \boldsymbol{0}$, *then*

$$0 \le X_j^{n+1}, \bar{X}_{\bar{j}^n}^{n+1}, X_{\mathrm{e}}^{n+1} \le \hat{X} \quad \text{for all } j, \tag{2.24}$$

$$0 \le \boldsymbol{C}_j^{n+1}, \bar{\boldsymbol{C}}_{\bar{j}^n}^{n+1}, \boldsymbol{C}_{\mathrm{e}}^{n+1} \le \hat{X} \quad \text{for all } j. \tag{2.25}$$

If $\boldsymbol{R}_{\boldsymbol{S}} \equiv \boldsymbol{0}$, *then*

$$\boldsymbol{S}_j^{n+1} \ge \boldsymbol{0} \text{ for all } j \text{ and } \boldsymbol{S}_{\mathrm{e}}^{n+1} \ge \boldsymbol{0}. \tag{2.26}$$

Proof. Proof of (2.24): We write the general update formula (2.23) as

$$X_j^{n+1} = \mathcal{H}_{X,j}^n\big(X_{j-1}^n, \dots, X_{j+3}^n\big)$$

and let this include the surface concentration $\bar{X}_{\bar{j}^n}^n$. For cells away from the moving surface, we refer to [12, Theorem 3.1] from which we also collect

$$v_{j+1/2}^{X,n,+} = \big(q_{j+1/2}^n + \gamma_{j+1/2}\big(v_{\mathrm{hs}}(X_{j+1}^n) - J_{j+1/2}^{\boldsymbol{C},n}\big)\big)^+ \le \frac{Q_{\mathrm{u}}^n}{A_{j+1/2}} + v_{\mathrm{hs}}(0) + \frac{D(\hat{X})}{h}.$$

To show the monotonicity for the cells near the surface, we introduce some notation. As before, we use tilde to denote the sum of all components of a vector. Formula (2.6) implies

$$\tilde{\Phi}_{\mathrm{e},\bar{j}^n+1/2}^{\boldsymbol{C},n} := A_{\bar{j}^n+1/2} v_{\mathrm{e},\bar{j}^n+1/2}^{X,n,-} X_{\bar{j}^n+1}^n, \quad \text{where} \quad v_{\mathrm{e},\bar{j}^n+1/2}^{X,n} := v_{\mathrm{hs}}(X_{\bar{j}^n+1}^n) - \frac{D(X_{\bar{j}^n+1}^n)}{h} - \frac{Q_{\mathrm{e}}^n}{A_{\bar{j}^n+1/2}},$$

and we set

$$\chi^+ := \chi_{\{v_{\bar{j}^n+1/2}^{X,n} \ge 0\}}, \qquad \chi^- := \chi_{\{v_{\bar{j}^n+1/2}^{X,n} \le 0\}}, \qquad \chi_{\mathrm{e}}^- := \chi_{\{v_{\mathrm{e},\bar{j}^n+1/2}^{X,n} \le 0\}},$$

$$\nu_1 := \hat{X}\frac{\|d\|}{h} + v_{\mathrm{hs}}(0) + \frac{D(\hat{X})}{h}, \qquad \nu_2 := \nu_1 + \hat{X}\|v_{\mathrm{hs}}'\|,$$

and calculate for $j = \bar{j}^n$

$$\frac{\partial v_{j+1/2}^{X,n,\pm}}{\partial X_j^n} = \chi^{\pm}\frac{d(X_j^n)}{h}, \qquad \frac{\partial v_{j+1/2}^{X,n,\pm}}{\partial X_{j+1}^n} = \chi^{\pm}\left(v_{\mathrm{hs}}'(X_{j+1}^n) - \frac{d(X_{j+1}^n)}{h}\right),$$

$$\frac{\partial \tilde{\Phi}_{j+1/2}^{\boldsymbol{C},n}}{\partial X_j^n} = A_{j+1/2}\left(\left(\chi^- X_{j+1}^n + \chi^+ X_j^n\right)\frac{d(X_j^n)}{h} + v_{j+1/2}^{X,n,+}\right) \le A_{j+1/2}\nu_1 + Q_{\mathrm{u}}^n,$$

$$\frac{\partial\tilde{\Phi}^{\boldsymbol{C},n}_{j+1/2}}{\partial X^n_{j+1}} = A_{j+1/2}\left(v^{X,n,-}_{j+1/2} + \left(\chi^- X^n_{j+1} + \chi^+ X^n_j\right)\left(v'_{\mathrm{hs}}(X^n_{j+1}) - \frac{d(X^n_{j+1})}{h}\right)\right) \le 0,$$
$$\frac{\partial\tilde{\Psi}^{\boldsymbol{C},n}_{\mathrm{f},j}}{\partial X^n_{j-1}} = 0, \qquad \frac{\partial\tilde{\Psi}^{\boldsymbol{C},n}_{\mathrm{f},j}}{\partial X^n_j} = 0,$$
$$\frac{\partial\tilde{\Psi}^{\boldsymbol{C},n}_{\mathrm{f},j}}{\partial X^n_{j+1}} = -\frac{\partial\tilde{\Phi}^{\boldsymbol{C},n}_{j+3/2}}{\partial X^n_{j+1}} \ge -A_{j+3/2}\nu_1 - Q^n_{\mathrm{u}}, \qquad \frac{\partial\tilde{\Psi}^{\boldsymbol{C},n}_{\mathrm{f},j}}{\partial X^n_{j+2}} = -\frac{\partial\tilde{\Phi}^{\boldsymbol{C},n}_{j+3/2}}{\partial X^n_{j+2}} \ge 0.$$

For ease of notation, we introduce

$$\boldsymbol{\Upsilon}^{\boldsymbol{C},n}_{\mathrm{f},j} := \boldsymbol{C}^n_j + \frac{A_{j+1}}{A_j}\boldsymbol{C}^n_{j+1} + \lambda_j\boldsymbol{\Psi}^{\boldsymbol{C},n}_{\mathrm{f},j}. \tag{2.27}$$

In the case $t_n \in T^{\mathrm{num}}_{\mathrm{f}}$, all the coefficients $\omega^{\mathrm{f},n}_j$ for $\tilde{\Upsilon}^{\boldsymbol{C},n}_{\mathrm{f},j}$ in (2.15) are non-negative, so it suffices to show that the derivatives of this function are non-negative under (CFL):

$$\frac{\partial\tilde{\Upsilon}^{\boldsymbol{C},n}_{\mathrm{f},j}}{\partial X^n_{j-1}} = \lambda_j\frac{\partial\tilde{\Psi}^{\boldsymbol{C},n}_{\mathrm{f},j}}{\partial X^n_{j-1}} = 0, \qquad \frac{\partial\tilde{\Upsilon}^{\boldsymbol{C},n}_{\mathrm{f},j}}{\partial X^n_{j+2}} = \lambda_j\frac{\partial\tilde{\Psi}^{\boldsymbol{C},n}_{\mathrm{f},j}}{\partial X^n_{j+2}} \ge 0,$$
$$\frac{\partial\tilde{\Upsilon}^{\boldsymbol{C},n}_{\mathrm{f},j}}{\partial X^n_j} = 1 + \lambda_j\frac{\partial\tilde{\Psi}^{\boldsymbol{C},n}_{\mathrm{f},j}}{\partial X^n_j} \ge 1 + 0 \ge 0, \qquad \frac{\partial\tilde{\Upsilon}^{\boldsymbol{C},n}_{\mathrm{f},j}}{\partial X^n_{j+1}} = \frac{A_{j+1}}{A_j} + \lambda_j\frac{\partial\tilde{\Psi}^{\boldsymbol{C},n}_{\mathrm{f},j}}{\partial X^n_{j+1}}$$
$$\ge \frac{A_{j+1}}{A_j} - \lambda_j\left(A_{j+3/2}\nu_1 + Q^n_{\mathrm{u}}\right) \ge \frac{A_{j+1}}{A_j}\left(1 - \tau\left(\frac{M_1\nu_1}{h} + \frac{\|Q\|_T}{A_{\min}h}\right)\right) \ge \frac{A_{j+1}}{A_j}(1-\tau\beta_1) \ge 0.$$

In the case $t_n \in T^{\mathrm{num}}_{\mathrm{e}}$, we first estimate

$$\frac{\partial\tilde{\Phi}^{\boldsymbol{C},n}_{\mathrm{e},j+1/2}}{\partial X^n_{j+1}} = A_{j+1/2}\left(\chi^-_{\mathrm{e}}\left(v'_{\mathrm{hs}}(X^n_{j+1}) - \frac{d(X^n_{j+1})}{h}\right)X_{j+1} + v^{X,n,-}_{\mathrm{e},j+1/2}\right) \ge -A_{j+1/2}\nu_2 - Q^n_{\mathrm{e}}.$$

Combining this estimate with those of the derivatives of $\tilde{\Psi}^{\boldsymbol{C},n}_{\mathrm{f},j}$, we obtain those for $\tilde{\Psi}^{\boldsymbol{C},n}_{\mathrm{e},j}$. Introducing

$$\boldsymbol{\Upsilon}^{\boldsymbol{C},n}_{\mathrm{e},j} := \boldsymbol{C}^n_j + \frac{A_{j+1}}{A_j}\boldsymbol{C}^n_{j+1} + \lambda_j\boldsymbol{\Psi}^{\boldsymbol{C},n}_{\mathrm{e},j}, \tag{2.28}$$

we see that the only derivative that differs from those above is

$$\frac{\partial\tilde{\Upsilon}^{\boldsymbol{C},n}_{\mathrm{e},j}}{\partial X^n_{j+1}} = \frac{A_{j+1}}{A_j} + \lambda_j\frac{\partial\tilde{\Psi}^{\boldsymbol{C},n}_{\mathrm{e},j}}{\partial X^n_{j+1}} = \frac{A_{j+1}}{A_j} + \lambda_j\left(\frac{\partial\tilde{\Phi}^{\boldsymbol{C},n}_{\mathrm{e},j+1/2}}{\partial X^n_{j+1}} - \frac{\partial\tilde{\Phi}^{\boldsymbol{C},n}_{j+3/2}}{\partial X^n_{j+1}}\right)$$
$$\ge \frac{A_{j+1}}{A_j} - \frac{\tau}{A_jh}\left(A_{j+1/2}\nu_2 + Q^n_{\mathrm{e}} + Q^n_{\mathrm{u}} + A_{j+3/2}\left(v_{\mathrm{hs}}(0) + \frac{D(\hat{X})}{h}\right)\right)$$
$$\ge \frac{A_{j+1}}{A_j}\left(1 - \frac{\tau}{h}\left(M_1\nu_2 + \frac{\|Q\|_T}{A_{\min}} + M_1\left(v_{\mathrm{hs}}(0) + \frac{D(\hat{X})}{h}\right)\right)\right) = \frac{A_{j+1}}{A_j}(1-\tau\beta_1) \ge 0.$$

We write

$$C^{(k),n+1}_{\mathrm{e}} = \mathcal{H}^{(k),n}_{\boldsymbol{C}_{\mathrm{e}}}\left(\boldsymbol{C}^n_{\mathrm{e}}, \boldsymbol{C}^n_{\bar{j}^n+1}\right)$$

for the update formula for one component (they are all equal) of the effluent concentration. Summing all the components, we obtain

$$X_{\mathrm{e}}^{n+1} = \mathcal{H}_{\boldsymbol{C}_{\mathrm{e}}}^{(k),n}\big(X_{\mathrm{e}}^{n}, X_{\bar{j}^n+1}^{n}\big)$$

for any fixed $k \in \{1, \dots, k_{\boldsymbol{C}}\}$. This formula is trivial for $t_n \in T_{\mathrm{f}}^{\mathrm{num}}$, and for $t_n \in T_{\mathrm{e}}^{\mathrm{num}}$, we get

$$\frac{\partial \mathcal{H}_{\boldsymbol{C}_{\mathrm{e}}}^{(k),n}}{\partial X_{\mathrm{e}}^{n}} = 1 - \lambda_1 Q_{\mathrm{e}}^{n} \geq 1 - \tau \frac{\|Q\|_T}{A_{\min} h} \geq 0, \qquad \frac{\partial \mathcal{H}_{\boldsymbol{C}_{\mathrm{e}}}^{(k),n}}{\partial X_{\bar{j}^n+1}^{n}} = -\lambda_1 \frac{\partial \tilde{\Phi}_{\mathrm{e},j+1/2}^{\boldsymbol{C},n}}{\partial X_{j+1}^{n}} \geq 0.$$

To prove the boundedness, the monotonicity in each variable of $\mathcal{H}_{X,j}^{n}$ and the assumption $v_{\mathrm{hs}}(\hat{X}) = 0$ are used to obtain, for $t_n \in T_{\mathrm{f}}^{\mathrm{num}}$ and $j = \bar{j}^n = \bar{j}^{n+1}$,

$$\begin{aligned}
0 &\leq \alpha^{n+1}\eta_j^{n+1}\lambda_j Q_{\mathrm{f}}^{n} X_{\mathrm{f}}^{n} = \mathcal{H}_{X,j}^{n}(0, \dots, 0) \leq X_j^{n+1} = \mathcal{H}_{X,j}^{n}\big(0, X_j^n, \dots, X_{j+3}^n\big) \\
&\leq \mathcal{H}_{X,j}^{n}\big(0, \alpha^n\hat{X}, \hat{X}, \hat{X}, \hat{X}\big) = \alpha^{n+1}\eta_j^{n+1}\left(\alpha^n\hat{X} + \frac{A_{j+1}}{A_j}\hat{X} + \lambda_j\big(Q_{\mathrm{f}}^{n}X_{\mathrm{f}}^{n} - Q_{\mathrm{u}}^{n}\hat{X}\big)\right) \\
&\leq \alpha^{n+1}\eta_j^{n+1}\hat{X}\left(\alpha^n + \frac{A_{j+1}}{A_j} + \lambda_j(Q_{\mathrm{f}}^{n} - Q_{\mathrm{u}}^{n})\right) \overset{(2.5)}{=} \alpha^{n+1}\hat{X}\eta_j^{n+1}\left(\frac{A_{j+1}}{A_j} + \alpha^{n+1}\right) = \alpha^{n+1}\hat{X}.
\end{aligned}$$

For $t_n \in T_{\mathrm{f}}^{\mathrm{num}}$ and $j = \bar{j}^n - 1 = \bar{j}^{n+1}$, we first see that (2.4) implies; cf. Figure 2.1 (c),

$$\alpha^{n+1}A_{\bar{j}^n-1} + A_{\bar{j}^n} - \alpha^n A_{\bar{j}^n} = (Q_{\mathrm{f}}^{n} - Q_{\mathrm{u}}^{n})\kappa, \tag{2.29}$$

which we use at the end of the estimate

$$\begin{aligned}
0 &\leq \alpha^{n+1}\theta^{n+1}\lambda_{\bar{j}^n-1}Q_{\mathrm{f}}X_{\mathrm{f}}^{n} = \mathcal{H}_{X,\bar{j}^n-1}^{n}(0, \dots, 0) \leq X_{\bar{j}^n-1}^{n+1} \\
&= \mathcal{H}_{X,\bar{j}^n-1}^{n}\big(0, 0, X_{\bar{j}^n}^{n}, X_{\bar{j}^n+1}^{n}, X_{\bar{j}^n+2}^{n}\big) \leq \mathcal{H}_{X,\bar{j}^n-1}^{n}\big(0, 0, \alpha^n\hat{X}, \hat{X}, \hat{X}\big) \\
&= \alpha^{n+1}\theta^{n+1}\left(\alpha^n\hat{X} + \frac{A_{\bar{j}^n+1}}{A_{\bar{j}^n}}\hat{X} + \lambda_{\bar{j}^n}\big(Q_{\mathrm{f}}^{n}X_{\mathrm{f}}^{n} - Q_{\mathrm{u}}^{n}\hat{X}\big)\right) \\
&\leq \alpha^{n+1}\hat{X}\theta^{n+1}\left(\alpha^n + \frac{A_{\bar{j}^n+1}}{A_{\bar{j}^n}} + \alpha^{n+1}\frac{A_{\bar{j}^n-1}}{A_{\bar{j}^n}} + 1 - \alpha^n\right) = \alpha^{n+1}\hat{X}.
\end{aligned}$$

In the case $j = \bar{j}^n = \bar{j}^{n+1} + 1$ (cf. Figure 2.1 (c)) we can still use (2.29) to obtain

$$\begin{aligned}
0 &\leq \theta^{n+1}\lambda_{\bar{j}^n}Q_{\mathrm{f}}X_{\mathrm{f}}^{n} = \mathcal{H}_{X,\bar{j}^n}^{n}(0, \dots, 0) \leq X_{\bar{j}^n}^{n+1} \\
&= \mathcal{H}_{X,\bar{j}^n}^{n}\big(0, 0, X_{\bar{j}^n}^{n}, X_{\bar{j}^n+1}^{n}, X_{\bar{j}^n+2}^{n}\big) \leq \mathcal{H}_{X,\bar{j}^n}^{n}\big(0, 0, \alpha^n\hat{X}, \hat{X}, \hat{X}\big) \\
&= \theta^{n+1}\left(\alpha^n\hat{X} + \frac{A_{\bar{j}^n+1}}{A_{\bar{j}^n}}\hat{X} + \lambda_{\bar{j}^n}\big(Q_{\mathrm{f}}^{n}X_{\mathrm{f}}^{n} - Q_{\mathrm{u}}^{n}\hat{X}\big)\right) \\
&\leq \hat{X}\theta^{n+1}\left(\alpha^n + \frac{A_{\bar{j}^n+1}}{A_{\bar{j}^n}} + \alpha^{n+1}\frac{A_{\bar{j}^n-1}}{A_{\bar{j}^n}} + 1 - \alpha^n\right) = \hat{X}.
\end{aligned}$$

A similar estimation can be made for the case $j = \bar{j}^n + 1 = \bar{j}^{n+1} + 2$. For the case $j = \bar{j}^n + 1 = \bar{j}^{n+1}$; see Figure 2.1 (a), we note that (2.4) implies

$$\alpha^{n+1}A_{\bar{j}^n+1} - (\alpha^n A_{\bar{j}^n} + A_{\bar{j}^n+1}) = (Q_{\mathrm{f}}^{n} - Q_{\mathrm{u}}^{n})\kappa,$$

which we use to estimate

$$\begin{aligned}
0 &\le \frac{A_{\bar{j}^n}}{A_{\bar{j}^n+1}}\lambda_{\bar{j}^n}Q_{\mathrm{f}}X_{\mathrm{f}}^n = \mathcal{H}^n_{X,\bar{j}^n+1}(0,\dots,0) \le X^{n+1}_{\bar{j}^n+1}\\
&= \mathcal{H}^n_{X,\bar{j}^n+1}\big(0,X^n_{\bar{j}^n},\dots,X^n_{\bar{j}^n+3}\big) \le \mathcal{H}^n_{X,\bar{j}^n+1}\big(0,\alpha^n\hat{X},\hat{X},\hat{X},\hat{X}\big)\\
&= \frac{A_{\bar{j}^n}}{A_{\bar{j}^n+1}}\left(\alpha^n\hat{X} + \frac{A_{\bar{j}^n+1}}{A_{\bar{j}^n}}\hat{X} + \lambda_{\bar{j}^n}\big(Q_{\mathrm{f}}^nX_{\mathrm{f}}^n - Q_{\mathrm{u}}^n\hat{X}\big)\right)\\
&\le \frac{A_{\bar{j}^n}}{A_{\bar{j}^n+1}}\hat{X}\left(\alpha^n + \frac{A_{\bar{j}^n+1}}{A_{\bar{j}^n}} + \alpha^{n+1}\frac{A_{\bar{j}^n+1}}{A_{\bar{j}^n}} - \left(\alpha^n + \frac{A_{\bar{j}^n+1}}{A_{\bar{j}^n}}\right)\right) = \alpha^{n+1}\hat{X}.
\end{aligned}$$

The remaining fill cases are similar; we omit details. For $t_n \in T_{\mathrm{e}}^{\mathrm{num}}$, similar estimations apply; the only difference is that $Q_{\mathrm{f}}X_{\mathrm{f}}^n$ is replaced by $\tilde{\Phi}^{\boldsymbol{C},n}_{\mathrm{e},j+1/2}$, which equals zero when the concentrations are zero, to prove the lower bound. For the upper bound, one uses (2.4) with $\bar{Q}^n = -Q_{\mathrm{e}}^n$ instead of Q_{f}^n. For the effluent, we get

$$0 = \mathcal{H}^n_{\boldsymbol{C}_{\mathrm{e}}}(0,0) \le X_{\mathrm{e}}^{n+1} = \mathcal{H}^n_{\boldsymbol{C}_{\mathrm{e}}}\big(X_{\mathrm{e}}^n, X^n_{\bar{j}^n+1}\big) \le \mathcal{H}^n_{\boldsymbol{C}_{\mathrm{e}}}\big(\hat{X},\hat{X}\big) = \hat{X} - \lambda_1(Q_{\mathrm{e}}^n + Q_{\mathrm{u}}^n)\hat{X} \le \hat{X}.$$

Proof of (2.25): This follows directly from (2.24), since each component of the update formula for $\boldsymbol{C}_j^n$ is equal to that of X_j^n (there is no reaction term).

Proof of (2.26): We start as in the proof of (2.24), use the notation and estimations from there, and prove monotonicity of each component of the right-hand side $\mathcal{H}^{(k),n}_{\boldsymbol{S},\bar{j}^n}$ of the update formula for component $S_j^{(k),n}$, which we write as S_j^n. We also skip the superscript (k) for components of other vectors. We let $\hat{\rho} := 1/(\rho_X - \hat{X})$ and

$$\nu_3 := \hat{\rho}\left((\rho_X + \hat{X})\frac{\|Q\|_T}{A_{\min}} + \left(v_{\mathrm{hs}}(0) + \frac{D(\hat{X})}{h}\right)\hat{X}\right).$$

The numerical fluxes are different and we get

$$\begin{aligned}
\frac{\partial\Phi^{\boldsymbol{S},n}_{j+1/2}}{\partial S_j^n} &= A_{j+1/2}\frac{(\rho_Xq_{j+1/2}^n - F^{X,n}_{j+1/2})^+}{\rho_X - X_j^n} \le A_{j+1/2}\hat{\rho}\big(\rho_Xq_{j+1/2}^n - v^{X,n,-}_{j+1/2}\hat{X}\big)\\
&= A_{j+1/2}\hat{\rho}\big(\rho_Xq_{j+1/2}^n + v^{X,n,+}_{j+1/2}\hat{X}\big)\\
&\le A_{j+1/2}\hat{\rho}\left(\rho_Xq_{j+1/2}^n + \left(q_{j+1/2}^n + v_{\mathrm{hs}}(0) + \frac{D(\hat{X})}{h}\right)\hat{X}\right) \le A_{j+1/2}\nu_3,\\
\frac{\partial\Phi^{\boldsymbol{S},n}_{j+1/2}}{\partial S_{j+1}^n} &= A_{j+1/2}\frac{(\rho_Xq_{j+1/2}^n - F^{X,n}_{j+1/2})^-}{\rho_X - X_{j+1}} \le 0.
\end{aligned}$$

Because of the similarities between $\Psi^{\boldsymbol{C},n}_{\mathrm{f},j}$ and $\Psi^{\boldsymbol{S},n}_{\mathrm{f},j}$, we only write the difference here:

$$\frac{\partial\Psi^{\boldsymbol{S},n}_{\mathrm{f},j}}{\partial S_{j+1}^n} = -\frac{\partial\Phi^{\boldsymbol{S},n}_{j+3/2}}{\partial S_{j+1}^n} \ge -A_{j+3/2}\nu_3.$$

To prove the monotonicity in the case $t_n \in T_{\mathrm{f}}^{\mathrm{num}}$, we conclude that the estimations are in fact similar to those in the proof of (2.24) with the following difference (where $\boldsymbol{\Upsilon}_{\mathrm{f},j}^{\boldsymbol{S},n}$ is defined analogously to (2.27) and $\Upsilon_{\mathrm{f},j}^{\boldsymbol{S},n}$ denotes an arbitrary component of that vector):

$$\frac{\partial \Upsilon_{\mathrm{f},j}^{\boldsymbol{S},n}}{\partial S_{j+1}^n} \geq \frac{A_{j+1}}{A_j}\left(1 - \tau\frac{M_1\nu_3}{h}\right) \geq \frac{A_{j+1}}{A_j}(1-\tau\beta_2) \geq 0.$$

To prove the monotonicity in the case $t_n \in T_{\mathrm{e}}^{\mathrm{num}}$, we first estimate

$$\frac{\partial \Phi_{\mathrm{e},j+1/2}^{\boldsymbol{S},n}}{\partial S_{j+1}^n} = \left(-\frac{A_{j+1/2}X_{j+1}^n}{\rho_X - X_{j+1}^n}\left(v_{\mathrm{hs}}(X_{j+1}^n) - \frac{D(X_{j+1}^n)}{h}\right) - Q_{\mathrm{e}}^n\right)^- \geq -A_{j+1/2}\hat{\rho}\hat{X}v_{\mathrm{hs}}(0) - Q_{\mathrm{e}}^n.$$

Following the procedure of the proof of (2.24) (with $\boldsymbol{\Upsilon}_{\mathrm{e},j}^{\boldsymbol{S},n}$ defined analogously to (2.28)), we now get

$$\begin{aligned}
\frac{\partial \Upsilon_{\mathrm{e},j}^{\boldsymbol{S},n}}{\partial S_{j+1}^n} &= \frac{A_{j+1}}{A_j} + \lambda_j \frac{\partial \Psi_{\mathrm{e},j}^{\boldsymbol{S},n}}{\partial S_{j+1}^n} = \frac{A_{j+1}}{A_j} + \lambda_j\left(\frac{\partial \tilde{\Phi}_{\mathrm{e},j+1/2}^{\boldsymbol{S},n}}{\partial S_{j+1}^n} - \frac{\partial \tilde{\Phi}_{j+3/2}^{\boldsymbol{S},n}}{\partial S_{j+1}^n}\right) \\
&\geq \frac{A_{j+1}}{A_j} - \lambda_j\left\{A_{j+1/2}\hat{\rho}\hat{X}v_{\mathrm{hs}}(0) + Q_{\mathrm{e}}^n + A_{j+3/2}\hat{\rho}\big(\rho_X q_{j+3/2}^n - F_{j+3/2}^X\big)^+\right\} \\
&\geq \frac{A_{j+1}}{A_j} - \lambda_j\Bigg\{A_{j+1/2}\hat{\rho}\hat{X}v_{\mathrm{hs}}(0) + Q_{\mathrm{e}}^n \\
&\qquad + \hat{\rho}\left(\rho_X Q_{\mathrm{u}}^n + A_{j+3/2}\hat{X}\left(\frac{Q_{\mathrm{u}}^n}{A_{j+3/2}} + v_{\mathrm{hs}}(0) + \frac{D(\hat{X})}{h}\right)\right)\Bigg\} \\
&\geq \frac{A_{j+1}}{A_j} - \frac{\tau}{A_j h}\Bigg\{A_{j+1/2}\hat{\rho}\hat{X}v_{\mathrm{hs}}(0) + Q_{\mathrm{e}}^n \\
&\qquad + \hat{\rho}\left((\rho_X + \hat{X})Q_{\mathrm{u}}^n + A_{j+3/2}\hat{X}\left(v_{\mathrm{hs}}(0) + \frac{D(\hat{X})}{h}\right)\right)\Bigg\} \\
&\geq \frac{A_{j+1}}{A_j}\left(1 - \frac{\tau M_1\hat{\rho}(\hat{X}v_{\mathrm{hs}}(0) + \nu_3)}{h}\right) \geq \frac{A_{j+1}}{A_j}\left(1 - \frac{\tau\beta_2}{h}\right) \geq 0.
\end{aligned}$$

For the updates of the effluent concentrations, we get the same result for $\boldsymbol{S}_{\mathrm{e}}^n$ as for $\boldsymbol{C}_{\mathrm{e}}^n$.

The proof of positivity can be done as in the proof of (2.24). □

Lemma 2.2. *If $\check{\boldsymbol{C}}_j^{n+1}, \check{\boldsymbol{S}}_j^{n+1} \geq \mathbf{0}$ for all j and (CFL) holds, then the second step of the splitting scheme (2.14), (2.19) and (2.21) (and the analogous formulas for $\boldsymbol{S}_j^{n+1}$) satisfy $\boldsymbol{C}_j^{n+1}, \boldsymbol{S}_j^{n+1} \geq \mathbf{0}$ for all j.*

Proof. Component k of (2.14) can be written and estimated by means of (1.2) and (1.4) as

$$C_j^{(k),n+1} = \check{C}_j^{(k),n+1} + \tau\sum_{l\in I_{\boldsymbol{C},k}^+}\sigma_{\boldsymbol{C}}^{(k,l)}r^{(l)}\big(\check{\boldsymbol{C}}_j^{n+1}, \check{\boldsymbol{S}}_j^{n+1}\big) + \tau\sum_{l\in I_{\boldsymbol{C},k}^-}\sigma_{\boldsymbol{C}}^{(k,l)}\bar{r}^{(l)}\big(\check{\boldsymbol{C}}_j^{n+1}, \check{\boldsymbol{S}}_j^{n+1}\big)\check{C}_j^{(k),n+1}$$

$$\geq \check{C}_j^{(k),n+1}\left(1+\tau\sum_{l\in I^-_{\boldsymbol{C},k}}\sigma_{\boldsymbol{C}}^{(k,l)}\bar{r}^{(l)}\big(\check{\boldsymbol{C}}_j^{n+1},\check{\boldsymbol{S}}_j^{n+1}\big)\right)\geq \check{C}_j^{(k),n+1}(1-\tau M_{\boldsymbol{C}})\geq 0,$$

where the latter inequality follows from (CFL). Consider now the formula (2.19) for the fill case (a) with the non-zero coefficient $\omega^{\mathrm{f},n}_{\bar{j}^n+1} := A_{\bar{j}^n}/A_{\bar{j}^n+1}$ (the others are trivial). Then component k of (2.19) is estimated by using the rewriting above applied to both reaction terms:

$$\begin{aligned}C^{(k),n+1}_{\bar{j}^n+1} &= \check{C}^{(k),n+1}_{\bar{j}^n+1}+\tau\left(\alpha^n\frac{A_{\bar{j}^n}}{A_{\bar{j}^n+1}}R^{(k)}_{\boldsymbol{C}}\left(\frac{\check{\boldsymbol{C}}^{n+1}_{\bar{j}^n}}{\alpha^n},\frac{\check{\boldsymbol{S}}^{n+1}_{\bar{j}^n}}{\alpha^n}\right)+R^{(k)}_{\boldsymbol{C}}\big(\check{\boldsymbol{C}}^{n+1}_{\bar{j}^n+1},\check{\boldsymbol{S}}^{n+1}_{\bar{j}^n+1}\big)\right)\\ &\geq \check{C}^{(k),n+1}_{\bar{j}^n+1}\left(1-\tau\left(\frac{A_{\bar{j}^n}}{A_{\bar{j}^n+1}}+1\right)M_{\boldsymbol{C}}\right)\geq \check{C}^{(k),n+1}_{\bar{j}^n+1}\big(1-\tau(M_2+1)M_{\boldsymbol{C}}\big)\geq 0,\end{aligned}$$

where the latter inequality follows from (CFL). For fill case (b), we get in the case $\omega^{\mathrm{f},n}_{\bar{j}^n+1} := \eta^{n+1}$

$$\begin{aligned}C^{(k),n+1}_{\bar{j}^n+1} &\geq \check{C}^{(k),n+1}_{\bar{j}^n+1}\left(1-\tau\eta^{n+1}\left(1+\frac{A_{\bar{j}^n+1}}{A_{\bar{j}^n}}\right)M_{\boldsymbol{C}}\right)\\ &\geq \check{C}^{(k),n+1}_{\bar{j}^n+1}\left(1-\tau\left(\frac{A_{\bar{j}^n}+A_{\bar{j}^n+1}}{\alpha^{n+1}A_{\bar{j}^n}+A_{\bar{j}^n+1}}\right)M_{\boldsymbol{C}}\right)\geq \check{C}^{(k),n+1}_{\bar{j}^n+1}\big(1-\tau(M_2+1)M_{\boldsymbol{C}}\big)\geq 0.\end{aligned}$$

The other cases are similar, for example, in case (c) with $\omega^{\mathrm{f},n}_{\bar{j}^n+1} := \theta^{n+1}$ one gets

$$C^{(k),n+1}_{\bar{j}^n+1}\geq \check{C}^{(k),n+1}_{\bar{j}^n+1}\left(1-\tau\left(\frac{A_{\bar{j}^n}+A_{\bar{j}^n+1}}{\alpha^{n+1}A_{\bar{j}^n-1}+A_{\bar{j}^n}+A_{\bar{j}^n+1}}\right)M_{\boldsymbol{C}}\right)\geq \check{C}^{(k),n+1}_{\bar{j}^n+1}\left(1-\tau M_{\boldsymbol{C}}\right)\geq 0.$$

The cases of extraction are the same and so are the analogous ones for $\boldsymbol{S}^n_{j+1}$. □

Lemma 2.3. *Consider the second step of the splitting scheme with formula (2.14) and the formula obtained by summing all vector components. If $\check{X}^{n+1}_j := \check{C}^{(1),n+1}+\cdots+\check{C}^{(k_{\boldsymbol{C}}),n+1}\leq \hat{X}$ and (CFL) holds, then the second step of the splitting scheme corresponding to (2.14) satisfies*

$$X^{n+1}_j = \check{X}^{n+1}_j+\tau\tilde{R}_{\boldsymbol{C}}\big(\check{\boldsymbol{C}}^{n+1}_j,\check{\boldsymbol{S}}^{n+1}_j\big)\leq \check{X}.$$

The analogous statement is true for the other update formulas near the surface.

Proof. If $\check{X}^{n+1}_j\geq \hat{X}-\varepsilon$, then $\tilde{R}_{\boldsymbol{C}}(\check{\boldsymbol{C}}^{n+1}_j,\check{\boldsymbol{S}}^{n+1}_j)=0$ by assumption (1.3). Otherwise $\check{X}^{n+1}_j < \hat{X}-\varepsilon$ and (CFL) gives that X^{n+1}_j is estimated by

$$X^{n+1}_j < \hat{X}-\varepsilon+\tau\tilde{M}\leq \hat{X}.$$

The rest of the update formulas are treated in the same way and the resulting formula contains an additional factor $\omega^{\mathrm{f},n}_j\in[0,1]$ multiplying τ, so the result also holds for that formula. □

2.2.6 Numerics for full mixing

During the react stage, mixing occurs due to aeration or the movement of an impeller. Then there is no relative velocity between the solids and the liquid, but reactions take place, and the time-dependent concentrations for the mixture below the surface are given by the ODEs (1.31).

Suppose the (PDE or numerical) solution $\boldsymbol{C}(z, T_0)$ is known at $t = T_0 = t_{n_0}$ when a period of complete mixing starts. The initial concentrations for the ODEs (1.31) are defined as the averages (for $k = 1, \dots, k_{\boldsymbol{C}}$; analogously for $\boldsymbol{S}$)

$$C^{(k)}(T_0) := \frac{1}{\bar{V}(T_0)} \int_{\tilde{z}(T_0)}^{B} A(\xi) C^{(k)}(\xi, T_0)\, \mathrm{d}\xi \approx \frac{h}{\bar{V}(T_0)} \sum_{i=1}^{N} A_i C_i^{(k),n_0} =: C_{\text{aver}}^{(k),n_0}.$$

The ODE system (1.31) can then be time integrated. If an ODE mixing period ends at $t = t_{\tilde{n}}$ and the PDE model is to be simulated thereafter, then the total mass below the surface is distributed among the cells by

$$C_j^{(k),\tilde{n}} := \begin{cases} 0 & \text{for } j = 1, \dots, \bar{j}^{\tilde{n}} - 1, \\ \alpha^{\tilde{n}} C_{\text{aver}}^{(k),\tilde{n}} = (z_{\bar{j}^{\tilde{n}}+1/2} - \bar{z}^{\tilde{n}}) C_{\text{aver}}^{(k),\tilde{n}} & \text{for } j = \bar{j}^{\tilde{n}}, \\ C_{\text{aver}}^{(k),\tilde{n}} & \text{for } j = \bar{j}^{\tilde{n}} + 1, \dots, N. \end{cases}$$

Recall that the ODEs (1.31) are averages of the PDE model (1.29a) and (1.29b) when the convective and diffusive terms are zero [15]. Therefore, if time integration is made with the explicit Euler method and (CFL) holds, then also the numerical approximations of the ODE solutions to (1.31) belong to Ω. In this way, the ODE iteration for the vectors $\boldsymbol{C}_{\text{aver}}$ and $\boldsymbol{S}_{\text{aver}}$ are computed by

$$\boldsymbol{C}_{\text{aver}}^{n+1} = \boldsymbol{C}_{\text{aver}}^{n} + \frac{\tau}{\bar{V}(T_0)} \left((Q_{\text{u}}^n - \bar{Q}^n) \boldsymbol{C}_{\text{aver}}^n + Q_{\text{f}}^n \boldsymbol{C}_{\text{f}}^n + \bar{V}(T_0) \boldsymbol{R}_{\boldsymbol{C}}(\boldsymbol{C}_{\text{aver}}^n, \boldsymbol{S}_{\text{aver}}^n) \right), \tag{2.30a}$$

$$\boldsymbol{S}_{\text{aver}}^{n+1} = \boldsymbol{S}_{\text{aver}}^{n} + \frac{\tau}{\bar{V}(T_0)} \left((Q_{\text{u}}^n - \bar{Q}^n) \boldsymbol{S}_{\text{aver}}^n + Q_{\text{f}}^n \boldsymbol{S}_{\text{f}}^n + \bar{V}(T_0) \boldsymbol{R}_{\boldsymbol{S}}(\boldsymbol{C}_{\text{aver}}^n, \boldsymbol{S}_{\text{aver}}^n) \right). \tag{2.30b}$$

2.2.7 Pseudocode for the splitting scheme

We present here a pseudocode for the updates of the concentrations $\boldsymbol{C}_j^n$ and $\boldsymbol{S}_j^n$ with the numerical splitting scheme. To distinguish between different time events, we use the three Boolean variables `mixing`, `mixingstart` and `mixingend`, which at a certain time point t_n are either equal to zero or one. For example, the variable `mixing` is equal to one during the entire mixing period, whereas `mixingstart` is equal to one only at the single time point when mixing starts.

Given:

Dimensions: H, B, $A(z)$
Volumetric flows: $Q_{\mathrm{f}}(t)$, $Q_{\mathrm{u}}(t)$, $Q_{\mathrm{e}}(t)$
Feed concentrations: $\boldsymbol{C}_{\mathrm{f}}(t)$, $\boldsymbol{S}_{\mathrm{f}}(t)$
Set-point concentration of dissolved oxygen: $S_{\mathrm{O}}^{\mathrm{sp}}$
Simulation time: T
No. of computational cells: N

Precomputations:

$h \leftarrow B/N$
Choose integer N_T such that $\tau \leftarrow T/N_T$ satisfies (CFL)
$t_n \leftarrow n\tau$, $n = 1, \ldots, N_T$
$\lambda \leftarrow \tau/h$
Solve $\bar{z}(t)$ by (1.21) for $0 < t \leq T$
Compute discrete values in time and space of all given and precomputed functions (see Section 2.2)

Inputs at time t_n:

Vectors of concentrations: $\boldsymbol{C}_j^n, \boldsymbol{S}_j^n$, $j = 1, \ldots, N$
Events: `mixing`, `mixingstart`, `mixingend`

for $j = 1, \ldots, \bar{j}^n - 2$ **do**
  $\boldsymbol{C}_j^{n+1} \leftarrow \boldsymbol{0}$, $\boldsymbol{S}_j^{n+1} \leftarrow \boldsymbol{0}$
end for
if `mixing` **then**
  $\boldsymbol{C}_{\bar{j}^n-1}^{n+1} \leftarrow \boldsymbol{0}$, $\boldsymbol{S}_{\bar{j}^n-1}^{n+1} \leftarrow \boldsymbol{0}$
  if `mixingstart` **then**
    $\boldsymbol{C}_{\mathrm{aver}}^n \leftarrow \frac{h}{V^n} \sum_{i=1}^N A_i \boldsymbol{C}_i^n$
    $\boldsymbol{S}_{\mathrm{aver}}^n \leftarrow \frac{h}{V^n} \sum_{i=1}^N A_i \boldsymbol{S}_i^n$
    $\boldsymbol{C}_{\bar{j}^n-1}^n \leftarrow \boldsymbol{0}$, $\boldsymbol{S}_{\bar{j}^n-1}^n \leftarrow \boldsymbol{0}$
  end if
  Compute $\boldsymbol{C}_{\mathrm{aver}}^{n+1}$, $\boldsymbol{S}_{\mathrm{aver}}^{n+1}$ from (2.30)
  for $j = \bar{j}^n, \ldots, N$ **do**
    $\boldsymbol{C}_j^{n+1} \leftarrow \boldsymbol{C}_{\mathrm{aver}}^{n+1}$, $\boldsymbol{S}_j^{n+1} \leftarrow \boldsymbol{S}_{\mathrm{aver}}^{n+1}$
    $S_j^{(3),n+1} \leftarrow S_{\mathrm{O}}^{\mathrm{sp}}$
  end for
  if `mixingend` **then**
    $\boldsymbol{C}_{\bar{j}^n}^{n+1} \leftarrow \boldsymbol{C}_{\mathrm{aver}}^n(\bar{z}^{n+1} - \bar{z}^n)$
    $\boldsymbol{S}_{\bar{j}^n}^{n+1} \leftarrow \boldsymbol{S}_{\mathrm{aver}}^n(\bar{z}^{n+1} - \bar{z}^n)$
  end if
  if $Q_{\mathrm{e}}^{n+1} > 0$ **then**
    $\boldsymbol{C}_{\mathrm{e}}^{n+1} \leftarrow \boldsymbol{C}_{\bar{j}^n}^{n+1}$, $\boldsymbol{S}_{\mathrm{e}}^{n+1} \leftarrow \boldsymbol{S}_{\bar{j}^n}^{n+1}$
  else
    $\boldsymbol{C}_{\mathrm{e}}^{n+1} \leftarrow \boldsymbol{0}$, $\boldsymbol{S}_{\mathrm{e}}^{n+1} \leftarrow \boldsymbol{0}$
  end if
  $\boldsymbol{C}_{\mathrm{u}}^{n+1} \leftarrow \boldsymbol{C}_{\mathrm{aver}}^{n+1}$, $\boldsymbol{S}_{\mathrm{u}}^{n+1} \leftarrow \boldsymbol{S}_{\mathrm{aver}}^{n+1}$
else if ((**not** `mixing`) **and** $Q_{\mathrm{e}}^n = 0$) **then**
  Compute $\check{\boldsymbol{C}}_{\bar{j}^n-1}^{n+1}, \check{\boldsymbol{C}}_{\bar{j}^n}^{n+1}, \check{\boldsymbol{C}}_{\bar{j}^n+1}^{n+1}$ from (2.15)
  Compute $\check{\boldsymbol{S}}_{\bar{j}^n-1}^{n+1}, \check{\boldsymbol{S}}_{\bar{j}^n}^{n+1}, \check{\boldsymbol{S}}_{\bar{j}^n+1}^{n+1}$ from (2.16)
  Compute $\boldsymbol{C}_{\bar{j}^n-1}^{n+1}, \boldsymbol{C}_{\bar{j}^n}^{n+1}, \boldsymbol{C}_{\bar{j}^n+1}^{n+1}$ from (2.19)
  Compute $\boldsymbol{S}_{\bar{j}^n-1}^{n+1}, \boldsymbol{S}_{\bar{j}^n}^{n+1}, \boldsymbol{S}_{\bar{j}^n+1}^{n+1}$ from (2.20)
  for $j = \bar{j}^n + 2, \ldots, N$ **do**
    Compute $\check{\boldsymbol{C}}_j^{n+1}$, $\check{\boldsymbol{S}}_j^{n+1}$ from (2.13)
    Compute $\boldsymbol{C}_j^{n+1}$, $\boldsymbol{S}_j^{n+1}$ from (2.14)
  end for
  $\boldsymbol{C}_{\mathrm{e}}^{n+1} \leftarrow \boldsymbol{0}$, $\boldsymbol{S}_{\mathrm{e}}^{n+1} \leftarrow \boldsymbol{0}$
  $\boldsymbol{C}_{\mathrm{u}}^{n+1} \leftarrow \boldsymbol{C}_{\mathrm{u}}^n + \lambda_{N+1}\big(\boldsymbol{\Phi}_{N+1/2}^{\boldsymbol{C},n} - Q_{\mathrm{u}}^n \boldsymbol{C}_{\mathrm{u}}^n\big)$
  $\boldsymbol{S}_{\mathrm{u}}^{n+1} \leftarrow \boldsymbol{S}_{\mathrm{u}}^n + \lambda_{N+1}\big(\boldsymbol{\Phi}_{N+1/2}^{\boldsymbol{S},n} - Q_{\mathrm{u}}^n \boldsymbol{S}_{\mathrm{u}}^n\big)$
else if ((**not** `mixing`) **and** $Q_{\mathrm{e}}^n > 0$) **then**
  $\boldsymbol{C}_{\bar{j}^n-1}^{n+1} \leftarrow \boldsymbol{0}$, $\boldsymbol{S}_{\bar{j}^n-1}^{n+1} \leftarrow \boldsymbol{0}$
  Compute $\check{\boldsymbol{C}}_{\bar{j}^n}^{n+1}, \check{\boldsymbol{C}}_{\bar{j}^n+1}^{n+1}$ from (2.17)
  Compute $\check{\boldsymbol{S}}_{\bar{j}^n}^{n+1}, \check{\boldsymbol{S}}_{\bar{j}^n+1}^{n+1}$ from (2.18)
  Compute $\boldsymbol{C}_{\bar{j}^n}^{n+1}$, $\boldsymbol{C}_{\bar{j}^n+1}^{n+1}$ from (2.21)
  Compute $\boldsymbol{S}_{\bar{j}^n}^{n+1}$, $\boldsymbol{S}_{\bar{j}^n+1}^{n+1}$ from (2.22)
  for $j = \bar{j}^n + 2, \ldots, N$ **do**
    Compute $\check{\boldsymbol{C}}_j^{n+1}$, $\check{\boldsymbol{S}}_j^{n+1}$ from (2.13)
    Compute $\boldsymbol{C}_j^{n+1}$, $\boldsymbol{S}_j^{n+1}$ from (2.14)
  end for
  $\boldsymbol{C}_{\mathrm{e}}^{n+1} \leftarrow \boldsymbol{C}_{\mathrm{e}}^n - \lambda_1\big(Q_{\mathrm{e}}^n \boldsymbol{C}_{\mathrm{e}}^n + \boldsymbol{\Phi}_{\mathrm{e},\bar{j}^n+1/2}^{\boldsymbol{C},n}\big)$
  $\boldsymbol{S}_{\mathrm{e}}^{n+1} \leftarrow \boldsymbol{S}_{\mathrm{e}}^n - \lambda_1\big(Q_{\mathrm{e}}^n \boldsymbol{S}_{\mathrm{e}}^n + \boldsymbol{\Phi}_{\mathrm{e},\bar{j}^n+1/2}^{\boldsymbol{S},n}\big)$
  $\boldsymbol{C}_{\mathrm{u}}^{n+1} \leftarrow \boldsymbol{C}_{\mathrm{u}}^n + \lambda_{N+1}\big(\boldsymbol{\Phi}_{N+1/2}^{\boldsymbol{C},n} - Q_{\mathrm{u}}^n \boldsymbol{C}_{\mathrm{u}}^n\big)$
  $\boldsymbol{S}_{\mathrm{u}}^{n+1} \leftarrow \boldsymbol{S}_{\mathrm{u}}^n + \lambda_{N+1}\big(\boldsymbol{\Phi}_{N+1/2}^{\boldsymbol{S},n} - Q_{\mathrm{u}}^n \boldsymbol{S}_{\mathrm{u}}^n\big)$
end if

Outputs at time t_{n+1}:

Vectors of concentration: $\boldsymbol{C}_j^{n+1}$, $\boldsymbol{S}_j^{n+1}$, $j = 1, \ldots, N$
Effluent vectors: $\boldsymbol{C}_{\mathrm{e}}^{n+1}$, $\boldsymbol{S}_{\mathrm{e}}^{n+1}$
Underflow vectors: $\boldsymbol{C}_{\mathrm{u}}^{n+1}$, $\boldsymbol{S}_{\mathrm{u}}^{n+1}$

Table 2.1: List of variables and units for the ASM1 model (used in Chapters 2, 3 and 4).

Material	Notation	Unit
Particulate inert organic matter	X_{I}	$(\mathrm{kg\ COD})\,\mathrm{m}^{-3}$
Slowly biodegradable substrate	X_{S}	$(\mathrm{kg\ COD})\,\mathrm{m}^{-3}$
Active heterotrophic biomass	$X_{\mathrm{B,H}}$	$(\mathrm{kg\ COD})\,\mathrm{m}^{-3}$
Active autotrophic biomass	$X_{\mathrm{B,A}}$	$(\mathrm{kg\ COD})\,\mathrm{m}^{-3}$
Particulate products arising from biomass decay	X_{P}	$(\mathrm{kg\ COD})\,\mathrm{m}^{-3}$
Particulate biodegradable organic nitrogen	X_{ND}	$(\mathrm{kg\ N})\,\mathrm{m}^{-3}$
Soluble inert organic matter	S_{I}	$(\mathrm{kg\ COD})\,\mathrm{m}^{-3}$
Readily biodegradable substrate	S_{S}	$(\mathrm{kg\ COD})\,\mathrm{m}^{-3}$
Oxygen	S_{O}	$-(\mathrm{kg\ COD})\,\mathrm{m}^{-3}$
Nitrate and nitrite nitrogen	S_{NO}	$(\mathrm{kg\ N})\,\mathrm{m}^{-3}$
$\mathrm{NH}_4^+ + \mathrm{NH}_3$ nitrogen	S_{NH}	$(\mathrm{kg\ N})\,\mathrm{m}^{-3}$
Soluble biodegradable organic nitrogen	S_{ND}	$(\mathrm{kg\ N})\,\mathrm{m}^{-3}$

2.3 The modified ASM1 model

The PDE model is derived in mass concentrations collected in the vectors $\boldsymbol{C}$ and $\boldsymbol{S}$, whereas the ASM1 model and the reaction terms are given in more easily measurable units; see Table 2.1, which variables we collect in the vectors $\tilde{\boldsymbol{C}}$ and $\tilde{\boldsymbol{S}}$. The following holds:

$$\begin{aligned} &\boldsymbol{C} := \boldsymbol{\Lambda_C}\tilde{\boldsymbol{C}}, \quad \text{where } \boldsymbol{\Lambda_C} := \mathrm{diag}(\kappa_0,\kappa_0,\kappa_0,\kappa_0,\kappa_0,1), \quad \tilde{\boldsymbol{C}} := (X_{\mathrm{I}}, X_{\mathrm{S}}, X_{\mathrm{B,H}}, X_{\mathrm{B,A}}, X_{\mathrm{P}}, X_{\mathrm{ND}})^{\mathrm{T}}, \\ &\boldsymbol{S} := \boldsymbol{\Lambda_S}\tilde{\boldsymbol{S}}, \quad \text{where } \boldsymbol{\Lambda_S} := \mathrm{diag}(\kappa_1,\kappa_2,1,1,1,1), \qquad \tilde{\boldsymbol{S}} := (S_{\mathrm{I}}, S_{\mathrm{S}}, S_{\mathrm{O}}, S_{\mathrm{NO}}, S_{\mathrm{NH}}, S_{\mathrm{ND}})^{\mathrm{T}}, \end{aligned} \tag{2.31}$$

where κ_i, $i = 0, 1, 2$, are conversion factors. Therefore, the total suspended solids concentration X is given by the formula (2.33). The same holds for the feed concentrations $\boldsymbol{C}_{\mathrm{f}}$ and $\boldsymbol{S}_{\mathrm{f}}$. The reaction vectors in the ASM1 model satisfy

$$\begin{aligned} \boldsymbol{R_C}(\boldsymbol{C},\boldsymbol{S}) &:= \boldsymbol{\sigma_C}\boldsymbol{r}(\boldsymbol{C},\boldsymbol{S}) = \boldsymbol{\Lambda_C}\boldsymbol{\sigma_C}\boldsymbol{r}(\tilde{\boldsymbol{C}},\tilde{\boldsymbol{S}}) = \boldsymbol{\Lambda_C}\boldsymbol{R_C}(\tilde{\boldsymbol{C}},\tilde{\boldsymbol{S}}), \\ \boldsymbol{R_S}(\boldsymbol{C},\boldsymbol{S}) &:= \boldsymbol{\sigma_S}\boldsymbol{r}(\boldsymbol{C},\boldsymbol{S}) = \boldsymbol{\Lambda_S}\boldsymbol{\sigma_S}\boldsymbol{r}(\tilde{\boldsymbol{C}},\tilde{\boldsymbol{S}}) = \boldsymbol{\Lambda_S}\boldsymbol{R_C}(\tilde{\boldsymbol{C}},\tilde{\boldsymbol{S}}). \end{aligned} \tag{2.32}$$

Since the governing PDEs (1.29a), (1.29b) are linear in $\boldsymbol{C}$ and $\boldsymbol{S}$, respectively, it is easy to see that after substitution of the vectors defined by (2.31) and (2.32), the conversion factors in the diagonal matrices can be canceled and one obtains the system:

$$\begin{aligned} A(z)\frac{\partial\tilde{\boldsymbol{C}}}{\partial t} + \frac{\partial}{\partial z}(\mathcal{V}_{\boldsymbol{C}}\tilde{\boldsymbol{C}}) &= \delta\big(z-\bar{z}(t)\big)Q_{\mathrm{f}}\tilde{\boldsymbol{C}}_{\mathrm{f}} + \gamma(z,t)A(z)\boldsymbol{R_C}(\tilde{\boldsymbol{C}},\tilde{\boldsymbol{S}}), \quad z\in\mathbb{R}, \\ A(z)\frac{\partial\tilde{\boldsymbol{S}}}{\partial t} + \frac{\partial}{\partial z}(\mathcal{V}_{\boldsymbol{S}}\tilde{\boldsymbol{S}}) &= \delta\big(z-\bar{z}(t)\big)Q_{\mathrm{f}}\tilde{\boldsymbol{S}}_{\mathrm{f}} + \gamma(z,t)A(z)\boldsymbol{R_S}(\tilde{\boldsymbol{C}},\tilde{\boldsymbol{S}}), \quad z\in\mathbb{R}. \end{aligned}$$

This system is thus the same as the original one (2.31)–(2.32) and we skip the tildes, but one must use (2.33) for the computation of X.

The alkalinity variable in the original ASM1 model [63] is removed since it does not influence any other variable. We introduce an extra Monod factor with a small half-saturation parameter $\bar{K}_{\mathrm{NH}}$ for the concentration S_{NH} in processes nos. 1 and 2 (components 1 and 2 of the vector $\boldsymbol{r}$, respectively) in order to satisfy condition (1.4) and guarantee non-negative solutions of the ODE system (1.5). The stoichiometric matrices of the reaction-rate vectors are

$$\boldsymbol{\sigma_C} := \begin{bmatrix} 0 & 0 & 0 & 0 & 0 & 0 & 0 & 0 \\ 0 & 0 & 0 & 1-f_{\mathrm{P}} & 1-f_{\mathrm{P}} & 0 & -1 & 0 \\ 1 & 1 & 0 & -1 & 0 & 0 & 0 & 0 \\ 0 & 0 & 1 & 0 & -1 & 0 & 0 & 0 \\ 0 & 0 & 0 & f_{\mathrm{P}} & f_{\mathrm{P}} & 0 & 0 & 0 \\ 0 & 0 & 0 & i_{\mathrm{XB}}-f_{\mathrm{P}}i_{\mathrm{XP}} & i_{\mathrm{XB}}-f_{\mathrm{P}}i_{\mathrm{XP}} & 0 & 0 & -1 \end{bmatrix},$$

$$\boldsymbol{\sigma_S} := \begin{bmatrix} 0 & 0 & 0 & 0 & 0 & 0 & 0 & 0 \\ -\dfrac{1}{Y_{\mathrm{H}}} & -\dfrac{1}{Y_{\mathrm{H}}} & 0 & 0 & 0 & 0 & 1 & 0 \\ -\dfrac{1-Y_{\mathrm{H}}}{Y_{\mathrm{H}}} & 0 & -\dfrac{4.57-Y_{\mathrm{A}}}{Y_{\mathrm{A}}} & 0 & 0 & 0 & 0 & 0 \\ 0 & -\dfrac{1-Y_{\mathrm{H}}}{2.86Y_{\mathrm{H}}} & \dfrac{1}{Y_{\mathrm{A}}} & 0 & 0 & 0 & 0 & 0 \\ -i_{\mathrm{XB}} & -i_{\mathrm{XB}} & -i_{\mathrm{XB}}-\dfrac{1}{Y_{\mathrm{A}}} & 0 & 0 & 1 & 0 & 0 \\ 0 & 0 & 0 & 0 & 0 & -1 & 0 & 1 \end{bmatrix},$$

and the eight processes are contained in the vector

$$\boldsymbol{r}(\boldsymbol{C},\boldsymbol{S}) := \begin{pmatrix} \mu_{\mathrm{H}}\mu(S_{\mathrm{NH}},\bar{K}_{\mathrm{NH}})\mu(S_{\mathrm{S}},K_{\mathrm{S}})\mu(S_{\mathrm{O}},K_{\mathrm{O,H}})X_{\mathrm{B,H}} \\ \mu_{\mathrm{H}}\mu(S_{\mathrm{NH}},\bar{K}_{\mathrm{NH}})\mu(S_{\mathrm{S}},K_{\mathrm{S}})\mu(K_{\mathrm{O,H}},S_{\mathrm{O}})\mu(S_{\mathrm{NO}},K_{\mathrm{NO}})\eta_{\mathrm{g}}X_{\mathrm{B,H}} \\ \mu_{\mathrm{A}}\mu(S_{\mathrm{NH}},K_{\mathrm{NH}})\mu(S_{\mathrm{O}},K_{\mathrm{O,A}})X_{\mathrm{B,A}} \\ b_{\mathrm{H}}X_{\mathrm{B,H}} \\ b_{\mathrm{A}}X_{\mathrm{B,A}} \\ k_{\mathrm{a}}S_{\mathrm{ND}}X_{\mathrm{B,H}} \\ k_{\mathrm{h}}\mu_7(X_{\mathrm{S}},X_{\mathrm{B,H}})\big(\mu(S_{\mathrm{O}},K_{\mathrm{O,H}})+\eta_{\mathrm{h}}\mu(K_{\mathrm{O,H}},S_{\mathrm{O}})\mu(S_{\mathrm{NO}},K_{\mathrm{NO}})\big) \\ k_{\mathrm{h}}\mu_8(X_{\mathrm{B,H}},X_{\mathrm{ND}})\big(\mu(S_{\mathrm{O}},K_{\mathrm{O,H}})+\eta_{\mathrm{h}}\mu(K_{\mathrm{O,H}},S_{\mathrm{O}})\mu(S_{\mathrm{NO}},K_{\mathrm{NO}})\big) \end{pmatrix}.$$

Here we define the Monod expression $\mu(A,B) := A/(A+B)$ and

$$\mu_7(X_{\mathrm{S}},X_{\mathrm{B,H}}) := \begin{cases} 0 & \text{if } X_{\mathrm{S}}=0 \text{ and } X_{\mathrm{B,H}}=0, \\ \dfrac{X_{\mathrm{S}}X_{\mathrm{B,H}}}{K_{\mathrm{X}}X_{\mathrm{B,H}}+X_{\mathrm{S}}} & \text{otherwise,} \end{cases}$$

$$\mu_8(X_{\mathrm{B,H}},X_{\mathrm{ND}}) := \begin{cases} 0 & \text{if } X_{\mathrm{S}}=0 \text{ and } X_{\mathrm{B,H}}=0, \\ \dfrac{X_{\mathrm{B,H}}X_{\mathrm{ND}}}{K_{\mathrm{X}}X_{\mathrm{B,H}}+X_{\mathrm{S}}} & \text{otherwise.} \end{cases}$$

These functions are introduced to obtain well-defined expressions if any concentration is zero. All the constants are given in Table 2.2.

Table 2.2: Example 2.1: Stoichiometric and kinetic parameters.

Symbol	Name	Value	Unit
Y_{A}	Yield for autotrophic biomass	0.24	$(\mathrm{g\,COD})(\mathrm{g\,N})^{-1}$
Y_{H}	Yield for heterotrophic biomass	0.57	$(\mathrm{g\,COD})(\mathrm{g\,COD})^{-1}$
f_{P}	Fraction of biomass leading to particulate products	0.1	dimensionless
i_{XB}	Mass of nitrogen per mass of COD in biomass	0.07	$(\mathrm{g\,N})(\mathrm{g\,COD})^{-1}$
i_{XP}	Mass of nitrogen per mass of COD in products from biomass	0.06	$(\mathrm{g\,N})(\mathrm{g\,COD})^{-1}$
μ_{H}	Maximum specific growth rate for heterotrophic biomass	4.0	d^{-1}
K_{S}	Half-saturation coefficient for heterotrophic biomass	20.0	$(\mathrm{g\,COD})\,\mathrm{m}^{-3}$
$K_{\mathrm{O,H}}$	Oxygen half-saturation coefficient for heterotrophic biomass	0.25	$-(\mathrm{g\,COD})\,\mathrm{m}^{-3}$
K_{NO}	Nitrate half-saturation coefficient for denitrifying heterotrophic biomass	0.5	$(\mathrm{g\,NO_3\text{-}N})\,\mathrm{m}^{-3}$
b_{H}	Decay coefficient for heterotrophic biomass	0.5	d^{-1}
η_{g}	Correction factor for μ_{H} under anoxic conditions	0.8	dimensionless
η_{h}	Correction factor for hydrolysis under anoxic conditions	0.35	dimensionless
k_{h}	Maximum specific hydrolysis rate	1.5	$(\mathrm{g\,COD})\,(\mathrm{g\,CODd})^{-1}$
K_{X}	Half-saturation coefficient for hydrolysis of slowly biodegradable substrate	0.02	$(\mathrm{g\,COD})(\mathrm{g\,COD})^{-1}$
μ_{A}	Maximum specific growth rate for autotrophic biomass	0.879	d^{-1}
$\bar{K}_{\mathrm{NH}}$	Ammonia half-saturation coefficient for aerobic and anaerobic growth of heterotrophs	0.007	$(\mathrm{g\,NH_3\text{-}N})\,\mathrm{m}^{-3}$
K_{NH}	Ammonia half-saturation coefficient for autotrophic biomass	1.0	$(\mathrm{g\,NH_3\text{-}N})\,\mathrm{m}^{-3}$
b_{A}	Decay coefficient for autotrophic biomass	0.132	d^{-1}
$K_{\mathrm{O,A}}$	Oxygen half-saturation coefficient for autotrophic biomass	0.5	$-(\mathrm{g\,COD})\,\mathrm{m}^{-3}$
k_{a}	Ammonification rate	0.08	$\mathrm{m}^3(\mathrm{g\,CODd})^{-1}$

Table 2.3: Example 2.1: Time functions for the simulated SBR cycle. 'Model' refers to either PDE (1.29) or ODE (1.31).

Stage	Time period [h]	$X_{\mathrm{f}}(t)$ [kg/m^3]	$Q_{\mathrm{f}}(t)$ [m^3/h]	$Q_{\mathrm{u}}(t)$ [m^3/h]	$Q_{\mathrm{e}}(t)$ [m^3/h]	Model
Fill	$0 \le t < 1$	5	790	0	0	PDE
React	$1 \le t < 3$	0	0	0	0	ODE
Settle	$3 \le t < 5$	0	0	0	0	PDE
Draw	$5 \le t < 5.5$	0	0	0	1570	PDE
Idle	$5.5 \le t < 6$	0	0	10	0	PDE

2.4 Numerical simulations

The numerical method in Section 2.2.4 with condition (CFL) is first used for the simulation of an SBR process. In Chapter 1, we demonstrated the process by letting the reaction terms model a denitrification process, which occurs when there is no oxygen present. Here, the reactions are a modified ASM1 model without alkalinity; see Table 2.1 for the six particulate and six soluble state variables, and Section 2.3 for the reaction terms. Those reaction terms are expressed in the measurable units of chemical oxygen demand (COD) (except for those involving N) given in Table 2.1, which require certain conversion factors to obtain the mass concentrations in which the present model is derived. In Section 2.3, we show that, due to the structure of the governing PDEs (1.29), the model and numerical scheme can be used straightforwardly also with the COD units if only the formula

$$X = \kappa_0(X_{\mathrm{I}} + X_{\mathrm{S}} + X_{\mathrm{B,H}} + X_{\mathrm{B,A}} + X_{\mathrm{P}}) + X_{\mathrm{ND}}, \quad \text{where } \kappa_0 = \frac{1}{1.45}\,\frac{\mathrm{g}}{\mathrm{g\,COD}} \tag{2.33}$$

is used instead of equation (1.1). The value of κ_0 is taken from [2, Table 6: WAS, CODp/VSS]. Furthermore, we assume that the mixing during the react stage is accompanied by aeration so that a controller maintains the set-point value of dissolved oxygen $S_{\mathrm{O}}^{\mathrm{sp}} = 8\,\mathrm{g/m^3}$. The constitutive functions used for sedimentation and compression are (see e.g. [104])

$$v_{\mathrm{hs}}(X) := \frac{v_0}{1 + (X/\breve{X})^{\eta}}, \qquad \sigma_{\mathrm{e}}(X) := \begin{cases} 0 & \text{if } X < X_{\mathrm{c}}, \\ \sigma_0(X - X_{\mathrm{c}}) & \text{if } X \ge X_{\mathrm{c}} \end{cases}$$

with $v_0 = 1.76 \times 10^{-3}\,\mathrm{m/s}$, $\breve{X} = 3.87\,\mathrm{kg/m^3}$, $\eta = 3.58$, $X_{\mathrm{c}} = 5\,\mathrm{kg/m^3}$ and $\sigma_0 = 0.2\,\mathrm{m^2/s^2}$. Other parameters are $\rho_X = 1050\,\mathrm{kg/m^3}$, $\rho_L = 998\,\mathrm{kg/m^3}$, $g = 9.81\,\mathrm{m/s^2}$, and $B = 3\,\mathrm{m}$.

We simulate one sequence of an SBR with the stages specified in Table 2.3. (This is the same scenario as in the first example of [15] with a denitrification reaction model and without oxygen supply.) Condition (CFL) implies the step length $\tau = 0.4708\,\mathrm{s}$. The initial concentrations have

been chosen as

$$\boldsymbol{C}^0(z) = \begin{cases} \mathbf{0} & \text{if } z < 2.0\,\text{m}, \\ (0.8889, 0.0295, 1.4503, 0.0904, 0.7371, 0.0025)^{\mathrm{T}} & \text{if } z \geq 2.0\,\text{m}, \end{cases}$$
$$\boldsymbol{S}^0(z) = \begin{cases} \mathbf{0} & \text{if } z < 2.0\,\text{m}, \\ (0.04, 0.0026, 0.0, 0.0333, 0.0004, 0.0009)^{\mathrm{T}} & \text{if } z \geq 2.0\,\text{m} \end{cases}$$

(with units as in Table 2.1) while the feed concentrations are [63]

$$\boldsymbol{C}_{\mathrm{f}}(t) = X_{\mathrm{f}}(t)\frac{(0.04,\ 0.16,\ 0.096,\ 1\cdot 10^{-6},\ 0,\ 0.01828)^{\mathrm{T}}}{(0.04+0.16+0.096+1\cdot 10^{-6})\kappa_0 + 0.01828},$$
$$\boldsymbol{S}_{\mathrm{f}}(t) = (0.04,\ 0.064,\ 0.0,\ 0.001,\ 0.0125,\ 0.0101)^{\mathrm{T}},$$

where the total solids feed concentration $X_{\mathrm{f}}(t)$ varies with time according to Table 2.3.

Figures 2.2 and 2.3 show the simulation results for the concentrations within the vessel of the particulate and soluble components, respectively. In regions where the concentrations satisfy $X < X_{\mathrm{c}}$, the governing system of PDEs (1.29) is hyperbolic [12] and discontinuities may appear in the solution as can be seen in the figures. The numerical scheme seems to resolve these accurately. At time $t = 1\,\text{h}$, the tank has been filled, the react stage starts and there is full mixing by aeration. Consequently, the available components in the tank are distributed homogeneously. During the react stage, the growth of biomass is slow but the fast consumption of S_{S} and increase of S_{NH} are visible in Figures 2.3(b) and (e), respectively. The nitrification process uses oxygen to produce nitrate and nitrite, which can be seen in plot (d). After the react stage, $t \geq 3\,\text{h}$, the oxygen is quickly consumed (plot (c)), but only where there is biomass and S_{S} and S_{NH} are positive.

The convergence of the numerical scheme is demonstrated in Figure 2.4, where some of the effluent concentrations are plotted. As was illustrated with the example of denitrification in [15] and the present one for the modified ASM1 model, simulations seem to satisfy the invariant-region property although we only have a proof of this for the splitting scheme of Section 2.2.5.

For the ASM1 example here and a given number of cells N, we calculate the L^1 relative difference between the simulation result of the two variants of the numerical scheme according to the following formula, where $\boldsymbol{C}_N$ is the result without splitting and $\boldsymbol{C}_N^{\mathrm{split}}$ with splitting:

$$\mathcal{D}_N(t) := \sum_{k=1}^{k_{\boldsymbol{C}}} \frac{\|(C_N^{(k)} - C_N^{\mathrm{split},(k)})(\cdot,t)\|_{L^1(0,B)}}{\|C_N^{\mathrm{split},(k)}(\cdot,t)\|_{L^1(0,B)}} + \sum_{k=1}^{k_{\boldsymbol{S}}} \frac{\|(S_N^{(k)} - S_N^{\mathrm{split},(k)})(\cdot,t)\|_{L^1(0,B)}}{\|S_N^{\mathrm{split},(k)}(\cdot,t)\|_{L^1(0,B)}}.$$

The result at time $t = T = 6\,\text{h}$ is shown in Table 2.4 together with the CPU times for the two methods. The relative difference $\mathcal{D}_N(T)$ drops to approximately one quarter as N is doubled (for large N), which only shows that the two schemes give very similar numerical solutions.

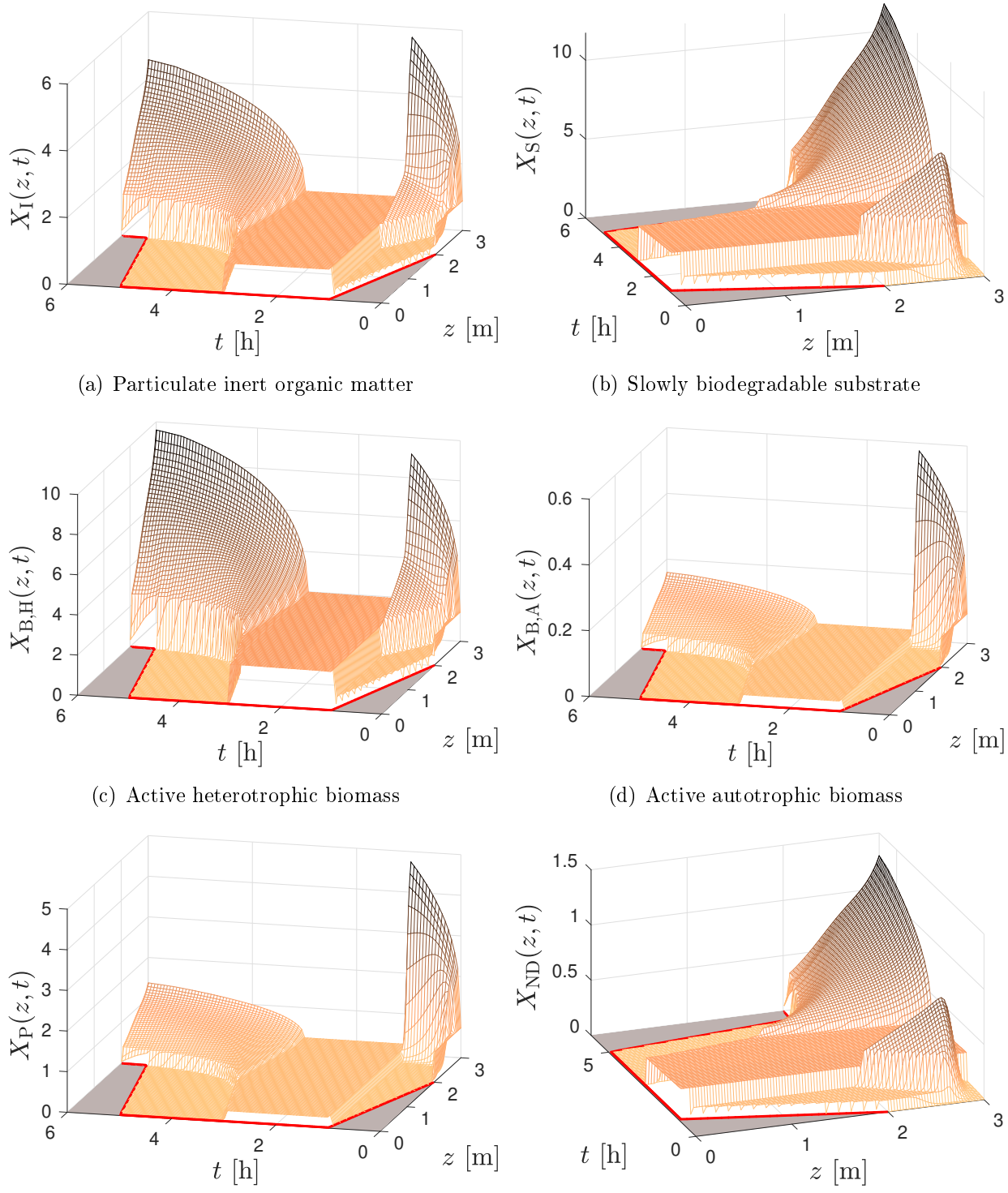

(a) Particulate inert organic matter

(b) Slowly biodegradable substrate

(c) Active heterotrophic biomass

(d) Active autotrophic biomass

(e) Particle products arising from biomass decay

(f) Particulate biodegradable organic nitrogen

Figure 2.2: Example 2.1: Concentrations (units as in Table 2.1) of the six solid components during a numerical simulation with $N = 100$ until $T = 6\,\mathrm{h}$. For visualization purposes, we do not plot zero concentrations above the surface, but fill this region with grey colour.

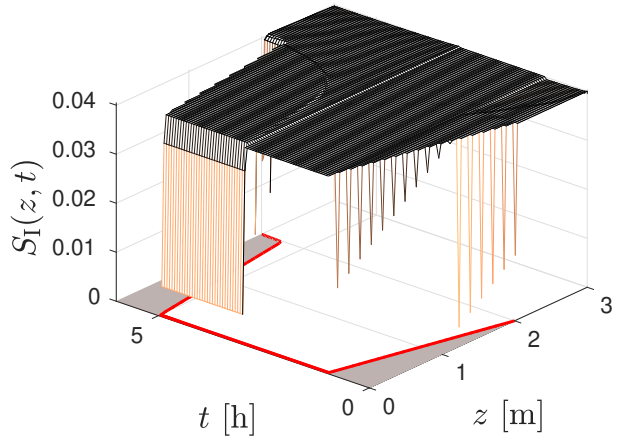

(a) Soluble inert organic matter

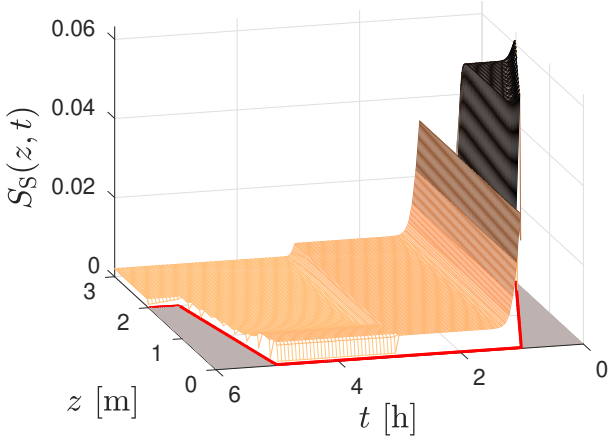

(b) Readily biodegradable substrate

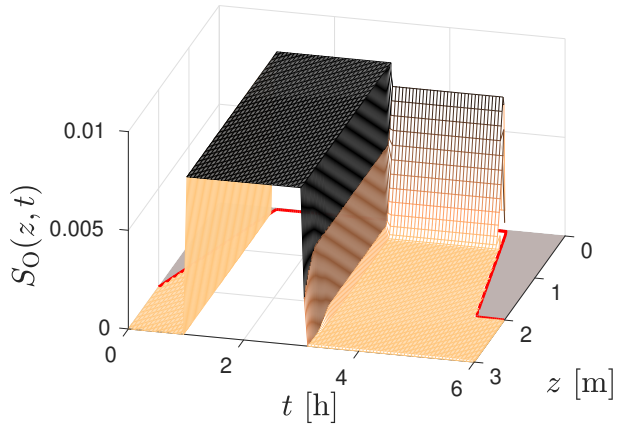

(c) Oxygen

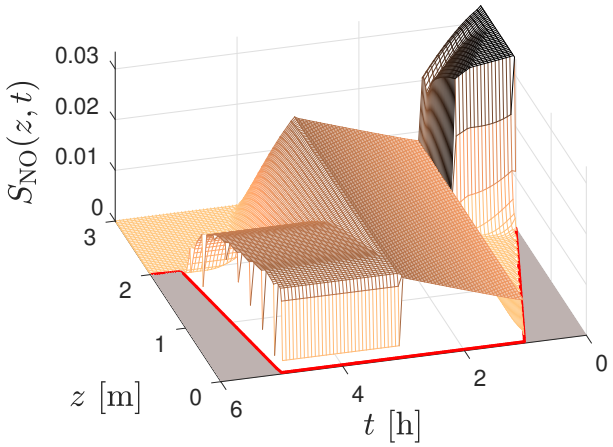

(d) Nitrate and nitrite nitrogen

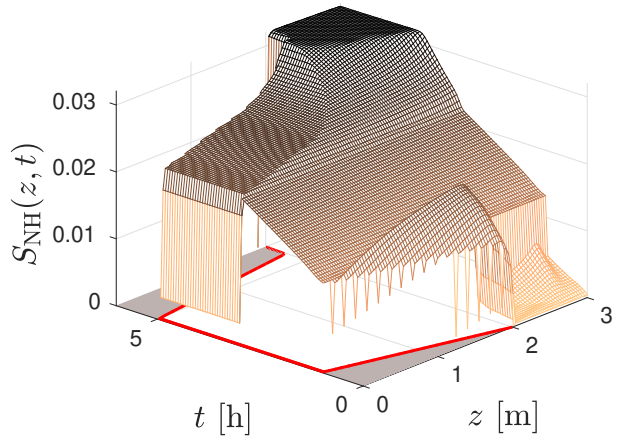

(e) $NH_4^+ + NH_3$ nitrogen

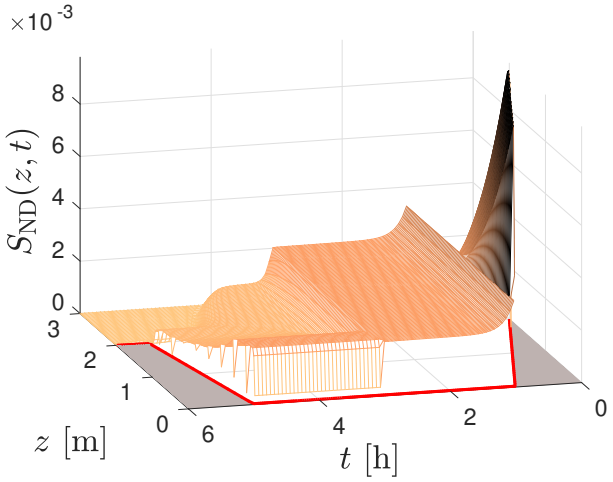

(f) Soluble biodegradable organic nitrogen

Figure 2.3: Example 2.1: Concentrations (units as in Table 2.1) of the six dissolved components during a numerical simulation with $N = 100$ until $T = 6\,\mathrm{h}$. The downwards-pointing peaks at large discontinuities arise because we do not plot zero concentration.

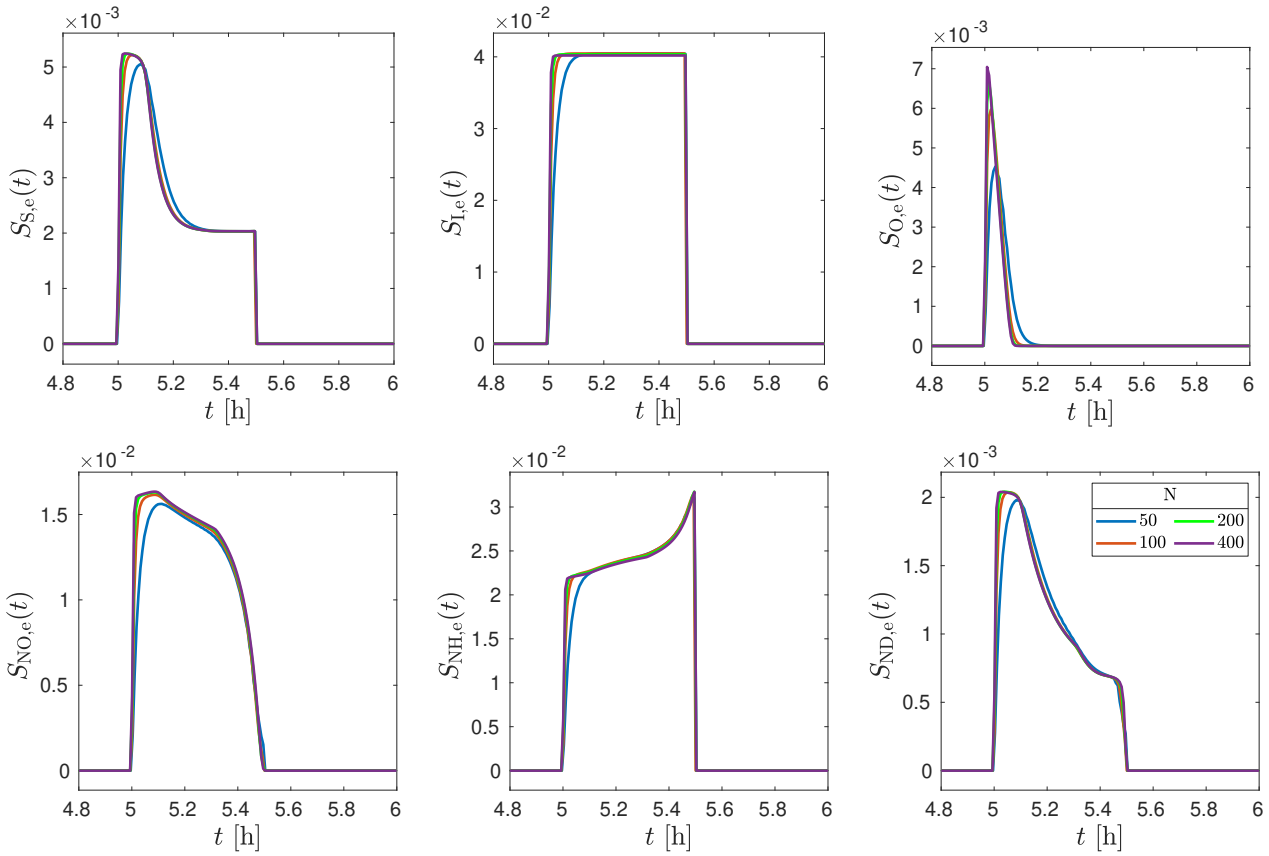

Figure 2.4: Example 2.1: Simulated effluent concentrations (units as in Table 2.1) during $t \in [4.8\,\text{h}, 6\,\text{h}]$ obtained by the discretizations where the number of computational cells within the tank is 50, 100, 200 and 400.

Table 2.4: Example 2.1: Relative differences $\mathcal{D}_N(T)$ at the final simulation time $T = 6$ h and CPU times for the respective simulation run on a standard PC.

		CPU time [s]	
N	$\mathcal{D}_N(T)$	Splitting	Without splitting
50	6.9791e-02	8.56	6.88
100	4.3824e-02	10.25	8.86
200	1.0518e-02	43.41	36.22
400	1.4123e-03	292.03	236.62
800	3.7985e-04	2616.10	1996.05

CHAPTER 3

A model of reactive settling of activated sludge: comparison with experimental data

3.1 Introduction

3.1.1 Scope

In this chapter, it is important to emphasize that we use a different approach than in Chapters 1 and 2. In those chapters, a model and a numerical scheme were developed for SBRs. In this chapter, however, our focus is on a type of continuous operation: SSTs, in contrast to SBRs that are sequential.

The purpose of Chapter 3 is to introduce a minor extension of the model of reactive settling formulated by nonlinear PDEs by [12] to include hydrodynamic dispersion, to present a numerical scheme for simulations, and first and foremost to calibrate and validate the model to real data from a pilot WRRF [77] where activated sludge reacts with dissolved substrates in an SST whose cross-sectional area varies with depth. For the biochemical reactions, the ASM1 is used [61]. This model is slightly adjusted to ensure that only non-negative concentrations are produced. In fact, the original ASM1 allows for consumption of ammonia when the concentration is zero, which causes unphysical negative concentrations. To avoid this, the reaction term for that variable is multiplied by a Monod factor which is close to one for most concentrations and tends to zero fast as the concentration tends to zero. This correction is also recommended by [60]. Standard parameter values for the ASM1 are otherwise used. For the settling-compression phenomenon, we use a three-parameter constitutive hindered-settling function and a two-parameter compression function. Hydrodynamic dispersion of particles and dissolved substrates are each included with one term and a longitudinal dispersivity parameter. The mixing that occurs near the feed inlet is modeled by a heuristic diffusion term that depends on the volumetric flows through the tank.

In a WRRF, wastewater is mainly treated through the ASP within a circuit of biological

reactors coupled with SSTs. The ASP is broadly described in well-known handbooks and monographs [30, 46, 86, 89]. To address some of the general experiences made with the ASP in real applications, we mention that SSTs contain a substantial amount of the activated sludge and reactions may take place even when oxygen is consumed. In fact, up to about one third of the total denitrification has been observed to take place within the SSTs [80, 99]. An excessive production of nitrogen in an SST, however, leads to bubbles that destroy the sedimentation properties of the flocculated sludge. On the other hand, some denitrification in the SSTs may be preferable, since one can then reduce the nitrate recirculation within the reactors and save pumping energy costs. The need to predict, quantify, and eventually control these and other effects clearly calls for the development of models of so-called reactive settling that include the spatial variability of reaction rates caused by the variation of local concentration of biomass due to hindered settling and compression. Such a model should depend on time (to handle the transient dynamics of biokinetic reactions within the ASP or the simpler process of denitrification) as well as include some spatial resolution, for instance in one space dimension aligned with gravity. From a mathematical point of view such a model is naturally posed by nonlinear PDEs. Reliable simulation models that deliver correct approximate solutions of the PDEs should then be developed, to be included in plant-wide simulation models [50].

Most previous one-dimensional sedimentation models assume a constant cross-sectional area. As pointed out by [77, 78], this is often not the case in plants, and such a model simplification may lead to a non-negligible error in the prediction of the process. This is also demonstrated in this chapter.

As is commonly seen, column batch-settling test data exhibit an initial so-called induction period when the (average) settling velocity increases slowly from zero due to initial turbulence and possibly other phenomena. The induction periods of the data were transformed away with the method by [45]. Then the five settling-compression parameters were obtained by a least-squares fit to the transformed batch data. The obtained batch-settling model is then augmented to include the mixing and the dispersion terms, whose parameters are fitted to one experimental steady-state scenario. Finally, the resulting model is compared to two other steady-state experiments not used in the calibration.

3.1.2 Outline of the chapter

Section 3.2 details the information and materials that were used to fit the reactive settling model with experimental data from a pilot plant with variable cross-sectional area (Section 3.2.1). The modified ASM1 for the biochemical reactions is used with temperature-adjusted standard coefficients presented in Section 3.2.2. The activated sludge batch sedimentation tests are given in Section 3.2.3. Section 3.2.4 shows three scenarios with different SBL heights as well as the feed concentrations of the scenarios. In Section 3.3 we present the model proposed in [12] with some modifications, hydrodynamic dispersion of the particles hidden in the suspension and in the substrates dissolved in the fluid is introduced, as well as, a term modeling

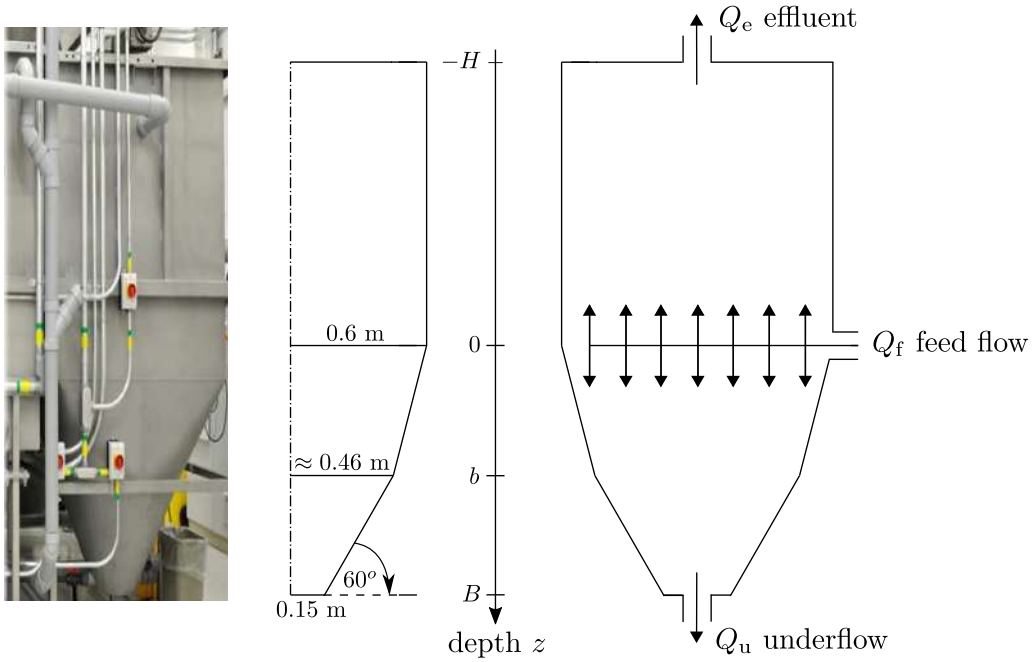

Figure 3.1: Schematic of half of the vertical cross-section of the vessel and the z-axis used for the model [77]. The dash-dotted line represents the axis of rotation for the conical part at the bottom.

the mixing of the suspension near the feed inlet. Section 3.3.2 is devoted to the description of the numerical scheme, starting with the spatial discretization, which requires the definition of numerical fluxes associated with the edges of the computational cells leading to the formulation of a spatially discrete and time-continuous line method. In Section 3.3.3 we prepare the batch test data by removing the induction period. In Section 3.4, we show the numerical simulations with the calibration of the sedimentation-compression model, as well as the calibration of the dispersion and mixing parameters fitted to a steady-state experimental scenario, compared with the experimental data.

3.2 Materials

3.2.1 Geometry of tank

A schematic of the tank is shown in Figure 3.1. We place a z-axis with its origin at the feed level, where the mixture of activated sludge and solubles are fed at the volumetric feed flow Q_f from the biological reactor. At the bottom, $z = B = 1.1$ m, there is an opening through which mixture may leave the unit a controllable volumetric underflow rate Q_u and at the top, $z = H = 1.25$ m, the effluent leaves the unit at rate $Q_e = Q_f - Q_u \geq 0$. Above the feed inlet, the tank is rectangular with dimensions 1.0×1.2 m^2 $= A_0$. The lowest part, in

$b = 0.57$ m $< z < B$, is a truncated cone with bottom radius $r = 0.15\,\mathrm{m}$. The middle part is has a shape that continuously changes from a (horizontal) rectangle at $z = 0$ to a circle with radius 0.46 m at $z = b$. The cross-sectional area in that part is approximated by a convex combination of the rectangle and the circle via

$$A(z) = \begin{cases} A_0 & \text{if } -H \le z < 0, \\ A_0 + \dfrac{z}{b}\left(\dfrac{\pi}{3}\left(\sqrt{3}r + B - b\right)^2 - A_0\right) & \text{if } 0 \le z < b, \\ \dfrac{\pi}{3}\left(\sqrt{3}r + B - z\right)^2 & \text{if } b \le z < B. \end{cases} \tag{3.1}$$

3.2.2 Activated sludge

We use the variables of ASM1, as detailed in Table 2.1, and introduce an addition component S_{ALK}, in $\boldsymbol{S}$, representing alkalinity measured in $[(\mathrm{mol\ CaCO3}), \mathrm{m}^{-3}]$. We assemble these variables into the following vectors:

$$\begin{aligned} \boldsymbol{C} &\coloneqq \left(X_{\mathrm{I}}, X_{\mathrm{S}}, X_{\mathrm{B,H}}, X_{\mathrm{B,A}}, X_{\mathrm{P}}, X_{\mathrm{ND}}\right)^{\mathrm{T}}, \\ \boldsymbol{S} &\coloneqq \left(S_{\mathrm{I}}, S_{\mathrm{S}}, S_{\mathrm{O}}, S_{\mathrm{NO}}, S_{\mathrm{NH}}, S_{\mathrm{ND}}, S_{\mathrm{ALK}}\right)^{\mathrm{T}}. \end{aligned}$$

These concentrations vary with both depth z from the feed level and the time $t \ge 0$.

The reaction rate vectors of (3.8) and (3.9) are $\boldsymbol{R_C}(\boldsymbol{C}, \boldsymbol{S}) = \boldsymbol{\sigma_C} \boldsymbol{r}(\boldsymbol{C}, \boldsymbol{S})$ and $\boldsymbol{R_S}(\boldsymbol{C}, \boldsymbol{S}) = \boldsymbol{\sigma_S} \boldsymbol{r}(\boldsymbol{C}, \boldsymbol{S})$, respectively. The stoichiometric matrix $\boldsymbol{\sigma_C}$ and vector $\boldsymbol{r}(\boldsymbol{C}, \boldsymbol{S})$, which contain the processes of biokinetic reactions for carbon and nitrogen removal, are the same as those given in Section 2.3 of Chapter 2. The stoichiometric matrix $\boldsymbol{\sigma_S}$ now has an additional row at the end for the alkalinity process, and is denoted as

$$\boldsymbol{\sigma_S} \coloneqq \begin{bmatrix} 0 & 0 & 0 & 0\ 0 & 0 & 0 & 0\ 0 \\ -\dfrac{1}{Y_{\mathrm{H}}} & -\dfrac{1}{Y_{\mathrm{H}}} & 0 & 0\ 0 & 0 & 1 & 0 \\ -\dfrac{1 - Y_{\mathrm{H}}}{Y_{\mathrm{H}}} & 0 & -\dfrac{4.57 - Y_{\mathrm{A}}}{Y_{\mathrm{A}}} & 0\ 0 & 0 & 0 & 0\ 0 \\ 0 & -\dfrac{1 - Y_{\mathrm{H}}}{2.86 Y_{\mathrm{H}}} & \dfrac{1}{Y_{\mathrm{A}}} & 0\ 0 & 0 & 0 & 0\ 0 \\ -i_{\mathrm{XB}} & -i_{\mathrm{XB}} & -i_{\mathrm{XB}} - \dfrac{1}{Y_{\mathrm{A}}} & 0\ 0 & 1 & 0\ 0 \\ 0 & 0 & 0 & 0\ 0 & -1 & 0 & 1 \\ -\dfrac{i_{\mathrm{XB}}}{14} & \dfrac{1 - Y_{\mathrm{H}}}{40.04 Y_{\mathrm{H}}} - \dfrac{i_{\mathrm{XB}}}{14} & -\dfrac{i_{\mathrm{XB}}}{14} - \dfrac{1}{7 Y_{\mathrm{A}}} & 0\ 0 & \dfrac{1}{14} & 0\ 0 \end{bmatrix},$$

with the constants given in Table 3.1.

Table 3.1: Stoichiometric and kinetic parameters at 26°C (see [41])

Symbol	Name	Value	Unit
Y_A	Yield for autotrophic biomass	0.24	$(g\,COD)(g\,N)^{-1}$
Y_H	Yield for heterotrophic biomass	0.67	$(g\,COD)(g\,COD)^{-1}$
f_P	Fraction of biomass leading to particulate products	0.08	dimensionless
i_{XB}	Mass of nitrogen per mass of COD in biomass	0.086	$(g\,N)(g\,COD)^{-1}$
i_{XP}	Mass of nitrogen per mass of COD in products from biomass	0.06	$(g\,N)(g\,COD)^{-1}$
μ_H	Maximum specific growth rate for heterotrophic biomass	9.11	d^{-1}
K_S	Half-saturation coefficient for heterotrophic biomass	20.0	$(g\,COD)\,m^{-3}$
$K_{O,H}$	Oxygen half-saturation coefficient for heterotrophic biomass	0.20	$-(g\,COD)\,m^{-3}$
K_{NO}	Nitrate half-saturation coefficient for denitrifying heterotrophic biomass	0.5	$(g\,NO_3\text{-}N)\,m^{-3}$
b_H	Decay coefficient for heterotrophic biomass	1.2	d^{-1}
η_g	Correction factor for μ_H under anoxic conditions	0.8	dimensionless
η_h	Correction factor for hydrolysis under anoxic conditions	0.4	dimensionless
k_h	Maximum specific hydrolysis rate	5.8	$(g\,COD)\,(g\,CODd)^{-1}$
K_X	Half-saturation coefficient for hydrolysis of slowly biodegradable substrate	0.058	$(g\,COD)(g\,COD)^{-1}$
μ_A	Maximum specific growth rate for autotrophic biomass	1.44	d^{-1}
$\bar{K}_{NH}$	Ammonia half-saturation coefficient for aerobic and anaerobic growth of heterotrophs	0.05	$(g\,NH_3\text{-}N)\,m^{-3}$
K_{NH}	Ammonia half-saturation coefficient for autotrophic biomass	1.0	$(g\,NH_3\text{-}N)\,m^{-3}$
b_A	Decay coefficient for autotrophic biomass	0.29	d^{-1}
$K_{O,A}$	Oxygen half-saturation coefficient for autotrophic biomass	0.4	$-(g\,COD)\,m^{-3}$
k_a	Ammonification rate	0.121	$m^3(gCODd)^{-1}$

3.2.3 Batch tests

The available data by [78] contain a series of 22 batch sedimentation tests in cylinders with initial concentrations between 1.1 g/l and 3.2 g/l of activated sludge. The sludge blanket levels

(SBLs), here measured from the bottom, were detected during 30 minutes; see Figure 3.2.

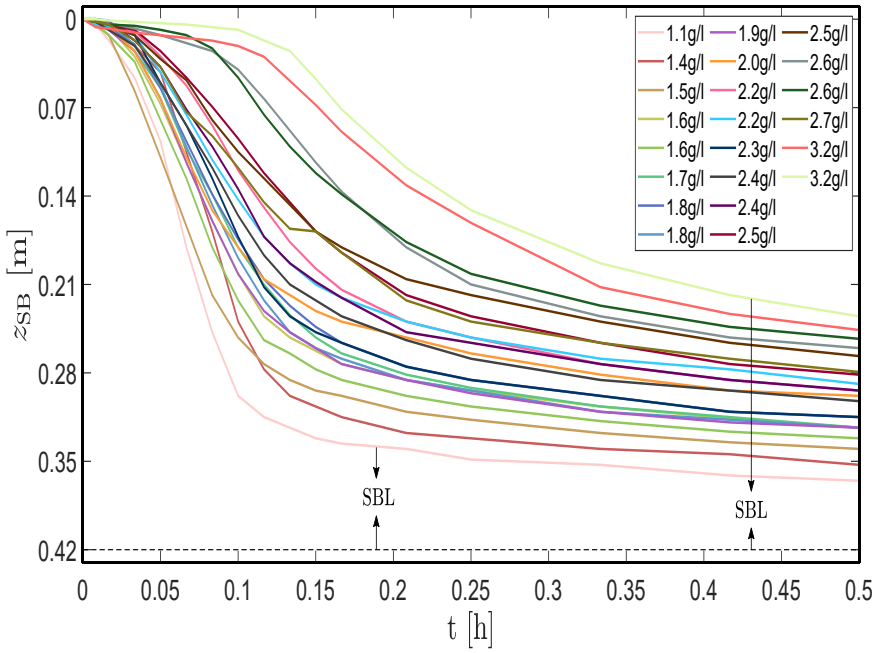

Figure 3.2: Sludge blanket position (z_{SB}) and sludge blanket level (SBL) data obtained from batch settling tests with various initial concentrations X_{init} [77].

3.2.4 Steady-state scenarios

In the measurement campaign of [78], three operational scenarios were applied to create SBLs at various heights: low (L), medium (M) and high (H). Scenario L with the lowest SBL, was obtained with the volumetric flows $Q_{\mathrm{f}} = 1.0$ m^3/h and $Q_{\mathrm{u}} = 0.5$ m^3/h. For Scenarios M and H, the lower values $Q_{\mathrm{f}} = 0.65$ m^3/h and $Q_{\mathrm{u}} = 0.15$ m^3/h were used (lower return flow to the reactor), which create higher SBLs. In Scenario H, the internal recycling in the bioreactor is also reduced to obtain a higher nitrate load to the sedimentation tank than in the other scenarios. The constant in time feed concentrations of the scenarios are shown in Table 3.2.

Table 3.2: Feed concentrations of the solids and substrates of the Scenarios L, M and H [77]. The units are given in Table 2.1.

	Scenario L	Scenario M	Scenario H
X_{I}	1053.50	914.08	1309.94
X_{S}	46.12	40.02	57.35
$X_{\mathrm{B,H}}$	1716.60	1489.41	2134.44
$X_{\mathrm{B,A}}$	107.71	93.45	133.92
X_{P}	872.55	757.08	1084.95
X_{ND}	0.04	3.30	4.73
S_{I}	14.8	17.0	18.0
S_{S}	0.01	0.01	0.01
S_{O}	4.5	5.2	4.48
S_{NO}	10.95	7.0	12.65
S_{NH}	0.022	0.01	0.021
S_{ND}	0.0	0.01	0.01
S_{ALK}	8.3	22	14.9

3.3 Methods

3.3.1 Model

The reactive settling model is based on [12] with some modifications. In the derivation of the model, we include hydrodynamic dispersion partly of solubles in the fluid outside the particles, and partly dispersion of the particles in the suspension. After the governing equations are derived, one may add an ad-hoc term modeling the mixing near the feed inlet [20].

The solid phase consists of flocculated particles of $k_{\boldsymbol{C}}$ types with mass concentrations of $C^{(1)}, \ldots, C^{(k_{\boldsymbol{C}})}$, which all have the same velocity v_X and density ρ_X. The total suspended solids (TSS) concentration is denoted by

$$X \coloneqq C^{(1)} + \cdots + C^{(k_{\boldsymbol{C}})} \quad \text{(mass concentrations)}. \tag{3.2}$$

The model is derived in mass concentration units and (3.2) is used during the derivation; however, since the ASM1 is expressed in units that are easier to measure, such as chemical oxygen demand (COD), conversion factors are needed to obtain the true mass concentration. As is commented on later, the entire model can in fact be used with the units in Table 2.1 if the TSS mass concentration is computed by [34]

$$X \coloneqq \kappa_0 \left(X_{\mathrm{I}} + X_{\mathrm{S}} + X_{\mathrm{B,H}} + X_{\mathrm{B,A}} + X_{\mathrm{P}}\right), \quad \text{where} \quad \kappa_0 = 0.75\,\mathrm{g}/(\mathrm{g}\,\mathrm{COD}). \tag{3.3}$$

The liquid phase consists of $k_{\boldsymbol{S}}$ dissolved substrates of concentrations $S^{(1)}, \dots, S^{(k_{\boldsymbol{S}})}$ with velocities $v^{(1)}, \dots, v^{(k_{\boldsymbol{S}})}$ and equal density ρ_L. We collect the unknown concentrations in the vectors $\boldsymbol{C}$ and $\boldsymbol{S}$, and let $\boldsymbol{R}_{\boldsymbol{C}}$ and $\boldsymbol{R}_{\boldsymbol{S}}$ denote vectors of the corresponding reaction terms. Let $\delta(z)$ denote the delta function and $\gamma(z)$ a characteristic function that is one inside the tank and zero outside. The balance law for each component yields

$$A(z)\frac{\partial C^{(k)}}{\partial t} + \frac{\partial}{\partial z}\big(A(z)v_X C^{(k)}\big) = \delta(z)C_{\mathrm{f}}^{(k)}(t)Q_{\mathrm{f}}(t) + \gamma(z)A(z)R_{\boldsymbol{C}}^{(k)}(\boldsymbol{C},\boldsymbol{S}) \tag{3.4}$$

for $k = 1, \dots, k_{\boldsymbol{C}}$ and

$$A(z)\frac{\partial S^{(k)}}{\partial t} + \frac{\partial}{\partial z}\big(A(z)v^{(k)} S^{(k)}\big) = \delta(z)S_{\mathrm{f}}^{(k)}(t)Q_{\mathrm{f}}(t) + \gamma(z)A(z)R_{\boldsymbol{S}}^{(k)}(\boldsymbol{C},\boldsymbol{S}) \tag{3.5}$$

for $k = 1, \dots, k_{\boldsymbol{S}}$.

It remains to specify the velocities v_X, v_L and $v^{(k)}$ by constitutive assumptions as described in Section 1.2.3 and in [12], the volume average velocity $q = q(z,t)$ of the mixture is given via and assumes that volume-changing reactions are negligible.

$$A(z)q(z,t) = \begin{cases} -Q_{\mathrm{e}}(t) = Q_{\mathrm{u}}(t) - Q_{\mathrm{f}}(t) & \text{for } z \le 0, \\ Q_{\mathrm{u}}(t) & \text{for } z > 0, \end{cases}$$

in (1.18), $Q_{\mathrm{u}}(t)$, $Q_{\mathrm{f}}(t)$ and $Q_{\mathrm{e}}(t)$ are given independent control funtions giving rise to a moving surface, whereas in an SST, only two of these are know and the third, often $Q_{\mathrm{e}}(t)$, is defined by the other two and possibly by volume-changing reactions in the tank [24] and the particle excess velocity is given by

$$v \coloneqq \gamma(z)\left(v_{\mathrm{hs}}(X) - d(X)\frac{\partial X}{\partial z} + v_{\mathrm{disp}}\right) = \gamma(z)\left(v_{\mathrm{hs}}(X) - \frac{\partial D(X)}{\partial z} + v_{\mathrm{disp}}\right),$$

where $v_{\mathrm{hs}}(X)$, $D(X)$ and $d(X)$ are given in Chapter 1.

The velocity v_{disp} is due to longitudinal dispersion of particles which is defined via the dispersion flux

$$v_{\mathrm{disp}}C^{(k)} = -\chi_{\{X<X_{\mathrm{c}}\}}d_X|q|\frac{\partial C^{(k)}}{\partial z}, \quad k = 1, \dots, k_{\boldsymbol{C}}, \tag{3.6}$$

where $\chi_{\{X<X_{\mathrm{c}}\}}$ is a characteristic function, which is one if $X < X_{\mathrm{c}}$ and zero otherwise, since the particles form a network for higher concentrations. Furthermore, d_X is the longitudinal dispersivity [m] of particles in the suspension. Summing the equalities in (3.6), utilizing (3.2) and dividing by X, one gets the formal definition

$$v_{\mathrm{disp}} = v_{\mathrm{disp}}(X, \partial_z X, z, t) \coloneqq -\chi_{\{X<X_{\mathrm{c}}\}}d_X|q(z,t)|\frac{\partial \log X}{\partial z}.$$

Each soluble component may also undergo dispersion with respect to the liquid average velocity:

$$\big(v^{(k)} - v_L\big)S^{(k)} = -d_L|v_L|\frac{\partial S^{(k)}}{\partial z}, \quad k = 1, \dots, k_{\boldsymbol{S}},$$

where d_L is the longitudinal dispersivity [m] of substrates within the liquid. On top of all these ingredients, we add still another heuristic term (mathematically, a diffusion term) containing the coefficient

$$d_{\mathrm{mix}}(z, Q_{\mathrm{u}}, Q_{\mathrm{e}}) := \begin{cases} \mathcal{E}(z, Q_{\mathrm{e}}) & \text{for } -\alpha_2 Q_{\mathrm{e}} < z < 0, \\ \mathcal{E}(z, Q_{\mathrm{u}}) & \text{for } 0 < z < \alpha_2 Q_{\mathrm{u}}, \\ 0 & \text{otherwise,} \end{cases} \tag{3.7}$$

where we define

$$\mathcal{E}(z, Q) := \alpha_1 (Q_{\mathrm{u}} + Q_{\mathrm{e}}) \exp\left(\frac{-z^2/(\alpha_2 Q)^2}{1 - |z|/(\alpha_2 Q)}\right).$$

The function d_{mix} accounts for the mixing effect due to the feed inlet, where α_1 and α_2 are parameters. The larger $Q_{\mathrm{f}} = Q_{\mathrm{u}} + Q_{\mathrm{e}}$ is, the larger is the effect, and the width above and below the inlet is influenced by Q_{e} and Q_{u}, respectively.

Substituting (1.22), (1.24), (3.6) and (3.7) into the balance laws (3.4) and (3.5), one obtains the system of nonlinear PDEs

$$A(z)\frac{\partial \boldsymbol{C}}{\partial t} + \frac{\partial}{\partial z}\big(A(z)\mathcal{V}_{\boldsymbol{C}}\boldsymbol{C}\big) = \frac{\partial}{\partial z}\left(A(z)\gamma(z)\Big(\chi_{\{X<X_{\mathrm{c}}\}} d_X |q| + d_{\mathrm{mix}}\Big)\frac{\partial \boldsymbol{C}}{\partial z}\right) + \delta(z)\boldsymbol{C}_{\mathrm{f}}(t)Q_{\mathrm{f}}(t) + \gamma(z)A(z)\boldsymbol{R}_{\boldsymbol{C}}(\boldsymbol{C}, \boldsymbol{S}), \tag{3.8}$$

$$A(z)\frac{\partial \boldsymbol{S}}{\partial t} + \frac{\partial}{\partial z}\big(A(z)\mathcal{V}_{\boldsymbol{S}}\boldsymbol{S}\big) = \frac{\partial}{\partial z}\left(A(z)\gamma(z)\Big(d_L|\mathcal{V}_{\boldsymbol{S}}| + d_{\mathrm{mix}}\Big)\frac{\partial \boldsymbol{S}}{\partial z}\right) + \delta(z)\boldsymbol{S}_{\mathrm{f}}(t)Q_{\mathrm{f}}(t) + \gamma(z)A(z)\boldsymbol{R}_{\boldsymbol{S}}(\boldsymbol{C}, \boldsymbol{S}), \tag{3.9}$$

where the velocity functions are

$$\mathcal{V}_{\boldsymbol{C}} = \mathcal{V}_{\boldsymbol{C}}(X, \partial_z X, z, t) := q(z,t) + \gamma(z)\left(v_{\mathrm{hs}}(X) - \frac{\partial D(X)}{\partial z}\right),$$

$$\mathcal{V}_{\boldsymbol{S}} = \mathcal{V}_{\boldsymbol{S}}(X, \partial_z X, z, t) := q(z,t) - \frac{X\gamma(z)}{\rho_X - X}\left(v_{\mathrm{hs}}(X) - \frac{\partial}{\partial z}\Big(D(X) + \chi_{\{0<X<X_{\mathrm{c}}\}} d_X |q(z,t)| \log X\Big)\right).$$

The reaction terms $\boldsymbol{R}_{\boldsymbol{C}}(\boldsymbol{C}, \boldsymbol{S})$ and $\boldsymbol{R}_{\boldsymbol{C}}(\boldsymbol{C}, \boldsymbol{S})$ are based on the model ASM1, as presented in Section 2.3, and include the implementation of the the alkalinity described in Section 3.2.2.That reaction model is expressed in units of Table 2.1 rather than the mass concentration units in which the present model is derived. Conversion factors between units are needed. As we have shown in Chapter 2, the structure of the governing PDEs (3.8), (3.9), where all the nonlinear coefficients depend on X and $\partial_z X$, and the equations are otherwise linear in $\boldsymbol{C}$ and $\boldsymbol{S}$, the model and numerical scheme can be used straightforwardly also with the COD units if only formula (3.3) is used.

The constitutive functions of hindered settling and sediment compressibility, denoted as $v_{\mathrm{hs}}(X)$ and $\sigma_{\mathrm{e}}(X)$, respectively, are the same as those given in equation (1.32) of Chapter 1.

3.3.2 Numerical method

Combining ingredients from Chapter 2 and in [12], we suggest the following numerical method for the approximate solution of (3.8), (3.9).

The height of the SST is divided into N internal computational cells, or layers, of depth $\Delta z = (B+H)/N$. The midpoint of layer j (numbered from above) has the coordinate $z = z_j$; hence, the layer is the interval $[z_{j-1/2}, z_{j+1/2}]$ and we denote its average concentration vector by $\boldsymbol{C}_j(t)$, which thus approximates $\boldsymbol{C}(z_j,t)$, and similarly for $\boldsymbol{S}$ of the system (3.8), (3.9) (we thus skip the tildes over numerical variables). Recall that X is always given by (3.3). The feed inlet at $z=0$ is located in the 'feed layer' $j_\mathrm{f} := \lceil H/\Delta z \rceil$, which is equal to the smallest integer larger than or equal to $H/\Delta z$. Above the interval $(-H, B)$, we add one layer to obtain the correct effluent concentrations via $\boldsymbol{C}_\mathrm{e}(t) := \boldsymbol{C}_0(t)$, and one layer below for the underflow concentration $\boldsymbol{C}_\mathrm{u}(t) := \boldsymbol{C}_{N+1}(t)$ (analogously for $\boldsymbol{S}$). For technical reasons, we set $\boldsymbol{C}_{-1} := \boldsymbol{0}$ and $\boldsymbol{C}_{N+2} := \boldsymbol{0}$, and analogously for other variables. The cross-sectional area is approximated by

$$A_{j+1/2} := \frac{1}{\Delta z}\int_{z_j}^{z_{j+1}} A(\xi)\,\mathrm{d}\xi \quad \text{and} \quad A_j := \frac{1}{\Delta z}\int_{z_{j-1/2}}^{z_{j+1/2}} A(\xi)\,\mathrm{d}\xi.$$

We let $\gamma_{j+1/2} := \gamma(z_{j+1/2})$ (similarly for other variables) and define the approximate volume average velocity

$$q_{j+1/2} := \begin{cases} -Q_\mathrm{e}(t)/A_{j+1/2} & \text{for } j < j_\mathrm{f}, \\ Q_\mathrm{u}(t)/A_{j+1/2} & \text{for } j \geq j_\mathrm{f}. \end{cases}$$

With δ_{j,j_f} denoting the Kronecker delta, which is 1 if $j = j_\mathrm{f}$ and zero otherwise, the method-of-lines (MOL) formulation of the numerical method is

$$\begin{aligned} \frac{\mathrm{d}\boldsymbol{C}_j}{\mathrm{d}t} &= -\frac{\boldsymbol{\Phi}^{\boldsymbol{C}}_{j+1/2} - \boldsymbol{\Phi}^{\boldsymbol{C}}_{j-1/2}}{A_j \Delta z} + \delta_{j,j_\mathrm{f}} \frac{\boldsymbol{C}_\mathrm{f} Q_\mathrm{f}}{A_j \Delta z} + \gamma_j \boldsymbol{R}_{C,j}, \\ \frac{\mathrm{d}\boldsymbol{S}_j}{\mathrm{d}t} &= -\frac{\boldsymbol{\Phi}^{\boldsymbol{S}}_{j+1/2} - \boldsymbol{\Phi}^{\boldsymbol{S}}_{j-1/2}}{A_j \Delta z} + \delta_{j,j_\mathrm{f}} \frac{\boldsymbol{S}_\mathrm{f} Q_\mathrm{f}}{A_j \Delta z} + \gamma_j \boldsymbol{R}_{S,j}. \end{aligned} \tag{3.10}$$

Defining $\chi(X) := \chi_{\{0<X<X_\mathrm{c}\}}(X)$, $a^+ := \max\{0,a\}$ and $a^- := \min\{0,a\}$, we may specify the numerical fluxes as follows. Utilizing the quantities

$$\begin{aligned} J^{\boldsymbol{C}}_{j+1/2} &:= \big(D(X_{j+1}) - D(X_j)\big)/\Delta z, \\ J^{\mathrm{d}}_{j+1/2} &:= \big(\chi(X_{j+1})|q_{j+1/2}|\log(X_{j+1}) - \chi(X_j)|q_{j-1/2}|\log(X_j)\big)/\Delta z, \\ v^X_{j+1/2} &:= q_{j+1/2} + \gamma_{j+1/2}\big(v_\mathrm{hs}(X_{j+1}) - J^{\boldsymbol{C}}_{j+1/2}\big), \\ v^L_{j+1/2} &:= \gamma_{j+1/2}(v_\mathrm{hs}(X_{j+1}) - J^{\boldsymbol{C}}_{j+1/2} - d_X J^{\mathrm{d}}_{j+1/2}), \\ F^X_{j+1/2} &:= v^{X,-}_{j+1/2} X_{j+1} + v^{X,+}_{j+1/2} X_j, \\ F^L_{j+1/2} &:= v^{L,-}_{j+1/2} X_{j+1} + v^{L,+}_{j+1/2} X_j, \end{aligned}$$

$$G^L_{j+1/2} \coloneqq \frac{((\rho_X - X_{j+1})q_{j+1/2} - F^L_{j+1/2})^-}{\rho_X - X_{j+1}} \boldsymbol{S}_{j+1} + \frac{((\rho_X - X_j)q_{j+1/2} - F^L_{j+1/2})^+}{\rho_X - X_j} \boldsymbol{S}_j,$$

we compute the numerical fluxes

$$\boldsymbol{\Phi}^{\boldsymbol{C}}_{j+1/2} \coloneqq A_{j+1/2}\left(v^{X,-}_{j+1/2}\boldsymbol{C}_{j+1} + v^{X,+}_{j+1/2}\boldsymbol{C}_j - \gamma_{j+1/2}\big(\chi(X_{j+1})|q_{j+1/2}| + d_{\mathrm{mix},j+1/2}\big)\frac{\boldsymbol{C}_{j+1} - \boldsymbol{C}_j}{\Delta z}\right),$$
$$\boldsymbol{\Phi}^{\boldsymbol{S}}_{j+1/2} \coloneqq A_{j+1/2}\left(G^L_{j+1/2} - \gamma_{j+1/2}\big(d_L|v^L_{j+1/2}| + d_{\mathrm{mix},j+1/2}\big)\frac{\boldsymbol{S}_{j+1} - \boldsymbol{S}_j}{\Delta z}\right).$$

Although any ODE solver can be used for the MOL system (3.10), it is not meaningful to use any higher order time-stepping algorithm since the spatial discretization is at most first-order accurate. If T is the simulation time, we let t_n, $n = 0, 1, \ldots, N_T$, denote the discrete time points and $\Delta t \coloneqq T/N_T$ the time step. For explicit schemes, the right-hand sides of Equations (3.10) are evaluated at time t_n. The value of a variable at t_n is denoted by $\boldsymbol{C}^n_j$, etc. and we set

$$Q^n_{\mathrm{f}} \coloneqq \frac{1}{\Delta t}\int_{t_n}^{t_{n+1}} Q_{\mathrm{f}}(t)\,\mathrm{d}t$$

and similarly for the time-dependent reaction terms. The time derivatives in (3.10) are approximated by

$$\frac{\mathrm{d}\boldsymbol{C}_j}{\mathrm{d}t}(t_n) \approx \frac{\boldsymbol{C}^{n+1}_j - \boldsymbol{C}^n_j}{\Delta t}.$$

This yields the explicit scheme

$$\boldsymbol{C}^{n+1}_j = \boldsymbol{C}^n_j + \frac{\Delta t}{A_j \Delta z}\big(-\boldsymbol{\Phi}^{\boldsymbol{C},n}_{j+1/2} + \boldsymbol{\Phi}^{\boldsymbol{C},n}_{j-1/2} + \delta_{j,j_{\mathrm{f}}}\boldsymbol{C}^n_{\mathrm{f}}Q^n_{\mathrm{f}} + \gamma_j A_j \Delta z\, \boldsymbol{R}^n_{\boldsymbol{C},j}\big),$$
$$\boldsymbol{S}^{n+1}_j = \boldsymbol{S}^n_j + \frac{\Delta t}{A_j \Delta z}\big(-\boldsymbol{\Phi}^{\boldsymbol{S},n}_{j+1/2} + \boldsymbol{\Phi}^{\boldsymbol{S},n}_{j-1/2} + \delta_{j,j_{\mathrm{f}}}\boldsymbol{S}^n_{\mathrm{f}}Q^n_{\mathrm{f}} + \gamma_j A_j \Delta z\, \boldsymbol{R}^n_{\boldsymbol{S},j}\big).$$

3.3.3 Preparation of batch-test data by removing the induction period

Approximate solutions of the system (3.8), (3.9) are obtained by the numerical method described in Section 3.3.2, which is an adjusted version the method by [12]. For the simulations we use 100 layers for the spatial discretization of the tank. The batch tests revealed that for $X > 3.2\,\mathrm{kg/m^2}$, the sludge exhibited compressibility, wherefore the critical concentration was set to $X_{\mathrm{c}} = 3.2\ \mathrm{kg/m^2}$. Other parameters are $\rho_X = 1050\,\mathrm{kg/m^3}$, $\Delta\rho = 52\,\mathrm{kg/m^3}$ and $g = 9.81\,\mathrm{m/s^2}$.

As in most batch settling tests presented in the literature, those in Figure 3.2 show an initial induction period when several phenomena occur, such as turbulence because of mixing before $t = 0$ to obtain a homogeneous initial concentration X_{init}, reflocculation of broken flocs and

possibly rising air bubbles. Such phenomena are not captured with the assumptions made above. A PDE model, with the constitutive functions $v_{\mathrm{hs}}(X)$ and $\sigma_{\mathrm{e}}(X)$ (see (1.32)), for the TSS concentration X during batch sedimentation in a column with constant cross-sectional area is (z is the depth from the top of the column)

$$\frac{\partial X}{\partial t} + \frac{\partial}{\partial z}\big(v_{\mathrm{hs}}(X)X\big) = \frac{\partial}{\partial z}\left(d(X)\frac{\partial X}{\partial z}\right). \tag{3.11}$$

To fit this to the batch data, we first transform away these phenomena with the technique by [45] before we calibrate the parameters of the constitutive functions.

Let $z = z_{\mathrm{p}}(t)$ be the path of a solid particle at the SBL that starts at depth $z_{\mathrm{p}}(0)$. In a suspension with ideal particles, e.g. glass beads, and $X_{\mathrm{init}} < X_{\mathrm{c}}$, it is well known that the sludge blanket initially decreases at a constant velocity $v_{\mathrm{hs}}(X_{\mathrm{init}})$. During the induction period, the velocity of each particle increases from zero to its maximum velocity $v_{\mathrm{hs}}(X_{\mathrm{init}})$. Thus, the velocity can be written as

$$z_{\mathrm{p}}'(t) = G(t)v_{\mathrm{hs}}(X_{\mathrm{init}}) \tag{3.12}$$

with a function G that satisfies $G(0) = 0$ and increases to one at the end of the induction period. For the sludges investigated by [45], the function

$$G(t) = 1 - \exp\big(-(t/\bar{t})^p\big) \tag{3.13}$$

was appropriate. Here $\bar{t}$ and p are parameters that depend on X_{init}. Thus, we have to fit such a function G for each batch test. The particle path is obtained by integrating (3.12):

$$z_{\mathrm{p}}(t) = z_{\mathrm{p}}(0) + v_{\mathrm{hs}}(X_{\mathrm{init}}) \int_0^t \big(1 - \exp\big(-(s/\bar{t})^p\big)\big)\,\mathrm{d}s. \tag{3.14}$$

Under the change of the time coordinate

$$\tau \coloneqq \int_0^t G(s)\,\mathrm{d}s, \quad t > 0, \tag{3.15}$$

then the data plotted against τ (instead of t) will be nearly straight lines – the induction period has been transformed away. We refer to [45] for justification.

Figure 3.3 (a) shows a batch test with an initially concave SBL curve during the induction period. To determine when that period ends, we take central finite differences of the data to obtain the velocity; see Figure 3.3 (b). The maximum velocity in that example occurs at approximately $t = 0.05$ h, i.e., we should have $G(0.05\ \mathrm{h}) \approx 1$. To data from the induction time interval one performs a nonlinear least-squares fit of the function $z_{\mathrm{p}}(t)$ to find the parameters $\bar{t}$ and p. The parameters in that example are (see the curve in Figure 3.3 (c))

$$\begin{aligned} v_{\mathrm{hs}}(X_{\mathrm{init}}) &= 8.9261 \times 10^{-4}\,\mathrm{m/s}, \\ \bar{t} &= 64.63\,\mathrm{s} \approx 1.795 \times 10^{-2}\,\mathrm{h}, \\ p &= 1.641. \end{aligned}$$

With these parameters, the rescaling of the time variable by (3.15) produces the new path of the sedimentation curve in Figure 3.3 (d).

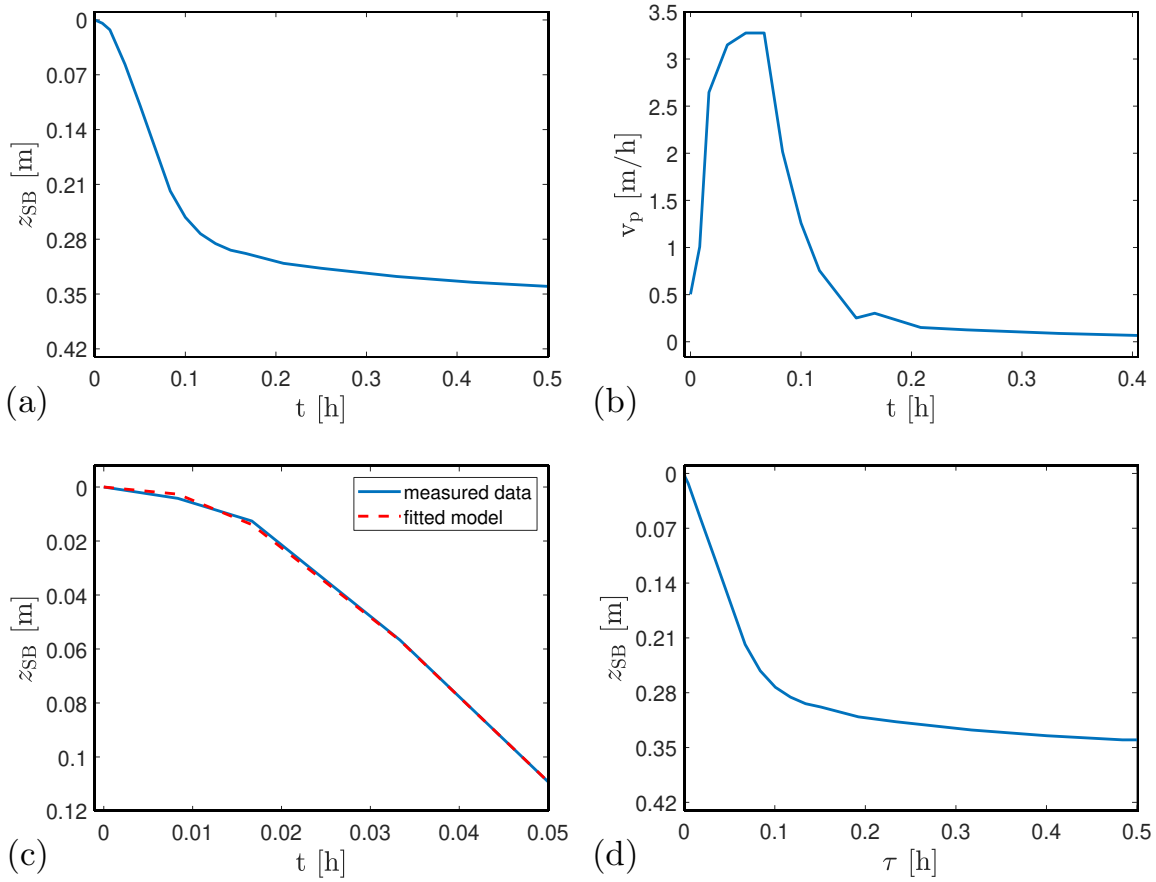

Figure 3.3: (a) A batch test with $X_{\text{init}} = 1.5\,\text{kg/m}^3$. The curve $z = z_{\text{p}}(t)$ is the location of a particle at the SBL. (b) Estimated velocity $v_{\text{p}}(t) := z'_{\text{p}}(t)$ of the curve shown in a. (c) The initial induction period of the curve in plot a and the fitted model (3.14). (d) The resulting batch sedimentation curve $z = z^{\text{data}}(\tau)$ after rescaling time with (3.15).

3.3.4 Calibration of the settling-compression model

We denote the transformed trajectories of the batch sedimentation curves by

$$z = z_j^{\text{data}}(\tau_i), \quad i = 1, \ldots, N_j, \quad j = 1, \ldots, N_{\text{exp}},$$

where N_j is the number of data points in experiment j, and N_{exp} is the number of batch experiments. Now, we proceed to find the optimal parameters (v_0, $\bar{X}$, η and σ_0) for the constitutive functions (1.32). This is done by minimizing the sum of squared errors

$$E(v_0, \bar{X}, \eta, \sigma_0) := \sum_{j=1}^{N_{\text{exp}}} \sum_{i=1}^{N_j} \left(z_j^{\text{data}}(\tau_i) - \hat{z}_j(\tau_i; v_0, \bar{X}, \eta, \sigma_0) \right)^2, \tag{3.16}$$

where $\hat{z}_j(\tau_i; v_0, \bar{X}, \eta, \sigma_0)$ is the estimated value by numerical simulation of the model (3.11) with the method by [11] with 100 spatial layers. The optimal parameters after minimizing the

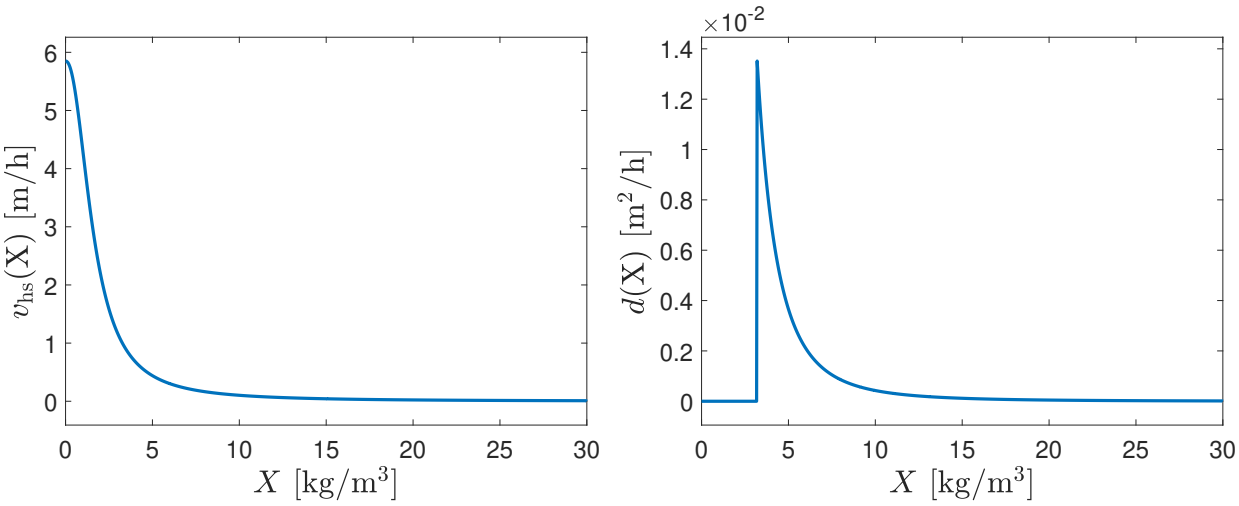

(a) hindered settling velocity (b) compression

Figure 3.4: Graphs of the constitutive functions.

objective function (3.16) with the robust Nelder-Mead simplex algorithm [93] are

$$v_0 = 5.85\,\mathrm{m/h}, \qquad \bar{X} = 1.59\,\mathrm{kg/m^3}, \qquad \eta = 2.19, \qquad \sigma_0 = 261901.56\,\mathrm{m^2/h^2}.$$

Graphs of the constitutive functions with these parameter values are shown in Figure 3.4. Finally, we show the outcome of the optimization by comparing some of the batch tests with the corresponding simulations in Figure 3.5.

3.3.5 Calibration of the dispersion and mixing parameters

In an attempt to improve the model calibrated from the batch experiments, we now use the experimental steady-state solution of Scenario M with its four data points of each concentration (except two for alkalinity) (see Figure 3.6) to calibrate the remaining parameters of the model

$$\boldsymbol{p} := (d_X, d_L, \alpha_1, \alpha_2)$$

with the error function

$$\begin{aligned} E_{\mathrm{disp}}(\boldsymbol{p}) := \sum_{j=1}^{4} \Bigg(& \frac{|X^{\mathrm{data}}(z_j) - \hat{X}(z_j;\boldsymbol{p})|}{\max_i\{X^{\mathrm{data}}(z_i)\}} + \frac{|(S_{\mathrm{I}}^{\mathrm{data}} + S_{\mathrm{S}}^{\mathrm{data}})(z_j) - (\hat{S}_{\mathrm{I}} + \hat{S}_{\mathrm{S}})(z_j;\boldsymbol{p})|}{\max_i\{(S_{\mathrm{I}}^{\mathrm{data}} + S_{\mathrm{S}}^{\mathrm{data}})(z_i)\}} \\ & + \frac{|S_{\mathrm{O}}^{\mathrm{data}}(z_j) - \hat{S}_{\mathrm{O}}(z_j;\boldsymbol{p})|}{\max_i\{S_{\mathrm{O}}^{\mathrm{data}}(z_i)\}} + \frac{|S_{\mathrm{NO}}^{\mathrm{data}}(z_j) - \hat{S}_{\mathrm{NO}}(z_j;\boldsymbol{p})|}{\max_i\{S_{\mathrm{NO}}^{\mathrm{data}}(z_i)\}} + \frac{|S_{\mathrm{NH}}^{\mathrm{data}}(z_j) - \hat{S}_{\mathrm{NH}}(z_j;\boldsymbol{p})|}{\max_i\{S_{\mathrm{NH}}^{\mathrm{data}}(z_i)\}} \Bigg) \\ & + \sum_{j=1}^{2} \frac{|S_{\mathrm{ALK}}^{\mathrm{data}}(z_j) - \hat{S}_{\mathrm{ALK}}(z_j;\boldsymbol{p})|}{\max_i\{S_{\mathrm{ALK}}^{\mathrm{data}}(z_i)\}}, \end{aligned} \tag{3.17}$$

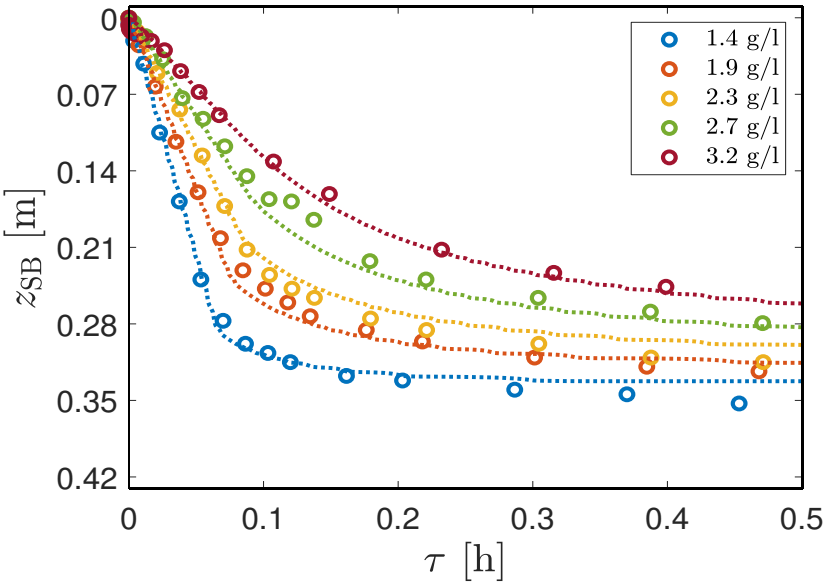

Figure 3.5: Selected sludge blanket level (SBL) trajectories in transformed time. Measured data (circles) compared with the optimized parameters in model (3.11) (dotted curves).

where $\hat{X}(z_j;\boldsymbol{p})$ is the steady-state approximation of X of the PDE system (3.8), (3.9) obtained by the numerical scheme (3.10) with 100 spatial layers (see Section 3.3.2) at $z = z_j$, analogously for the other concentrations. The variables labeled by "data" are the experimental data points from Scenario M.

We use the Nelder-Mead algorithm also for the minimization of E_{disp}, whose value at $\boldsymbol{p}$ is obtained by simulating to a steady state. Such simulations are made with the numerical scheme in Section 3.3.2 and need initial conditions preferably close to the expected steady state. Since the nature of the Nelder-Mead algorithm is to compare only function values at the corners of a simplex and most of the time no large step is taken, we choose the initial conditions in the following way:

i. Given the starting point $\boldsymbol{p}^0$ of the optimization iteration (e.g. $\boldsymbol{p}^0 = \boldsymbol{0}$), simulate from any initial data $\boldsymbol{C}_{\text{init}}(z)$ to obtain approximate steady states $\hat{\boldsymbol{C}}(z;\boldsymbol{p}^0)$ (analogously for $\boldsymbol{S}$), which give the value $E_{\text{disp}}(\boldsymbol{p}^0)$.

ii. For optimization iteration $k \geq 1$, i.e., given $\boldsymbol{p}^k$, simulate with the initial data $\boldsymbol{C}_{\text{init}}(z) = \hat{\boldsymbol{C}}(z;\boldsymbol{p}^{k-1})$ (analogously for $\boldsymbol{S}$) to obtain $E_{\text{disp}}(\boldsymbol{p}^k)$.

The optimal vector of parameters for Scenario M is

$$\boldsymbol{p}^* = (0.00222\,\text{m}^{-1}, 0.03523\,\text{h/m}^2, 0.03659\,\text{m}, 0.03126\,\text{m}).$$

The corresponding approximate steady-state profiles are shown in Figure 3.6. To investigate the impact with and without the mixing term d_{mix}, we also carried out the optimization with

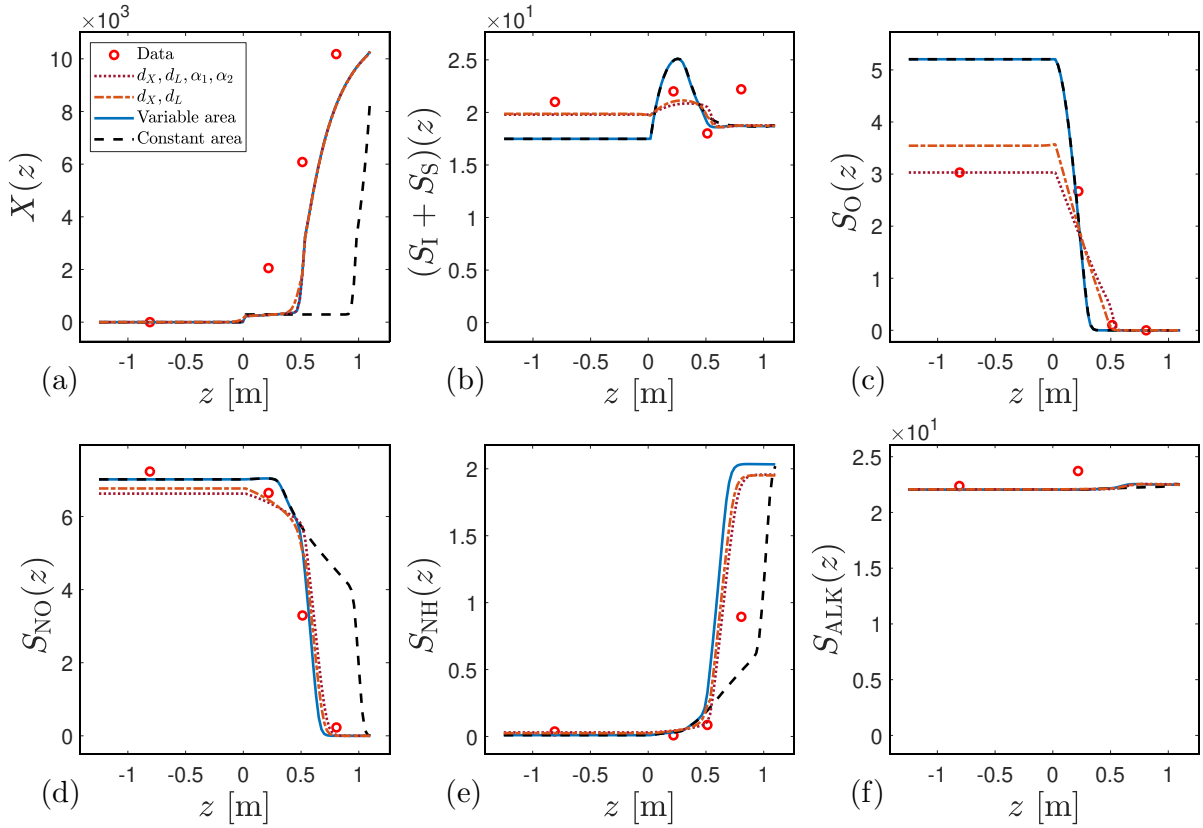

Figure 3.6: Scenario M: Concentrations in units given in Table 2.1: (a) total suspended solids, (b) soluble chemical oxygen demand, (c) oxygen, (d) nitrate and nitrite nitrogen, (e) $NH_4^+ + NH_3$ nitrogen, (f) alkalinity. Each plot shows experimental data (circles), simulation results at steady state ($T = 24$ h in Figures 3.7 and 3.8) with a varying cross-sectional area (3.1) (solid line) and constant cross-sectional area (dashed line), both obtained with $d_X = d_L = 0$, $\alpha_1 = \alpha_2 = 0$, with optimized parameters $(d_X, d_L, \alpha_1, \alpha_2)$ (dotted line), and (d_X, d_L) (dash-dotted line).

the reduced vector of parameters $\boldsymbol{u} := (d_X, d_L)$ (instead of $\boldsymbol{p}$) and found the optimum point

$$\boldsymbol{u}^* = (0.4080\,\mathrm{m}^{-1}, 0.01876\,\mathrm{h/m}^2).$$

The corresponding steady states are also shown in Figure 3.6.

3.4 Results

Figure 3.6 shows the experimental data of Scenario M together with simulated steady states of four different models. The solid blue curves show the simulated steady states with the model calibrated from the batch experiments only; that is, with only the constitutive functions for hindered settling and compression, and neither mixing nor dispersion ($\boldsymbol{p} = \boldsymbol{0}$). As a comparison, the dashed black curves show the results when instead a cylindrical tank is used. That tank

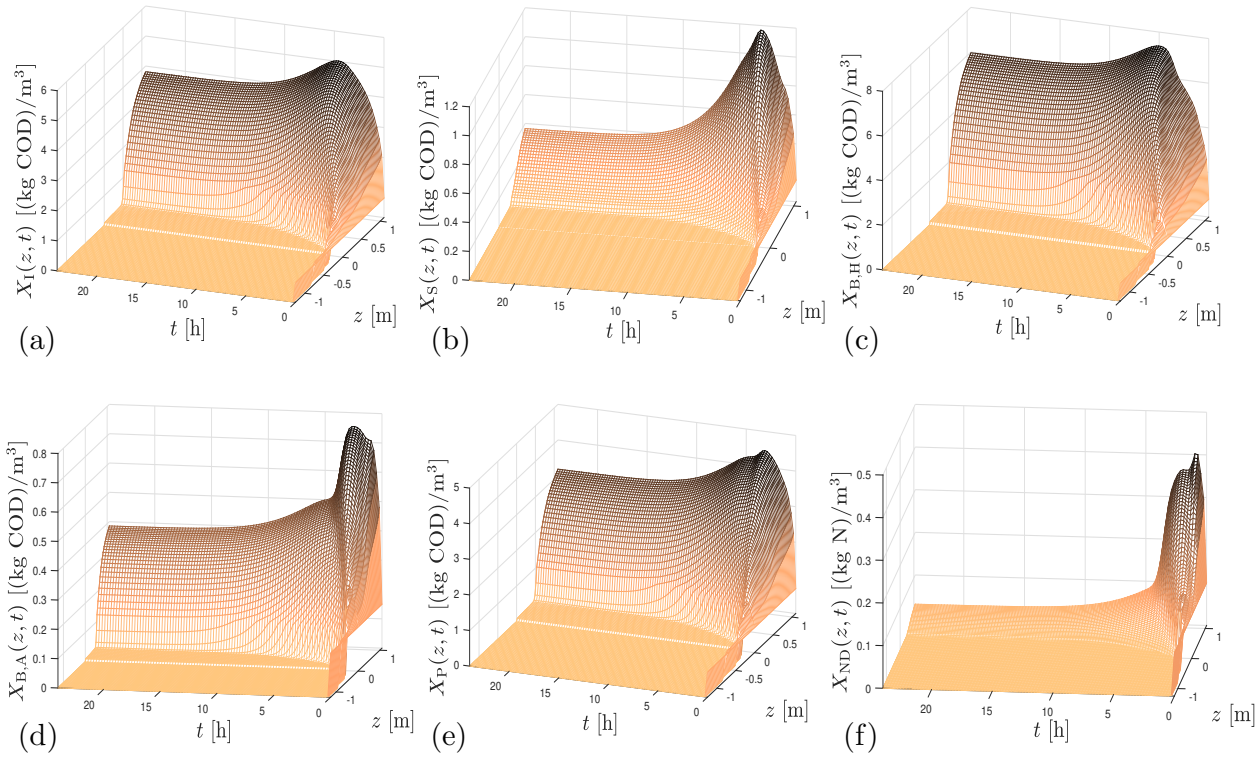

Figure 3.7: Scenario M: Numerical simulation of solids during 24 h: (a) particulate inert organic matter, (b) slowly biodegradable substrate, (c) active heterotrophic biomass, (d) active autotrophic biomass, (e) particle products arising from biomass decay and (f) particulate biodegradable organic nitrogen.

has the same height and volume as the one in Figure 3.1, which means that the cross-sectional area is $A = 0.9362\,\mathrm{m}^2$; otherwise the conditions are the same. A substantial improvement when allowing for a variable cross-sectional area in the model instead of a constant one is already seen in Figure 3.6. The two remaining curves in each subplot show the steady states when partly only d_X and d_L are fitted (and $\alpha_1 = \alpha_2 = 0$), and partly when all four parameters $\boldsymbol{p}$ has been used in the fitting.

The three remaining variants of the model (with a variable cross-sectional area) fitted to the data shown in Figure 3.6 capture the data reasonably, but not perfectly. This may have several reasons. We use the ASM1 model with standard parameters [60], since the available data are not sufficient to recalibrate that model. We have also insisted in estimating the parameters of the sedimentation-compression constitutive functions to the batch experiments separately, and then use one SST scenario to estimate the rest of the parameters. We believe that this approach is conceptually more consistent than letting the sedimentation-compression parameters be free in the second step to get a better fit with the risk of getting unrealistic parameters for the sedimentation-compression phenomenon.

For purpose of demonstration, we show in Figures 3.7 and 3.8 a full dynamic simulation of

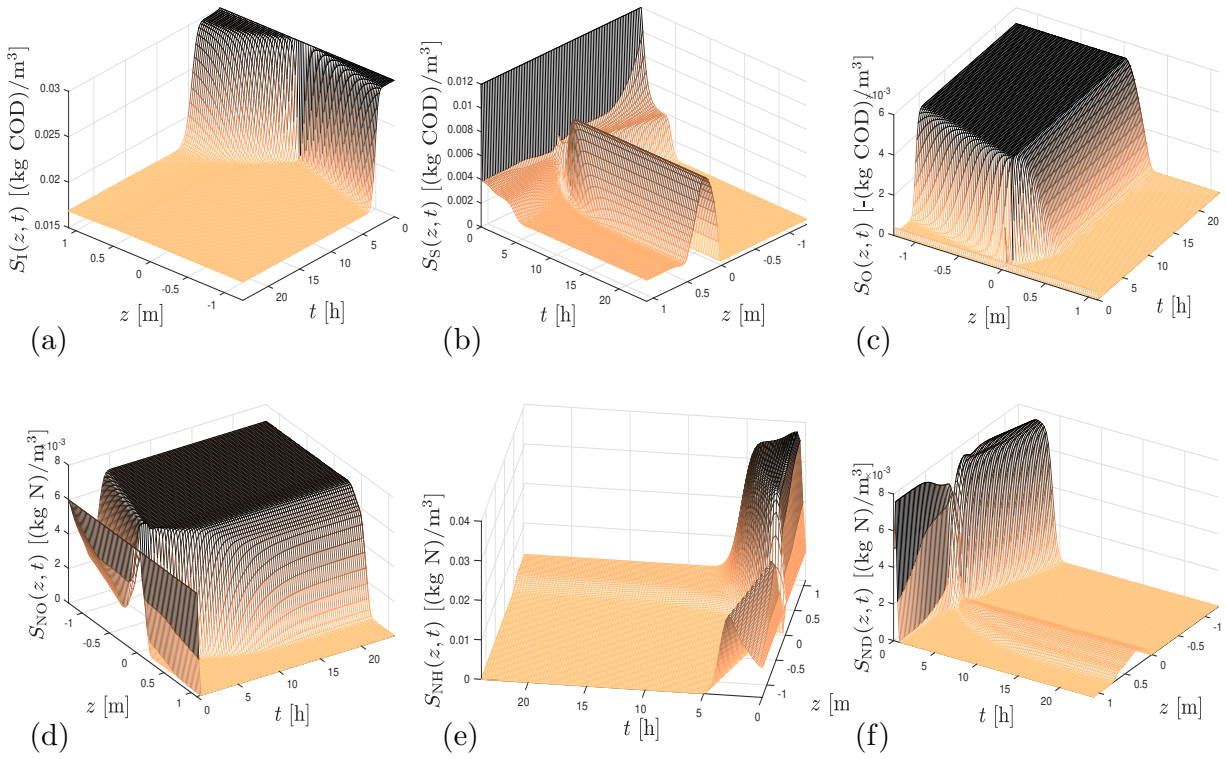

Figure 3.8: Scenario M: Numerical simulation of solubles during 24 h: (a) soluble inert organic matter, (b) readily biodegradable substrate, (c) oxygen, (d) nitrate and nitrite nitrogen, (e) $NH_4^+ + NH_3$ nitrogen, (f) soluble biodegradable organic nitrogen.

all concentrations (except alkalinity) with the feed input concentrations shown in Table 3.2 and with the constant initial concentrations

$$\boldsymbol{C}_{\text{init}} = (650, 150, 800, 150, 700, 100)^{\text{T}},$$
$$\boldsymbol{S}_{\text{init}} = (30, 12, 0.4, 6, 7.5, 5, 2.83)^{\text{T}},$$

with units as in Table 2.1. The simulation is performed until $T = 24\,\text{h}$, where the system is in approximate steady state. As a validation, we keep the parameter values obtained for Scenario M and with these simulate Scenarios L and H; see Figures 3.9 and 3.10. In addition, Figure 3.11 shows the simulated total nitrogen in the tank calculated with the formula by [34].

The results indicate that simulation accuracy is significantly increased if the variability of the cross-sectional area is taken into account, even if the resulting model is still a spatially one-dimensional one. The additional inclusion of the parameters for dispersion only (d_X, d_L) improved the estimation of the concentration S_O in all three scenarios, but no improvement occurred for the prediction of other concentrations, except for X of Scenario L to some extent. The additional inclusion of the mixing parameters (α_1, α_2) caused only a small improvement in Scenario M (only in S_O), whereas it neither improved the model prediction of Scenarios L nor H. The more parameters in a model, the better fit to the data used for calibration is possible (Figure 3.6); however, the validation against other data may not improve (Figures 3.9 and 3.10).

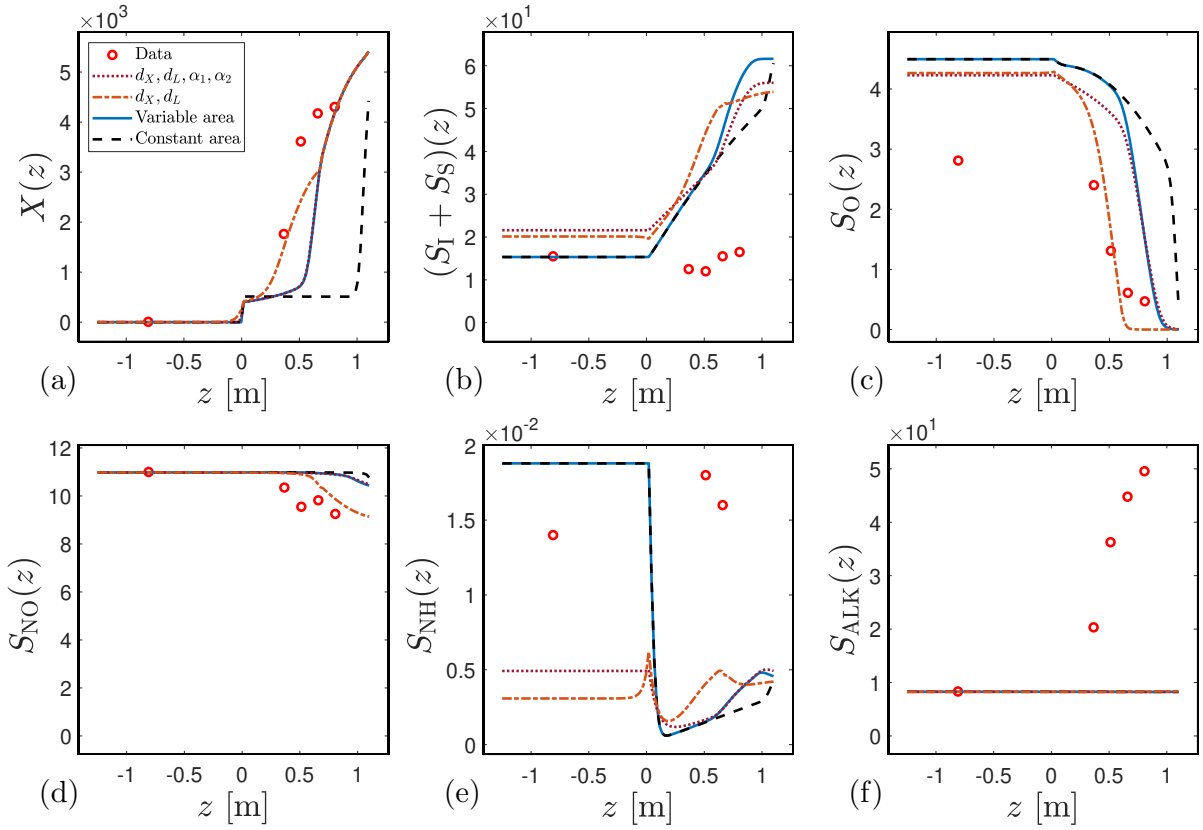

Figure 3.9: Scenario L: Concentrations in units given in Table 2.1. Each plot shows five points of experimental data (circles) and simulation results at steady state (produced by four variants of the fitted model) based only on Scenario M.

A possible reason for this may be the heuristic modeling of the mixing phenomenon. A more probable reason is the small number of data points available along with an over-parametrized model. Indeed, the values of (d_X, d_L), the two first components of $\boldsymbol{p}^*$, differ substantially from those of $\boldsymbol{u}^*$. Furthermore, the phenomena of dispersion and mixing are mathematically both of diffusion type that smoothes large derivatives; hence, these parameters can to some extent compensate for each other and make it difficult to identify unique parameters.

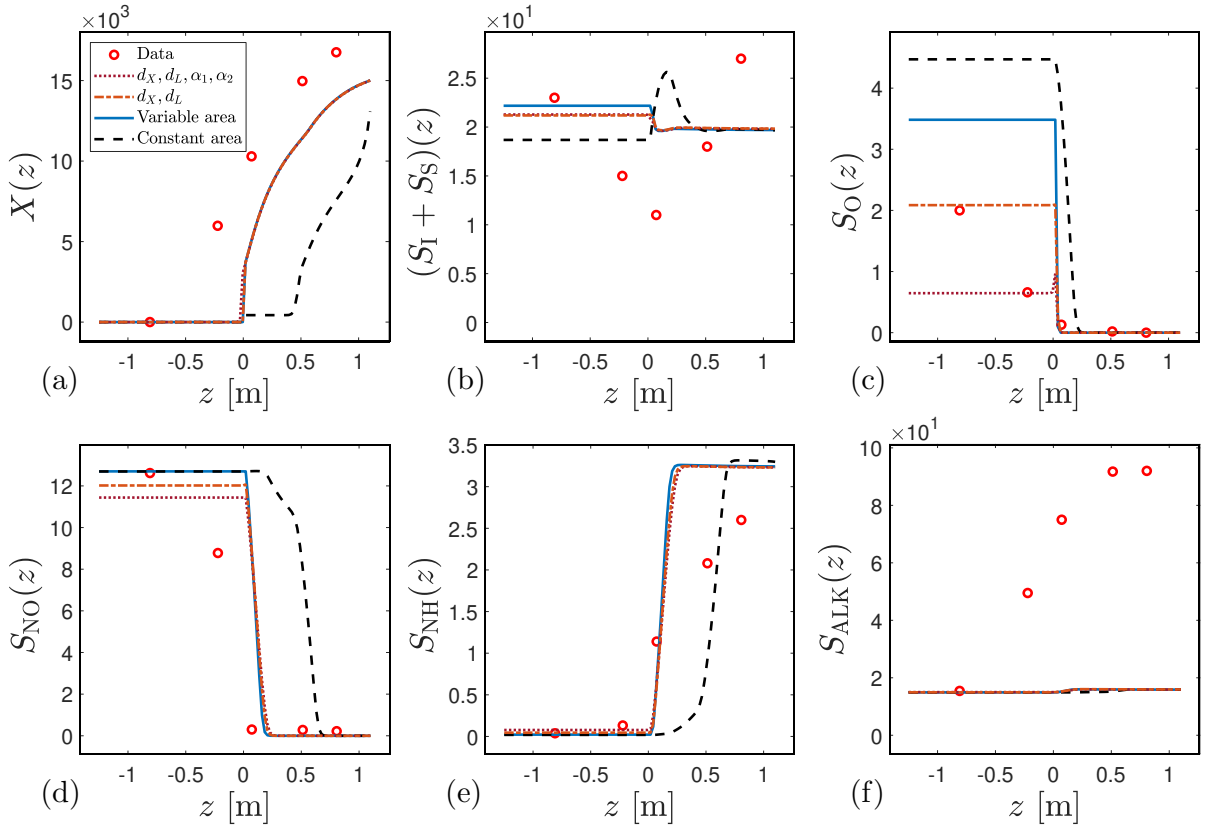

Figure 3.10: Scenario H: Concentrations in units given in Table 2.1. Each plot shows five points of experimental data (circles) and simulation results at steady state (produced by four variants of the fitted model) based only on Scenario M.

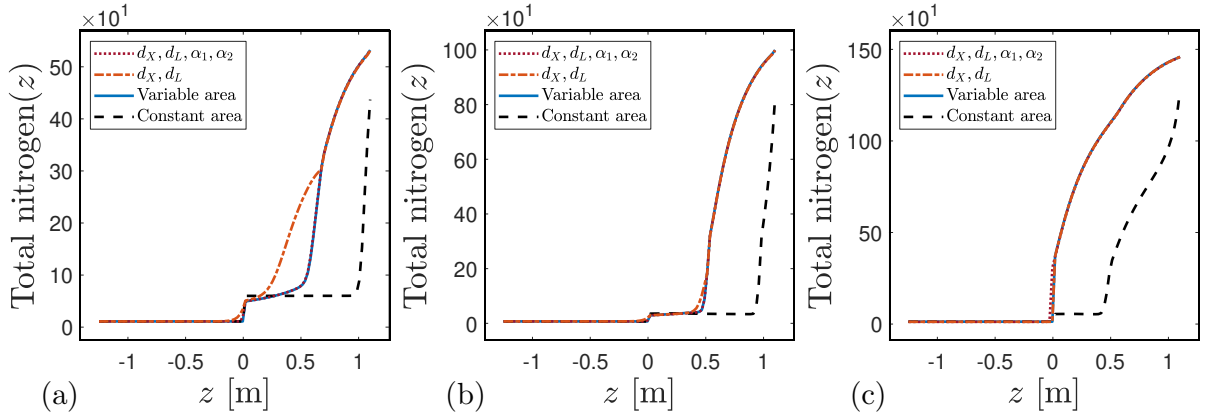

Figure 3.11: Simulated steady states of total nitrogen for (a) Scenario L, (b) Scenario M and (c) Scenario H with the four variants of the fitted model.

CHAPTER 4

Numerical schemes for a moving-boundary convection-diffusion-reaction model of sequencing batch reactors

4.1 Introduction

4.1.1 Scope

An SBR is a tank designed for the sedimentation of a suspension composed of solid particles of biomass that react with substrates (nutrients) dissolved in a liquid. This process is a fundamental stage of purification in wastewater treatment plants. Due to the presence of living biomass (activated sludge; bacteria), biochemical reactions always occur. In our previous SBR model by Bürger et al. [15, 16], a nonlinear, strongly degenerating convection-diffusion-reaction model of an SBR was introduced, taking into account the moving boundary due to the bulk flows of SBR stages. Additionally, a numerical scheme defined on a fixed spatial grid preserves positivity was developed, which will be referred to as SBR2 in this chapter. Within that approach, one needs to carefully track the upper boundary as it moves through the computational grid for the numerical solution, as shown in Figure 4.1. The purpose of the present chapter is to introduce an alternative explicit scheme that, after a suitable transformation of the time-dependent spatial domain, is defined on a fixed computational grid. Moreover, a semi-implicit variant is introduced that allows for more efficient simulations due to a more favourable Courant-Friedrichs-Lewy (CFL) condition.

The moving boundary, denoted by $\bar{z} := \bar{z}(t)$, where $t \geq 0$ is time, is a known function given by the bulk flows acting on the SBR. The curve $t \mapsto \bar{z}(t)$ defines a spatial change of variables, where in the new variable ξ, the top and bottom boundaries are located at $\xi = 0$ and $\xi = 1$, respectively. The sought vector unknowns, in the variable ξ, are the solid phase and liquid

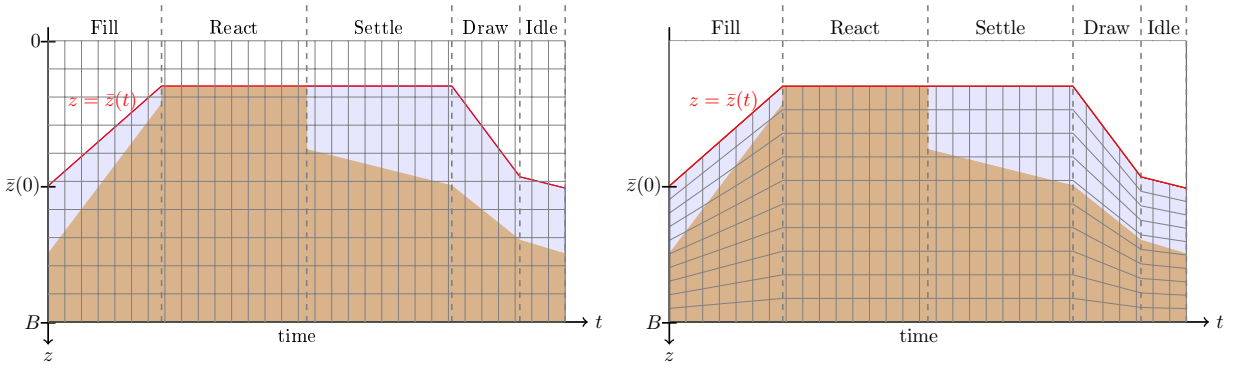

Figure 4.1: Comparison of computational meshes for SBR simulation with fixed mesh size (left; see Chapter 2 and [16]) and variable mesh size (right; see this chapter and [14]).

substrate components

$$\boldsymbol{C} \coloneqq \boldsymbol{C}(\xi,t) \coloneqq (C^{(1)}(\xi,t),\dots,C^{(k_{\boldsymbol{C}})}(\xi,t))^{\mathrm{T}}, \quad \boldsymbol{S} \coloneqq \boldsymbol{S}(\xi,t) \coloneqq (S^{(1)}(\xi,t),\dots,S^{(k_{\boldsymbol{S}})}(\xi,t))^{\mathrm{T}}.$$

The model equations for $0 < \xi < 1$ are given by

$$\begin{aligned}
\frac{\partial \boldsymbol{C}}{\partial t} + \frac{\partial}{\partial \xi}\big(U_{\boldsymbol{C}}(X,\xi,t)\boldsymbol{C}\big) &= \frac{\partial}{\partial \xi}\left(\gamma(\xi)\beta(t)^2\frac{\partial \mathcal{D}(X)}{\partial \xi}\right) \\
&\quad + \beta(t)\bar{z}'(t)\boldsymbol{C} + \delta(\xi)\beta(t)q_{\mathrm{f}}(t)\boldsymbol{C}_{\mathrm{f}}(t) + \gamma(\xi)\boldsymbol{R}_{\boldsymbol{C}}(\boldsymbol{C},\boldsymbol{S}), \\
\frac{\partial \boldsymbol{S}}{\partial t} + \frac{\partial}{\partial \xi}\big(U_{\boldsymbol{S}}(X,\xi,t)\boldsymbol{S}\big) &= \frac{\partial}{\partial \xi}\left(\frac{\gamma(\xi)\beta(t)^2}{\rho_X - X}\frac{\partial \mathcal{D}(X)}{\partial \xi}\right) \\
&\quad + \beta(t)\bar{z}'(t)\boldsymbol{S} + \delta(\xi)\beta(t)q_{\mathrm{f}}(t)\boldsymbol{S}_{\mathrm{f}}(t) + \gamma(\xi)\boldsymbol{R}_{\boldsymbol{S}}(\boldsymbol{C},\boldsymbol{S}),
\end{aligned} \tag{4.1}$$

where $U_{\boldsymbol{C}}$ and $U_{\boldsymbol{S}}$ are velocity functions related to the velocities of the solid and liquid phases, respectively, $X \coloneqq (C^{(1)}+\cdots+C^{(k_{\boldsymbol{C}})})/c$ is the total solids concentration, c is a conversion factor, β is a given time dependent function, ρ_X is the (constant) mass density of solids, and $\mathcal{D}(X)$ is an integrated diffusion coefficient describing compressibility of the sediment. It is assumed that $\mathcal{D}(X) = 0$ for $X \le X_{\mathrm{c}}$, where $X_{\mathrm{c}} > 0$ is a critical concentration beyond which the solid particles are assumed to touch each other, so the system (4.1) is of first order wherever $X \le X_{\mathrm{c}}$, and therefore is strongly degenerate. The second term in the right-hand side of both equations is due to the change of variables in the spatial partial derivative, while the third term contains the feed concentrations $\boldsymbol{C}_{\mathrm{f}}$ and $\boldsymbol{S}_{\mathrm{f}}$ for the solid and liquid phases, respectively, the feed velocity q_{f}, and the Dirac symbol δ. The last terms model the chemical reactions between the components of the solid and liquid phases, where $\boldsymbol{R}_{\boldsymbol{C}}$ and $\boldsymbol{R}_{\boldsymbol{S}}$ are vectors of reaction terms, and γ is the characteristic function that equals one inside the tank and zero outside. The system (4.1) is coupled to transport equations modeling the concentrations in the extraction pipe connected at $\xi = 0$. (The variables and functions arising in (4.1) are precisely defined in later parts of this chapter.)

Many of the properties defined in Chapter 1 and 2 will be used in this chapter.

4.1.2 Outline of the chapter

The remainder of this chapter is organized as follows. In Section 4.2, we review the SBR model, starting with assumptions on the tank and the one-dimensional model, and explaining the relation between the moving boundary and bulk flows (Section 4.2.1). The one-dimensional model of the reactive settling process in the tank is obtained from the balance laws of mass of all the particulate and soluble components. The details of the formulation of the model are outlined in Section 4.2.2, starting from the solid and liquid components and reactions within the biokinetic reaction model (as an example, we here employ the model ASM1) followed by a summary of the sedimentation-compression model that has also been employed in previous works. The balance laws for the SBR are coupled with transport equations for the pipe. During the react stage with full mixing, the PDEs are replaced by a system of ODEs. While these model ingredients are reviewed from our previous treatment [15, 16], one of the three decisive novelties of the present approach, namely the transformation of the moving boundary model to a fixed computational domain, is formulated in Section 4.2.3. The second novelty is the reformulation of the governing model in terms of the vector of percentages $\boldsymbol{p}$ (of the solid components, with respect to X) done in Section 4.2.4.

An explicit numerical scheme for the solution of the transformed governing model is introduced in Section 4.3. This scheme is based on a standard discretization in space and time of the computational domain (Section 4.3.1). The explicit numerical scheme, presented in Section 4.3.2, is based on the percentage and fixed-domain formulations of Sections 4.2.3 and 4.2.4 and combines upwind discretizations for transport terms, the Engquist-Osher numerical flux [47] for nonlinear flux terms, and a central difference formula for nonlinear degenerating diffusion terms arising in the governing models, combined with appropriate discretizations of the reaction terms. The scheme is complemented by a suitable discretization of the ODEs describing the mixing stage (Section 4.3.3). It is assumed that the spatial mesh width $\Delta\xi$ and the time step τ are related by a CFL condition outlined in Section 4.3.4, and we prove in Section 4.3.5 that this scheme is monotone, with the consequence that an invariant-region principle holds, i.e., solids concentrations are nonnegative and less or equal a maximal one, percentages are nonnegative and sum up to one, and substrate concentrations are nonnegative. The CFL condition for the explicit scheme essentially bounds $\tau/\Delta\xi^2$.

A more favorable CFL condition that only bounds $\tau/\Delta\xi$ is associated with a semi-implicit scheme for the governing PDE model, which is the third novelty introduced in Section 4.4. At each time step, it consists of a nonlinear semi-implicit scheme for the PDE for X, which is described in Section 4.4.1, where we also demonstrate that the nonlinear equations are well posed, i.e., possess a unique solution that depends continuously on data. The solution of the nonlinear equations is achieved by Newton-Raphson method (Section 4.4.2). Once the scalar function X has been updated, one proceeds to update the vectors $\boldsymbol{p}$ and $\boldsymbol{S}$. This is done by an implicit version of the corresponding $\boldsymbol{p}$- and $\boldsymbol{S}$-schemes of Section 4.3. This version is, however, linearly implicit and only requires the solution of one linear system per time

step, see Section 4.4.3. In Section 4.4.4, it is proved that the semi-implicit scheme has the same monotonicity and invariant-region properties as its explicit counterpart (cf. Section 4.3.5) but does so under the more favorable CFL condition. Numerical examples that illustrate the performance of the numerical schemes of Sections 4.3 and 4.4 are presented in Section 4.6.

4.2 A model of a sequencing batch reactor (SBR)

We here review the assumptions of the general SBR model in [15] and refer to [16] for a full description of the numerical scheme SBR2. That model will then be slightly reformulated, which allows for a semi-implicit numerical scheme to be developed. The sedimentation and compaction properties of the flocculated sludge are namely assumed to depend on the total concentration X and not on the concentrations of the individual components since these are flocculated to larger particles. Each flocculated particle consists of several individual components, which can be described as percentages of the total concentration X. For simplicity of writing, we confine here to a constant cross-sectional area A, which is the most common case in the applications.

4.2.1 Assumptions on the tank and the 1D model

The reactor tank is assumed to be a cylindrical vessel with constant horizontal cross-sectional area A; see Figure 2. We place a fixed z-axis indicating the depth from the top ($z = 0$) to the bottom at $z = B$. At the surface of the mixture, located at $z = \bar{z}(t)$, a floating device connected to a pipe allows one to feed the tank at given volumetric feed flow $Q_{\mathrm{f}}(t)$ [m^3/s] and feed concentrations $\boldsymbol{C}_{\mathrm{f}}(t)$ and $\boldsymbol{S}_{\mathrm{f}}(t)$. The floating device can alternatively extract mixture at a given volume rate $Q_{\mathrm{e}}(t)$ during the draw stage. One cannot fill and draw simultaneously. The extraction pipe is modeled by a half-line and the flow through it by a linear advection PDE. The concentrations in the pipe are denoted by $\boldsymbol{C}_{\mathrm{e}}(t)$ and $\boldsymbol{S}_{\mathrm{e}}(t)$. At the bottom, $z = B$, one can withdraw mixture at a given volume rate $Q_{\mathrm{u}}(t) \geq 0$, and the corresponding output concentrations there are denoted by $\boldsymbol{C}_{\mathrm{u}}(t)$ and $\boldsymbol{S}_{\mathrm{u}}(t)$. We define the bulk velocities

$$q_{\mathrm{u}}(t) := Q_{\mathrm{u}}(t)/A, \qquad q_{\mathrm{e}} := Q_{\mathrm{e}}(t)/A, \qquad q_{\mathrm{f}} := Q_{\mathrm{f}}(t)/A.$$

The volume of the mixture at time t, given in (1.8), which is defined as

$$\bar{V}(t) := A\big(B - \bar{z}(t)\big). \tag{4.2}$$

The surface location $\bar{z}(t)$, specified in (2.2), is determined by the given volumetric flows, since by differentiation of (4.2),

$$\bar{z}'(t) = -\frac{\bar{V}'(t)}{A} = \frac{Q_{\mathrm{u}}(t) - \bar{Q}(t)}{A}, \quad \text{where} \quad \bar{Q}(t) := \begin{cases} -Q_{\mathrm{e}}(t) < 0 & \text{if } t \in T_{\mathrm{e}}, \\ Q_{\mathrm{f}}(t) \geq 0 & \text{if } t \in T_{\mathrm{f}}. \end{cases}$$

Clearly, $\bar{z}$ is given at any time, so the model under consideration is a *moving* boundary problem, but not a *free* boundary problem. That said, we emphasize that because of the volumetric flows, no boundary *conditions* need to be imposed since the conservation law implies natural output concentrations when reactions and sedimentation are assumed to occur inside the tank only.

4.2.2 A model of reactive settling with moving boundary

Biochemical reaction model and solid and liquid components

Two constitutive functions describe the sedimentation-compression process of the flocculated particles that consist of several components. These functions are stated in terms of the solids in suspension X. This quantity equals the sum of either all or of most of the particulate concentrations; the precise definition of X depends on the specific reaction model. Any biochemical reaction model can be used such as one of the standard ASMx activated sludge models. Within the ASMx models, concentrations are usually expressed in terms of more easily measurable units such as chemical oxygen demand (COD) (see Table 2.1 in Chapter 2), wherefore conversion factors have to be used to obtain the mass concentrations. We here use the ASM1 model (see Section 2.3), in which the particulate concentrations are (in ASM1 units)

$$X_{\mathrm{I}}, X_{\mathrm{S}}, X_{\mathrm{B,H}}, X_{\mathrm{B,A}}, X_{\mathrm{P}}, X_{\mathrm{ND}},$$

and the corresponding definition of the total suspended solids concentration is

$$X \coloneqq c(X_{\mathrm{I}} + X_{\mathrm{S}} + X_{\mathrm{B,H}} + X_{\mathrm{B,A}} + X_{\mathrm{P}}), \quad \text{where } c = 0.75\,\mathrm{g/(g\,COD)}.$$

The concentration X_{ND} is not in the definition of X, since X_{ND} represents the nitrogen that is already part of X_{S}. To ensure (for mathematical reasons) that the total solids concentration X equals the sum of all particulate components, we replace the variable X_{S} by $X_{\mathrm{S-ND}} \coloneqq X_{\mathrm{S}} - X_{\mathrm{ND}}$, representing the slowly biodegradable substrate less part. organic nitrogen measured in $[(\mathrm{kg\ COD}), \mathrm{m}^{-3}]$

$$\begin{aligned} \boldsymbol{C} &\coloneqq \big(X_{\mathrm{I}}, X_{\mathrm{S-ND}}, X_{\mathrm{B,H}}, X_{\mathrm{B,A}}, X_{\mathrm{P}}, X_{\mathrm{ND}}\big)^{\mathrm{T}} \quad (\text{i.e., } k_{\boldsymbol{C}} = 6), \\ \boldsymbol{S} &\coloneqq \big(S_{\mathrm{I}}, S_{\mathrm{S}}, S_{\mathrm{O}}, S_{\mathrm{NO}}, S_{\mathrm{NH}}, S_{\mathrm{ND}}\big)^{\mathrm{T}} \quad (\text{i.e., } k_{\boldsymbol{S}} = 6). \end{aligned}$$

Moreover, we define

$$X \coloneqq c\big(C^{(1)} + \cdots + C^{(k_{\boldsymbol{C}})}\big), \qquad p^{(k)}X \coloneqq cC^{(k)}, \qquad \boldsymbol{p}X \coloneqq c\boldsymbol{C}. \tag{4.3}$$

Similar conversion factors as c appear for the soluble concentrations; however, we will divide these factors away directly, since the left-hand sides of the governing equations to be presented are linear in $\boldsymbol{C}$ and $\boldsymbol{S}$ apart from the coefficients, which are nonlinear functions of X.

Reaction terms

The nonlinear reaction terms are given by

$$\begin{aligned} &\boldsymbol{\Lambda_C}\boldsymbol{R_C}(\boldsymbol{C},\boldsymbol{S}), \quad \text{where} \quad \boldsymbol{R_C}(\boldsymbol{C},\boldsymbol{S}) \coloneqq \boldsymbol{\sigma_C}\boldsymbol{r}(\boldsymbol{C},\boldsymbol{S}),\\ &\boldsymbol{\Lambda_S}\boldsymbol{R_S}(\boldsymbol{C},\boldsymbol{S}), \quad \text{where} \quad \boldsymbol{R_S}(\boldsymbol{C},\boldsymbol{S}) \coloneqq \boldsymbol{\sigma_S}\boldsymbol{r}(\boldsymbol{C},\boldsymbol{S}), \end{aligned}$$

which model the increase in (COD) concentration per time unit; see Table 2.1. Here, $\boldsymbol{\Lambda_C} = \operatorname{diag}(c,c,c,c,c,1)$ and $\boldsymbol{\Lambda_S}$ are diagonal matrices with conversion factors, $\boldsymbol{\sigma_C}$ and $\boldsymbol{\sigma_S}$ are constant stoichiometric matrices, and $\boldsymbol{r}(\boldsymbol{C},\boldsymbol{S}) \geq \boldsymbol{0}$ is a vector of nonlinear functions modeling the reaction processes; see Table 2.1.

We assume that if a solid component is not present, $p^{(k)} = 0$, then no more such can vanish, i.e. $R_{\boldsymbol{C}}^{(k)}(\boldsymbol{C},\boldsymbol{S})|_{p^{(k)}=0} = 0$, where $R_{\boldsymbol{C}}^{(k)}$ denotes the k-th component of $\boldsymbol{R_C}$.

Balance laws

The balance law of each material component gives the system of PDEs

$$\begin{aligned} \frac{\partial \boldsymbol{C}}{\partial t} + \frac{\partial}{\partial z}\big(\mathcal{V}_{\boldsymbol{C}}(X,\partial_z X,z,t)\boldsymbol{C}\big) &= \delta\big(z-\bar{z}(t)\big)q_{\mathrm{f}}(t)\boldsymbol{C}_{\mathrm{f}} + \gamma(z,t)\boldsymbol{R_C}(\boldsymbol{C},\boldsymbol{S}),\\ \frac{\partial \boldsymbol{S}}{\partial t} + \frac{\partial}{\partial z}\big(\mathcal{V}_{\boldsymbol{S}}(X,\partial_z X,z,t)\boldsymbol{S}\big) &= \delta\big(z-\bar{z}(t)\big)q_{\mathrm{f}}(t)\boldsymbol{S}_{\mathrm{f}} + \gamma(z,t)\boldsymbol{R_S}(\boldsymbol{C},\boldsymbol{S}), \end{aligned} \tag{4.4}$$

modeling reactive settling for $z \in \mathbb{R}$, where we have divided away the COD factors c etc. in each equation, $\delta(\cdot)$ $[\mathrm{m}^{-1}]$ is the delta symbol, and the total velocities are

$$\begin{aligned} \mathcal{V}_{\boldsymbol{C}} = \mathcal{V}_{\boldsymbol{C}}(X,\partial_z X,z,t) &\coloneqq q(z,t) + \gamma(z,t)\big(v_{\mathrm{hs}}(X) - \partial_z D(X)\big),\\ \mathcal{V}_{\boldsymbol{S}} = \mathcal{V}_{\boldsymbol{S}}(X,\partial_z X,z,t) &\coloneqq q(z,t) - \gamma(z,t)\frac{(v_{\mathrm{hs}}(X) - \partial_z D(X))X}{\rho_X - X}. \end{aligned}$$

The pipe of extraction is modeled as a half line $x \geq 0$ (upwards) with $x = 0$ coupled at $z = \bar{z}(t)$. Any concentration is assumed to follow the advection equations

$$\frac{\partial \boldsymbol{C}_{\mathrm{pipe}}}{\partial t} + q_{\mathrm{e}}(t)\frac{\partial \boldsymbol{C}_{\mathrm{pipe}}}{\partial x} = \boldsymbol{0}, \quad \frac{\partial \boldsymbol{S}_{\mathrm{pipe}}}{\partial t} + q_{\mathrm{e}}(t)\frac{\partial \boldsymbol{S}_{\mathrm{pipe}}}{\partial x} = \boldsymbol{0}. \tag{4.5}$$

The extraction concentrations in the pipe are given by complicated formulas due to the moving boundary; see [15]. With the variable change suggested below, these will be obtained more easily.

Equations during the react stage

During periods of mixing, the system of PDEs (4.4) reduces to the system of ODEs

$$\bar{V}(t)\boldsymbol{C}'(t) = \big(Q_{\mathrm{u}}(t) - \bar{Q}(t)\big)\boldsymbol{C} + Q_{\mathrm{f}}(t)\boldsymbol{C}_{\mathrm{f}}(t) + \bar{V}(t)\boldsymbol{R_C}(\boldsymbol{C},\boldsymbol{S}),$$

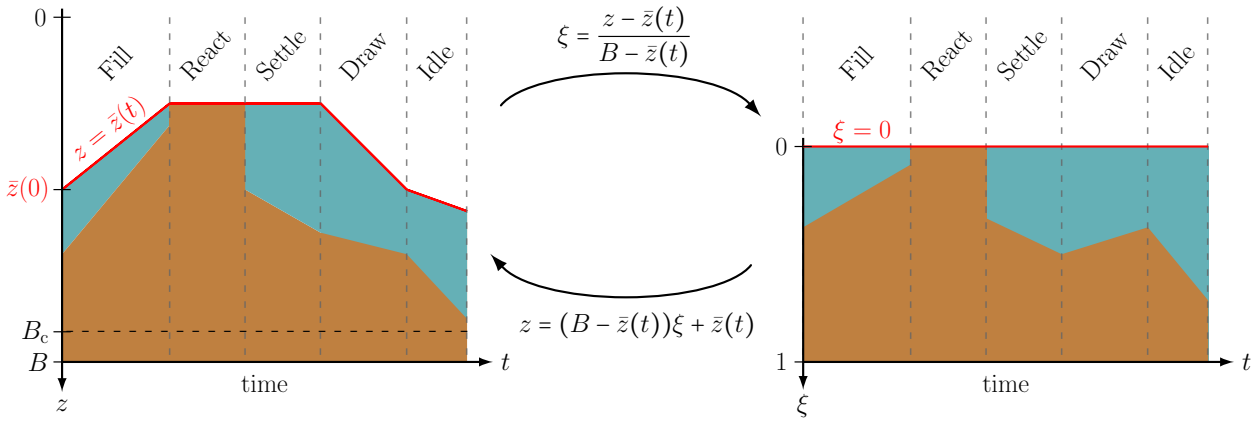

Figure 4.2: Evolution of a concentration profile varying with respect to time at the five SBR stages in the space variable z (left) and new variable ξ (right). The moving boundary $z = \bar{z}(t)$ (red line) is mapped to the constant line $\xi = 0$. The mappings $z = z(\xi, t)$ and $\xi = \xi(z, t)$ are shown in the middle.

$$\bar{V}(t)\boldsymbol{S}'(t) = \big(Q_{\mathrm{u}}(t) - \bar{Q}(t)\big)\boldsymbol{S} + Q_{\mathrm{f}}(t)\boldsymbol{S}_{\mathrm{f}}(t) + \bar{V}(t)\boldsymbol{R}_{\boldsymbol{S}}(\boldsymbol{C}, \boldsymbol{S}),$$

for the homogeneous concentrations in $\bar{z}(t) < z < B$, where all concentrations depend only on time since they are averages in the tank. In the region $z < \bar{z}(t)$ all concentrations are zero, whereas the outlet concentrations are $\boldsymbol{C}_{\mathrm{u}}(t) = \boldsymbol{C}(t)$ and $\boldsymbol{C}_{\mathrm{e}}(t) = \boldsymbol{C}(t)$ (if $Q_{\mathrm{e}}(t) > 0$) (analogously for $\boldsymbol{S}$).

4.2.3 Model equations on a fixed domain

To solve the model equations (4.4)–(4.5) without complicated formulas for the outlet concentrations, we transform the time-varying interval $[\bar{z}(t), B]$ to the fixed domain $[0, 1]$ for all $t \geq 0$ by introducing the space variable, for all $z \in \mathbb{R}$,

$$\xi = \xi(z, t) := \frac{z - \bar{z}(t)}{B - \bar{z}(t)} \qquad \Leftrightarrow \qquad z = (B - \bar{z}(t))\xi + \bar{z}(t). \tag{4.6}$$

where it is assumed that $B - \bar{z}(t) \geq B_{\mathrm{c}} > 0$ for all $t \geq 0$ for some constant B_{c}. We define the unknowns of the model in the new variable ξ by $\tilde{X}(\xi(z, t), t) := X(z, t)$ (analogously for the rest of the unknowns and space dependent functions). The partial derivatives are

$$\frac{\partial \xi}{\partial t} = -\bar{z}'(t)\frac{1 - \xi}{B - \bar{z}(t)} =: \alpha(\xi, t), \qquad \frac{\partial \xi}{\partial z} = \frac{1}{B - \bar{z}(t)} =: \beta(t).$$

Clearly, the sign of α depends uniquely on the slope $\bar{z}'$ and therefore on t, while $\beta(t) > 0$ for all $t > 0$. Then the time and space partial derivatives are transformed as

$$\frac{\partial X}{\partial t} = \frac{\partial \tilde{X}}{\partial \xi}\frac{\partial \xi}{\partial t} + \frac{\partial \tilde{X}}{\partial t} = \alpha(\xi, t)\frac{\partial \tilde{X}}{\partial \xi} + \frac{\partial \tilde{X}}{\partial t}, \quad \frac{\partial X}{\partial z} = \frac{\partial \tilde{X}}{\partial \xi}\frac{\partial \xi}{\partial z} = \beta(t)\frac{\partial \tilde{X}}{\partial \xi} = \frac{\partial}{\partial \xi}\big(\beta(t)\tilde{X}\big).$$

It will be convenient to rewrite the term

$$\alpha(\xi,t)\frac{\partial \tilde{X}}{\partial \xi} = \frac{\partial}{\partial \xi}\big(\alpha(\xi,t)\tilde{X}\big) - \frac{\partial \alpha(\xi,t)}{\partial \xi}\tilde{X} = \frac{\partial}{\partial \xi}\big(\alpha(\xi,t)\tilde{X}\big) - \beta(t)\bar{z}'(t)\tilde{X}$$

(anticipating the transformation of $\partial \boldsymbol{C}/\partial t$ in (4.4) etc.). The characteristic function becomes

$$\gamma(z,t) = \chi_{\{\bar{z}(t)<z<B\}}(z) = \tilde{\chi}_{\{0<\xi<1\}}(\xi) =: \tilde{\gamma}(\xi).$$

The delta symbol in (4.4) is formally transformed via the Heaviside function H as

$$\begin{aligned} H\big(z-\bar{z}(t)\big) &= H\big(\xi(B-\bar{z}(t))\big) =: \tilde{H}(\xi), \\ \delta\big(z-\bar{z}(t)\big) &= H'\big(z-\bar{z}(t)\big) = \tilde{H}'(\xi) = \tilde{H}'(\xi)\beta(t) = \tilde{\delta}(\xi)\beta(t). \end{aligned}$$

The bulk velocity becomes $q(z,t) = q_{\mathrm{u}}(t)\chi_{\{z>\bar{z}(t)\}}(z) = q_{\mathrm{u}}(t)\tilde{H}(\xi)$. Equations (4.4) can be written in the new variable ξ as the system

$$\begin{aligned} \frac{\partial \boldsymbol{C}}{\partial t} + \frac{\partial}{\partial \xi}\big(\tilde{\mathcal{V}}_{\boldsymbol{C}}(X,\partial_\xi X,\xi,t)\boldsymbol{C}\big) &= \beta(t)\bar{z}'(t)\boldsymbol{C} + \delta(\xi)\beta(t)q_{\mathrm{f}}(t)\boldsymbol{C}_{\mathrm{f}} + \gamma(\xi)\boldsymbol{R}_{\boldsymbol{C}}(\boldsymbol{C},\boldsymbol{S}) \\ \frac{\partial \boldsymbol{S}}{\partial t} + \frac{\partial}{\partial \xi}\big(\tilde{\mathcal{V}}_{\boldsymbol{S}}(X,\partial_\xi X,\xi,t)\boldsymbol{S}\big) &= \beta(t)\bar{z}'(t)\boldsymbol{S} + \delta(\xi)\beta(t)q_{\mathrm{f}}(t)\boldsymbol{S}_{\mathrm{f}} + \gamma(\xi)\boldsymbol{R}_{\boldsymbol{S}}(\boldsymbol{C},\boldsymbol{S}), \end{aligned} \tag{4.7}$$

where we directly have removed the tilde above $\boldsymbol{C}$, $\boldsymbol{S}$, X, γ, H, and δ, and

$$\begin{aligned} \tilde{\mathcal{V}}_{\boldsymbol{C}}(X,\partial_\xi X,\xi,t) &\coloneqq \tilde{q}(\xi,t) + \gamma(\xi)\beta(t)\left(v_{\mathrm{hs}}(X) - \beta(t)\partial_\xi D(X)\right), \\ \tilde{\mathcal{V}}_{\boldsymbol{S}}(X,\partial_\xi X,\xi,t) &\coloneqq \tilde{q}(\xi,t) - \gamma(\xi)\beta(t)\frac{f(X) - \beta(t)\partial_\xi \mathcal{D}(X)}{\rho_X - X}, \end{aligned}$$

where $\tilde{q}(\xi,t) \coloneqq \alpha(\xi,t) + \beta(t)q_{\mathrm{u}}(t)\tilde{H}(\xi)$ (temporary definition),

$$f(X) \coloneqq v_{\mathrm{hs}}(X)X, \tag{4.8}$$

and

$$\mathcal{D}(X) \coloneqq \int_{X_{\mathrm{c}}}^{X} a(s)\,\mathrm{d}s, \quad \text{where} \quad a(s) \coloneqq sd(s),$$

$d(s)$ is the compression function, which is provided in Equation (1.24) of Chapter (1). Clearly, the governing equations (4.7) can be expressed in the form (4.1) if we define

$$U_{\boldsymbol{C}}(X,\xi,t) \coloneqq \tilde{q}(\xi,t) + \gamma(\xi)\beta(t)v_{\mathrm{hs}}(X), \quad U_{\boldsymbol{S}}(X,\xi,t) \coloneqq \tilde{q}(\xi,t) - \gamma(\xi)\beta(t)\frac{f(X)}{\rho_X - X}.$$

Equations (4.7) hold for $\xi \in \mathbb{R}$ when $t \in T_{\mathrm{f}}$ if it is assumed that all concentrations are zero above the surface $\xi < 0$. In particular, for the underflow zone $z > B \Leftrightarrow \xi > 1$, the equations are

$$\frac{\partial \boldsymbol{C}}{\partial t} + \big(\alpha(\xi,t) + \beta(t)q_{\mathrm{u}}(t)\big)\frac{\partial \boldsymbol{C}}{\partial \xi} = \beta(t)\bar{z}'(t)\boldsymbol{C}, \quad \frac{\partial \boldsymbol{S}}{\partial t} + \big(\alpha(\xi,t) + \beta(t)q_{\mathrm{u}}(t)\big)\frac{\partial \boldsymbol{S}}{\partial \xi} = \beta(t)\bar{z}'(t)\boldsymbol{S}.$$

To ensure that fluxes have correct units across the surface during extraction ($t \in T_\mathrm{e}$), we also need to transform the extraction pipe. The pipe is originally modeled by the upwards-pointing x-axis with bulk flow upwards $q_\mathrm{e}(t)$ and coupled to the z-axis by $-x = z - \bar{z}(t)$. Consequently, the transformation for the extraction pipe is

$$\xi(x,t) \coloneqq \frac{-x}{B - \bar{z}(t)}, \tag{4.9}$$

and $\boldsymbol{C}_\mathrm{pipe}(x,t) = \tilde{\boldsymbol{C}}(\xi(x,t),t)$. Then we get

$$\frac{\partial \boldsymbol{C}_\mathrm{pipe}}{\partial t} = -\frac{\partial \tilde{\boldsymbol{C}}}{\partial \xi}\xi\bar{z}'(t)\beta(t) + \frac{\partial \tilde{\boldsymbol{C}}}{\partial t} = -\left(\frac{\partial(\xi\tilde{\boldsymbol{C}})}{\partial \xi} - \tilde{\boldsymbol{C}}\right)\bar{z}'(t)\beta(t) + \frac{\partial \tilde{\boldsymbol{C}}}{\partial t}, \quad \frac{\partial \boldsymbol{C}_\mathrm{pipe}}{\partial x} = -\frac{\partial \tilde{\boldsymbol{C}}}{\partial \xi}\beta(t).$$

Equations (4.5) are transformed to (we immediately remove the tildes)

$$\begin{aligned}
\frac{\partial \boldsymbol{C}}{\partial t} - \frac{\partial}{\partial \xi}\big(\beta(t)(\xi\bar{z}'(t) + q_\mathrm{e}(t))\boldsymbol{C}\big) &= -\bar{z}'(t)\beta(t)\boldsymbol{C}, \\
\frac{\partial \boldsymbol{S}}{\partial t} - \frac{\partial}{\partial \xi}\big(\beta(t)(\xi\bar{z}'(t) + q_\mathrm{e}(t))\boldsymbol{S}\big) &= -\bar{z}'(t)\beta(t)\boldsymbol{S}, \quad \xi < 0.
\end{aligned}$$

(In comparison to (4.7), there is a minus sign on the right-hand side here.) With the bulk velocity redefined as

$$\tilde{q}(\xi,t) \coloneqq \begin{cases} 0 & \text{if } \xi < 0 \text{ and } q_\mathrm{e}(t) = 0, \\ -\beta(t)(\xi\bar{z}'(t) + q_\mathrm{e}(t)) = -\beta(t)(\xi(q_\mathrm{u}(t) + q_\mathrm{e}(t)) + q_\mathrm{e}(t)) & \text{if } \xi < 0 \text{ and } q_\mathrm{e}(t) > 0, \\ \alpha(\xi,t) + \beta(t)q_\mathrm{u}(t) = \beta(t)(\xi\bar{z}'(t) + q_\mathrm{u}(t) - \bar{z}'(t)) & \text{if } \xi > 0, \end{cases}$$

we thus get the governing equations

$$\begin{aligned}
\frac{\partial \boldsymbol{C}}{\partial t} + \frac{\partial}{\partial \xi}\big(\tilde{\mathcal{V}}_{\boldsymbol{C}}(X, \partial_\xi X, \xi, t)\boldsymbol{C}\big) &= \operatorname{sgn}(\xi)\bar{z}'(t)\beta(t)\boldsymbol{C} + \delta(\xi)\beta(t)q_\mathrm{f}(t)\boldsymbol{C}_\mathrm{f} + \gamma(\xi)\boldsymbol{R}_{\boldsymbol{C}}(\boldsymbol{C},\boldsymbol{S}), \\
\frac{\partial \boldsymbol{S}}{\partial t} + \frac{\partial}{\partial \xi}\big(\tilde{\mathcal{V}}_{\boldsymbol{S}}(X, \partial_\xi X, \xi, t)\boldsymbol{S}\big) &= \operatorname{sgn}(\xi)\bar{z}'(t)\beta(t)\boldsymbol{S} + \delta(\xi)\beta(t)q_\mathrm{f}(t)\boldsymbol{S}_\mathrm{f} + \gamma(\xi)\boldsymbol{R}_{\boldsymbol{S}}(\boldsymbol{C},\boldsymbol{S}),
\end{aligned} \tag{4.10}$$

for $\xi \in \mathbb{R}$ and $t \in T_\mathrm{e}$. These equations hold for all $t > 0$ if we for $t \in T_\mathrm{f}$ define all concentrations in $\xi < 0$ to be zero; then the system is reduced to (4.7). The salient point of these transformations is that the outlet concentrations are now simply defined by

$$\begin{aligned}
\boldsymbol{C}_\mathrm{e}(t) &= \boldsymbol{C}(0^-,t), \qquad \boldsymbol{S}_\mathrm{e}(t) = \boldsymbol{S}(0^-,t) \qquad \text{if } t \in T_\mathrm{e}, \\
\boldsymbol{C}_\mathrm{u}(t) &= \boldsymbol{C}(1^+,t), \qquad \boldsymbol{S}_\mathrm{u}(t) = \boldsymbol{S}(1^+,t) \qquad \text{if } t \in T_\mathrm{f} \text{ and } Q_\mathrm{u}(t) > 0.
\end{aligned} \tag{4.11}$$

For other times the outlet concentrations are defined to be zero.

During periods of mixing and $t \in T_\mathrm{f}$, the following ODEs for time-dependent concentrations $\boldsymbol{C}(t)$ and $\boldsymbol{S}(t)$ are obtained by averaging Equations (4.7), i.e., integrating over the interval $[0^-, 1)$ when the convective and diffusive terms are zero:

$$\begin{aligned}
\boldsymbol{C}'(t) &= \beta(t)\bar{z}'(t)\boldsymbol{C} + \beta(t)q_\mathrm{f}(t)\boldsymbol{C}_\mathrm{f}(t) + \boldsymbol{R}_{\boldsymbol{C}}(\boldsymbol{C},\boldsymbol{S}), \\
\boldsymbol{S}'(t) &= \beta(t)\bar{z}'(t)\boldsymbol{S} + \beta(t)q_\mathrm{f}(t)\boldsymbol{S}_\mathrm{f}(t) + \boldsymbol{R}_{\boldsymbol{S}}(\boldsymbol{C},\boldsymbol{S}).
\end{aligned} \tag{4.12}$$

The same ODEs are indeed obtained for $t \in T_\mathrm{e}$ (then $\boldsymbol{C}_\mathrm{f}(t) = \boldsymbol{S}_\mathrm{f}(t) = 0$).

4.2.4 Model equations with percentages

The restrictive part of the explicit CFL condition of an explicit scheme is due to the second-order derivative term containing the function $D(X)$.This function is provided in Equation (1.24), which depends only on the scalar variable X. The governing model will be rewritten so that the convective and diffusive terms are clearly seen. Furthermore, to establish boundedness on the total particulate concentration, $0 \le X \le \hat{X}$, we will rewrite the model in terms of percentages $\boldsymbol{p}$; see (4.3). We define the flux and reaction term of the total solids concentration X by

$$F(\xi,t,X) \coloneqq \tilde{q}(\xi,t)X + \gamma(\xi)\beta(t)f(X), \qquad R(\boldsymbol{C},\boldsymbol{S}) \coloneqq c\sum_{k=1}^{k_{\boldsymbol{C}}} R_{\boldsymbol{C}}^{(k)}(\boldsymbol{C},\boldsymbol{S}).$$

Then we can write

$$\tilde{\mathcal{V}}_{\boldsymbol{C}}X = F(\xi,t,X) - \gamma(\xi)\beta(t)^2\partial_\xi\mathcal{D}(X), \quad \tilde{\mathcal{V}}_{\boldsymbol{S}} = \frac{\tilde{q}(\xi,t)\rho_X - F(\xi,t,X) + \gamma(\xi)\beta(t)^2\partial_\xi\mathcal{D}(X)}{\rho_X - X}.$$

By first multiplying the first equation of (4.10) by c and adding the vector components corresponding to (4.3), one obtains the scalar equation

$$\begin{aligned}\frac{\partial X}{\partial t} + \frac{\partial F(\xi,t,X)}{\partial \xi} = \frac{\partial\big(\gamma(\xi)\beta(t)^2\partial_\xi\mathcal{D}(X)\big)}{\partial\xi} \\ + \beta(t)\operatorname{sgn}(\xi)\bar{z}'(t)X + \beta(t)\delta(\xi)q_{\mathrm{f}}(t)X_{\mathrm{f}} + \gamma(\xi)R(\boldsymbol{p}X/c,\boldsymbol{S})\end{aligned} \tag{4.13}$$

for X. The concentrations $\boldsymbol{C} = \boldsymbol{p}X/c$ and $\boldsymbol{S}$ are given by the system (4.10), which we now can rewrite with the unknowns X, $\boldsymbol{p}$ and $\boldsymbol{S}$:

$$\begin{aligned}\frac{\partial(\boldsymbol{p}X)}{\partial t} + \frac{\partial(F(\xi,t,X)\boldsymbol{p})}{\partial\xi} = \frac{\partial\big(\boldsymbol{p}\gamma(\xi)\beta(t)^2\partial_\xi\mathcal{D}(X)\big)}{\partial\xi} + \beta(t)\operatorname{sgn}(\xi)\bar{z}'(t)\boldsymbol{p}X \\ + \beta(t)\delta(\xi)q_{\mathrm{f}}(t)\boldsymbol{p}_{\mathrm{f}}X_{\mathrm{f}} + \gamma(\xi)c\boldsymbol{R}_{\boldsymbol{C}}(\boldsymbol{p}X/c,\boldsymbol{S}),\end{aligned} \tag{4.14}$$

$$\frac{\partial\boldsymbol{S}}{\partial t} + \frac{\partial\big(\tilde{\mathcal{V}}_{\boldsymbol{S}}\boldsymbol{S}\big)}{\partial\xi} = \beta(t)\operatorname{sgn}(\xi)\bar{z}'(t)\boldsymbol{S} + \beta(t)\delta(\xi)q_{\mathrm{f}}(t)\boldsymbol{S}_{\mathrm{f}} + \gamma(\xi)\boldsymbol{R}_{\boldsymbol{S}}(\boldsymbol{p}X/c,\boldsymbol{S}). \tag{4.15}$$

Not all equations in (4.14) need to be solved; one may solve only the first $k_{\boldsymbol{C}} - 1$ ones and set $p^{(k_{\boldsymbol{C}})} = 1 - (p^{(1)} + \cdots + p^{(k_{\boldsymbol{C}}-1)})$. The output concentrations for $\boldsymbol{p}$ and X are defined as in (4.11).

The mixing ODEs (4.12) are converted analogously:

$$\begin{aligned}X'(t) &= \beta(t)\bar{z}'(t)X + \beta(t)q_{\mathrm{f}}(t)X_{\mathrm{f}}(t) + R(\boldsymbol{p}X/c,\boldsymbol{S}),\\ (\boldsymbol{p}X)'(t) &= \beta(t)\bar{z}'(t)\boldsymbol{p}X + \beta(t)q_{\mathrm{f}}(t)\boldsymbol{p}_{\mathrm{f}}(t)X_{\mathrm{f}}(t) + c\boldsymbol{R}_{\boldsymbol{C}}(\boldsymbol{p}X/c,\boldsymbol{S}),\\ \boldsymbol{S}'(t) &= \beta(t)\bar{z}'(t)\boldsymbol{S} + \beta(t)q_{\mathrm{f}}(t)\boldsymbol{S}_{\mathrm{f}}(t) + \boldsymbol{R}_{\boldsymbol{S}}(\boldsymbol{p}X/c,\boldsymbol{S}).\end{aligned} \tag{4.16}$$

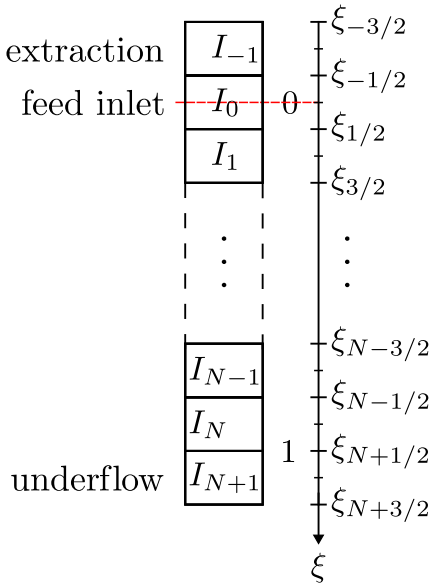

Figure 4.3: Schematic of the division of the computational domain into cells.

4.3 Explicit numerical scheme

4.3.1 Discretization in space and time

To discretize the PDE system (4.13)–(4.15), we define $\Delta\xi := 1/(N+1/2)$ for an integer N, $\xi_j := j\Delta\xi$, and let cell j be the interval $I_j := [\xi_{j-1/2}, \xi_{j+1/2}]$; see Figure 4.3. Thus, the feed inlet is located in the middle of I_0, which makes the numerical fluxes at the cell boundaries easy to define. The bottom of the tank is located at $\xi = \xi_{N+1/2} = (N+1/2)\Delta\xi = 1$. Given a total simulation time T and the total number of discrete time points N_T, we define the time step $\tau := T/N_T$, which is supposed to satisfy a suitable CFL condition, and the discrete time points t^n, $n = 0, 1, \ldots, N_T$. The total particulate concentration is denoted by $X_j^n \approx X(\xi_j, t^n)$, and analogous notation is used for other concentrations. The underflow concentration is captured by an additional cell $j = N+1$ below the tank. The extraction concentrations can be obtained in an analogous way in an additional cell I_{-1}. For both the explicit and implicit schemes the outlet concentrations are defined by $\boldsymbol{p}_\mathrm{e} = \boldsymbol{p}_{-1}^n$ and $\boldsymbol{p}_\mathrm{u} = \boldsymbol{p}_{N+1}^n$, and similarly for X and $\boldsymbol{S}$.

4.3.2 Explicit scheme

For ease of notation, we introduce $a^+ = \max\{0, a\}$, $a^- = \min\{0, a\}$, the upwind and the divergence operators by

$$\begin{aligned} \mathrm{Upw}(a; b, c) &:= \max\{a, 0\}b + \min\{a, 0\}c = a^+ b + a^- c, \qquad \text{for } a, b, c \in \mathbb{R}, \\ [\Delta\boldsymbol{\Phi}]_j^n &:= \boldsymbol{\Phi}_{j+1/2}^n - \boldsymbol{\Phi}_{j-1/2}^n. \end{aligned}$$

We define the Kronecker delta and the characteristic function for the mixture in the tank by

$$\delta_{j,0} \coloneqq \int_{I_j} \delta(\xi)\,\mathrm{d}\xi = \begin{cases} 1 & \text{if } j = 0, \\ 0 & \text{if } j \neq 0, \end{cases} \qquad \gamma_j \coloneqq \begin{cases} \gamma(\xi_j) & \text{if } j \neq 0, \\ \frac{1}{2} & \text{if } j = 0. \end{cases}$$

The term $\operatorname{sgn}(\xi)\beta(t)\bar{z}'(t)X(\xi,t)$ in (4.13) is approximated by the average

$$\frac{1}{\Delta\xi}\int_{\xi_{-1/2}}^{\xi_{1/2}} \operatorname{sgn}(\xi)\beta^n(\bar{z}')^n X(\xi,)\,\mathrm{d}\xi = \begin{cases} 0 & \text{if } q_{\mathrm{e}}^n > 0, \\ \frac{1}{2}\beta^n(\bar{z}')^n X_0^n = \frac{1}{2}\beta^n(q_{\mathrm{u}}^n - q_{\mathrm{f}}^n)X_0^n & \text{if } q_{\mathrm{e}}^n = 0, \end{cases}$$

for $j = 0$, where we recall that $X(\xi,t) = 0$ for $\xi < 0$ if $q_{\mathrm{e}}(t) = 0$, and analogously for $\boldsymbol{S}$ instead of X. For the numerical update formulas, we define

$$\kappa_j^n \coloneqq \begin{cases} 1 - \tau\beta^n(\bar{z}')^n = 1 - \tau\beta^n(q_{\mathrm{u}}^n + q_{\mathrm{e}}^n) & \text{if } j < 0 \text{ and } q_{\mathrm{e}}^n > 0, \\ 1 & \text{if } j < 0 \text{ and } q_{\mathrm{e}}^n = 0 \text{ or } j = 0 \text{ and } q_{\mathrm{e}}^n > 0, \\ 1 - \frac{\tau}{2}\beta^n(q_{\mathrm{u}}^n - q_{\mathrm{f}}^n) & \text{if } j = 0 \text{ and } q_{\mathrm{e}}^n = 0, \\ 1 + \tau\beta^n(\bar{z}')^n & \text{if } j > 0, \end{cases} \tag{4.17}$$

Finally, we define

$$\tilde{q}_{j+1/2}^n \coloneqq \tilde{q}(\xi_{j+1/2}, t^n) = \begin{cases} 0 & \text{if } j = -2, -1 \text{ and } q_{\mathrm{e}}^n = 0, \\ -\beta^n(\xi_{j+1/2}(q_{\mathrm{u}}^n + q_{\mathrm{e}}^n) + q_{\mathrm{e}}^n) & \text{if } j = -2, -1 \text{ and } q_{\mathrm{e}}^n > 0, \\ \alpha_{j+1/2}^n + \beta^n q_{\mathrm{u}}^n & \text{if } j = 0, \dots, N+1. \end{cases}$$

An explicit approximation of the system (4.13)–(4.15) is now obtained by following ideas from [12, 23]. We assume that the function f defined by (4.8) has a unique maximum at $X^* \in (0, \hat{X})$. The Engquist-Osher numerical flux [47]

$$\mathcal{E}_{j+1/2}^n \coloneqq \gamma_{j+1/2}\left(f(0) + \int_0^{X_j^n} \max\{0, f'(s)\}\,\mathrm{d}s + \int_0^{X_{j+1}^n} \min\{0, f'(s)\}\,\mathrm{d}s\right) \tag{4.18}$$

is used, which for a unimodal flux function f is

$$\mathcal{E}_{j+1/2}^n(X_j^n, X_{j+1}^n) = \gamma_{j+1/2}\begin{cases} f(X_j^n) & \text{if } X_j^n, X_{j+1}^n \leq X^*, \\ f(X^*) & \text{if } X_{j+1}^n \leq X^* < X_j^n, \\ -f(X^*) + f(X_j^n) + f(X_{j+1}^n) & \text{if } X_j^n \leq X^* < X_{j+1}^n, \\ f(X_{j+1}^n) & \text{if } X^* < X_j^n, X_{j+1}^n. \end{cases}$$

The diffusive term and the other fluxes are discretized by

$$\mathcal{J}_{j+1/2}^n \coloneqq \gamma_{j+1/2}\frac{(\beta^n)^2}{\Delta\xi}\big(\mathcal{D}(X_{j+1}^n) - \mathcal{D}(X_j^n)\big), \quad j = -2, \dots, N+1, \tag{4.19}$$

$$\mathcal{B}_{j+1/2}^n \coloneqq \operatorname{Upw}(\tilde{q}_{j+1/2}^n; X_j^n, X_{j+1}^n), \tag{4.20}$$

$$\mathcal{F}^n_{j+1/2} \coloneqq \mathcal{B}^n_{j+1/2} + \beta^n \mathcal{E}^n_{j+1/2}$$
$$= \begin{cases} 0 & \text{if } j = -2, -1 \text{ and } q^n_{\mathrm{e}} = 0, \\ -\beta^n\big(\xi_{j+1/2}(q^n_{\mathrm{u}} + q^n_{\mathrm{e}}) + q^n_{\mathrm{e}}\big)X^n_{j+1} & \text{if } j = -2, -1 \text{ and } q^n_{\mathrm{e}} > 0, \\ \mathrm{Upw}(\alpha^n_{j+1/2} + \beta^n q^n_{\mathrm{u}}; X^n_j, X^n_{j+1}) + \beta^n \mathcal{E}^n_{j+1/2} & \text{if } j = 0, \dots, N-1, \\ (\alpha^n_{j+1/2} + \beta^n q^n_{\mathrm{u}})X^n_j & \text{if } j = N, N+1, \end{cases} \tag{4.21}$$
$$\Phi^n_{j+1/2} \coloneqq \mathcal{F}^n_{j+1/2} - \mathcal{J}^n_{j+1/2}. \tag{4.22}$$

We have $\alpha_{N+1/2} = 0$, and when $q_{\mathrm{e}} > 0$, we assume that $\Delta\xi$ is sufficiently small, so that all fluxes at the top $\xi = \xi_{-1/2}$ and bottom $\xi_{N+1/2}$ are directed out of the tank, which means that no boundary values are needed. The numerical fluxes are then defined, for $j = -2, \dots, N+1$, by

$$\boldsymbol{\Phi}^n_{\boldsymbol{p},j+1/2} \coloneqq \mathrm{Upw}(\Phi^n_{j+1/2}; \boldsymbol{p}^n_j, \boldsymbol{p}^n_{j+1}), \tag{4.23}$$
$$\boldsymbol{\Phi}^n_{\boldsymbol{S},j+1/2} \coloneqq \mathrm{Upw}\left(\rho_X \tilde{q}^n_{j+1/2} - \Phi^n_{j+1/2}; \frac{\boldsymbol{S}^n_j}{\rho_X - X^n_j}, \frac{\boldsymbol{S}^n_{j+1}}{\rho_X - X^n_{j+1}}\right).$$

With an Euler time step, $\lambda \coloneqq \tau/\Delta\xi$, and $\mu \coloneqq \tau/\Delta\xi^2$, we can formulate the explicit scheme as follows. For the boundary layers $j = -1$ and $j = N+1$, we set

$$X^{n+1}_{-1} = 0, \quad \boldsymbol{p}^{n+1}_{-1} = \boldsymbol{0}, \quad \boldsymbol{S}^{n+1}_{-1} = \boldsymbol{0} \quad \text{if } q^n_{\mathrm{e}} = 0, \tag{4.24}$$
$$X^{n+1}_{N+1} = 0, \quad \boldsymbol{p}^{n+1}_{N+1} = \boldsymbol{0}, \quad \boldsymbol{S}^{n+1}_{N+1} = \boldsymbol{0} \quad \text{if } q^n_{\mathrm{u}} = 0. \tag{4.25}$$

Otherwise, we have for $j = -1, \dots, N+1$,

$$X^{n+1}_j = \kappa^n_j X^n_j - \lambda[\Delta\mathcal{F}]^n_j + \lambda[\Delta\mathcal{J}]^n_j + \lambda\delta_{j,0}\beta^n q^n_{\mathrm{f}} X^n_{\mathrm{f}} + \tau\gamma_j R(\boldsymbol{p}^n_j X^n_j/c, \boldsymbol{S}^n_j), \tag{4.26}$$
$$\boldsymbol{p}^{n+1}_j X^{n+1}_j = \kappa^n_j \boldsymbol{p}^n_j X^n_j - \lambda[\Delta\boldsymbol{\Phi}_{\boldsymbol{p}}]^n_j + \lambda\delta_{j,0}\beta^n q^n_{\mathrm{f}} \boldsymbol{p}^n_{\mathrm{f}} X^n_{\mathrm{f}} + \tau\gamma_j c\boldsymbol{R}_{\boldsymbol{C}}(\boldsymbol{p}^n_j X^n_j/c, \boldsymbol{S}^n_j), \tag{4.27}$$
$$\boldsymbol{S}^{n+1}_j = \kappa^n_j \boldsymbol{S}^n_j - \lambda[\Delta\boldsymbol{\Phi}_{\boldsymbol{S}}]^n_j + \lambda\delta_{j,0}\beta^n q^n_{\mathrm{f}} \boldsymbol{S}^n_{\mathrm{f}} + \tau\gamma_j \boldsymbol{R}_{\boldsymbol{S}}(\boldsymbol{p}^n_j X^n_j/c, \boldsymbol{S}^n_j). \tag{4.28}$$

Scheme (4.26) is solved first, then the others. If $X^{n+1}_j = 0$, then the value of $\boldsymbol{p}^{n+1}_j$ is irrelevant, and can be set to $\boldsymbol{p}^{n+1}_j \coloneqq \boldsymbol{p}^n_j$. For the cells outside the tank, the scheme for X is reduced to the following. If $q^n_{\mathrm{e}} = 0$, then (4.24) handles $j = -1$; otherwise, we define $q^n_{\mathrm{out}} \coloneqq q^n_{\mathrm{u}} + q^n_{\mathrm{e}}$ and utilize

$$X^{n+1}_{-1} = \big(1 - \tau\beta^n q^n_{\mathrm{out}}\big)X^n_{-1} + \lambda\beta^n\big((\xi_{-1/2}q^n_{\mathrm{out}} + q^n_{\mathrm{e}})X^n_0 - (\xi_{-3/2}q^n_{\mathrm{out}} + q^n_{\mathrm{e}})X^n_{-1}\big), \tag{4.29}$$

On the other hand, if $q^n_{\mathrm{u}} = 0$, then (4.25) is in effect for $j = N+1$; otherwise,

$$X^{n+1}_{N+1} = (1 + \tau\beta^n q^n_{\mathrm{out}})X^n_{N+1} - \lambda\big((\alpha^n_{N+3/2} + \beta^n q^n_{\mathrm{u}})X^n_{N+1} - \beta^n q^n_{\mathrm{u}} X^n_N\big). \tag{4.30}$$

Similar update formulas hold for $\boldsymbol{p}$ and $\boldsymbol{S}$. The resulting approximate concentrations are transformed back to the original z- and x-coordinates via (4.6) and (4.9), respectively.

4.3.3 Numerics during mixing

Suppose a (PDE or numerical) solution $X(\xi, T_0)$ (or $p^{(k)}(\xi, T_0)$ or $S^{(k)}(\xi, T_0)$) is known at $t = T_0 = t_{n_0}$ when a period of complete mixing starts. The initial concentrations for the ODEs (4.16) are defined as the averages (analogously for $p^{(k)}$ and $S^{(k)}$)

$$X(T_0) \coloneqq \int_0^1 X(\xi, T_0)\,\mathrm{d}\xi \approx \Delta\xi\left(\frac{X_0^{n_0}}{2} + X_1^{n_0} + \cdots + X_N^{n_0}\right).$$

The ODE system (4.16) can then approximately be integrated in time with an Euler step. If an ODE mixing period ends at $t = t^n$ with the values $X(t^n)$, and the PDE model is to be simulated thereafter, then the value of each component k is allocated to all cells in the tank; $X_j^n \coloneqq X(t^n)$, $j = 0, \ldots, N$.

4.3.4 CFL condition

We denote the solution variables by $\boldsymbol{\mathcal{U}} \coloneqq (X, \boldsymbol{p}^{\mathrm{T}}, \boldsymbol{S}^{\mathrm{T}})^{\mathrm{T}}$ and define the constants

$$\|f\| \coloneqq \max_{0\le X\le \hat{X}} |f(X)|, \qquad M_R \coloneqq \frac{1}{c}\sup_{\substack{\boldsymbol{\mathcal{U}}\in\Omega\\ 1\le k\le k_{\boldsymbol{C}}}}\left|\frac{\partial R}{\partial C^{(k)}}\right|,$$

$$M_{q1} \coloneqq \max_{0\le t\le T}\{q_{\mathrm{u}}(t) + q_{\mathrm{e}}(t), q_{\mathrm{f}}(t)\}, \quad M_{q2} \coloneqq \max_{0\le t\le T}\big(\max\{q_{\mathrm{f}}(t), q_{\mathrm{e}}(t)\} + 2q_{\mathrm{u}}(t)\big)$$

$$\zeta \coloneqq \frac{1}{B - B_{\mathrm{c}}}, \qquad C_1 \coloneqq \zeta(M_{q2} + \|f'\|),$$

$$C_2 \coloneqq \zeta^2\|a\|, \qquad M_{\boldsymbol{\xi}} \coloneqq \sup_{\substack{\boldsymbol{\mathcal{U}}\in\Omega,\\ 1\le k\le k_{\boldsymbol{\xi}}}}\sum_{l\in I^-_{\boldsymbol{\xi},k}} |\sigma^{(k,l)}_{\boldsymbol{\xi}}|\bar{r}^{(l)}_{\boldsymbol{\xi}}(\boldsymbol{C}, \boldsymbol{S}), \quad \boldsymbol{\xi}\in\{\boldsymbol{C}, \boldsymbol{S}\}.$$

The time step τ and the spatial mesh width $\Delta\xi$ should satisfy the CFL condition

$$\tau\left(\zeta M_{q1} + \max\{M_R, M_{\boldsymbol{C}}, M_{\boldsymbol{S}}\} + \frac{2}{\Delta\xi}\max\left\{C_1 + \frac{C_2}{\Delta\xi}, \frac{1}{\rho_X - \hat{X}}\left(\zeta\rho_X + C_1\hat{X} + \frac{C_2\hat{X}}{\Delta\xi}\right)\right\}\right) \le 1. \tag{CFL}$$

4.3.5 Monotonicity and invariant region property

In what follows, we demonstrate that the solution variables $\boldsymbol{\mathcal{U}} = (X, \boldsymbol{p}^{\mathrm{T}}, \boldsymbol{S}^{\mathrm{T}})^{\mathrm{T}}$ produced by the explicit numerical scheme stays in the set

$$\Omega \coloneqq \left\{\boldsymbol{\mathcal{U}} \in \mathbb{R}^{1+k_{\boldsymbol{C}}+k_{\boldsymbol{S}}} : 0 \le X \le \hat{X},\ \boldsymbol{p} \ge 0,\ p^{(1)} + \cdots + p^{(k_{\boldsymbol{C}})} = 1,\ \boldsymbol{S} \ge 0\right\}$$

provided that this property holds for the initial values. Our proofs rely on the following lemma, which follows directly from the definition (4.18).

Lemma 4.1. *Assume that $0 \le X_j \le \hat{X}$ for all j. Then the Engquist-Osher flux $\mathcal{E}_{j+1/2} = \mathcal{E}_{j+1/2}(X_j, X_{j+1})$ applied on the unimodal function $0 \le f \in C^1$ satisfies*

$$-\|f'\| \le \frac{\partial \mathcal{E}_{j+1/2}}{\partial X_{j+1}} \le 0 \le \frac{\partial \mathcal{E}_{j+1/2}}{\partial X_j} \le \|f'\|, \quad \left|\frac{\partial [\Delta \mathcal{E}]_j}{\partial X_j}\right| \le \|f'\|, \quad \frac{\mathcal{E}_{j+1/2}}{X_j} \le \|f'\|, \quad \frac{\mathcal{E}_{j+1/2}}{X_{j+1}} \le \|f'\|.$$

Lemma 4.2. *If $\boldsymbol{\mathcal{U}}_j^n \in \Omega$ for all j, then the following estimates hold for $j = -1, \dots, N+1$:*

$$\kappa_j^n \ge 1 - \zeta \tau M_{q1}, \tag{4.31}$$

$$|\tilde{q}_{j+1/2}^n| \le \zeta(\max\{q_{\mathrm{f}}^n, q_{\mathrm{e}}^n\} + 2q_{\mathrm{u}}^n) \le \zeta M_{q2}, \tag{4.32}$$

$$\frac{\partial [\Delta \mathcal{B}]_j^n}{\partial X_k^n} \begin{cases} = -\tilde{q}_{j-1/2}^{n,+} \le 0 & \text{if } k = j-1, \\ \le \zeta M_{q2}, & \text{if } k = j, \\ = \tilde{q}_{j+1/2}^{n,-} \le 0, & \text{if } k = j+1, \\ = 0 & \text{otherwise,} \end{cases} \tag{4.33}$$

$$\left|\frac{\partial}{\partial X_k} R(\boldsymbol{p}_j^n X_j^n / c, \boldsymbol{S}_j^n)\right| \begin{cases} \le M_R & \text{if } k = j, \\ = 0 & \text{if } k \ne j, \end{cases} \tag{4.34}$$

$$\max\left\{\Phi_{j+1/2}^{n,+}, -\Phi_{j-1/2}^{n,-}\right\} \le \left(\zeta(M_{q2} + \|f'\|) + \frac{\zeta^2 \|a\|}{\Delta \xi}\right) X_j^n \tag{4.35}$$

Proof. By the definition of the transformation of variables,

$$-q_{\mathrm{f}}(t) \le \bar{z}'(t) \le q_{\mathrm{u}}(t) + q_{\mathrm{e}}(t), \qquad -\zeta(q_{\mathrm{u}}(t) + q_{\mathrm{e}}(t)) \le \alpha(\xi, t) \le \zeta q_{\mathrm{f}}(t), \qquad 0 < \beta(t) \le \zeta.$$

These inclusions directly imply (4.31) since

$$\kappa_j^n \ge 1 - \tau\zeta \max\{q_{\mathrm{u}}^n + q_{\mathrm{e}}^n, q_{\mathrm{f}}^n\} \ge 1 - \tau\zeta M_{q1}.$$

To prove (4.32) we observe that when $q_{\mathrm{e}}^n = 0$, then $\tilde{q}_{-1/2}^n = \tilde{q}_{-3/2}^n = 0$, and when $q_{\mathrm{e}}^n > 0$ and $j = -1, -2$,

$$\tilde{q}_{j+1/2}^n = -\beta^n\left(\xi_{j+1/2}(q_{\mathrm{u}}^n + q_{\mathrm{e}}^n) + q_{\mathrm{e}}^n\right) \ge -\zeta q_{\mathrm{e}}^n. \tag{4.36}$$

For $j = 0, \dots, N$, (we recall that if $q_{\mathrm{f}}^n > 0$, then $q_{\mathrm{e}}^n = 0$ and vice versa)

$$\tilde{q}_{j+1/2}^n = \alpha_{j+1/2}^n + \beta^n q_{\mathrm{u}}^n = \beta^n\left(-(\bar{z}')^n(1 - \xi_{j+1/2}) + q_{\mathrm{u}}^n\right) \begin{cases} \le \zeta(q_{\mathrm{f}}^n + q_{\mathrm{u}}^n) & \text{if } q_{\mathrm{e}}^n = 0, \\ \ge -\zeta(q_{\mathrm{u}}^n + q_{\mathrm{e}}^n) & \text{if } q_{\mathrm{e}}^n > 0, \end{cases} \tag{4.37}$$

and for $j = N+1$,

$$\tilde{q}_{N+3/2}^n = \frac{(\bar{z}')^n \Delta\xi + q_{\mathrm{u}}^n}{B - \bar{z}^n} \le \zeta(q_{\mathrm{out}}^n \Delta\xi + q_{\mathrm{u}}^n) \le \zeta((1 + \Delta\xi)q_{\mathrm{u}}^n + q_{\mathrm{e}}^n). \tag{4.38}$$

From (4.36) to (4.38) we now deduce (4.32). Next, computing the difference of the flux

$$\mathcal{B}_{j+1/2}^n = \tilde{q}_{j+1/2}^{n,+} X_j^n + \tilde{q}_{j+1/2}^{n,-} X_{j+1}^n$$

and differentiating this expression with respect to X_k^n we obtain

$$\frac{\partial[\Delta\mathcal{B}]_j^n}{\partial X_k^n} = \frac{\partial}{\partial X_k^n}\big(\tilde{q}_{j+1/2}^{n,+}X_j^n + \tilde{q}_{j+1/2}^{n,-}X_{j+1}^n - \tilde{q}_{j-1/2}^{n,+}X_{j-1}^n - \tilde{q}_{j-1/2}^{n,-}X_j^n\big)$$
$$= \begin{cases} -\tilde{q}_{j-1/2}^{n,+} \le 0 & \text{if } k = j-1, \\ \tilde{q}_{j+1/2}^{n,+} - \tilde{q}_{j-1/2}^{n,-} \le \zeta\big((1+\Delta\xi)q_{\mathrm{u}}^n + \max\{q_{\mathrm{e}}^n, q_{\mathrm{f}}^n\}\big) \le \zeta M_{q2} & \text{if } k = j, \\ \tilde{q}_{j+1/2}^{n,-} \le 0 & \text{if } k = j+1, \\ 0 & \text{otherwise.} \end{cases}$$

This proves (4.33). For the reaction term, the cases $k \neq j$ are trivial. Assuming that $k = j$ and differentiating we obtain

$$\left|\frac{\partial}{\partial X_j} R(\boldsymbol{p}_j^n X_j^n/c, \boldsymbol{S}_j^n)\right| = \frac{1}{c}\left|(\boldsymbol{p}_j^n)^{\mathrm{T}}\nabla_{\boldsymbol{C}} R\right| \le \frac{1}{c}\sum_{i=1}^{k_{\boldsymbol{C}}} p_j^{(i),n}\left|\frac{\partial R}{\partial C_j^{(i),n}}\right| = M_R\sum_{i=1}^{k_{\boldsymbol{C}}} p_j^{(i),n} = M_R,$$

which implies (4.34). Finally, (4.35) follows from

$$\Phi_{j+1/2}^{n,+} = \big(\mathcal{B}_{j+1/2}^n + \beta^n\mathcal{E}_{j+1/2}^n - \mathcal{J}_{j+1/2}^n\big)^+ \le \tilde{q}_{j+1/2}^{n,+}X_j^n + \zeta\|f'\|X_j^n + \gamma_{j+1/2}\frac{(\beta^n)^2}{\Delta\xi}\mathcal{D}(X_j^n)$$
$$\le \left(\zeta(M_{q2} + \|f'\|) + \zeta^2\frac{\|a\|}{\Delta\xi}\right)X_j^n,$$
$$-\Phi_{j-1/2}^{n,-} = -\big(\mathcal{B}_{j-1/2}^n + \beta^n\mathcal{E}_{j-1/2}^n - \mathcal{J}_{j-1/2}^n\big)^- \le \tilde{q}_{j-1/2}^{n,+}X_j^n + \zeta\|f'\|X_j^n + \gamma_{j+1/2}\frac{(\beta^n)^2}{\Delta\xi}\mathcal{D}(X_j^n)$$
$$\le \left(\zeta(M_{q2} + \|f'\|) + \frac{\zeta^2\|a\|}{\Delta\xi}\right)X_j^n.$$

□

Lemma 4.3. *If $\boldsymbol{\mathcal{U}}_j^n \in \Omega$ for all j and (CFL) is in effect, then $0 \le X_j^{n+1} \le \hat{X}$ for all j.*

Proof. We write the update formula (4.26) for $j = -1, \dots, N+1$ as

$$X_j^{n+1} = \mathcal{H}_X^n\big(X_{j-1}^n, X_j^n, X_{j+1}^n\big)$$

and we shall show that $\mathcal{H}_X^n$ is a monotone function in each of its variables. We recall that

$$\lambda[\Delta\mathcal{J}]_j^n = \mu(\beta^n)^2\big(\gamma_{j+1/2}\big(\mathcal{D}(X_{j+1}^{n+1}) - \mathcal{D}(X_j^{n+1})\big) - \gamma_{j-1/2}\big(\mathcal{D}(X_j^{n+1}) - \mathcal{D}(X_{j-1}^{n+1})\big)\big),$$

$a = \mathcal{D}'$, and we differentiate to obtain, by means of (CFL) and Lemmas 4.1 and 4.2,

$$\frac{\partial X_j^{n+1}}{\partial X_{j-1}^n} = -\lambda\frac{\partial[\Delta\mathcal{B}]_j^n}{\partial X_{j-1}^n} - \lambda\beta^n\frac{\partial[\Delta\mathcal{E}]_j^n}{\partial X_{j-1}^n} + \lambda\frac{\partial[\Delta\mathcal{J}]_j^n}{\partial X_{j-1}^n}$$
$$= \lambda\tilde{q}_{j-1/2}^{n,+} + \lambda\beta^n\frac{\partial\mathcal{E}_{j-1/2}}{\partial X_{j-1}^n} + \mu(\beta^n)^2\gamma_{j-1/2}a(X_{j-1}^n) \ge 0,$$

$$\begin{aligned}\frac{\partial X_j^{n+1}}{\partial X_j^n} &= \kappa^n - \lambda\frac{\partial[\Delta\mathcal{B}]_j^n}{\partial X_j^n} - \lambda\beta^n\frac{\partial[\Delta\mathcal{E}]_j^n}{\partial X_j^n} + \lambda\frac{\partial[\Delta\mathcal{J}]_j^n}{\partial X_j^n} + \frac{\partial}{\partial X_j}R(\boldsymbol{p}_j^n X_j^n/c, \boldsymbol{S}_j^n)\\ &\geq 1 - \tau\zeta M_{q1} - \lambda\zeta M_{q2} - \zeta\lambda\|f'\| - \mu\zeta^2 2\|a\| - \tau M_R \geq 0,\\ \frac{\partial X_j^{n+1}}{\partial X_{j+1}^n} &= -\lambda\frac{\partial[\Delta\mathcal{B}]_j^n}{\partial X_{j+1}^n} - \lambda\beta^n\frac{\partial[\Delta\mathcal{E}]_j^n}{\partial X_{j+1}^n} = -\lambda\tilde{q}_{j+1/2}^{n,-} - \lambda\beta^n\frac{\partial\mathcal{E}_{j+1/2}}{\partial X_{j+1}^n} \geq 0.\end{aligned}$$

The proved monotonicity of $\mathcal{H}_X^n$ and the assumptions (1.3) imply that, for $j \neq 0$,

$$\begin{aligned}0 &= \mathcal{H}_X^n(0,0,0) \leq X_j^{n+1} = \mathcal{H}_X^n(X_{j-1}^n, X_j^n, X_{j+1}^n) \leq \mathcal{H}_X^n(\hat{X},\hat{X},\hat{X})\\ &= \kappa_j^n\hat{X} - \lambda(\tilde{q}_{j+1/2}^n - \tilde{q}_{j-1/2}^n)\hat{X}\\ &= \begin{cases}\hat{X}\big(1 - \tau\beta^n q_{\text{out}}^n - \lambda\beta^n(-(\xi_{-1/2}q_{\text{out}}^n + q_{\text{e}}^n) + (\xi_{-3/2}q_{\text{out}}^n + q_{\text{e}}^n))\big)\\ = \hat{X}\big(1 - \tau\beta^n q_{\text{out}}^n - \lambda\beta^n(\frac{\Delta\xi}{2}q_{\text{out}}^n - \frac{3\Delta\xi}{2}q_{\text{out}}^n)\big) = \hat{X} & \text{if } j=-1 \text{ and } q_{\text{e}}^n > 0,\\ \hat{X} & \text{if } j=-1 \text{ and } q_{\text{e}}^n = 0,\\ \hat{X}\big(1 + \tau\beta^n(\bar{z}')^n\\ \quad -\lambda\beta^n(-(\bar{z}')^n(1-\xi_{j+1/2}) + (\bar{z}')^n(1-\xi_{j-1/2}))\big) = \hat{X} & \text{if } j \geq 1.\end{cases}\end{aligned}$$

For $j = 0$ we have, since $\alpha(\xi_{1/2}, t) = -\bar{z}'(t)(1-\Delta\xi/2)\beta(t)$, and assuming $X_{\text{f}}^n \leq \hat{X}$,

$$\begin{aligned}0 \leq \lambda\beta^n X_{\text{f}}^n q_{\text{f}}^n &= \mathcal{H}_X^n(0,0,0) \leq X_0^{n+1} = \mathcal{H}_X^n(X_{-1}^n, X_0^n, X_1^n) \leq \mathcal{H}_X^n(\hat{X},\hat{X},\hat{X})\\ &= \begin{cases}\kappa_0^n\hat{X} - \lambda\big(\alpha_{1/2}^n + \beta^n q_{\text{u}}^n + \beta^n(-\frac{\Delta\xi}{2}q_{\text{out}}^n + q_{\text{e}}^n)\big)\hat{X}\\ = \hat{X}\big(1 - \tau\beta^n q_{\text{out}}^n - \lambda(-q_{\text{out}}^n(1-\frac{\Delta\xi}{2})\beta^n + \beta^n q_{\text{u}}^n + \beta^n(-\frac{\Delta\xi}{2}q_{\text{out}}^n + q_{\text{e}}^n))\big)\\ = \hat{X}(1 - \tau\beta^n q_{\text{out}}^n) \leq \hat{X} & \text{if } q_{\text{e}}^n > 0,\\ \kappa_0^n\hat{X} - \lambda\big(\alpha_{1/2}^n + \beta^n q_{\text{u}}^n\big)\hat{X} + \lambda\beta^n X_{\text{f}}^n q_{\text{f}}^n\\ = (1 - \frac{\tau}{2}\beta^n q_{\text{out}}^n)\hat{X} - \lambda\big(-(q_{\text{u}}^n - q_{\text{f}}^n)(1-\frac{\Delta\xi}{2})\beta^n + \beta^n q_{\text{u}}^n\big)\hat{X} + \lambda\beta^n X_{\text{f}}^n q_{\text{f}}^n\\ = \hat{X} - \lambda\big(-(q_{\text{u}}^n - q_{\text{f}}^n)\beta^n + \beta^n q_{\text{u}}^n\big)\hat{X} + \lambda\beta^n X_{\text{f}}^n q_{\text{f}}^n\\ = \hat{X} - \lambda\beta^n(\hat{X} - X_{\text{f}}^n)q_{\text{f}}^n \leq \hat{X} & \text{if } q_{\text{e}}^n = 0.\end{cases}\end{aligned}$$

□

Lemma 4.4. *If $\boldsymbol{\mathcal{U}}_j^n \in \Omega$ for all j and (CFL) holds, then*

$$p_j^{(k),n+1} \geq 0 \quad \text{for all } k = 1,\dots,k_{\boldsymbol{C}} \text{ and all } j. \tag{4.39}$$

Proof. If $X_j^{n+1} = 0$, we define

$$p_j^{(k),n+1} \coloneqq p_j^{(k),n} \in [0,1] \quad \text{for all } k = 1,\dots,k_{\boldsymbol{C}}. \tag{4.40}$$

If $X_j^{n+1} > 0$, we have for each $k \in \{1,\dots,k_{\boldsymbol{C}}\}$

$$\begin{aligned}p_j^{(k),n+1}X_j^{n+1} &= \kappa_j^n p_j^{(k),n}X_j^n - \lambda\big(\Phi_{j+1/2}^{n,+}p_j^{(k),n} + \Phi_{j+1/2}^{n,-}p_{j+1}^{(k),n} - \Phi_{j-1/2}^{n,+}p_{j-1}^{(k),n} - \Phi_{j-1/2}^{n,-}p_j^{(k),n}\big)\\ &\quad + \lambda\delta_{j,0}\beta^n q_{\text{f}}^n p_{\text{f}}^{(k),n}X_{\text{f}}^n + \tau\gamma_j c R_j^{(k),n}(\boldsymbol{p}_j^n X_j^n/c, \boldsymbol{S}_j^n)\end{aligned}$$

$$
\begin{aligned}
&\geq (1-\zeta\tau M_{q1})\, p_j^{(k),n} X_j^n - 2\lambda \left(\zeta(M_{q2}+\|f'\|) + \frac{\zeta^2\|a\|}{\Delta\xi}\right) p_j^{(k),n} X_j^n \\
&\quad + \tau c \sum_{l\in I^-_{\boldsymbol{C},k}} \sigma_{\boldsymbol{C}}^{(k,l)} \bar{r}^{(l)}\big(\boldsymbol{p}_j^n X_j^n/c, \boldsymbol{S}_j^n\big) p_j^{(k),n} X_j^n/c \\
&\geq \left(1-\zeta(\tau M_{q1}) - \frac{2\tau}{\Delta\xi}\left(\zeta(M_{q2}+\|f'\|) + \frac{\zeta^2\|a\|}{\Delta\xi}\right) + \tau M_{\boldsymbol{C}}\right) p_j^{(k),n} X_j^n \geq 0.
\end{aligned}
$$

This implies (4.39). □

Lemma 4.5. *If $\boldsymbol{\mathcal{U}}_j^n \in \Omega$ for all j and (CFL) holds, then*

$$
p_j^{(1),n+1} + \cdots + p_j^{(k_{\boldsymbol{C}}),n+1} = 1 \quad \text{for all } j. \tag{4.41}
$$

Proof. If $X_j^{n+1} = 0$, then by (4.40),

$$
p_j^{(1),n+1} + \cdots + p_j^{(k_{\boldsymbol{C}}),n+1} = p_j^{(1),n} + \cdots + p_j^{(k_{\boldsymbol{C}}),n} = 1,
$$

so let us assume that $X_j^{n+1} > 0$. We sum up all equations in (4.27) and utilize that

$$
p_j^{(1),n} + \cdots + p_j^{(k_{\boldsymbol{C}},n)} = 1
$$

along with

$$
\begin{aligned}
\sum_{k=1}^{k_{\boldsymbol{C}}} [\Delta\Phi_{\boldsymbol{p}}^{(k)}]_j^n &= \sum_{k=1}^{k_{\boldsymbol{C}}} \big(\mathrm{Upw}(\Phi_{\boldsymbol{p},j+1/2}^{(k),n}, p_j^{(k),n}, p_{j+1}^{(k),n}) - \mathrm{Upw}(\Phi_{\boldsymbol{p},j-1/2}^{(k),n}, p_j^{(k),n}, p_{j+1}^{(k),n})\big) \\
&= \sum_{k=1}^{k_{\boldsymbol{C}}} \big(\Phi_{j+1/2}^{n,+} p_j^{(k),n} + \Phi_{j+1/2}^{n,-} p_{j+1}^{(k),n} - \Phi_{j-1/2}^{n,+} p_{j-1}^{(k),n} - \Phi_{j-1/2}^{n,-} p_j^{(k),n}\big) \\
&= \Phi_{j+1/2}^{n,+} + \Phi_{j+1/2}^{n,-} - \Phi_{j-1/2}^{n,+} - \Phi_{j-1/2}^{n,-} = [\Delta\Phi]_j^n.
\end{aligned}
$$

Then the sum of the equations in (4.27) is

$$
X_j^{n+1} \sum_{k=1}^{k_{\boldsymbol{C}}} p_j^{(k),n+1} = \kappa_j^n X_j^n - \lambda [\Delta\Phi]_j^n + \lambda \delta_{j,0} \beta^n q_{\mathrm{f}}^n X_{\mathrm{f}}^n + \tau\gamma_j R(\boldsymbol{p}_j^n X_j^n/c, \boldsymbol{S}_j^n). \tag{4.42}
$$

The right-hand side is identical to that of (4.26). Hence, subtracting (4.42) from (4.26) we get

$$
X_j^{n+1}\big(1 - (p_j^{(1),n+1} + \cdots + p_j^{(k_{\boldsymbol{C}}),n+1})\big) = 0,
$$

which proves the desired result (4.41). □

Lemma 4.6. *If $\boldsymbol{\mathcal{U}}_j^n \in \Omega$ for all j and (CFL) holds, then*

$$
S_j^{(k),n+1} \geq 0 \quad \text{for all } k = 1, \ldots, k_{\boldsymbol{S}} \text{ and all } j.
$$

Proof. From the update formula for a component $S_j^{(k),n}$ of $\boldsymbol{S}_j^n$ we get

$$\begin{aligned}
S_j^{(k),n+1} &= \kappa_j^n S_j^{(k),n} - \lambda\bigg(\frac{S_j^{(k),n}}{\rho_X - X_j^n}(\rho_X \tilde{q}_{j+1/2}^n - \Phi_{j+1/2}^n)^+ + \frac{S_{j+1}^{(k),n}}{\rho_X - X_{j+1}^n}(\rho_X \tilde{q}_{j+1/2}^n - \Phi_{j+1/2}^n)^- \\
&\quad - \frac{S_{j-1}^{(k),n}}{\rho_X - X_{j-1}^n}(\rho_X \tilde{q}_{j-1/2}^n - \Phi_{j-1/2}^n)^+ - \frac{S_j^{(k),n}}{\rho_X - X_j^n}(\rho_X \tilde{q}_{j-1/2}^n - \Phi_{j-1/2}^n)^- \bigg) \\
&\quad + \lambda \delta_{j,0} \beta^n q_{\mathrm{f}}^n S_{\mathrm{f}}^{(k),n} + \tau \gamma_j R_{\boldsymbol{S},j}^{(k),n}(\boldsymbol{p}_j^n X_j^n / c, \boldsymbol{S}_j^n) \\
&\geq (1 - \tau\zeta M_{q1})\, S_j^{(k),n} - \frac{\lambda S_j^{(k),n}}{\rho_X - X_j^n}\big((\rho_X \tilde{q}_{j+1/2}^n - \Phi_{j+1/2}^n)^+ - (\rho_X \tilde{q}_{j-1/2}^n - \Phi_{j-1/2}^n)^- \big) \\
&\quad + \tau \sum_{l \in I_{\boldsymbol{S},k}^-} \sigma_{\boldsymbol{S}}^{(k,l)} \bar{r}^{(l)}\big(\boldsymbol{p}_j^n X_j^n / c, \boldsymbol{S}_j^n\big) S_j^{(k),n} \\
&\geq \left(1 - \tau\zeta M_{q1} - \frac{2\tau\zeta}{\Delta\xi(\rho_X - \hat{X})}\left((\rho_X + \hat{X}) M_{q2} + \|f'\| \hat{X} + \frac{\zeta \|a\| \hat{X}}{\Delta\xi} \right) + \tau M_C \right) S_j^{(k),n} \geq 0.
\end{aligned}$$

□

4.4 A semi-implicit scheme

4.4.1 Semi-implicit scheme for the update of X

To obtain a semi-implicit scheme, we write out several terms in (4.26)–(4.28) and evaluate those containing the coefficient $\mu = \tau/\Delta\xi^2$ at time t_{n+1}. Then (4.26) becomes

$$\begin{aligned}
X_j^{n+1} &= \kappa_j^n X_j^n - \lambda [\Delta \mathcal{F}]_j^n \\
&\quad + (\beta^n)^2 \mu \big(\gamma_{j+1/2}(\mathcal{D}(X_{j+1}^{n+1}) - \mathcal{D}(X_j^{n+1})) - \gamma_{j-1/2}(\mathcal{D}(X_j^{n+1}) - \mathcal{D}(X_{j-1}^{n+1})) \big) \\
&\quad + \lambda \delta_{j,0} \beta^n q_{\mathrm{f}}^n X_{\mathrm{f}}^n + \tau \gamma_j R(\boldsymbol{p}_j^n X_j^n / c, \boldsymbol{S}_j^n)
\end{aligned} \tag{4.43}$$

For $j = -1$ and $j = N+1$, many terms are zero and this formula is in fact explicit; see (4.29) and (4.30). For $j = 0, \dots, N$, one has to solve a system of $(N+1) \times (N+1)$ nonlinear equations. For the further analysis, it is is useful to rewrite (4.26) as a two-step implicit-explicit scheme:

1. Given X_j^n for $j = -1, \dots, N+1$, calculate $\tilde{X}_j^{n+1}$ from

$$\tilde{X}_j^{n+1} = \kappa_j^n X_j^n - \lambda [\Delta \mathcal{F}]_j^n + \lambda \delta_{j,0} \beta^n q_{\mathrm{f}}^n X_{\mathrm{f}}^n + \tau \gamma_j R(\boldsymbol{p}_j^n X_j^n / c, \boldsymbol{S}_j^n), \quad j = -1, \dots, N+1. \tag{4.44}$$

2. Let

$$X_{-1}^{n+1} = \tilde{X}_{-1}^{n+1}, \quad X_{N+1}^{n+1} = \tilde{X}_{N+1}^{n+1}, \tag{4.45}$$

and compute $\boldsymbol{X}^{n+1} = (X_0^{n+1}, \dots, X_N^{n+1})^{\mathrm{T}}$ by solving the nonlinear system of equations

$$\boldsymbol{X}^{n+1} + (\beta^n)^2 \mu \boldsymbol{T} \begin{pmatrix} \mathcal{D}(X_0^{n+1}) \\ \mathcal{D}(X_1^{n+1}) \\ \vdots \\ \mathcal{D}(X_N^{n+1}) \end{pmatrix} = \tilde{\boldsymbol{X}}^{n+1}, \quad \boldsymbol{T} \coloneqq \begin{bmatrix} 1 & -1 & & & \\ -1 & 2 & -1 & & \\ & \ddots & \ddots & \ddots & \\ & & -1 & 2 & -1 \\ & & & -1 & 1 \end{bmatrix} \tag{4.46}$$

where $\tilde{\boldsymbol{X}}^{n+1} \coloneqq (\tilde{X}_0^{n+1}, \dots, \tilde{X}_N^{n+1})^{\mathrm{T}}$.

In what follows, we assume that the CFL condition for the semi-implicit scheme

$$\tau \left(\zeta M_{q1} + \max\{M_R, M_{\boldsymbol{C}}, M_{\boldsymbol{S}}\} + \frac{2}{\Delta\xi} \max\left\{ C_1, \frac{\zeta \rho_X + C_1 \hat{X}}{\rho_X - \hat{X}} \right\} \right) \leq 1 \tag{CFL-SI}$$

is in effect. Notice that (CFL-SI) arises from (CFL) from the fact that $a \equiv 0$ and hence $C_2 = 0$, and therefore stipulates a bound on $\tau/\Delta\xi$, but not on $\tau/\Delta\xi^2$.

To ensure that the system (4.46) has a unique solution at all, we follow a strategy similar to that of [19]: we first assume that (4.46) has a solution and show that the scheme is monotone and satisfies an invariant region property. We then invoke a topological degree argument to show that (4.46) indeed has a solution, and show that it depends Lipschitz continuously on the solution at the previous time step. As a consequence, the whole scheme (4.44)–(4.46) is well defined.

Lemma 4.7. *Assume that τ and $\Delta\xi$ satisfy (CFL-SI). Then the scheme (4.44)–(4.46) is monotone, i.e. there exist functions $\mathcal{K}_j^n$, $j = -1, \dots, N+1$, such that*

$$X_j^{n+1} = \mathcal{K}_j^n \big(X_{-1}^n, X_0^n, X_1^n, \dots, X_N^n, X_{N+1}^n, t^n \big), \quad j = -1, \dots, N+1,$$

that are monotone in each X-argument.

Proof. By repeating the monotonicity part of the proof of Lemma 4.3 we see that under the condition (CFL-SI), the scheme (4.44) is monotone, i.e., i.e., $\partial \tilde{X}_j^{n+1} / \partial X_k^n \geq 0$ for all $-1 \leq j, k \leq N+1$, so by (4.45) the statement immediately holds for $j = -1$ and $j = N+1$. In what follows, we define for a vector $\boldsymbol{X} = (X_0, \dots, X_N)^{\mathrm{T}}$ the Jacobian matrix of the left-hand side of (4.46), namely

$$\boldsymbol{\mathcal{J}}(\boldsymbol{X}) \coloneqq \boldsymbol{I}_{N+1} + (\beta^n)^2 \mu \boldsymbol{T} \operatorname{diag}\big(a(X_0), \dots, a(X_N) \big). \tag{4.47}$$

We wish to show that

$$\frac{\partial X_j^{n+1}}{\partial X_k^n} \geq 0 \quad \text{for all } 1 \leq k, j \leq n.$$

To this end we introduce for $k = 0, \dots, N$ the vectors

$$\frac{\partial \boldsymbol{X}^{n+1}}{\partial X_k^n} := \left(\frac{\partial X_0^{n+1}}{\partial X_k^n}, \dots, \frac{\partial X_N^{n+1}}{\partial X_k^n} \right)^{\mathrm{T}}, \quad \frac{\partial \tilde{\boldsymbol{X}}^{n}}{\partial X_k^n} := \left(\frac{\partial \tilde{X}_0^{n}}{\partial X_k^n}, \dots, \frac{\partial \tilde{X}_N^{n}}{\partial X_k^n} \right)^{\mathrm{T}}$$

Assume that for given $\boldsymbol{X}^n$, the vector $\boldsymbol{X}^{n+1}$ is a solution to (4.43). Then

$$\boldsymbol{\mathcal{J}}(\boldsymbol{X}^{n+1}) \frac{\partial \boldsymbol{X}^{n+1}}{\partial X_k^n} = \frac{\partial \tilde{\boldsymbol{X}}^{n}}{\partial X_k^n}, \quad k = 0, \dots, N.$$

We already know that $\partial \tilde{\boldsymbol{X}}^{n} / \partial X_k^n \geq \boldsymbol{0}$. On the other hand, for any $\boldsymbol{X}$, the matrix $(\boldsymbol{\mathcal{J}}(\boldsymbol{X}))^{\mathrm{T}}$ is a strictly diagonally dominant L-matrix and therefore an M-matrix; in particular, $(\boldsymbol{\mathcal{J}}(\boldsymbol{X}))^{\mathrm{T}}$ has a non-negative inverse, and therefore also $(\boldsymbol{\mathcal{J}}(\boldsymbol{X}))^{-1}$ is non-negative, hence

$$\frac{\partial \boldsymbol{X}^{n+1}}{\partial X_k^n} = \big(\boldsymbol{\mathcal{J}}(\boldsymbol{X}^{n+1})\big)^{-1} \frac{\partial \tilde{\boldsymbol{X}}^{n}}{\partial X_k^n} \geq \boldsymbol{0}, \quad k = 0, \dots, N.$$

□

Lemma 4.8. *If $\boldsymbol{\mathcal{U}}_j^n \in \Omega$ for all j and (CFL-SI) is in effect, then*

$$0 \leq X_j^{n+1} \leq \hat{X} \quad \text{for all } j = -1, \dots, N+1. \tag{4.48}$$

Proof. Repeating the second part of the proof of Lemma 4.3 under the assumption $a \equiv 0$ we see that under the condition (CFL-SI),

$$0 \leq \tilde{X}_j^{n+1} \leq \hat{X} \quad \text{for all } j = -1, \dots, N+1. \tag{4.49}$$

This directly proves (4.48) for $j = -1$ and $j = N+1$. Furthermore, we define

$$\varpi_{j+1/2}^n := \begin{cases} (\mathcal{D}(X_{j+1}^n) - \mathcal{D}(X_j^n))/(X_{j+1}^n - X_j^n) & \text{if } X_{j+1}^n \neq X_j^n, \\ 0 & \text{otherwise,} \end{cases} \quad j = 0, \dots, N-1,$$

and write the nonlinear scheme (4.46) as $\boldsymbol{M}(\boldsymbol{X}^{n+1}) \boldsymbol{X}^{n+1} = \tilde{\boldsymbol{X}}^{n+1}$, where the entries $(m_{ij})_{0 \leq i,j \leq N}$ of the tridiagonal matrix $\boldsymbol{M} = \boldsymbol{M}(\boldsymbol{X}^{n+1})$ are given by

$$\begin{aligned} m_{j,j-1} &= -(\beta^n)^2 \mu \varpi_{j-1/2}^{n+1}, \quad j = 1, \dots, N, \\ m_{jj} &= 1 + (\beta^n)^2 \mu \big(\varpi_{j-1/2}^{n+1} + \varpi_{j+1/2}^{n+1} \big), \quad j = 1, \dots, N-1, \\ m_{j,j+1} &= -(\beta^n)^2 \mu \varpi_{j+1/2}^{n+1}, \quad j = 0, \dots, N-1, \\ m_{00} &= 1 + (\beta^n)^2 \mu \varpi_{1/2}^{n+1}, \quad m_{NN} = 1 + (\beta^n)^2 \mu \varpi_{N-1/2}^{n+1}. \end{aligned}$$

Since $\varpi_{j+1/2}^{n+1} \geq 0$ for all j, $\boldsymbol{M}$ is a strictly diagonally dominant L-matrix and therefore an M-matrix, that is $\boldsymbol{M}^{-1}$ exists and $\boldsymbol{M}^{-1} \geq \boldsymbol{0}$, i.e., if we write $\boldsymbol{M}^{-1} = (\bar{m}_{jk})_{0 \leq j,k \leq N}$, then $\bar{m}_{jk} \geq 0$. Since

$$X_j^{n+1} = \bar{m}_{j,0} \tilde{X}_0^{n+1} + \bar{m}_{j,1} \tilde{X}_1^{n+1} + \dots + \bar{m}_{j,N} \tilde{X}_N^{n+1}, \tag{4.50}$$

this property implies that $X_j^{n+1} \geq 0$. On the other hand, since

$$m_{jj} - \sum_{\substack{k=0 \\ k \neq j}}^{N} |m_{jk}| \geq 1 \quad \text{and} \quad \sum_{k=0}^{N} m_{jk} = 1 \quad \text{for all } j = 0, \dots, N,$$

we have $\boldsymbol{M}\mathbf{1} = \mathbf{1}$ with $\mathbf{1} := (1, \dots, 1)^{\mathrm{T}}$, hence $\boldsymbol{M}^{-1}\mathbf{1} = \mathbf{1}$, that is $\bar{m}_{j,0} + \bar{m}_{j,1} + \cdots + \bar{m}_{j,N} = 1$. In view of the upper bound in (4.49) we then deduce from (4.50) that $X_j^{n+1} \leq \hat{X}$ for $j = 0, \dots, N$. □

In what follows, we define $\boldsymbol{\mathcal{X}} := (X_{-1}, X_0, X_1, \dots, X_N, X_{N+1})^{\mathrm{T}} \in \mathbb{R}^{N+3}$. The following lemma and its proof closely follow [19, Lemma 3.3, part (a)].

Lemma 4.9. *Assume that the condition* (CFL-SI) *is in effect and that* $\boldsymbol{\mathcal{X}}^n \in [0, \hat{X}]^{N+3}$. *Then the scheme* (4.43), *or equivalently,* (4.44)–(4.46), *admits a solution* $\boldsymbol{\mathcal{X}}^{n+1} \in [0, \hat{X}]^{N+3}$.

Proof. The existence of $\boldsymbol{\mathcal{X}}^{n+1}$ follows by adopting an argument used in[49] to prove the existence of a solution of implicit schemes for hyperbolic equations based on topological degree theory [40]. To this end, let us write the scheme in the form

$$\boldsymbol{\mathcal{X}}^{n+1} - \boldsymbol{\mathcal{E}}(\boldsymbol{\mathcal{X}}^{n+1}, t^n) = \tilde{\boldsymbol{\mathcal{X}}}^{n+1}(\boldsymbol{\mathcal{X}}^n, t^n). \tag{4.51}$$

Here $\tilde{\boldsymbol{\mathcal{X}}}^{n+1}(\cdot, t^n) : \mathbb{R}^{N+3} \to \mathbb{R}^{N+3}$ is a continuous function defined by (4.44), and $\boldsymbol{\mathcal{E}}(\cdot, t^n) : \mathbb{R}^{N+3} \to \mathbb{R}^{N+3}$ is another continuous function defined in an obvious way by (4.45), (4.46). By Lemma 4.8, if $\boldsymbol{\mathcal{X}}^{n+1}$ satisfies (4.51), then $\boldsymbol{\mathcal{X}}^{n+1} \in [0, \hat{X}]^{N+3}$. On the other hand we know (and have used that) if $a \equiv 0$ and hence $\mathcal{D} \equiv 0$, then the explicit scheme for the hyperbolic case

$$\boldsymbol{\mathcal{X}}^{n+1} = \tilde{\boldsymbol{\mathcal{X}}}^{n+1}(\boldsymbol{\mathcal{X}}^n, t^n), \tag{4.52}$$

which corresponds to the scheme (4.44), satisfies the same bound, i.e., $\tilde{\boldsymbol{\mathcal{X}}}^{n+1}(\boldsymbol{\mathcal{X}}^n, t^n) \in [0, \hat{X}]^{N+3}$. Consequently, if $B_R \subset \mathbb{R}^{N+3}$ is a ball with center $\mathbf{0}$ and sufficiently large radius R, then (4.51) has no solution on the boundary of B_R, and one can define the topological degree of the mapping $\mathrm{Id} - \boldsymbol{\mathcal{E}}$ associated with the set B_R and the point $\tilde{\boldsymbol{\mathcal{X}}}^{n+1}(\boldsymbol{\mathcal{X}}^n, t^n)$, that is, $\deg(\mathrm{Id} - \boldsymbol{\mathcal{E}}, B_R, \tilde{\boldsymbol{\mathcal{X}}}^{n+1}(\boldsymbol{\mathcal{X}}^n, t^n))$. Furthermore, if $\alpha \in [0, 1]$, then the same argument allows us to define $\deg(\mathrm{Id} - \alpha\boldsymbol{\mathcal{E}}, B_R, \tilde{\boldsymbol{\mathcal{X}}}^{n+1}(\boldsymbol{\mathcal{X}}^n, t^n))$. The property of invariance of degree under continuous transformations then asserts that the latter quantity does not depend on α, hence

$$\deg\big(\mathrm{Id} - \boldsymbol{\mathcal{E}}, B_R, \tilde{\boldsymbol{\mathcal{X}}}^{n+1}(\boldsymbol{\mathcal{X}}^n, t^n)\big) = \deg\big(\mathrm{Id}, B_R, \tilde{\boldsymbol{\mathcal{X}}}^{n+1}(\boldsymbol{\mathcal{X}}^n, t^n)\big) = 1,$$

where the equality for $\alpha = 0$ holds since we can solve the scheme (4.52) in a unique way. This proves that (4.51) has a solution in B_R, where we already have proved that the solution belongs to $[0, \hat{X}]^{N+3}$. □

Lemma 4.10. *Assume that the condition (CFL-SI) is in effect and that $\boldsymbol{\mathcal{X}}^n, \boldsymbol{\mathcal{Y}}^n \in [0, \hat{X}]^{N+3}$, and that $\boldsymbol{\mathcal{X}}^{n+1}$ and $\boldsymbol{\mathcal{Y}}^{n+1}$ are both computed by scheme (4.43), or equivalently, (4.44)–(4.46). Then there exists a constant $C > 0$ such that*

$$\|\boldsymbol{\mathcal{X}}^{n+1} - \boldsymbol{\mathcal{Y}}^{n+1}\|_1 \le (1 + C\Delta t)\|\boldsymbol{\mathcal{X}}^n - \boldsymbol{\mathcal{Y}}^n\|_1. \tag{4.53}$$

This means that the solution of (4.44)–(4.46) depends Lipschitz continuously on $\boldsymbol{\mathcal{X}}^n$, and in particular, setting $\boldsymbol{\mathcal{X}}^n = \boldsymbol{\mathcal{Y}}^n$, we obtain uniqueness.

Proof. We define $\vartheta_j^n := Y_j^n - X_j^n$ for $j = -1, \dots, N+1$ and the quantities

$$\theta_j^{n+1} := \begin{cases} \mu(\beta^n)^2(\mathcal{D}(Y_j^{n+1}) - \mathcal{D}(X_j^{n+1}))/\vartheta_j^{n+1} \ge 0 & \text{if } \vartheta_j^{n+1} \ne 0, \\ 0 & \text{otherwise,} \end{cases} \qquad j = -1, \dots, N+1.$$

Furthermore, we let $\mathcal{E}_{j+1/2}(\boldsymbol{X}^n)$ and $\mathcal{E}_{j+1/2}(\boldsymbol{Y}^n)$ be the Engquist-Osher numerical fluxes (4.18) applied to $\boldsymbol{X}^n$ and $\boldsymbol{Y}^n$, and similarly for $\mathcal{B}_{j+1/2}^n$ and $\mathcal{F}_{j+1/2}^n$. Clearly,

$$\begin{aligned}
&\mathcal{F}_{j+1/2}^n(\boldsymbol{Y}^n) - \mathcal{F}_{j+1/2}^n(\boldsymbol{X}^n) \\
&= \mathcal{B}_{j+1/2}^n(\boldsymbol{Y}^n) - \mathcal{B}_{j+1/2}^n(\boldsymbol{X}^n) + \beta^n\big(\mathcal{E}_{j+1/2}^n(\boldsymbol{Y}^n) - \mathcal{E}_{j+1/2}^n(\boldsymbol{X}^n)\big) \\
&= \mathrm{Upw}\big(\tilde{q}_{j+1/2}^n; \vartheta_j^n, \vartheta_{j+1}^n\big) + \beta^n\gamma_{j+1/2}\left(\int_{X_j^n}^{Y_j^n} (f')^+(s)\,\mathrm{d}s + \int_{X_{j+1}^n}^{Y_{j+1}^n} (f')^-(s)\,\mathrm{d}s\right) \\
&= \eta_{j+1/2}^n\vartheta_j^n - \nu_{j+1/2}^n\vartheta_{j+1}^n,
\end{aligned}$$

where we define

$$\begin{aligned}
\eta_{j+1/2}^n &:= (\tilde{q}_{j+1/2}^n)^+ + \gamma_{j+1/2}\int_0^1 (f')^+\big(X_j^n + \sigma(Y_j^n - X_j^n)\big)\,\mathrm{d}\sigma \ge 0, \\
\nu_{j+1/2}^n &:= -\left((\tilde{q}_{j+1/2}^n)^- + \gamma_{j+1/2}\int_0^1 (f')^-\big(X_{j+1}^n + \sigma(Y_{j+1}^n - X_{j+1}^n)\big)\,\mathrm{d}\sigma\right) \ge 0,
\end{aligned}$$

hence

$$-\lambda\big([\Delta\mathcal{F}(\boldsymbol{Y})]_j^n - [\Delta\mathcal{F}(\boldsymbol{X})]_j^n\big) = -\lambda\big(\eta_{j+1/2}^n + \nu_{j-1/2}^n\big)\vartheta_j^n + \lambda\eta_{j-1/2}^n\vartheta_{j-1}^n + \lambda\nu_{j+1/2}^n\vartheta_{j+1}^n.$$

With this in mind, we obtain from (4.43) and the corresponding scheme for Y_j^n

$$\begin{aligned}
\vartheta_{-1}^{n+1} &= \big(\kappa_{-1}^n - \lambda(\eta_{-1/2}^n + \nu_{-3/2}^n)\big)\vartheta_{-1}^n + \lambda\nu_{-1/2}^n\vartheta_0^n, \\
\big(1 + \theta_0^{n+1}\big)\vartheta_0^{n+1} &= \big(\kappa_0^n - \lambda(\eta_{1/2}^n + \nu_{-1/2}^n)\big)\vartheta_0^n + \lambda\nu_{1/2}^n\vartheta_1^n + \lambda\eta_{-1/2}^n\vartheta_{-1}^n + \theta_1^{n+1}\vartheta_1^{n+1} \\
&\quad + \tau\gamma_0\big(R(\boldsymbol{p}_0^nY_0^n/c, \boldsymbol{S}_0^n) - R(\boldsymbol{p}_0^nX_0^n/c, \boldsymbol{S}_0^n)\big), \\
\big(1 + 2\theta_j^{n+1}\big)\vartheta_j^{n+1} &= \big(\kappa_j^n - \lambda(\eta_{j+1/2}^n + \nu_{j-1/2}^n)\big)\vartheta_j^n + \lambda\nu_{j+1/2}^n\vartheta_{j+1}^n + \lambda\eta_{j-1/2}^n\vartheta_{j-1}^n \\
&\quad + \theta_{j+1}^{n+1}\vartheta_{j+1}^{n+1} + \theta_{j-1}^{n+1}\vartheta_{j-1}^{n+1} \\
&\quad + \tau\gamma_j\big(R(\boldsymbol{p}_j^nY_j^n/c, \boldsymbol{S}_j^n) - R(\boldsymbol{p}_j^nX_j^n/c, \boldsymbol{S}_j^n)\big), \quad j = 1, \dots, N-1, \\
\big(1 + \theta_N^{n+1}\big)\vartheta_N^{n+1} &= \big(\kappa_N^n - \lambda(\eta_{N+1/2}^n + \nu_{N-1/2}^n)\big)\vartheta_N^n + \lambda\nu_{N+1/2}^n\vartheta_{N+1}^n + \lambda\eta_{N-1/2}^n\vartheta_{N-1}^n \\
&\quad + \theta_{N-1}^{n+1}\vartheta_{N-1}^{n+1} + \tau\gamma_N\big(R(\boldsymbol{p}_N^nY_N^n/c, \boldsymbol{S}_N^n) - R(\boldsymbol{p}_N^nX_N^n/c, \boldsymbol{S}_N^n)\big), \\
\vartheta_{N+1}^{n+1} &= \big(\kappa_{N+1}^n - \lambda(\eta_{N+3/2}^n + \nu_{N+1/2}^n)\big)\vartheta_{N+1}^n + \lambda\eta_{N+1/2}^n\vartheta_N^n.
\end{aligned} \tag{4.54}$$

Finally, we define

$$\rho_j^n := \int_0^1 \partial_s R\Big((\boldsymbol{p}_j^n/c)\big(X_j^n + \sigma(Y_j^n - X_j^n)\big), \boldsymbol{S}_j^n\Big)\,\mathrm{d}\sigma, \quad j = 0, \dots, N,$$

such that

$$\tau\gamma_j\big(R(\boldsymbol{p}_j^n Y_j^n/c, \boldsymbol{S}_j^n) - R(\boldsymbol{p}_j^n X_j^n/c, \boldsymbol{S}_j^n)\big) = \tau\gamma_j\rho_j^n\vartheta_j^n, \quad j = 0, \dots, N.$$

Consequently, we may write (4.54) as

$$\begin{aligned}
\vartheta_{-1}^{n+1} &= \big(\kappa_{-1}^n - \lambda(\eta_{-1/2}^n + \nu_{-3/2}^n)\big)\vartheta_{-1}^n + \lambda\nu_{-1/2}^n\vartheta_0^n,\\
\big(1+\theta_0^{n+1}\big)\vartheta_0^{n+1} &= \big(\kappa_0^n - \lambda(\eta_{1/2}^n + \nu_{-1/2}^n) + \tau\gamma_0\rho_0^n\big)\vartheta_0^n + \lambda\nu_{1/2}^n\vartheta_1^n + \lambda\eta_{-1/2}^n\vartheta_{-1}^n + \theta_1^{n+1}\vartheta_1^{n+1},\\
\big(1+2\theta_j^{n+1}\big)\vartheta_j^{n+1} &= \big(\kappa_j^n - \lambda(\eta_{j+1/2}^n + \nu_{j-1/2}^n) + \tau\gamma_j\rho_j^n\big)\vartheta_j^n + \lambda\nu_{j+1/2}^n\vartheta_{j+1}^n\\
&\quad + \lambda\eta_{j-1/2}^n\vartheta_{j-1}^n + \theta_{j+1}^{n+1}\vartheta_{j+1}^{n+1} + \theta_{j-1}^{n+1}\vartheta_{j-1}^{n+1}, \quad j = 1, \dots, N-1,\\
\big(1+\theta_N^{n+1}\big)\vartheta_N^{n+1} &= \big(\kappa_N^n - \lambda(\eta_{N+1/2}^n + \nu_{N-1/2}^n) + \tau\gamma_N\rho_N^N\big)\vartheta_N^n + \lambda\eta_{N-1/2}^n\vartheta_{N-1}^n\\
&\quad + \lambda\nu_{N+1/2}^n\vartheta_{N+1}^n + \theta_{N-1}^{n+1}\vartheta_{N-1}^{n+1},\\
\vartheta_{N+1}^{n+1} &= \big(\kappa_{N+1}^n - \lambda(\eta_{N+3/2}^n + \nu_{N+1/2}^n)\big)\vartheta_{N+1}^n + \lambda\eta_{N+1/2}^n\vartheta_N^n.
\end{aligned}$$

Since by (CFL-SI), all coefficients in these equations are nonnegative, we get

$$\begin{aligned}
\big|\vartheta_{-1}^{n+1}\big| &\le \big(\kappa_{-1}^n - \lambda(\eta_{-1/2}^n + \nu_{-3/2}^n)\big)|\vartheta_{-1}^n| + \lambda\nu_{-1/2}^n|\vartheta_0^n|,\\
\big(1+\theta_0^{n+1}\big)\big|\vartheta_0^{n+1}\big| &\le \big(\kappa_0^n - \lambda(\eta_{1/2}^n + \nu_{-1/2}^n) + \tau\gamma_0\rho_0^n\big)|\vartheta_0^n| + \lambda\nu_{1/2}^n|\vartheta_1^n|\\
&\quad + \lambda\eta_{-1/2}^n|\vartheta_{-1}^n| + \theta_1^{n+1}\big|\vartheta_1^{n+1}\big|,\\
\big(1+2\theta_j^{n+1}\big)\big|\vartheta_j^{n+1}\big| &\le \big(\kappa_j^n - \lambda(\eta_{j+1/2}^n + \nu_{j-1/2}^n) + \tau\gamma_j\rho_j^n\big)\big|\vartheta_j^n\big| + \lambda\nu_{j+1/2}^n\big|\vartheta_{j+1}^n\big|\\
&\quad + \lambda\eta_{j-1/2}^n\big|\vartheta_{j-1}^n\big| + \theta_{j+1}^{n+1}\big|\vartheta_{j+1}^{n+1}\big| + \theta_{j-1}^{n+1}\big|\vartheta_{j-1}^{n+1}\big|, \quad j = 1, \dots, N-1,\\
\big(1+\theta_N^{n+1}\big)\big|\vartheta_N^{n+1}\big| &\le \big(\kappa_N^n - \lambda(\eta_{N+1/2}^n + \nu_{N-1/2}^n) + \tau\gamma_N\rho_N^N\big)|\vartheta_N^n| + \lambda\eta_{N-1/2}^n\big|\vartheta_{N-1}^n\big|\\
&\quad + \lambda\nu_{N+1/2}^n\big|\vartheta_{N+1}^n\big| + \theta_{N-1}^{n+1}\big|\vartheta_{N-1}^{n+1}\big|,\\
\big|\vartheta_{N+1}^{n+1}\big| &\le \big(\kappa_{N+1}^n - \lambda(\eta_{N+3/2}^n + \nu_{N+1/2}^n)\big)\big|\vartheta_{N+1}^n\big| + \lambda\eta_{N+1/2}^n|\vartheta_N^n|.
\end{aligned}$$

Summing over these inequalities, canceling terms, rewriting the result again in terms of $\{Y_j^n\}$ and $\{X_j^n\}$, and taking into account that $\nu_{-3/2}^n \ge 0$ and $\eta_{N+3/2}^n$ we obtain the inequality

$$\begin{aligned}
\sum_{j=-1}^{N+1}\big|Y_j^{n+1} - X_j^{n+1}\big| &\le \sum_{j=-1}^{N+1}\big(\kappa_j^n + \tau\gamma_j\rho_j^n\big)\big|Y_j^n - X_j^n\big|\\
&\quad - \lambda\nu_{-3/2}^n|Y_{-1}^n - X_{-1}^n| - \lambda\eta_{N+3/2}^n|Y_{N+1}^n - X_{N+1}^n|\\
&\le \sum_{j=-1}^{N+1}(1 + C\tau)\big|Y_j^n - X_j^n\big|,
\end{aligned}$$

that is, (4.53), where we take into account that $\kappa_j^n \le 1 + C\tau$ with a suitable constant $C > 0$ (see (4.17)) and that the quantities ρ_j^n are uniformly bounded. □

System (4.46) can be written as $\boldsymbol{\varphi}(\boldsymbol{X}^{n+1}) = \boldsymbol{0}$, where $\boldsymbol{\varphi}$ is a nonlinear vector function defined by the left-hand side of (4.46) and $\boldsymbol{\mathcal{J}}_{\boldsymbol{\varphi}} \in \mathbb{R}^{(N+1)\times(N+1)}$ is its associated Jacobian matrix.

4.4.2 Numerical solution of the nonlinear system

The Newton-Raphson method applied to (4.46) reads

$$\boldsymbol{\mathcal{J}}_{\boldsymbol{\varphi}}(\boldsymbol{u}^{[k]})(\boldsymbol{u}^{[k+1]}-\boldsymbol{u}^{[k]})=-\boldsymbol{\varphi}(\boldsymbol{u}^{[k]}),\quad k=0,1,\dots, \tag{4.55}$$

with the Jacobian matrix $\boldsymbol{\mathcal{J}}_{\boldsymbol{\varphi}}(\boldsymbol{u})$ given by (4.47) (recall that $a=\mathcal{D}'$). The iteration starts with the initial vector $\boldsymbol{u}^{[0]}:=\boldsymbol{X}^n$ and evolves formally according to (4.55) until the termination criterion

$$\frac{\|\boldsymbol{u}^{[k+1]}-\boldsymbol{u}^{[k]}\|_1}{\|\boldsymbol{u}^{[k]}\|_1}<\varepsilon$$

is reached, where $\varepsilon>0$ is the tolerance and $\|\cdot\|_1$ is the ℓ_1-norm. After convergence, we set $\boldsymbol{X}^{n+1}:=\boldsymbol{u}^{[k+1]}$. Since the matrix $\boldsymbol{\mathcal{J}}_{\boldsymbol{\varphi}}(\boldsymbol{u})$ is strictly diagonally dominant by columns for all $\boldsymbol{u}$, it is invertible and the iteration (4.55) is well defined.

4.4.3 Update of the percentage vector $\boldsymbol{p}_j^n$ and the soluble concentrations $\boldsymbol{S}_j^n$

An inspection of the proof of Lemma 4.4 reveals that although the update formula for the percentages (4.27) is an explicit upwind scheme, it is still associated with a CFL condition that imposes a bound on $\tau/\Delta\xi^2$ due to the presence of differences of $\mathcal{D}$-values divided by $\Delta\xi$ in the convective flux, cf. (4.19), (4.22) and (4.23). Consequently, to remove this shortcoming so that the whole semi-implicit scheme (and not just the update formula for X) is associated with a CFL bound on $\tau/\Delta\xi$ only, we need to resort to an implicit difference scheme.

We write out all terms in (4.27) and evaluate those containing μ at the time t_{n+1}:

$$\begin{aligned}\boldsymbol{p}_j^{n+1}X_j^{n+1}=\kappa_j^n\boldsymbol{p}_j^nX_j^n-\lambda\big(&\Phi_{j+1/2}^{n,n+1,+}\boldsymbol{p}_j^{n+1}+\Phi_{j+1/2}^{n,n+1,-}\boldsymbol{p}_{j+1}^{n+1}-\Phi_{j-1/2}^{n,n+1,+}\boldsymbol{p}_{j-1}^{n+1}-\Phi_{j-1/2}^{n,n+1,-}\boldsymbol{p}_j^{n+1}\big)\\&+\lambda\delta_{j,0}\beta^nq_{\mathrm{f}}^n\boldsymbol{p}_{\mathrm{f}}^nX_{\mathrm{f}}^n+c\tau\gamma_j\boldsymbol{R}_{\boldsymbol{C}}(\boldsymbol{p}_j^nX_j^n/c,\boldsymbol{S}_j^n),\end{aligned} \tag{4.56}$$

where

$$\Phi_{j+1/2}^{n,n+1}:=\mathcal{F}_{j+1/2}^n-\mathcal{J}_{j+1/2}^{n+1}.$$

For the cells outside the tank, this reduces to (4.24) if $q_{\mathrm{e}}=0$ and $j=-1$; otherwise,

$$\begin{aligned}\boldsymbol{p}_{-1}^{n+1}X_{-1}^{n+1}&=(1-\tau\beta^nq_{\mathrm{out}}^n)\boldsymbol{p}_{-1}^nX_{-1}^n+\lambda\beta^n\big((\xi_{-1/2}q_{\mathrm{out}}^n+q_{\mathrm{e}}^n)\boldsymbol{p}_0^nX_0^n-\big(\xi_{-3/2}q_{\mathrm{out}}^n+q_{\mathrm{e}}^n\big)\boldsymbol{p}_{-1}^nX_{-1}^n\big),\\
\boldsymbol{p}_{N+1}^{n+1}X_{N+1}^{n+1}&=(1+\tau\beta^nq_{\mathrm{out}}^n)\boldsymbol{p}_{N+1}^nX_{N+1}^n-\lambda\big((\alpha_{N+3/2}^n+\beta^nq_{\mathrm{u}}^n)\boldsymbol{p}_{N+1}^nX_{N+1}^n-\beta^nq_{\mathrm{u}}^n\boldsymbol{p}_N^nX_N^n\big),\end{aligned}$$

where we recall that $q_{\mathrm{out}}^n:=q_{\mathrm{u}}^n+q_{\mathrm{e}}^n$. Let us focus the cells $j=0,\dots,N$ and put all the unknowns in a matrix (cells in rows and solid components in columns):

$$\boldsymbol{P}^n:=\begin{bmatrix}(\boldsymbol{p}_0^n)^{\mathrm{T}}\\(\boldsymbol{p}_1^n)^{\mathrm{T}}\\\vdots\\(\boldsymbol{p}_N^n)^{\mathrm{T}}\end{bmatrix},\qquad\boldsymbol{W}^n:=\begin{bmatrix}(\lambda\beta^nq_{\mathrm{f}}^n\boldsymbol{p}_{\mathrm{f}}^nX_{\mathrm{f}}^n+c\frac{\tau}{2}\boldsymbol{R}_{\boldsymbol{C}}(\boldsymbol{p}_0^nX_0^n/c,\boldsymbol{S}_0^n))^{\mathrm{T}}\\c\tau\boldsymbol{R}_{\boldsymbol{C}}(\boldsymbol{p}_1^nX_1^n/c,\boldsymbol{S}_1^n)^{\mathrm{T}}\\\vdots\\c\tau\boldsymbol{R}_{\boldsymbol{C}}(\boldsymbol{p}_N^nX_N^n/c,\boldsymbol{S}_N^n)^{\mathrm{T}}\end{bmatrix},$$

$$\boldsymbol{M}(\boldsymbol{\Phi},\boldsymbol{X}) \coloneqq \operatorname{diag}(\boldsymbol{X}) + \lambda \begin{bmatrix} \Phi^+_{1/2}-\Phi^-_{-1/2} & \Phi^-_{1/2} & 0 & \cdots & 0 \\ -\Phi^+_{1/2} & \Phi^+_{3/2}-\Phi^-_{1/2} & \ddots & \ddots & \vdots \\ 0 & -\Phi^+_{3/2} & \ddots & \ddots & 0 \\ \vdots & \ddots & \ddots & \Phi^+_{N-1/2}-\Phi^-_{N-3/2} & \Phi^-_{N-1/2} \\ 0 & \cdots & 0 & -\Phi^+_{N-1/2} & \Phi^+_{N+1/2}-\Phi^-_{N-1/2} \end{bmatrix}.$$

where for a vector $\boldsymbol{X}$ we define $\operatorname{diag}(\boldsymbol{X}) \coloneqq \operatorname{diag}(X_0,\dots,X_N)$. With $\boldsymbol{\kappa} \coloneqq (\kappa_0,\dots,\kappa_N)^{\mathrm{T}}$, we get the linear system

$$\boldsymbol{M}(\boldsymbol{\Phi}^{n,n+1},\boldsymbol{X}^{n+1})\boldsymbol{P}^{n+1} = \operatorname{diag}(\boldsymbol{\kappa}^n)\operatorname{diag}(\boldsymbol{X}^n)\boldsymbol{P}^n + \boldsymbol{W}^n =: \boldsymbol{\Theta}^n. \tag{4.57}$$

In the case $X_j^{n+1}=0$ the percentage vector $\boldsymbol{p}_j^{n+1}$ is irrelevant and one can define $\boldsymbol{p}_j^{n+1} \coloneqq \boldsymbol{p}_j^n$. Then Equation (4.57) should be modified in the following way. Row j is removed in $\boldsymbol{p}^{n+1}$, $\boldsymbol{p}^n$ and $\boldsymbol{W}^n$, and both row j and column j should be removed in the matrices $\boldsymbol{M}(\boldsymbol{\Phi}^{n,n+1},\boldsymbol{X}^{n+1})$, $\operatorname{diag}(\boldsymbol{\kappa}^n)$ and $\operatorname{diag}(\boldsymbol{X}^n)$. Then, one verifies that $\boldsymbol{M}(\boldsymbol{\Phi}^{n,n+1},\boldsymbol{X}^{n+1})$ is strictly diagonally dominant by columns, and therefore invertible without any restrictions. Thus, the implicit scheme (4.57) is well defined. Furthermore, $\boldsymbol{M}(\boldsymbol{\Phi}^{n,n+1},\boldsymbol{X}^{n+1})^{\mathrm{T}}$ is an M-matrix and hence has a non-negative inverse.

4.4.4 Monotonicity and invariant region property

Lemma 4.11. *If $\boldsymbol{\mathcal{U}}_j^n \in \Omega$ for all j and (CFL-SI) holds, then*

$$p_j^{(k),n+1} \geq 0 \quad \text{for all } k=1,\dots,k_{\boldsymbol{C}} \text{ and all } j.$$

Proof. Since $(\boldsymbol{M}(\boldsymbol{\Phi}^{n,n+1},\boldsymbol{X}^{n+1}))^{-1} \geq \boldsymbol{0}$, we estimate each entry of $\boldsymbol{\Theta}^n =: (\Theta^n_{jk})$. By Lemma 4.2,

$$\begin{aligned}
\Theta^n_{0,k} &= \kappa^n X_0^n p_0^{(k),n} + \lambda\beta^n q_{\mathrm{f}}^n \boldsymbol{p}_{\mathrm{f}}^n X_{\mathrm{f}}^n + c\frac{\tau}{2} R^{(k)}_{\boldsymbol{C}}(\boldsymbol{p}_0^n X_0^n/c, \boldsymbol{S}_0^n) \\
&\geq (1-\tau\zeta M_{q1})\, X_0^n p_0^{(k),n} + 0 + c\frac{\tau}{2}\sum_{l\in I^-_{\boldsymbol{C},k}} \sigma^{(k,l)}_{\boldsymbol{C}}\bar{r}^{(l)}\big(\boldsymbol{p}_0^n X_0^n/c, \boldsymbol{S}_0^n\big) p_0^{(k),n} X_0^n/c \\
&\geq (1-\tau\zeta M_{q1} - \tau M_{\boldsymbol{C}}/2)\, p_0^{(k),n} X_0^n \geq 0,
\end{aligned}$$

whereas for all the other $j \neq 0$,

$$\Theta^n_{j,k} = \kappa^n X_j^n p_j^{(k),n} + c\tau R^{(k)}_{\boldsymbol{C}}(\boldsymbol{p}_j^n X_j^n/c, \boldsymbol{S}_j^n) \geq (1-\tau\zeta M_{q1} - \tau M_{\boldsymbol{C}})\, p_j^{(k),n} X_j^n \geq 0.$$

□

Lemma 4.12. *If $\boldsymbol{\mathcal{U}}_j^n \in \Omega$ for all j and (CFL-SI) holds, then*

$$p_j^{(1),n+1} + \cdots + p_j^{(k_{\boldsymbol{C}}),n+1} = 1 \quad \text{for all } j. \tag{4.58}$$

Proof. If $X_j^{n+1} = 0$, then by definition,

$$p_j^{(1),n+1} + \cdots + p_j^{(k_C),n+1} = p_j^{(1),n} + \cdots + p_j^{(k_C),n} = 1,$$

so let us assume that $X_j^{n+1} > 0$. We sum up all equations in (4.56) and use the notation

$$\mathcal{P}_j^{n+1} \coloneqq p_j^{(1),n+1} + \cdots + p_j^{(k_C),n+1}$$

to obtain

$$\begin{aligned} X_j^{n+1}\mathcal{P}_j^{n+1} = \kappa_j^n X_j^n \\ - \lambda\big(\Phi_{j+1/2}^{n,n+1,+}\mathcal{P}_j^{(k),n+1} + \Phi_{j+1/2}^{n,n+1,-}\mathcal{P}_{j+1}^{(k),n+1} - \Phi_{j-1/2}^{n,n+1,+}\mathcal{P}_{j-1}^{(k),n+1} - \Phi_{j-1/2}^{n,n+1,-}\mathcal{P}_j^{(k),n+1}\big) \\ + \lambda\delta_{j,0}\beta^n q_{\mathrm{f}}^n X_{\mathrm{f}}^n + \tau\gamma_j R(\boldsymbol{p}_j^n X_j^n/c, \boldsymbol{S}_j^n). \end{aligned}$$

We subtract component j of Equation (4.44), let $y_j^{n+1} \coloneqq \mathcal{P}_j^{n+1} - 1$ and obtain

$$X_j^{n+1} y_{j+1}^{n+1} = -\lambda\big(\Phi_{j+1/2}^{n,n+1,+} y_j^{n+1} + \Phi_{j+1/2}^{n,n+1,-} y_{j+1}^{n+1} - \Phi_{j-1/2}^{n,n+1,+} y_{j-1}^{n+1} - \Phi_{j-1/2}^{n,n+1,-} y_j^{n+1}\big).$$

Thus, with $\boldsymbol{y}_{j+1}^{n+1} \coloneqq (y_0^{n+1}, \ldots, y_N^{n+1})^{\mathrm{T}}$, we get $\boldsymbol{M}^{n,n+1}\boldsymbol{y}_{j+1}^{n+1} = \boldsymbol{0}$, which implies $\boldsymbol{y}_{j+1}^{n+1} = \boldsymbol{0}$, i.e. we obtain (4.58). □

For Equation (4.15) we have

$$\begin{aligned} \boldsymbol{S}_j^{n+1} = \kappa_j^n \boldsymbol{S}_j^n - \lambda\Bigg(\frac{(\rho_X\tilde{q}^n - \mathcal{F}^n + \mathcal{J}^{n+1})_{j+1/2}^+}{\rho_X - X_j^{n+1}}\boldsymbol{S}_j^{n+1} + \frac{(\rho_X\tilde{q}^n - \mathcal{F}^n + \mathcal{J}^{n+1})_{j+1/2}^-}{\rho_X - X_{j+1}^{n+1}}\boldsymbol{S}_{j+1}^{n+1} \\ - \frac{(\rho_X\tilde{q}^n - \mathcal{F}^n + \mathcal{J}^{n+1})_{j-1/2}^+}{\rho_X - X_{j-1}^{n+1}}\boldsymbol{S}_{j-1}^{n+1} - \frac{(\rho_X\tilde{q}^n - \mathcal{F}^n + \mathcal{J}^{n+1})_{j-1/2}^-}{\rho_X - X_j^{n+1}}\boldsymbol{S}_j^{n+1} \Bigg) \\ + \lambda\delta_{j,0}\beta^n q_{\mathrm{f}}^n \boldsymbol{S}_{\mathrm{f}}^n + \tau\gamma_j \boldsymbol{R}_{\boldsymbol{S}}(\boldsymbol{p}_j^n X_j^n/c, \boldsymbol{S}_j^n). \end{aligned}$$

For $j = -1, N+1$, this scheme is explicit and analogous to those above. For $j = 0, \ldots, N$, we write the formula in matrix form as follows. Define

$$\theta_{j+1/2}^{n,n+1} \coloneqq (\rho_X\tilde{q}^n - \mathcal{F}^n + \mathcal{J}^{n+1})_{j+1/2}, \qquad y_j^n \coloneqq \frac{1}{\rho_X - X_j^n},$$

$$\boldsymbol{\mathcal{S}}^n \coloneqq \begin{bmatrix} (\boldsymbol{S}_0^n)^{\mathrm{T}} \\ (\boldsymbol{S}_1^n)^{\mathrm{T}} \\ \vdots \\ (\boldsymbol{S}_N^n)^{\mathrm{T}} \end{bmatrix}, \qquad \boldsymbol{\mathcal{W}}^n \coloneqq \begin{bmatrix} (\lambda\beta^n q_{\mathrm{f}}^n \boldsymbol{S}_{\mathrm{f}}^n + \frac{\tau}{2}\boldsymbol{R}_{\boldsymbol{S}}(\boldsymbol{p}_0^n X_0^n/c, \boldsymbol{S}_0^n))^{\mathrm{T}} \\ \tau\boldsymbol{R}_{\boldsymbol{S}}(\boldsymbol{p}_1^n X_1^n/c, \boldsymbol{S}_1^n)^{\mathrm{T}} \\ \vdots \\ \tau\boldsymbol{R}_{\boldsymbol{S}}(\boldsymbol{p}_N^n X_N^n/c, \boldsymbol{S}_N^n)^{\mathrm{T}} \end{bmatrix}.$$

Since $\tilde{q}_{-1/2}^n \le 0$ and $\tilde{q}_{N+1/2}^n \ge 0$, we have

$$\theta_{-1/2}^{n,n+1,+} = \rho_X\tilde{q}_{-1/2}^{n+1,+} = 0, \quad \theta_{N+1/2}^{n,n+1,-} = \rho_X\tilde{q}_{N+1/2}^{n+1,-} = 0.$$

Then we form the tridiagonal matrix

$$\boldsymbol{M}_{\boldsymbol{S}}(\boldsymbol{\theta},\boldsymbol{y}) \coloneqq \boldsymbol{I}_{N+1} + \lambda \begin{bmatrix} (\theta^+_{1/2}-\theta^-_{-1/2})y_0 & \theta^-_{1/2}y_1 & 0 & \cdots & 0 \\ -\theta^+_{1/2}y_0 & (\theta^+_{3/2}-\theta^-_{1/2})y_1 & \ddots & \ddots & \vdots \\ 0 & -\theta^+_{3/2}y_1 & \ddots & \ddots & 0 \\ \vdots & \ddots & \ddots & (\theta^+_{N-1/2}-\theta^-_{N-3/2})y_{N-1} & \theta^-_{N-1/2}y_N \\ 0 & \cdots & 0 & -\theta^+_{N-1/2}y_{N-1} & (\theta^+_{N+1/2}-\theta^-_{N-1/2})y_N \end{bmatrix}.$$

Then we get the linear system

$$\boldsymbol{M}_{\boldsymbol{S}}(\boldsymbol{\theta}^{n,n+1},\boldsymbol{y}^{n+1})\boldsymbol{\mathcal{S}}^{n+1} = \operatorname{diag}(\boldsymbol{\kappa}^n)\boldsymbol{\mathcal{S}}^n + \boldsymbol{\mathcal{W}}^n. \tag{4.59}$$

The matrix $\boldsymbol{M}_{\boldsymbol{S}}(\boldsymbol{\theta}^{n,n+1},\boldsymbol{y}^{n+1})$ is diagonally dominant by columns; hence its transpose is an M-matrix and invertible with a non-negative inverse, so that (4.59) defines $\boldsymbol{\mathcal{S}}^{n+1}$.

Lemma 4.13. *If $\boldsymbol{\mathcal{U}}^n_j \in \Omega$ for all j and (CFL-SI) holds, then*

$$S^{(k),n+1}_j \geq 0 \quad \text{for all } k = 1,\dots,k_{\boldsymbol{S}} \text{ and all } j.$$

Proof. This is similar to the proof of Lemma 4.11. The element (j,k), $j \neq 0$, of the matrix on the right-hand side of (4.59) is estimated by

$$\kappa^n S^{(k),n}_j + \tau R^{(k)}_{\boldsymbol{S}}(\boldsymbol{p}^n_j X^n_j/c, \boldsymbol{S}^n_j) \geq (1 - \tau\zeta M_{q1} - \tau M_{\boldsymbol{S}})\, S^{(k),n}_j \geq 0.$$

□

4.5 A modified ASM1 model

The ASM1 model is described in, for example, [63]. For the reason of reformulating the PDE model to include percentages of the particulate concentrations, we have redefined the second component from X_{S} to $X_{\mathrm{S-ND}} \coloneqq X_{\mathrm{S}} - X_{\mathrm{ND}}$. Then the variables are

$$\boldsymbol{C} = \left(X_{\mathrm{I}}, X_{\mathrm{S-ND}}, X_{\mathrm{B,H}}, X_{\mathrm{B,A}}, X_{\mathrm{P}}, X_{\mathrm{ND}}\right)^{\mathrm{T}}, \quad \boldsymbol{S} = \left(S_{\mathrm{I}}, S_{\mathrm{S}}, S_{\mathrm{O}}, S_{\mathrm{NO}}, S_{\mathrm{NH}}, S_{\mathrm{ND}}\right)^{\mathrm{T}},$$

with units given in Table 2.1. The stoichiometric matrix $\boldsymbol{\sigma}_{\boldsymbol{S}}$ for the solid components and the vector $\boldsymbol{r}(\boldsymbol{C},\boldsymbol{S})$, which contain the processes of biokinetic reactions for carbon and nitrogen removal, are the same as those given in Section 2.3 of Chapter 2. The stoichiometric matrix $\boldsymbol{\sigma}_{\boldsymbol{C}}$ for the substrates is denoted as

$$\boldsymbol{\sigma}_{\boldsymbol{C}} \coloneqq \begin{bmatrix} 0 & 0 & 0 & 0 & 0 & 0 & 0 & 0 \\ 0 & 0 & 0 & 1-f_{\mathrm{P}}(1+i_{\mathrm{XP}})-i_{\mathrm{XB}} & 1-f_{\mathrm{P}}(1+i_{\mathrm{XP}})-i_{\mathrm{XB}} & 0 & -1 & 1 \\ 1 & 1 & 0 & -1 & 0 & 0 & 0 & 0 \\ 0 & 0 & 1 & 0 & -1 & 0 & 0 & 0 \\ 0 & 0 & 0 & f_{\mathrm{P}} & f_{\mathrm{P}} & 0 & 0 & 0 \\ 0 & 0 & 0 & i_{\mathrm{XB}}-f_{\mathrm{P}}i_{\mathrm{XP}} & i_{\mathrm{XB}}-f_{\mathrm{P}}i_{\mathrm{XP}} & 0 & 0 & -1 \end{bmatrix}$$

with the constants given in Table 4.1.

Table 4.1: Stoichiometric and kinetic parameters.

Symbol	Name	Value	Unit
Y_A	Yield for autotrophic biomass	0.24	$(g\,COD)(g\,N)^{-1}$
Y_H	Yield for heterotrophic biomass	0.67	$(g\,COD)(g\,COD)^{-1}$
f_P	Fraction of biomass leading to particulate products	0.08	dimensionless
i_{XB}	Mass of nitrogen per mass of COD in biomass	0.086	$(g\,N)(g\,COD)^{-1}$
i_{XP}	Mass of nitrogen per mass of COD in products from biomass	0.06	$(g\,N)(g\,COD)^{-1}$
μ_H	Maximum specific growth rate for heterotrophic biomass	6.0	d^{-1}
K_S	Half-saturation coefficient for heterotrophic biomass	20.0	$(g\,COD)\,m^{-3}$
$K_{O,H}$	Oxygen half-saturation coefficient for heterotrophic biomass	0.2	$-(g\,COD)\,m^{-3}$
K_{NO}	Nitrate half-saturation coefficient for denitrifying heterotrophic biomass	0.5	$(g\,NO_3\text{-}N)\,m^{-3}$
b_H	Decay coefficient for heterotrophic biomass	0.62	d^{-1}
η_g	Correction factor for μ_H under anoxic conditions	0.8	dimensionless
η_h	Correction factor for hydrolysis under anoxic conditions	0.4	dimensionless
k_h	Maximum specific hydrolysis rate	3.0	$(g\,COD)\,(g\,COD)^{-1}d^{-1}$
K_X	Half-saturation coefficient for hydrolysis of slowly biodegradable substrate	0.03	$(g\,COD)(g\,COD)^{-1}$
μ_A	Maximum specific growth rate for autotrophic biomass	0.8	d^{-1}
$\bar{K}_{NH}$	Ammonia half-saturation coefficient for aerobic and anaerobic growth of heterotrophs	0.05	$(g\,NH_3\text{-}N)\,m^{-3}$
K_{NH}	Ammonia half-saturation coefficient for autotrophic biomass	1.0	$(g\,NH_3\text{-}N)\,m^{-3}$
b_A	Decay coefficient for autotrophic biomass	0.15	d^{-1}
$K_{O,A}$	Oxygen half-saturation coefficient for autotrophic biomass	0.4	$-(g\,COD)\,m^{-3}$
k_a	Ammonification rate	0.08	$m^3(g\,COD)^{-1}d^{-1}$

4.6 Numerical simulations

For all the examples, we consider a cylindrical SBR of depth $B = 3\,\mathrm{m}$ and cross-sectional area $A = 400\,\mathrm{m}^2$, and the reactive settling process of an activated sludge described by the ASM1 model [63]; see Table 2.1. The constitutive functions used in the examples are

$$v_{\mathrm{hs}}(X) := \frac{v_0}{1 + (X/\breve{X})^\eta}, \quad \sigma_{\mathrm{e}}(X) := \begin{cases} 0 & \text{if } X < X_{\mathrm{c}}, \\ \sigma_0(X - X_{\mathrm{c}}) & \text{if } X \geq X_{\mathrm{c}} \end{cases}$$

with $v_0 = 1.76 \times 10^{-3}\,\mathrm{m/s}$, $\breve{X} = 3.87\,\mathrm{kg/m^3}$, $\eta = 3.58$, $X_{\mathrm{c}} = 5\,\mathrm{kg/m^3}$ and $\sigma_0 = 0.2\,\mathrm{m^2/s^2}$. Other parameters are $\rho_X = 1050\,\mathrm{kg/m^3}$, $\rho_L = 998\,\mathrm{kg/m^3}$, $g = 9.81\,\mathrm{m/s^2}$, and $B_{\mathrm{c}} = 2\,\mathrm{m}$. To satisfy (1.25), one could multiply $v_{\mathrm{hs}}(X)$ by a function that is one for most concentrations but tends to zero smoothly as $X \to \hat{X}^-$, where the maximum concentration $\hat{X}$ is set to a large number; e.g. $\hat{X} = 30\ \mathrm{kg/m^3}$ for activated sludge that we simulate here. When $\sigma_0 > 0$, the second-order derivative compression term will balance the convective flux and the particulate concentration X never reaches $\hat{X}$ in simulations. To run the scheme with $\sigma_0 = 0$, an alternative is to set a concentration X^{t} from which we redefine and extend the settling velocity function by its tangent as

$$v_{\mathrm{hs}}(X) := \begin{cases} \dfrac{v_0}{1 + (X/\breve{X})^\eta} & \text{if } 0 \leq X \leq X^{\mathrm{t}}, \\ v_{\mathrm{hs}}(X^{\mathrm{t}}) + v'_{\mathrm{hs}}(X^{\mathrm{t}})(X - X^{\mathrm{t}}) & \text{if } X^{\mathrm{t}} < X \leq \hat{X}, \end{cases}$$

where $\hat{X}$ is given by the intersection of the tangent with the X-axis (zero velocity), i.e.,

$$\hat{X} := X^{\mathrm{t}} - \frac{v_{\mathrm{hs}}(X^{\mathrm{t}})}{v'_{\mathrm{hs}}(X^{\mathrm{t}})}.$$

We here utilize $X^{\mathrm{t}} = 25\,\mathrm{kg/m^3}$, such that $\hat{X} = 31.992\,\mathrm{kg/m^3}$.

The initial concentrations have been chosen as

$$\boldsymbol{C}^0(z) = \begin{cases} \boldsymbol{0} & \text{if } z < 2.0\,\mathrm{m}, \\ (0.8889, 0.0295, 1.4503, 0.0904, 0.7371, 0.0025)^{\mathrm{T}} & \text{if } z \geq 2.0\,\mathrm{m}, \end{cases}$$

$$\boldsymbol{S}^0(z) = \begin{cases} \boldsymbol{0} & \text{if } z < 2.0\,\mathrm{m}, \\ (0.04, 0.0026, 0.0, 0.0333, 0.0004, 0.0009)^{\mathrm{T}} & \text{if } z \geq 2.0\,\mathrm{m} \end{cases}$$

(with units as in Table 2.1) while the feed concentrations are [63]

$$\boldsymbol{C}_{\mathrm{f}}(t) = \frac{X_{\mathrm{f}}(t)}{(0.04 + 0.16 + 0.096 + 1 \cdot 10^{-6})c}(0.04,\ 0.16 - 0.01828,\ 0.096,\ 1 \cdot 10^{-6},\ 0,\ 0.01828)^{\mathrm{T}},$$

$$\boldsymbol{S}_{\mathrm{f}}(t) = (0.04,\ 0.064,\ 0.0,\ 0.001,\ 0.0125,\ 0.0101)^{\mathrm{T}},$$

where the total solids feed concentration $X_{\mathrm{f}}(t)$ is given by Table 4.2. When plotting the particulate concentrations, we prefer to plot $X_{\mathrm{S}} = C^{(2)} + X_{\mathrm{ND}} = C^{(2)} + C^{(6)}$ and $X_{\mathrm{ND}} = C^{(6)}$ rather than $C^{(2)} = X_{\mathrm{S-ND}}$. All results are shown after transforming back to the original coordinates.

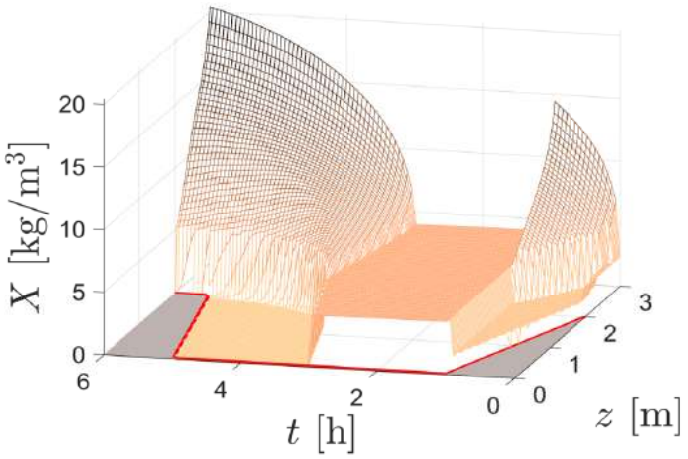

Figure 4.4: Example 4.1: Simulated concentration (semi-implicit scheme, $N = 100$) of total suspended solids.

4.6.1 Example 4.1

It is the purpose of this example to illustrate the SBR model as a whole. (The performance of the three numerical schemes SBR2 in [16], and the explicit and semi-implicit ones here in terms of errors and efficiency is studied in Examples 4.2 and 4.3.) We simulated the five stages of an SBR as outlined in Table 4.2. The duration of the whole cycle of stages during a couple of hours is realistic. The results are illustrated in Figures 4.4 to 4.7, which depict the concentration profiles of total suspended solids, particulate, and soluble components within the reactor vessel, respectively.

Table 4.2: Example 4.1: Time functions for the simulation.

Stage	Time period [h]	$X_{\mathrm{f}}(t)$[kg/m^3]	$Q_{\mathrm{f}}(t)$[m^3/h]	$Q_{\mathrm{u}}(t)$[m^3/h]	$Q_{\mathrm{e}}(t)$[m^3/h]	Model
Fill	$0 \le t < 1$	5	790	0	0	PDE
React	$1 \le t < 3$	0	0	0	0	ODE
Settle	$3 \le t < 5$	0	0	0	0	PDE
Draw	$5 \le t < 5.5$	0	0	0	1570	PDE
Idle	$5.5 \le t < 6$	0	0	10	0	PDE

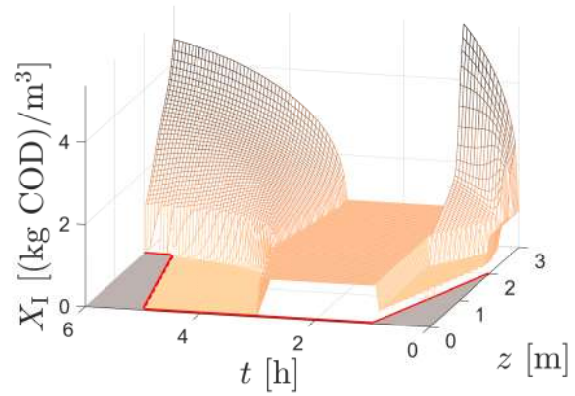

(a) Particulate inert organic matter

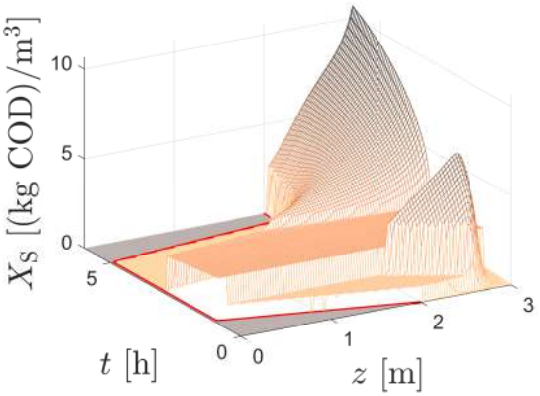

(b) Slowly biodegradable substrate

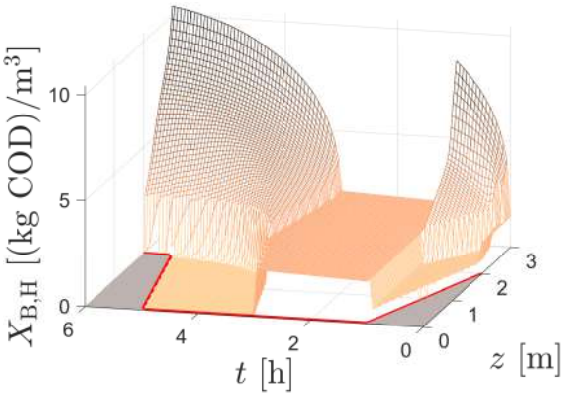

(c) Active heterotrophic biomass

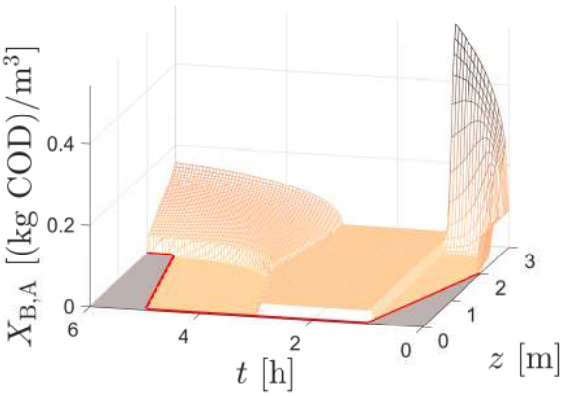

(d) Active autotrophic biomass

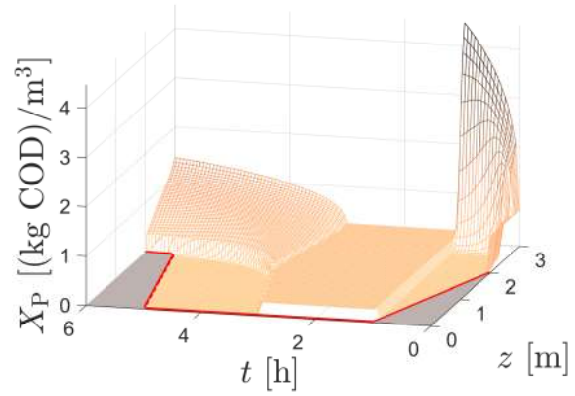

(e) Particle products from biomass decay

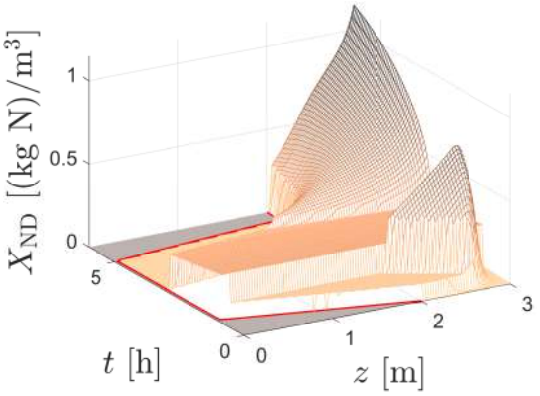

(f) Particulate biodegradable organic nitrogen

Figure 4.5: Example 4.1: Simulated concentrations of solid components (semi-implicit scheme, $N = 100$).

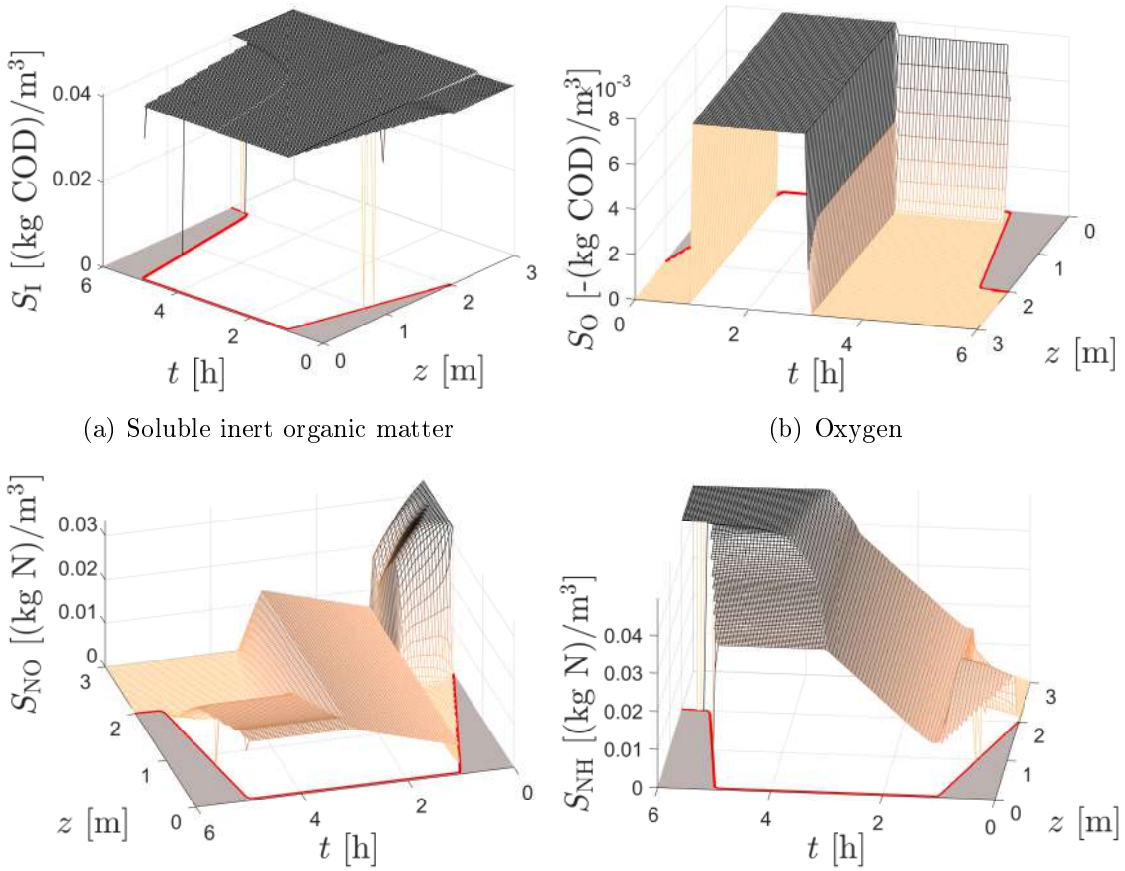

(a) Soluble inert organic matter

(b) Oxygen

(c) Nitrate and nitrite nitrogen

(d) $NH4_4^+ + NH_3$ nitrogen

Figure 4.6: Example 4.1: Simulated densities (semi-implicit scheme, $N = 100$) of soluble components (part 1).

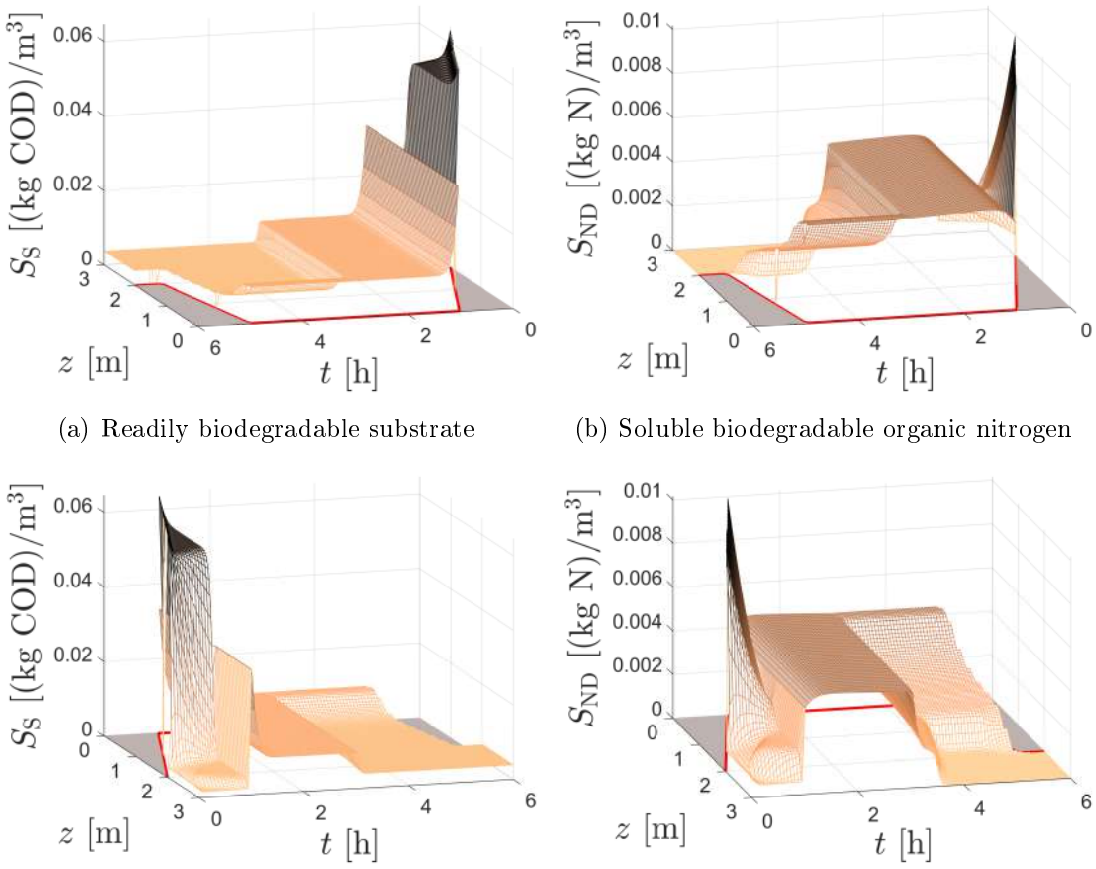

(a) Readily biodegradable substrate

(b) Soluble biodegradable organic nitrogen

(c) Readily biodegradable substrate

(d) Soluble biodegradable organic nitrogen

Figure 4.7: Example 4.1: Simulated densities (semi-implicit scheme, $N = 100$) of soluble components (part 2).

4.6.2 Example 4.2

The prime motivation of this example is to study the numerical errors of the two new schemes defined for the PDE model and the scheme SBR2 of [16]. To this end we consider the scenario defined by Table 4.3, which refers to a shorter period of total simulated time ($T = 1\,\mathrm{h}$) and does not include a react stage (for which the original SBR model, as studied in Example 4.1, stipulates a model by a system of ODEs). We calculated a reference solution, using the same feed conditions as in Example 1 with $N = N_{\mathrm{ref}} := 4800$. This solution was obtained by the explicit scheme of Section 4.3.2. The relative approximate numerical error

$$e_N^{\mathrm{rel}}(t) := \sum_{k=1}^{k_C} \frac{\|C_N^{(k)} - C_{N_{\mathrm{ref}}}^{(k)}(\cdot,t)\|_{L^1(0,B)}}{\|C_{N_{\mathrm{ref}}}^{(k)}(\cdot,t)\|_{L^1(0,B)}} + \sum_{k=1}^{k_S} \frac{\|S_N^{(k)} - S_{N_{\mathrm{ref}}}^{(k)}(\cdot,t)\|_{L^1(0,B)}}{\|S_{N_{\mathrm{ref}}}^{(k)}(\cdot,t)\|_{L^1(0,B)}}.$$

compares the approximate solution to the reference solution at a given time point t for a specific number of cells N.

Table 4.3: Example 4.2: Time functions for the simulation of the reference solution.

Time period [h]	$X_\mathrm{f}(t)[\mathrm{kg/m^3}]$	$Q_\mathrm{f}(t)[\mathrm{m^3/h}]$	$Q_\mathrm{u}(t)[\mathrm{m^3/h}]$	$Q_\mathrm{e}(t)[\mathrm{m^3/h}]$	Model
$0 \leq t < 0.3$	5	2660	0	0	PDE
$0.3 \leq t < 0.85$	0	0	0	0	PDE
$0.85 \leq t < 0.95$	0	0	0	6000	PDE
$0.95 \leq t < 1$	0	0	100	0	PDE

In Figures 4.8 and 4.9, we demonstrate the convergence of the numerical solutions, all produced with the semi-implicit scheme and a tolerance $\varepsilon = 10^{-8}$, to the reference solution. That value was chosen by previous experience. The effect of the tolerance parameter ε itself is studied in Table 4.4 for simulations done with $N = 50$, 100, and 200, in terms of the average number of iterations during the simulation, the relative error, and CPU time. It turns out that the relative error depends only marginally on the choice of ε. As one should expect, the average number of iterations (of the Newton-Raphson scheme, per time step), as well as the CPU time for the whole simulation, consistently increase with decreasing ε. Overall, it appears that the relative error and CPU time, and therefore efficiency, does not depend critically on ε (at least for the model functions and parameters chosen here).

For the same configuration, we compare in Table 4.5 and Figure 4.10 the relative errors and CPU times obtained by the three schemes SBR2 of [16], and the explicit and semi-implicit schemes of Sections 4.3 and 4.4, respectively. For both explicit and semi-implicit schemes, simulations were performed for $N = 25, \ldots, 1600$ using the Engquist-Osher flux (4.18). The semi-implicit scheme was calculated with the tolerance $\varepsilon = 10^{-8}$. It turns out that with the exception of very coarse discretizations, the semi-implicit scheme is significantly more efficient in error reduction per CPU time than its explicit counterpart due to its more favorable CFL condition, and is more efficient also than SBR2 for sufficiently fine discretizations. It is noteworthy that all schemes converge to the same solution.

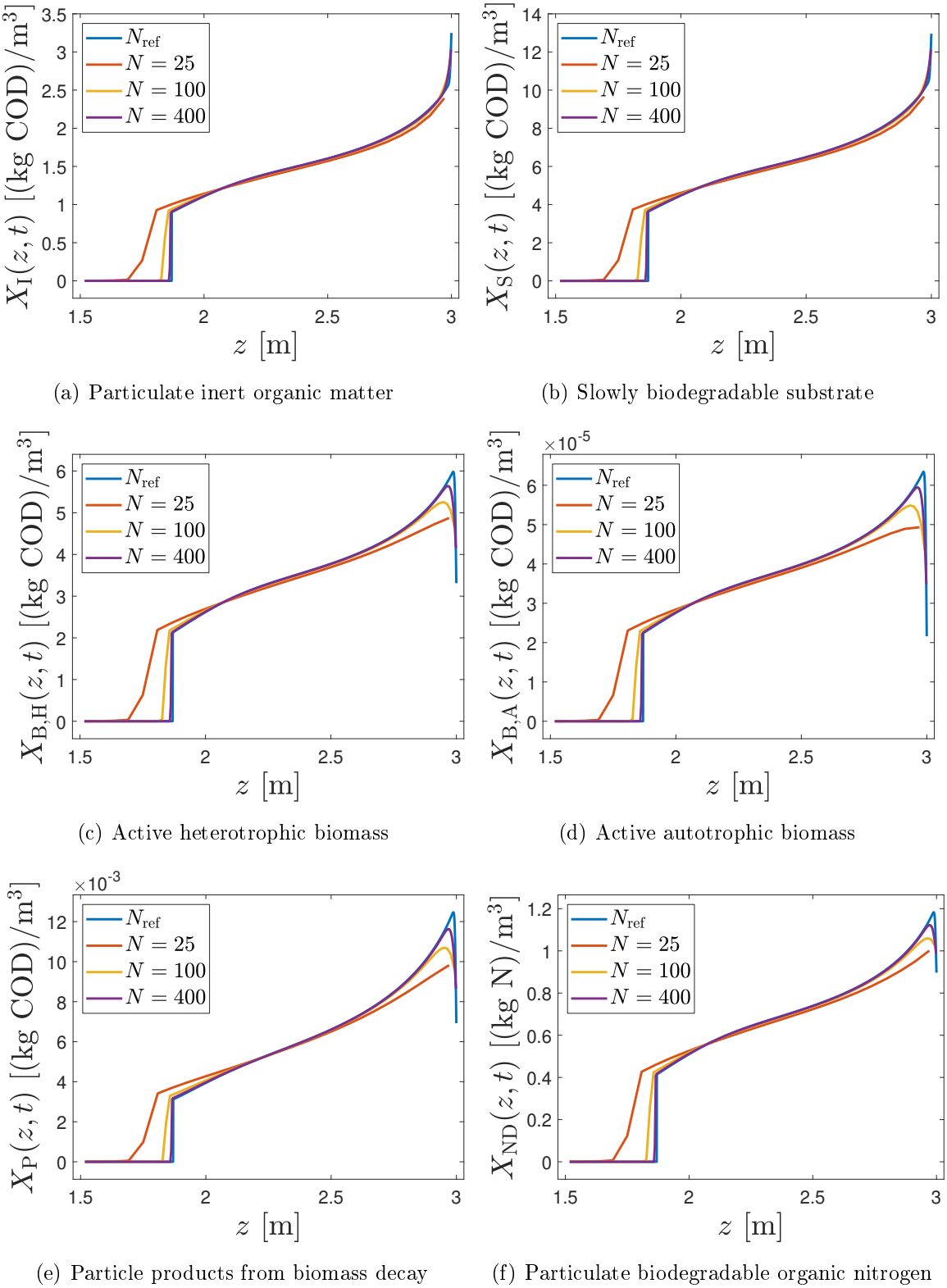

(a) Particulate inert organic matter

(b) Slowly biodegradable substrate

(c) Active heterotrophic biomass

(d) Active autotrophic biomass

(e) Particle products from biomass decay

(f) Particulate biodegradable organic nitrogen

Figure 4.8: Example 4.2: Simulated concentrations (semi-implicit scheme) at $T = 1\,\text{h}$ of soluble components.

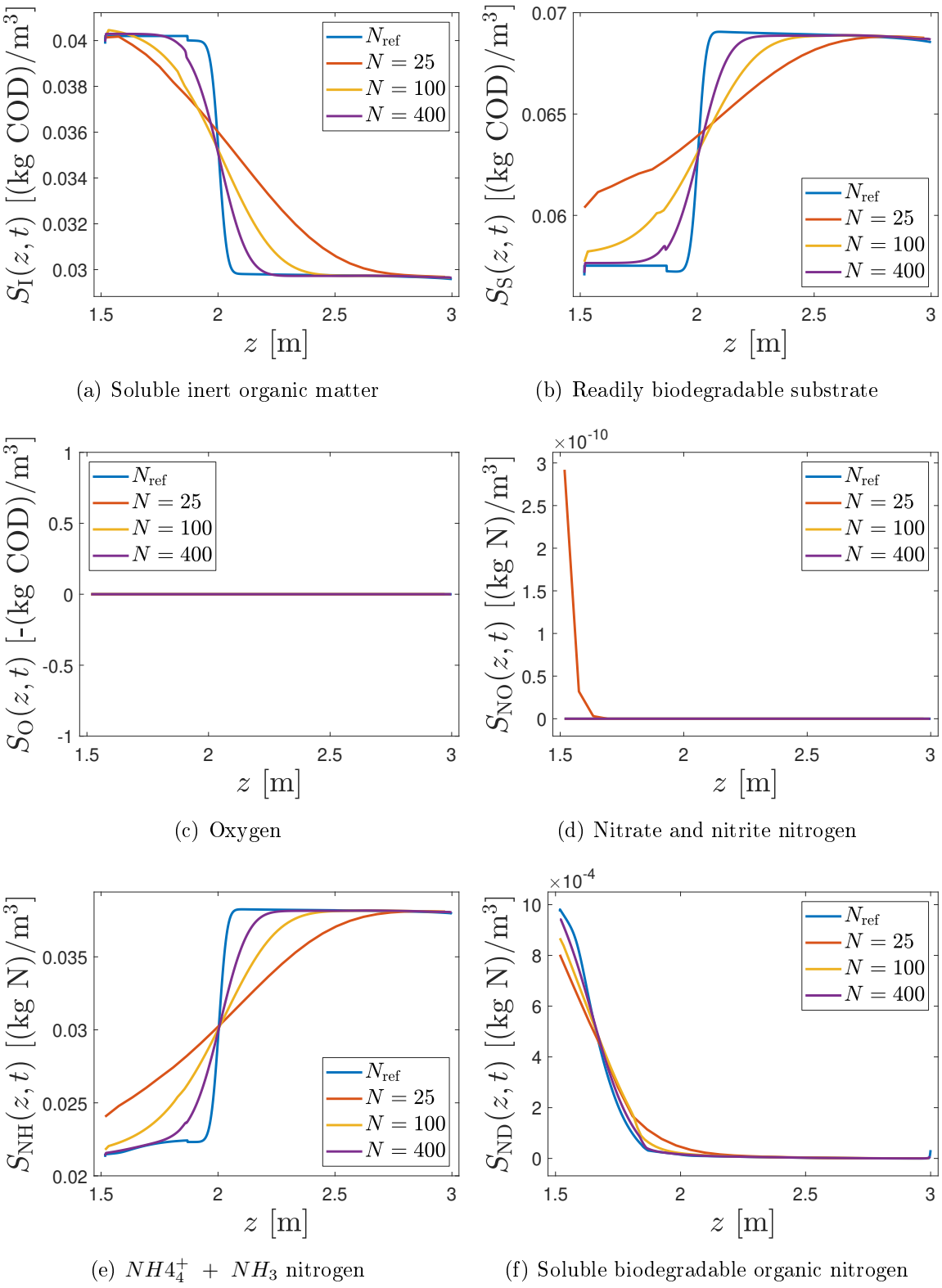

(a) Soluble inert organic matter

(b) Readily biodegradable substrate

(c) Oxygen

(d) Nitrate and nitrite nitrogen

(e) $NH4_4^+ + NH_3$ nitrogen

(f) Soluble biodegradable organic nitrogen

Figure 4.9: Example 4.2: Simulated concentrations (semi-implicit scheme) at $T = 1\,\mathrm{h}$ of soluble components.

Table 4.4: Example 4.2: Effect of the tolerance ε on the average number of iterations in the Newton-Raphson method, the errors e_N^{rel} and CPU times during a simulation of $T = 1\,\text{h}$. The errors are computed with the reference solution obtained by the explicit scheme with $N = 4800$ and the Godunov numerical flux.

	ε	Avg. iterations	$e_N^{\text{rel}}(t)$	CPU [s]
$N = 50$	1E-1	1.00	0.0497756500328602	0.1250
	1E-2	1.03	0.0497756500328602	0.1406
	1E-3	1.60	0.0497679356628912	0.1797
	1E-4	2.00	0.0497674399512266	0.1953
	1E-5	2.01	0.0497674389897926	0.1875
	1E-6	2.04	0.0497674143163951	0.1797
	1E-7	2.12	0.0497674123749513	0.1953
	1E-8	2.77	0.0497674121051164	0.2109
	1E-9	2.92	0.0497674120899535	0.2344
	1E-10	2.96	0.0497674120878119	0.2188
	1E-11	3.07	0.0497674120875128	0.2422
	1E-12	3.69	0.0497674120874927	0.2560
$N = 100$	1E-1	1.00	0.0244467141865713	0.3984
	1E-2	1.01	0.0244467141865713	0.4062
	1E-3	1.21	0.0244432794902836	0.4453
	1E-4	2.00	0.0244427209345141	0.6719
	1E-5	2.01	0.0244427236620445	0.5938
	1E-6	2.02	0.0244427043886650	0.6172
	1E-7	2.06	0.0244427032349412	0.6250
	1E-8	2.17	0.0244427031258883	0.7188
	1E-9	2.87	0.0244427030983648	0.7656
	1E-10	2.97	0.0244427030958998	0.7812
	1E-11	3.01	0.0244427030956931	0.7734
	1E-12	3.11	0.0244427030956539	0.8672
$N = 200$	1E-1	1.00	0.0115032639159754	1.4609
	1E-2	1.00	0.0115032639159754	1.4766
	1E-3	1.07	0.0115029463554388	1.6406
	1E-4	1.86	0.0115009448742330	2.0234
	1E-5	2.01	0.0115008746422637	2.2578
	1E-6	2.02	0.0115008746587289	2.2188
	1E-7	2.03	0.0115008741995477	2.1250
	1E-8	2.08	0.0115008740687287	2.2656
	1E-9	2.24	0.0115008740547202	2.3281
	1E-10	2.91	0.0115008740528361	2.7812
	1E-11	3.00	0.0115008740526303	2.7812
	1E-12	3.03	0.0115008740526086	2.9609

Table 4.5: Example 4.2: Errors e_N^{rel} and CPU times at simulated time $T = 1\,\text{h}$. The errors have been computed with the reference solution obtained by explicit scheme with $N = 4800$ and the Godunov numerical flux. The abbreviation SBR2 refers to the scheme in [16] (without variable transformation).

		SBR2		Explicit		Semi-implicit	
	N	$e_N^{\text{rel}}(t)$	CPU [s]	$e_N^{\text{rel}}(t)$	CPU [s]	$e_N^{\text{rel}}(t)$	CPU [s]
	25	1.6483	0.0391	1.2053	0.0391	1.2099	0.0469
	50	0.9230	0.0703	0.7688	0.1035	0.7732	0.0938
	100	0.4704	0.2090	0.4368	0.3340	0.4414	0.2070
$T = 0.4\,\text{h}$	200	0.2551	0.7969	0.2384	1.7969	0.2416	0.5508
	400	0.1352	5.2441	0.1261	11.9395	0.1286	2.0234
	800	0.0743	40.9023	0.0645	89.9941	0.0665	7.4453
	1600	0.0409	316.4102	0.0379	717.4668	0.0397	27.5156
	25	1.5691	0.0900	1.2901	0.0920	1.2959	0.0880
	50	0.8327	0.1320	0.7835	0.1590	0.7880	0.1360
	100	0.4204	0.3240	0.4392	0.4590	0.4451	0.3190
$T = 0.75\,\text{h}$	200	0.2125	1.4766	0.2304	3.1797	0.2345	1.0234
	400	0.1103	9.5469	0.1218	20.7266	0.1250	3.6797
	800	0.0595	79.1719	0.0620	175.6562	0.0644	14.2188
	1600	0.0327	646.8438	0.0371	1421.2190	0.0392	55.6470
	25	1.1617	0.0469	1.0747	0.0508	1.0573	0.0566
	50	0.6580	0.0957	0.6966	0.1191	0.7078	0.1289
	100	0.3760	0.3555	0.4519	0.6797	0.4627	0.3984
$T = 1\,\text{h}$	200	0.1877	1.9004	0.2821	4.0605	0.2919	1.3066
	400	0.1075	12.4375	0.1658	27.0586	0.1737	4.8535
	800	0.0644	104.6543	0.0896	237.3340	0.0966	18.8379
	1600	0.0418	822.3809	0.0439	2362.8570	0.0495	75.5801

4.6.3 Example 4.3

We investigate the impact of a moving mesh with three different spatial grids, compared to a fixed grid; see Figure 4.11. The simulation conditions are given in Table 4.6. The semi-implicit scheme is used with the Engquist-Osher flux and $\varepsilon = 10^{-8}$. The data in Table 4.6, which contemplate no solids feed or discharge but a moving boundary, have been chosen in such a way that the solution converges quickly in time to a stationary one with a layer of sediment at the bottom produced by the settling of the initially homogeneous suspension that is not affected by the moving boundary. Figures 4.11 (a), (c) and (e) show that the numerical solution of the SBR2 scheme reproduces this property at any of the chosen discretizations $N = 100$, $N = 200$ or $N = 400$ while the solution produced by the semi-implicit scheme is not stationary due to

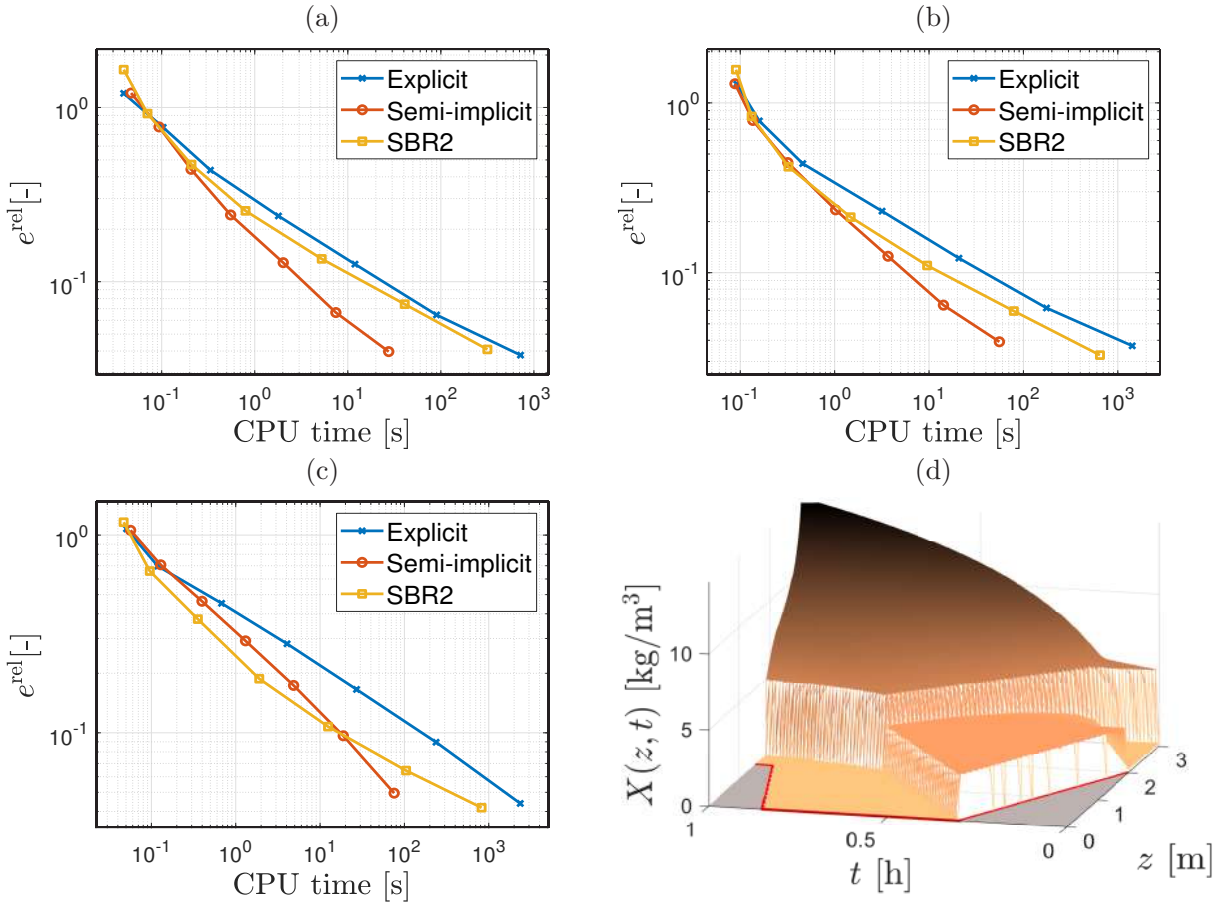

Figure 4.10: Example 4.2: error versus CPU time for various values of N (Table 4.5) at simula times (a) $T = 0.4\,\mathrm{h}$, (b) $T = 0.75\,\mathrm{h}$ and (c) $T = 1\,\mathrm{h}$; (d) simulated total suspended solids concentration ($N = 4800$) during 1 h (reference solution).

the effect of the moving mesh. The deviation from a stationary solution seems, however, to decrease with increasing N.

Table 4.6: Example 4.3: Time functions for the simulation.

Time period [h]	$X_{\mathrm{f}}(t)$[kg/m^3]	$Q_{\mathrm{f}}(t)$[m^3/h]	$Q_{\mathrm{u}}(t)$[m^3/h]	$Q_{\mathrm{e}}(t)$[m^3/h]	Model
$0 \le t < 25$	0	0	0	0	PDE
$25 \le t < 35$	0	0	0	84	PDE
$35 \le t < 45$	0	0	0	0	PDE
$45 \le t < 60$	0	40	0	0	PDE
$60 \le t < 70$	0	0	0	0	PDE

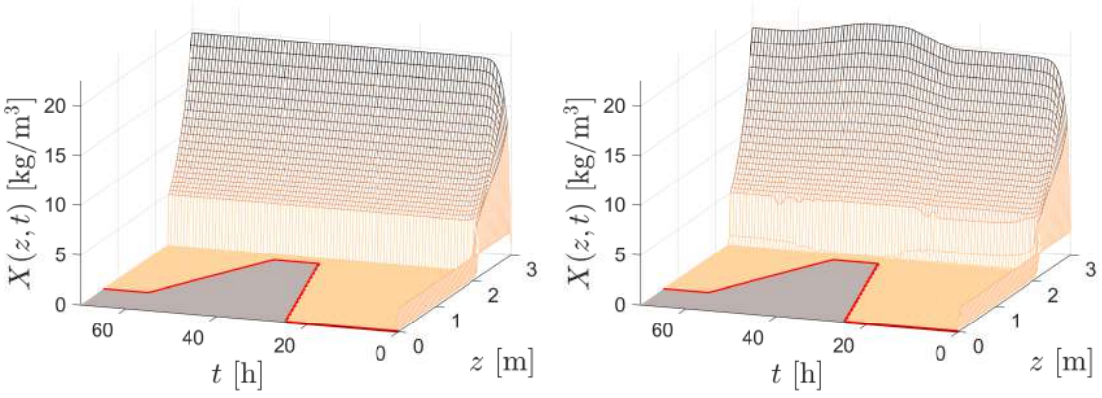

(a) SBR2 with $N = 100$

(b) Semi-implicit with $N = 100$

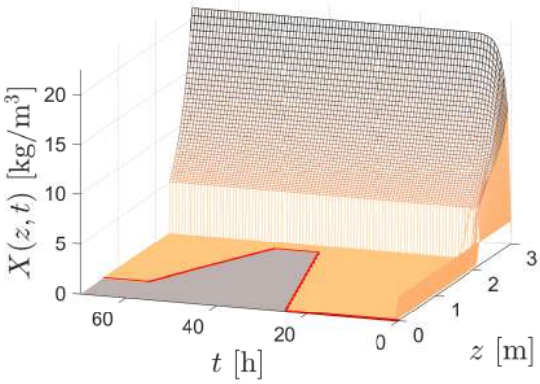

(c) SBR with $N = 200$

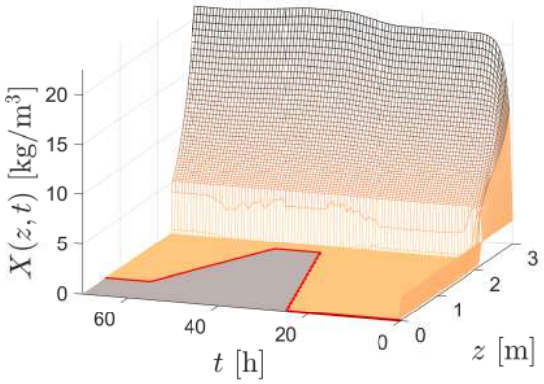

(d) Semi-implicit with $N = 200$

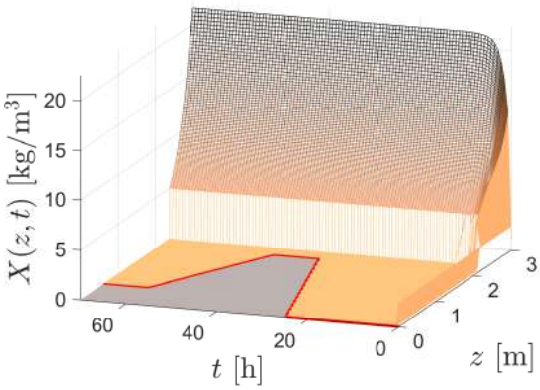

(e) SBR with $N = 400$

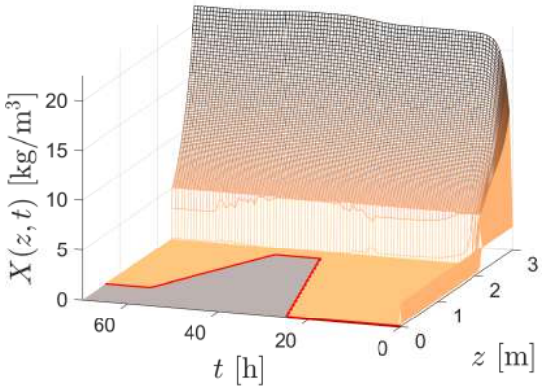

(f) Semi-implicit with $N = 400$

Figure 4.11: Example 4.3: simulations of the scenario of Table 4.6 with the indicated schemes and values of N. The fixed-mesh scheme SBR2 reproduces a steady-state profile while numerical solutions by scheme semi-implicit are affected by the moving mesh.

Conclusions and future works

Conclusions

Here we present a summary with the main contributions and conclusions of the thesis.

- In Chapter 1, we described a general model of multi-component reactive settling of flocculated particles given by a quasi-one-dimensional PDE system with moving boundary (1.26). Fill and draw of mixture at the moving surface can be made at any time and a specific application is the SBR process. The unknowns are concentrations of biomass particles and soluble substrates, and the reaction terms of the PDE model can be given by any model of biochemical reactions in wastewater treatment.

  The moving boundary can be precomputed with the ODE (1.21) containing the volumetric flows in and out of the tank. We employ the positivity-preserving numerical scheme outlined in Chapter 2 to simulate the SBR process when denitrification occurs in a tank with either constant or a varying cross-sectional area and when extreme cases of fill and draw occur.

- In Chapter 2, we discuss the numerical scheme for the multi-component reactive settling model, which was derived in Chapter 1 (Section 1.2). This model features a quasi-one-dimensional PDE system with moving boundary. The numerical scheme in Section 2.2.4 is designed to ensure conservation of mass across the surface during fill and draw. Away from the moving boundary, the scheme is the same as in [12], where it is demonstrated that its order of convergence is not more than one. The extra treatment near the surface will of course not improve that. An indication of the convergence of the numerical scheme as the mesh size is reduced is shown in Figure 2.4.

  The main result of this chapter is an invariant-region property (Theorem 2.1) for the numerical solution if the scheme is computed in a Lie-Trotter-Kato splitting way, where the first step computes intermediate variables without including reaction terms and the next step incorporates the evaluation of the reaction terms in the intermediate variables. Then, all the concentrations are non-negative, and the solids concentrations never exceed the maximal packing one. In particular, the scheme is monotone when the reaction terms

are zero. Simulations with or without splitting have shown to produce very similar outputs, and this is demonstrated by the diminishing relative error between such simulations in Table 2.4.

A proof of convergence of the method (as the cell size tends to zero) to a suitably defined entropy solution is still pending, along with the corresponding well-posedness analysis that addresses existence, uniqueness. That said, we point out that available convergence analyses for related strongly degenerate, scalar PDEs with discontinuous flux (cf., e.g., [26, 71, 72]) rely on the monotonicity of the underlying scheme as well as a uniform bound on the numerical solution, among other properties. Theorem 2.1 and its proof may be therefore viewed as a partial result to prove convergence of the numerical scheme presented herein.

Given a moving boundary and a fixed spatial discretization for the numerical scheme, local mass balances have been used to obtain correct update formulas for numerical cells near the surface.

This results in a scheme with several cases depending on the surface movement. A certain limitation of the explicit numerical scheme, used with or without splitting, is the restrictive CFL condition (where the time step is essentially proportional to the square of the cell size), implying that very small-time steps are needed if accurate approximations on a fine spatial mesh are sought. An alternative approach would be to transform the PDE system and have a fixed number of cells below the moving surface, as shown in Chapter 4. The advantage of the present fixed-cell-size numerical scheme is, however, that the model can more easily be generalized to include further sources or sinks at fixed locations, a desirable feature in applications to wastewater treatment.

- Chapter 3, a reactive-settling PDE model with standard ASM1 parameters and several constitutive assumptions on the movement of particles and dissolved substrates have been calibrated to experimental data: 22 conventional batch sedimentation experiments and one steady-state scenario of an SST in a pilot plant. The predictability of the model was evaluated to two further experimental SST scenarios. The properties of hindered settling and compression at high concentrations for the flocculated particles were successfully fitted to 22 conventional batch sedimentation experiments; see Figure 3.2. This was possible after the effects of the initial induction period of each test had been transformed away. One experimental steady-state scenario (about four data points along the depth of the tank for each concentration) was thereafter used for the additional calibration of terms in the equations modeling hydrodynamic dispersion of partly the particles, and partly the dissolved substrates. Adding more terms and parameters of course always leads to a better fit to the data used in the calibration. Therefore, two experimental scenarios were used for validation.

  The most substantial improvement between the model variants is to allow for a variable cross-sectional area instead of a constant one. There is a substantial difference in the

predicted nitrogen content in an SST during steady state; see Figure 3.11, which is one of the main purposes of the reactive-settling modeling. The inclusion of hydrodynamic dispersion modeled with two parameters leads only to such a small improvement in the predictability of the model that it is hardly worth the extra effort. The additional inclusion of a term modeling the mixing of the suspension near the feed inlet neither lead to any improved predictability. The overall conclusion is thus that a careful treatment of batch-settling data to calibrate the sedimentation-compression model was sufficient to ensure good predictability of the reactive settling process in a pilot SST.

- Chapter 4, the numerical results show that the two versions of the numerical scheme presented herein, the explicit one of Section 4.3.2 and the semi-implicit one of Section 4.4, generate physically relevant solutions (as is expressed by the invariant region principle) and are working alternatives to the scheme SBR2 in Chapter 2 of the PDE model advanced in Chapter 1. Moreover, as Example 4.2 clearly illustrates, there is a substantial gain in CPU times and efficiency of the semi-implicit version if compared with the explicit version. This gain is, of course, due to the more favorable CFL condition (CFL-SI) (for the semi-implicit scheme) that allows a larger time step than in (CFL) (for the explicit scheme). The degree of this advantage depends, of course, on the constitutive functions and parameters used, so it is important to emphasize that it appears for choices of these constitutive ingredients that are largely considered typical for activated sludge [13, 17, 79, 104].

  The SBR2 scheme of Chapter 2 is based on a fixed grid with respect to z, and the moving interface $\bar{z}(t)$ needs to be tracked explicitly. This movement gives rise to a number of cases of boundary cells of time-dependent size that need to be handled separately. That treatment is fairly involved and the approach presented in this chapter is in general easier to implement, and for the semi-implicit variant turns out to be more efficient. That said, we should mention that the fixed-grid approach from [16] has certain advantages in situations where the method must keep a consolidated bed invariant under movements of $\bar{z}(t)$ above it, as illustrated by Example 4.3. Moreover, this approach can be more easily extended to additional inlets or outlets in the reactor. It is therefore interesting to note that the observed convergence of the three schemes discussed tend to the same solution, as evidenced by Table 4.5 and Figure 4.10 (a), which supports that the treatment in [16] is correct.

  With respect to limitations, we which mention that the approach of [16] involves a vessel with variable cross-sectional area; this model ingredient has been left out in this chapter for simplicity and is not expected to make the formulation and analysis significantly more difficult. We also note that while it has been proven that the schemes are monotone and obey an invariant-region principle and numerical evidence of convergence has been presented, a rigorous convergence proof is still missing but can possibly be obtained by combining analyses of weakly coupled degenerate parabolic systems [65], numerical methods for zero-flux boundary value problems [19, 73], and studies of triangular systems

of conservation laws and degenerate convection-diffusion equations [21, 22, 31]. (In the latter reference, convergence proofs decisively depend on usage of the Engquist-Osher flux with its separable upwind and downwind contributions; this has partly motivated usage of that particular numerical flux in the present chapter).

Another extension, improvement and application of the model and numerical methods are conceivable. For instance, both scheme versions are only first-order accurate in space and time; this order can possibly be improved by applying more sophisticated variable extrapolation or maximum-principle-preserving weighted essentially non-oscillatory (WENO) techniques (cf., e.g., [70] and references cited in that work) combined with changing between the implicit and explicit steps in a more involved manner as is done in implicit-explicit (IMEX) schemes, cf., e.g., [9].

We emphasize that within the present approach soluble components are supposed to be transported passively with the fluid and are subject to the reaction terms. In some of the figures this property causes fairly sharp concentration profiles when one expects that the evolution of solute concentrations should be subject to additional effects such as dispersion/diffusion. In fact, diffusion driven by the gradient of the respective concentration was the unique mechanism of spatial propagation of solutes considered in one of the first efforts to model reactive settling by PDEs [13]. It would not be a problem to include diffusion in the present approach as an additional mechanism of solute transport, with the effect to be an overall blurring of profiles.

Future Work

- In the literature, all contributions in SBR optimization have been developed based on ODEs that model the biochemical reactions occurring during the filling and reaction stages. In future work, the model and numerical methods described in Chapters 1, 2 and 4 will allow investigations and contributions to the optimization of the reactive settling of the SBR process, which consists of five stages: filling, reaction, sedimentation, extraction, quiescence and removal, see Figure 2. Each of these stages can have sub-periods of mixing, with or without aeration, which influence the efficiency of the biochemical reactions; see [68, 107]. Contributions will be made to a general bi-objective optimization problem for the design and periodic operation of an SBR plant for a constant set of inputs (e.g., climatic conditions) that can be formulated as: Minimizing both construction cost and operating costs subject to the plant delivering effluent concentrations below the limits allowed by emission regulations. The construction cost is clearly related to the size of the plant, while the operating costs consist mainly of energy costs required for aeration of the reactor [4]. Another aspect of interest is the implementation of several SBRs coupled in series or parallel, with synchronized stages allowing, for example, to obtain a continuous effluent flow of a certain quality. This approach would allow a more accurate

comparison between SBRs and continuously operating SSTs, as one or the other can be preferred depending on the size of the plant and other practical considerations, as mentioned in [46].

- Another application with potential modeling advantages is the use of SBR with a porous bottom. In this process, the fluid is filtered through a filter medium, such as a filter cloth or membrane. This media has the property of retaining the suspended solids in the wastewater, while allowing the fluid to pass through. Although applying pressure can accelerate the filtration process, the increasing hydraulic resistance of the sediment accumulated at the bottom of the reactor can counteract the applied pressure, which can reduce the efficiency of the process. This phenomenon gives rise to a free boundary problem [18, 25], which adds complexity to the SBR model, as the trajectory of the piston pressing the fluid through the filter media depends on how the hydraulic resistance of the bottom changes over time. Understanding how this hydraulic resistance affects the piston trajectory is critical to improving the efficiency of the filtering process.

- As mentioned in several studies [33, 35, 58, 69], bubble formation is a critical problem in wastewater treatment plants with activated sludge, as it decreases the overall performance of the plant and causes operational problems. During the reaction stage of the SBR, complete biological nitrogen removal is aimed for. However, a substantial part of this is still present, such as nitrite, which is not completely removed, releasing nitrogen gas during the sedimentation phase. This release of nitrogen gas causes the formation of small bubbles in the activated sludge, resulting in the flotation of the sludge blanket in the tank. The attachment of the nitrogen gas bubbles to the particulate material occurs during the sedimentation stage of the SBR, in a zone of reverse flow, which implies that the nitrogen gas bubbles move upwards while the solid particles settle, resulting in the attachment of the bubbles to the particles. In future work, the model described in Chapter 4 will be extended to include the aforementioned aggregation process. In addition, it will be necessary to introduce an additional PDE for a third variable, e.g. the number of solid particles attached to a single bubble at each spatial position and time. The inclusion of this new PDE will allow modeling of the dynamics of gas bubbles and solid particles attached in the reactor, which will help to better understand the mechanisms governing sludge blanket formation and flotation in SBRs.

Conclusiones y Trabajos Futuros

Conclusiones

A continuación presentamos un resumen con las principales aportaciones y conclusiones de la tesis.

- En el Capítulo 1, describimos un modelo general de sedimentación reactiva multicomponente de partículas floculadas dado por un sistema EDP cuasi unidimensional con frontera móvil (1.26). El llenado y la extracción de la mezcla en la superficie móvil pueden realizarse en cualquier momento y una aplicación específica es el proceso SBR. Las incógnitas son las concentraciones de partículas de biomasa y sustratos solubles, y los términos de reacción del modelo de EDP se pueden dar por cualquier modelo de reacciones bioquímicas en el tratamiento de aguas residuales.

  La frontera móvil puede calcularse previamente con la EDO (1.21) que contiene los flujos volumétricos de entrada y salida del tanque. Empleamos el esquema numérico que preserva la positividad descrita en el Capítulo 2 para simular el proceso del SBR cuando la desnitrificación se produce en un tanque con área de sección transversal constante o variable y cuando ocurren casos extremos de llenado y extracción.

- En el Capítulo 2 , discutimos el esquema numérico para el modelo de sedimentación reactiva multicomponente, que se derivó en el Capítulo 1 (Sección 1.2). Este modelo presenta un sistema de EDP cuasi unidimensional con frontera móvil. El esquema numérico en la Sección 2.2.4 está diseñado para garantizar la conservación de la masa a través de la superficie durante el llenado y la extracción. Lejos de la frontera móvil, el esquema es el mismo que en [12], donde se demuestra que su orden de convergencia no es superior a uno. El tratamiento adicional cerca de la superficie, por supuesto, no mejorará esto. Una indicación de la convergencia del esquema numérico a medida que se reduce el tamaño de la malla se muestra en la Figura 2.4.

  El resultado principal de este capítulo es una propiedad de región invariante (Teorema 2.1) para la solución numérica si el esquema se calcula de manera de división de Lie-Trotter-Kato, donde el primer paso calcula las variables intermedias sin incluir los términos de reacción y el siguiente paso incorpora la evaluación de los términos de reacción en las

variables intermedias. Entonces, todas las concentraciones son no negativas, y las concentraciones de sólidos nunca superan la máxima de empaquetamiento. En particular, el esquema es monótono cuando los términos de reacción son cero. Las simulaciones con o sin división han demostrado producir resultados muy similares, y esto se demuestra mediante el error relativo decreciente entre tales simulaciones en la Tabla 2.4.

Una prueba de la convergencia del método (a medida que el tamaño de la celda tiende a cero) a una solución de entropía adecuadamente definida aún está pendiente, junto con el análisis de buen planteamiento correspondiente que aborda la existencia, unicidad. Dicho esto, señalamos que los análisis de convergencia disponibles para EDP escalares fuertemente degeneradas y relacionadas con flujo discontinuo (véase, por ejemplo, [26, 71, 72]) se basan en la monotonía del esquema subyacente, así como en la existencia y unicidad de la solución numérica, entre otras propiedades. El Teorema 2.1 y su prueba pueden considerarse, por lo tanto, como un resultado parcial para demostrar la convergencia del esquema numérico aquí presentado.

Dada una frontera móvil y una discretización espacial fija para el esquema numérico, se han utilizado balances de masa locales para obtener fórmulas de actualización correctas para las celdas numéricas cercanas a la superficie. Esto resulta en un esquema con varios casos dependiendo del movimiento de la superficie.

Una cierta limitación del esquema numérico explícito, utilizado con o sin división, es la restrictiva condición CFL (donde el paso de tiempo es esencialmente proporcional al cuadrado del tamaño de la celda), lo que implica que se necesitan pasos de tiempo muy pequeños si se buscan aproximaciones precisas en una malla espacial fina. Un enfoque alternativo sería transformar el sistema EDP y tener un número fijo de celdas por debajo de la superficie móvil, como se muestra en el Capítulo 4. La ventaja del presente esquema numérico de tamaño de celda fija es, sin embargo, que el modelo puede generalizarse más fácilmente para incluir más fuentes o sumideros en ubicaciones fijas, una característica deseable en aplicaciones al tratamiento de aguas residuales.

- El Capítulo 3, se ha calibrado un modelo EDP de sedimentación reactiva con parámetros ASM1 estándar y varias hipótesis constitutivas sobre el movimiento de partículas y sustratos disueltos con datos experimentales: 22 experimentos convencionales de sedimentación por lotes y un escenario en estado estacionario de un SST en una planta piloto. La predictibilidad del modelo se evaluó con otros dos escenarios experimentales de SST. Las propiedades de sedimentación obstaculizada y compresión a altas concentraciones para las partículas floculadas se ajustaron con éxito a 22 experimentos de sedimentación por lotes convencionales; véase la Figura 3.2. Esto fue posible una vez transformados los efectos del periodo de inducción inicial de cada ensayo. A continuación, se utilizó un escenario experimental de estado estacionario (unos cuatro puntos de datos a lo largo de la profundidad del tanque para cada concentración) para la calibración adicional de términos en las ecuaciones que modelan la dispersión hidrodinámica de parte de las partículas

y parte de los sustratos disueltos. Por supuesto, añadir más términos y parámetros siempre conduce a un mejor ajuste de los datos utilizados en la calibración. Por lo tanto, se utilizaron dos escenarios experimentales para la validación.

La mejora más sustancial entre las variantes del modelo es permitir un área de sección transversal variable en lugar de una constante. Hay una diferencia sustancial en el contenido de nitrógeno predicho en un SST durante el estado estacionario; véase la Figura 3.11, que es uno de los principales objetivos del modelado de sedimentación reactiva. La inclusión de la dispersión hidrodinámica modelada con dos parámetros sólo conduce a una mejora tan pequeña en la predictibilidad del modelo que apenas merece la pena el esfuerzo adicional. La inclusión adicional de un término que modele la mezcla de la suspensión cerca de la entrada de alimentación tampoco conduce a ninguna mejora de la predictibilidad. La conclusión general es, por tanto, que un tratamiento cuidadoso de los datos de sedimentación por lotes para calibrar el modelo de sedimentación-compresión fue suficiente para asegurar una buena predictibilidad del proceso de sedimentación reactiva en un SST piloto.

- El Capítulo 4, los resultados numéricos muestran que las dos versiones del esquema numérico aquí presentado, el explícito de la Sección 4.3.2 y el semi-implícito en la Sección 4.4, generan soluciones físicamente relevantes (como lo expresa el principio de la región invariante) y son alternativas funcionales al esquema SBR2 en el Capítulo 2 del modelo EDP avanzado en el Capítulo 1. Por otra parte, como el Ejemplo 4.2 ilustra claramente, hay una ganancia sustancial en tiempos de CPU y la eficiencia de la versión semi-implícita si se compara con la versión explícita. Esta ganancia se debe, por supuesto, a la condición CFL más favorable (CFL-SI) (para el esquema semi-implícito) que permite un paso de tiempo mayor que en (CFL) (para el esquema explícito). El grado de esta ventaja depende, por supuesto, de las funciones constitutivas y los parámetros utilizados, por lo que es importante enfatizar que aparece para elecciones de estos ingredientes constitutivos que en gran medida se consideran típicas para lodos activados [13, 17, 79, 104].

  El esquema SBR2 del Capítulo 2 se basa en una malla fija con respecto a z, y la superficie móvil $\bar{z}(t)$ necesita ser rastreada explícitamente. Este movimiento da lugar a una serie de casos de celdas de límite de tamaño dependiente del tiempo que deben tratarse por separado. Ese tratamiento es bastante complicado y el enfoque presentado en este capítulo es, en general, más fácil de implementar, y para la variante semi-implícita resulta ser más eficiente. Dicho esto, mencionamos que el enfoque de malla fija de [16] tiene ciertas ventajas en situaciones en las que el método debe mantener invariante un lecho consolidado bajo movimientos de $\bar{z}(t)$ por encima de él, como se ilustra en el Ejemplo 4.3. Además, este enfoque puede extenderse más fácilmente a entradas o salidas adicionales en el reactor. Por lo tanto, es interesante señalar que la convergencia observada de los tres esquemas discutidos tienden a la misma solución, como lo demuestran la Tabla 4.5 y la Figura 4.10 (a), lo que apoya que el tratamiento en [16] es correcto.

Con respecto a las limitaciones, mencionamos que el planteamiento de [16] implica un recipiente con área de sección transversal variable; este componente del modelo se ha omitido aquí por simplicidad y no se espera que dificulte significativamente la formulación y el análisis. También hay que señalar que, si bien se ha demostrado que los esquemas son monótonos y obedecen a un principio de región invariante y se ha presentado evidencia numérica de convergencia, todavía falta una prueba rigurosa de convergencia, pero posiblemente se puede obtener mediante la combinación de análisis de sistemas parabólicos degenerados débilmente acoplados [65], métodos numéricos para problemas de valor límite de flujo cero [19, 73], y estudios de sistemas triangulares de leyes de conservación y ecuaciones de convección-difusión degeneradas [21, 22, 31]. (En esta última referencia, las pruebas de convergencia dependen decisivamente de la utilización del flujo Engquist-Osher con sus contribuciones separables a favor y en contra del flujo; esto ha motivado en parte el uso de ese flujo numérico particular en el presente capítulo).

Son concebibles otras ampliaciones, mejoras y aplicaciones del modelo y de los métodos numéricos. Por ejemplo, ambas versiones del esquema solo tienen una precisión de primer orden en el espacio y tiempo; este orden puede mejorarse aplicando técnicas más sofisticadas de extrapolación de variables o técnicas ponderadas esencialmente no oscilatorias (WENO, por sus siglas en inglés) que preservan el principio máximo (véase, por ejemplo, [70] y las referencias citadas en ese trabajo) combinadas con el cambio entre los pasos implícitos y explícitos de una manera más compleja, como se hace en los esquemas implícito-explícito (IMEX), véase, por ejemplo, [9].

Destacamos que en el presente enfoque se supone que los componentes solubles se transportan pasivamente con el fluido y están sujetos a los términos de reacción. En algunas de las figuras esta propiedad causa perfiles de concentración bastante agudos cuando uno espera que la evolución de las concentraciones de soluto debería estar sujeta a efectos adicionales como la dispersión/difusión. De hecho, la difusión impulsada por el gradiente de la concentración respectiva fue el único mecanismo de propagación espacial de solutos considerado en uno de los primeros esfuerzos por modelizar la sedimentación reactiva mediante EDPs [13]. No sería un problema incluir la difusión en el enfoque actual como un mecanismo adicional de transporte de solutos, con el efecto de difuminar globalmente los perfiles.

Trabajo Futuro

- En la literatura, todos los aportes en la optimización del SBR, se han desarrollado modelos basados en EDOs que modelan las reacciones bioquímicas ocurridas durante las etapas de llenado y reacción. En trabajos futuros, el modelo y los métodos numéricos descritos en los Capítulos 1, 2 y 4 permitirá realizar investigaciones y contribuciones en la optimización de la sedimentación reactiva del proceso de SBR, el cual consta de cinco etapas:

llenado, reacción, sedimentación, extracción, reposo y remoción, ver Figura 4. Cada una de estas etapas pueden tener sub-períodos de mezcla, con o sin aireación, que influyen en la eficacia de las reacciones bioquímicas; ver [68, 107]. Se realizarán contribuciones a un problema general de optimización bi-objetivo para el diseño y operación periódica de una planta SBR para un conjunto constante de datos de entradas (por ejemplo, condiciones climáticas) que se pueda formular como: Minimizar tanto el costo de construcción como los costos de funcionamiento sujetos a que la planta entregue concentraciones de efluentes por debajo de los límites permitidos por las normativas de emisión. El costo de construcción está claramente relacionado con el tamaño de la planta, mientras que los costos de operación consisten principalmente en costos de energía requeridos para la aireación del reactor [4]. Otro aspecto de interés es la implementación de varios SBR acoplados en serie o paralelo, con etapas sincronizadas que permitan, por ejemplo, obtener un flujo continuo de efluente de cierta calidad. Este enfoque permitiría una comparación más precisa entre los SBR y los SST de funcionamiento continuo, ya que se puede preferir uno u otro en función del tamaño de la planta y de otras consideraciones prácticas, como se menciona en [46].

- Otra aplicación con posibles ventajas de modelado es el uso del SBR con fondo poroso. En este proceso, el líquido se filtra a través de un medio filtrante, como puede ser una tela filtrante o una membrana. Este medio tiene la propiedad de retener los sólidos suspendidos en el agua residual, mientras permite el paso del fluido. Aunque aplicar presión puede acelerar el proceso de filtración, la creciente resistencia hidráulica del sedimento acumulado en el fondo del reactor puede contrarrestar la presión aplicada, lo que puede reducir la eficiencia del proceso. Este fenómeno da origen a un problema de frontera libre [18, 25], el cual añade complejidad al modelo SBR, ya que la trayectoria del pistón que presiona el fluido a través del medio filtrante depende de cómo cambia la resistencia hidráulica del fondo a lo largo del tiempo. Comprender como esta resistencia hidráulica afecta la trayectoria del pistón es fundamental para mejorar la eficacia del proceso de filtrado.

- Como se menciona en diversos estudios [33, 35, 58, 69], la formación de burbujas es un problema crítico en las plantas de tratamiento de aguas residuales con lodos activados, ya que disminuyen el rendimiento general de la planta y causan problemas operativos. Durante la etapa de reacción del SBR, se busca la eliminación biológica completa del nitrógeno. Sin embargo, una parte sustancial de esto, sigue presente, como lo es el nitrito, que no se elimina por completo, liberando gas nitrógeno durante la fase de sedimentación. Esta liberación de gas nitrógeno provoca la formación de pequeñas burbujas en el lodo activado, dando como resultado la flotación del manto de lodo en el tanque. La adhesión de las burbujas de gas nitrógeno al material particulado ocurre durante la etapa de sedimentación del SBR, en una zona de flujo en sentido contrario, lo que implica que las burbujas de gas nitrógeno se mueven hacia arriba mientras las partículas sólidas sedimentan [75], produciéndose la unión de las burbujas a las partículas. En trabajos futuros, se

ampliará el modelo descrito en el Capítulo 4 para incluir el proceso de agregación mencionado. Además, será necesario introducir una EDP adicional para una tercera variable, por ejemplo, el número de partículas sólidas adheridas a una sola burbuja en cada posición espacial y tiempo. La inclusión de esta nueva EDP permitirá modelar la dinámica de las burbujas de gas y las partículas sólidas adheridas en el reactor, lo que ayudara a comprender mejor los mecanismos que rigen la formación y flotación del manto de lodo en los SBRs.

References

[1] Adimurthi, J. Jaffré, and G. D. V. Gowda, *Godunov-type methods for conservation laws with a flux function discontinuous in space*, SIAM J. Numer. Anal., 42 (2004), pp. 179–208.

[2] M. Ahnert, T. Schalk, H. Brückner, J. Effenberger, V. Kuehn, and P. Krebs, *Organic matter parameters in wwtp–a critical review and recommendations for application in activated sludge modelling*, Water Sci. Technol., 84 (2021), pp. 2093–2112.

[3] J. Alex, S. G. E. Rönner-Holm, M. Hunze, and N. C. Holm, *A combined hydraulic and biological SBR model*, Wat. Sci. Tech., 64 (2011), pp. 1025–1031.

[4] L. Åmand, G. Olsson, and B. Carlsson, *Aeration control–a review*, Water Sci. Technol., 67 (2013), pp. 2374–2398.

[5] M. M. Amin, M. H. Khiadani, A. Fatehizadeh, and E. Taheri, *Validation of linear and non-linear kinetic modeling of saline wastewater treatment by sequencing batch reactor with adapted and non-adapted consortiums*, Desalination, 344 (2014), pp. 228–235.

[6] H. M. Anderson and R. V. Edwards, *A finite differencing scheme for the dynamic simulation of continuous sedimentation*, AIChE Symposium Series, 77 (1981), pp. 227–238.

[7] B. Andreianov, K. H. Karlsen, and N. H. Risebro, *A theory of L^1-dissipative solvers for scalar conservation laws with discontinuous flux*, Arch. Ration. Mech. Anal., 201 (2011), pp. 1–60.

[8] W. Bennett, N. Nikiforakis, and R. Klein, *A moving boundary flux stabilization method for cartesian cut-cell grids using directional operator splitting*, J. Comput. Phys., 368 (2018), pp. 333–358.

[9] S. Boscarino, R. Bürger, P. Mulet, G. Russo, and L. M. Villada, *Linearly implicit IMEX Runge-Kutta methods for a class of degenerate convection-diffusion problems*, SIAM J. Sci. Comput., 37 (2015), pp. B305–B331.

[10] M. C. Bournazou, K. Hooshiar, H. Arellano-Garcia, G. Wozny, and G. Lyberatos, *Model based optimization of the intermittent aeration profile for sbrs under partial nitrification*, Water Res., 47 (2013), pp. 3399–3410.

[11] R. Bürger, J. Careaga, and S. Diehl, *A simulation model for settling tanks with varying cross-sectional area*, Chem. Eng. Commun., 204 (2017), pp. 1270–1281.

[12] R. Bürger, J. Careaga, and S. Diehl, *A method-of-lines formulation for a model of reactive settling in tanks with varying cross-sectional area*, IMA J. Appl. Math., 86 (2021), pp. 514–546.

[13] R. Bürger, J. Careaga, S. Diehl, C. Mejías, I. Nopens, E. Torfs, and P. A. Vanrolleghem, *Simulations of reactive settling of activated sludge with a reduced biokinetic model*, Computers Chem. Eng., 92 (2016), pp. 216–229.

[14] R. Bürger, J. Careaga, S. Diehl, and R. Pineda, *Numerical schemes for a moving-boundary convection-diffusion-reaction model of sequencing batch reactors.* Preprint 2023–11, Centro de Investigación en Ingeniería Matemática (CI^{2}MA), Universidad de Concepción, Chile.

[15] R. Bürger, J. Careaga, S. Diehl, and R. Pineda, *A moving-boundary model of reactive settling in wastewater treatment. part 1: Governing equations*, Appl. Math. Model., 106 (2022), pp. 390–401.

[16] R. Bürger, J. Careaga, S. Diehl, and R. Pineda, *A moving-boundary model of reactive settling in wastewater treatment. part 2: Numerical scheme*, Appl. Math. Model., 111 (2022), pp. 247–269.

[17] R. Bürger, J. Careaga, S. Diehl, and R. Pineda, *A model of reactive settling of activated sludge: Comparison with experimental data*, Chem. Eng. Sci., 267 (2023), p. 118244.

[18] R. Bürger, F. Concha, and K. H. Karlsen, *Phenomenological model of filtration processes: 1. Cake formation and expression*, Chem. Eng. Sci., 56 (2001), pp. 4537–4553.

[19] R. Bürger, A. Coronel, and M. Sepúlveda, *A semi-implicit monotone difference scheme for an initial-boundary value problem of a strongly degenerate parabolic equation modeling sedimentation-consolidation processes*, Math. Comp., 75 (2006), pp. 91–112.

[20] R. Bürger, S. Diehl, S. Farås, I. Nopens, and E. Torfs, *A consistent modelling methodology for secondary settling tanks: a reliable numerical method*, Water Sci. Tech., 68 (2013), pp. 192–208.

[21] R. Bürger, S. Diehl, M. C. Martí, and Y. Vásquez, *A degenerating convection-diffusion system modelling froth flotation with drainage*, IMA J. Appl. Math., 87 (2022), pp. 1151–1190.

[22] R. Bürger, S. Diehl, M. C. Martí, and Y. Vásquez, *A difference scheme for a triangular system of conservation laws with discontinuous flux modeling three-phase flows*, Netw. Heterog. Media, 18 (2023), pp. 140–190.

[23] R. Bürger, S. Diehl, and C. Mejías, *A difference scheme for a degenerating convection-diffusion-reaction system modelling continuous sedimentation*, ESAIM: Math. Modelling Numer. Anal., 52 (2018), pp. 365–392.

[24] R. Bürger, S. Diehl, and I. Nopens, *A consistent modelling methodology for secondary settling tanks in wastewater treatment*, Water Res., 45 (2011), pp. 2247–2260.

[25] R. Bürger, H. Frid, and K. H. Karlsen, *On a free boundary problem for a strongly degenerate quasi-linear parabolic equation with an application to a model of pressure filtration*, SIAM J. Math. Anal., 34 (2002), pp. 611–635.

[26] R. Bürger, K. H. Karlsen, and J. D. Towers, *A model of continuous sedimentation of flocculated suspensions in clarifier-thickener units*, SIAM J. Appl. Math., 65 (2005), pp. 882–940.

[27] M. Caluwé, D. Daens, R. Blust, L. Geuens, and J. Dries, *The sequencing batch reactor as an excellent configuration to treat wastewater from the petrochemical industry*, Water Sci. Tech., 75 (2016), pp. 793–801.

[28] J. Chancelier, M. Cohen de Lara, and F. Pacard, *Analysis of a conservation PDE with discontinuous flux: a model of settler*, SIAM J. Appl. Math., 54 (1994), pp. 954–995.

[29] G. Chauvon, J. L. Vasel, and A. V. Wouwer, *Dynamic simulation and optimisation of a sbr wastewater treatment system*, in 2016 20th International Conference on System Theory, Control and Computing (ICSTCC), 2016, pp. 198–203.

[30] G. Chen, M. C. M. van Loosdrecht, G. A. Ekama, and D. Brdjaniovic, *Biological Wastewater Treatment*, IWA Publishing, London, UK, second ed., 2020.

[31] G. M. Coclite, S. Mishra, and N. H. Risebro, *Convergence of an Engquist-Osher scheme for a multi-dimensional triangular system of conservation laws*, Math. Comp., 79 (2010), pp. 71–94.

[32] M. Coelho, C. Russo, and O. Araujo, *Optimization of a sequencing batch reactor for biological nitrogen removal*, Water Res., 34 (2000), pp. 2809–2817.

[33] M. C. Collivignarelli, M. Baldi, A. Abbà, F. M. Caccamo, M. Carnevale Miino, E. C. Rada, and V. Torretta, *Foams in wastewater treatment plants: From causes to control methods*, Appl. Sci., 10 (2020), p. 2716.

[34] J. B. Copp, *The COST simulation benchmark – description and simulator manual*, tech. rep., Luxembourg: Office for Official Publications of the European Communities, 2002.

[35] A. Dapena-Mora, B. Arrojo, J. L. Campos, A. Mosquera-Corral, and R. Méndez, *Improvement of the settling properties of anammox sludge in an sbr*, J. Chem. Technol. Biotechnol., 79 (2004), pp. 1417–1420.

[36] J. De Clercq, *Batch and Continuous Settling of Activated Sludge: In-Depth Monitoring and 1D Compressive Modelling*, PhD thesis, Faculty of Engineering, Ghent University, 2006.

[37] J. De Clercq, M. Devisscher, I. Boonen, P. A. Vanrolleghem, and J. Defrancq, *A new one-dimensional clarifier model – verification using full-scale experimental data*, Water Sci. Tech., 47 (2003), pp. 105–112.

[38] J. De Clercq, F. Jacobs, D. J. Kinnear, I. Nopens, R. A. Dierckx, J. Defrancq, and P. A. Vanrolleghem, *Detailed spatio-temporal solids concentration profiling during batch settling of activated sludge using a radiotracer*, Water Res., 39 (2005), pp. 2125–2135.

[39] J. De Clercq, I. Nopens, J. Defrancq, and P. A. Vanrolleghem, *Extending and calibrating a mechanistic hindered and compression settling model for activated sludge using in-depth batch experiments*, Water Res., 42 (2008), pp. 781–791.

[40] K. Deimling, *Nonlinear Functional Analysis*, Springer-Verlag, Berlin, 1985.

[41] DHI, *West models guide, asm1temp [activated sludge model no. 1 with temperature correction and ammonium limitation for aerobic and anoxic growth of heterotrophs]*. http://doc.mikepoweredbydhi.help/webhelp/2017/TornadoModels/WEST_Models_Guide/Categories/ASM1Temp/ASM1Temp.htm, accessed September 2022.

[42] S. Diehl, *On scalar conservation laws with point source and discontinuous flux function*, SIAM J. Math. Anal., 26 (1995), pp. 1425–1451.

[43] S. Diehl, *A conservation law with point source and discontinuous flux function modelling continuous sedimentation*, SIAM J. Appl. Math., 56 (1996), pp. 388–419.

[44] S. Diehl, *Dynamic and steady-state behavior of continuous sedimentation*, SIAM J. Appl. Math., 57 (1997), pp. 991–1018.

[45] S. Diehl, *Numerical identification of constitutive functions in scalar nonlinear convection–diffusion equations with application to batch sedimentation*, Appl. Num. Math., 95 (2015), pp. 154–172.

[46] R. Droste and R. Gear, *Theory and Practice of Water and Wastewater Treatment*, Wiley, Hoboken, NJ, USA, 2nd ed., 2019.

[47] B. Engquist and S. Osher, *One-sided difference approximations for nonlinear conservation laws*, Math. Comp., 36 (1981), pp. 321–351.

[48] S. Evje and K. H. Karlsen, *Degenerate convection-diffusion equations and implicit monotone difference schemes*, in Hyperbolic Problems: Theory, Numerics, Applications, Vol. I (Zürich, 1998), vol. 129 of Internat. Ser. Numer. Math., Birkhäuser, Basel, 1999, pp. 285–294.

[49] R. Eymard, T. Gallouët, and R. Herbin, *Finite volume methods*, in Handbook of Numerical Analysis, Vol. VII, Handb. Numer. Anal., VII, North-Holland, Amsterdam, 2000, pp. 713–1020.

[50] X. Flores-Alsina, K. Gernaey, and U. Jeppsson, *Benchmarking biological nutrient removal in wastewater treatment plants: Influence of mathematical model assumptions*, Water Sci. Tech., 65 (2012), pp. 1496–1505.

[51] L. Formaggia and A. Scotti, *Positivity and conservation properties of some integration schemes for mass action kinetics*, SIAM J. Num. Anal., 49 (2011), pp. 1267–1288.

[52] P. François, F. Locatelli, J. Laurent, and K. Bekkour, *Experimental study of activated sludge batch settling velocity profile*, Flow Meas, 48 (2016), pp. 112–117.

[53] E. Freytez, A. Márquez, M. Pire, E. Guevara, and S. Perez, *Nitrogenated substrate removal modeling in sequencing batch reactor oxic-anoxic phases*, J. Environ. Eng., 145 (2019), p. 04019068.

[54] P. Gajardo, H. Ramírez, and A. Rapaport, *Minimal time sequential batch reactors with bounded and impulse controls for one or more species*, SIAM J. Control Optim., 47 (2008), pp. 2827–2856.

[55] K. V. Gernaey, U. Jeppsson, D. J. Batstone, and P. Ingildsen, *Impact of reactive settler models on simulated WWTP performance*, Water Sci. Tech., 53 (2006), pp. 159–167.

[56] T. Gimse and N. H. Risebro, *Solution of the Cauchy problem for a conservation law with a discontinuous flux function*, SIAM J. Math. Anal., 23 (1992), pp. 635–648.

[57] J. Guerrero, X. Flores-Alsina, A. Guisasola, J. A. Baeza, and K. V. Gernaey, *Effect of nitrite, limited reactive settler and plant design configuration on the predicted performance of simultaneous C/N/P removal WWTPs*, Bioresource Tech., 136 (2013), pp. 680–688.

[58] F. Guo, Z.-P. Wang, K. Yu, and T. Zhang, *Detailed investigation of the microbial community in foaming activated sludge reveals novel foam formers*, Sci. Rep., 5 (2015), pp. 1–9.

[59] J. Hamilton, R. Jain, P. Antoniou, S. A. Svoronos, B. Koopman, and G. Lyberatos, *Modeling and pilot-scale experimental verification for predenitrification process*, J. Environ. Eng., 118 (1992), pp. 38–55.

[60] H. Hauduc, L. Rieger, I. Takács, A. Héduit, P. Vanrolleghem, and S. Gillot, *A systematic approach for model verification: application on seven published activated sludge models*, Water Sci. Technol., 61 (2010), pp. 825–839.

[61] M. Henze, C. P. L. Grady, W. Gujer, G. V. R. Marais, and T. Matsuo, *Activated sludge model no.* 1, Tech. Rep. 1, IAWQ, London, UK, 1987.

[62] M. Henze, C. P. L. Grady, W. Gujer, G. V. R. Marais, and T. Matsuo, *A general model for single-sludge wastewater treatment systems*, Water Res., 21 (1987), pp. 505–515.

[63] M. Henze, Gujer, T. W., Mino, and M. C. M. van Loosdrecht, *Activated Sludge Models ASM1, ASM2, ASM2d and ASM3*, IWA Scientific and Technical Report No. 9, IWA Publishing, London, UK, 2000.

[64] H. Holden, K. H. Karlsen, K.-A. Lie, and N. H. Risebro, *Splitting Methods for Nonlinear Partial Differential Equations with Rough coefficients: Analysis and MATLAB programs*, European Mathematical Society Publishing House, Zürich, Switzerland, 2010.

[65] H. Holden, K. H. Karlsen, and N. H. Risebro, *On uniqueness and existence of entropy solutions of weakly coupled systems of nonlinear degenerate parabolic equations*, Electron. J. Differential Equations, (2003), p. 46.

[66] Z. Hu, R. A. Ferraina, J. F. Ericson, A. A. MacKay, and B. F. Smets, *Biomass characteristics in three sequencing batch reactors treating a wastewater containing synthetic organic chemicals*, Water Res., 39 (2005), pp. 710–720.

[67] I. Irizar, *A mathematical framework for optimum design and operation of SBR processes*, J. Water Process Eng., 39 (2021), p. 101703.

[68] R. L. Irvine, L. H. Ketchum Jr, and T. Asano, *Sequencing batch reactors for biological wastewater treatment*, Crit Rev Environ Sci Technol., 18 (1989), pp. 255–294.

[69] D. Jenkins, M. G. Richard, and G. T. Daigger, *Manual on the causes and control of activated sludge bulking, foaming, and other solids separation problems*, Crc Press, 2003.

[70] Y. Jiang and Z. Xu, *Parametrized maximum principle preserving limiter for finite difference WENO schemes solving convection-dominated diffusion equations*, SIAM J. Sci. Comput., 35 (2013), pp. A2524–A2553.

[71] K. H. Karlsen, N. H. Risebro, and J. D. Towers, *Upwind difference approximations for degenerate parabolic convection-diffusion equations with a discontinuous coefficient*, IMA J. Numer. Anal., 22 (2002), pp. 623–664.

[72] K. H. Karlsen, N. H. Risebro, and J. D. Towers, *L^1 stability for entropy solutions of nonlinear degenerate parabolic convection-diffusion equations with discontinuous coefficients*, Trans. Royal Norwegian Society Sci. Letters (Skr. K. Nor. Vidensk. Selsk.), 3 (2003), pp. 1–49.

[73] K. H. Karlsen and J. D. Towers, *Convergence of monotone schemes for conservation laws with zero-flux boundary conditions*, Adv. Appl. Math. Mech., 9 (2017), pp. 515–542.

[74] J. Kauder, N. Boes, C. Pasel, and J.-D. Herbell, *Combining models ADM1 and ASM2d in a sequencing batch reactor simulation*, Chem. Eng. Technol., 30 (2007), pp. 1100–1112.

[75] J. H. Kim, H. S. Kim, and B. H. Lee, *Combination of sequential batch reactor (sbr) and dissolved ozone flotation-pressurized ozone oxidation (dof-po 2) processes for treatment of pigment processing wastewater*, Environ. Eng. Res., 16 (2011), pp. 97–102.

[76] Y. Kim, C. Yoo, Y. Kim, and I.-B. Lee, *Simulation and activated sludge model-based iterative learning control for a sequencing batch reactor*, Environ. Eng. Sci., 26 (2009), pp. 661–671.

[77] G. Kirim, *Modelling and model-based optimization of N-removal WRRFs: reactive settling, conventional & short-cut N-removal processes*, PhD thesis, Université Laval, 2022.

[78] G. Kirim, E. Torfs, and P. Vanrolleghem, *A 1-d reactive Bürger-Diehl settler model for SST denitrification considering clarifier geometry*, in Proceedings: 10th IWA Symposium on Modelling and Integrated Assessment (Watermatex 2019), 2019. Copenhagen, Denmark, Sept. 1–4, 2019.

[79] G. Kirim, E. Torfs, and P. . A. Vanrolleghem, *An improved 1d reactive Bürger–Diehl settler model for secondary settling tank denitrification*, Water Environ. Res., 94 (2022), p. e10825.

[80] G. Koch, R. Pianta, P. Krebs, and H. Siegrist, *Potential of denitrification and solids removal in the rectangular clarifier*, Water Res., 33 (1999), pp. 309–318.

[81] J. Kocijan and N. Hvala, *Sequencing batch-reactor control using gaussian-process models*, Bioresource Technol., 137 (2013), pp. 340–348.

[82] D. Li, H. Z. Yang, and X. F. Liang, *Application of Bayesian networks for diagnosis analysis of modified sequencing batch reactor*, Adv. Mater. Res., 610-613 (2012), pp. 1139–1145.

[83] Z. Li, R. Qi, B. Wang, Z. Zou, G. Wei, and M. Yang, *Cost-performance analysis of nutrient removal in a full-scale oxidation ditch process based on kinetic modeling*, J. Environ. Sci., 25 (2013), pp. 26–32.

[84] F. Locatelli, P. François, J. Laurent, F. Lawniczak, M. Dufresne, J. Vazquez, and K. Bekkour, *Detailed velocity and concentration profiles measurement during activated sludge batch settling using an ultrasonic transducer*, Sep. Sci. Tech., 50 (2015), pp. 1059–1065.

[85] C. Lu, W. Huang, and E. S. Van Vleck, *The cutoff method for the numerical computation of nonnegative solutions of parabolic pdes with application to anisotropic diffusion and lubrication-type equations*, J. Comput. Phys., 242 (2013), pp. 24–36.

[86] J. Makinia and E. Zaborowska, *Mathematical Modelling and Computer Simulation of Activated Sludge Systems*, IWA Publishing, London, UK, 2nd ed., 2020.

[87] D. Massé, *Comprehensive model of anaerobic digestion of swine manure slurry in a sequencing batch reactor*, Water Res., 34 (2000), pp. 3087–3106.

[88] T. Meadows, M. Weedermann, and G. S. K. Wolkowicz, *Global analysis of a simplified model of anaerobic digestion and a new result for the chemostat*, SIAM J. Appl. Math., 79 (2019), pp. 668–689.

[89] L. Metcalf and H. P. Eddy, *Wastewater Engineering. Treatment and Resource Recovery*, McGraw-Hill, New York, USA, 5th ed., 2014.

[90] J. D. Murray, *Mathematical biology: I. An introduction*, vol. 17, Springer, New York, NY, third ed ed., 2002.

[91] U. Nations, *Sustainable development goals*. https://www.un.org/sustainabledevelopment/, accessed November 2022.

[92] U. Nations, *Water and sanitation*. https://www.un.org/sustainabledevelopment/water-and-sanitation/, accessed November 2022.

[93] J. A. Nelder and R. Mead, *A simplex method for function minimization*, Comput. J, 7 (1965), pp. 308–313.

[94] B.-J. Ni, A. Joss, and Z. Yuan, *Modeling nitrogen removal with partial nitritation and anammox in one floc-based sequencing batch reactor*, Water Res., 67 (2014), pp. 321–329.

[95] G. S. Ostace, V. M. Cristea, and P. S. Agachi, *Evaluation of different control strategies of the waste water treatment plant based on a modified activated sludge model no. 3*, Environ. Eng. Management J., 11 (2012), pp. 147–164.

[96] V. Pambrun, E. Paul, and M. Spérandio, *Control and modelling of partial nitrification of effluents with high ammonia concentrations in sequencing batch reactor*, Chem. Eng. Process. Process Intensif., 47 (2008), pp. 323–329.

[97] R. Piotrowski, M. Lewandowski, and A. Paul, *Mixed integer nonlinear optimization of biological processes in wastewater sequencing batch reactor*, J. Process Control, 84 (2019), pp. 89–100.

[98] T. Popple, J. Williams, E. May, G. Mills, and R. Oliver, *Evaluation of a sequencing batch reactor sewage treatment rig for investigating the fate of radioactively labelled pharmaceuticals: Case study of propranolol*, Water Res., 88 (2016), pp. 83–92.

[99] H. Siegrist, P. Krebs, R. Bühler, I. Purtschert, C. Rock, and R. Rufer, *Denitrification in secondary clarifiers*, Water Sci. Tech., 31 (1995), pp. 205–214.

[100] G. Sin, G. Insel, D. Lee, and P. Vanrolleghem, *Optimal but robust n and p removal in sbrs: a model-based systematic study of operation scenarios*, Water Sci. Technol., 50 (2004), pp. 97–105.

[101] M. Singh and R. K. Srivastava, *Sequencing batch reactor technology for biological wastewater treatment: a review*, Asia-Pacific J. Chem. Eng., 6 (2010), pp. 3–13.

[102] B. Song, Z. Tian, R. van der Weijden, C. Buisman, and J. Weijma, *High-rate biological selenate reduction in a sequencing batch reactor for recovery of hexagonal selenium*, Water Res., 193 (2021), p. 116855.

[103] S. M. Souza, O. Q. F. Araújo, and M. A. Z. Coelho, *Model-based optimization of a sequencing batch reactor for biological nitrogen removal*, Bioresource Tech., 99 (2008), pp. 3213–3223.

[104] E. Torfs, S. Balemans, F. Locatelli, S. Diehl, R. Bürger, J. Laurent, P. François, and I. Nopens, *On constitutive functions for hindered settling velocity in 1-d settler models: Selection of appropriate model structure*, Water Res., 110 (2017), pp. 38–47.

[105] P. Vanrolleghem, D. Van der Schueren, G. Krikilion, K. Grijspeerdt, P. Willems, and W. Verstraete, *On-line quantification of settling properties with in-sensor-experiments in an automated settlometer*, Water Sci. Tech., 33 (1996), pp. 37–51.

[106] S. Wang and C. K. Gunsch, *Effects of selected pharmaceutically active compounds on treatment performance in sequencing batch reactors mimicking wastewater treatment plants operations*, Water Res., 45 (2011), pp. 3398–3406.

[107] N. E. I. WATER, *Sequencing batch reactor design and operational considerations*, 2005.

[108] X. Zhang and C.-W. Shu, *Maximum-principle-satisfying and positivity-preserving high-order schemes for conservation laws: survey and new developments*, Proc. Math. Phys. Eng. Sci. P ROY SOC A-MATH PHY, 467 (2011), pp. 2752–2776.